THE SYNTHESIS, DOPING, AND CHARACTERIZATION OF GRAPHENE FILMS

A Dissertation
Presented to
The Academic Faculty

by

Hossein Sojoudi

In Partial Fulfillment
of the Requirements for the Degree
Doctor of Philosophy in the
George W. Woodruff School of Mechanical Engineering

Georgia Institute of Technology
December 2012

THE SYNTHESIS, DOPING, AND CHARACTERIZATION OF GRAPHENE FILMS

Approved by:

Dr. Samuel Graham, Advisor
School of Mechanical Engineering
Georgia Institute of Technology

Dr. Baratunde Cola
School of Mechanical Engineering
Georgia Institute of Technology

Dr. Hamid Garmestani
School of School of Materials Science and Engineering
Georgia Institute of Technology

Dr. Kyriaki Kalaitzidou
School of Mechanical Engineering
Georgia Institute of Technology

Dr. Jiang Zhigang
School of Physics
Georgia Institute of Technology

Dr. Dennis Hess
School of Chemical & Biomolecular Engineering
Georgia Institute of Technology

Date Approved: 08/07/2012

To my parents Laeya Abdali Bovani and Mohammad Sojoudi

ACKNOWLEDGEMENTS

But by the grace of God who has been faithful and has provided me with the energy, support, time, motivation, and intellect necessary for the research presented in this dissertation. I would like to thank my family for their patience for not being able to see me for more than four years, for their love, support, and prayers during this time. I especially thank my parents who have always been a constant support in every endeavor I have set out to do; for that I am most appreciative. I would like to thank my parents for their love, endless support, and encouragement. I thank my siblings, Lida, Omid, and Rita. It really meant a lot to have loving siblings who I knew wanted me to achieve to my fullest ability and who would do whatever they could to enable that. I acknowledge Amir Mahdi and Reza, my nephews, and Asal and Mahdia, my nieces for their support and love. I am thankful to my long time roommate, Ehsan Najafabadi, for the many, many discussions about science, religion, and life that we have shared in our time at GT together. Ehsan served as a true friend throughout this process.

This dissertation could not have been completed without dedicated help and support from numerous people. I begin by thanking my advisor, Professor Samuel Graham, who provided me continuous encouragement and confidence for completing my research. I am glad and appreciative to have had the opportunity to work under his advisement. I am grateful for the environment facilitated by Prof. Graham, which promoted scientific growth and maturity. I also wish to express my gratitude to my dissertation committee members: Professors Dennis Hess, Hamid Garmestani, Zhigang Jiang, Kyriaki Kalaitzidou, and Baratunde Cola for their helpful advice offered during my dissertation completion process. I would like to specially thank Dr. Zhigang Jiang at the Georgia Tech Physics Department, who always had his door open whenever I had questions and needed help.

Special thanks go to Dr. Jeffrey Donnell who helped me in writing my thesis and my articles, providing me quick, valuable feedback during my PhD career at Georgia Tech. I would like to thank Dr. Anusha Venkatachalam for the time she took to answer my questions with regards to the electrical engineering and physics aspects of my research, and Dr. Jimmy Granstrom who was always supportive and willing to extend collaboration with other research groups. I would like to thank Fernando Reiter, former group member of Graham's group, who worked with me on the composite project and spent countless nights in the lab working on many projects.

I acknowledge all of my friends who provided a nice environment during this process. I am appreciative of the friendship rendered by Farzad Sadeghi, William James, Yishak Habtemichael, Samuel Kim, Anne Mallow, and Timothy Hsu. I would also like to thank the remaining Graham group members past and present Dr. Anuradha Bulusu, Prem kumar Nagarathnam, Parisa Pour Shahid Saeed Abadi, Fatma Nazli Donmezer, Yongjin Kim, Hyungchul Kim, Sukwon Choi, Steven Walker, Minseok Ha, Shweta Natarajan, and David Samet.

I appreciate the help I received from the management and staff members at the Microelectronics Research Center (MiRC) at the Georgia institute of Technology. Special thanks to Gary Spinner and Walter Henderson who were willing to help at all times during my research.

I wish to thank Professors Laren Tolbert and Clifford Henderson for giving me critical feedback on my research and for helping me with most of the electrical date measurements. I would like to thank Jose Baltazar who worked with me closely for more than a year and helped with many device measurements. He was not only a great collaborator and researcher but also a great friend that I found during my research. I have to thank him for countless nights and weekends we spent on campus to get the results on time.

I also wish to acknowledge Prof. Bernard Kippelen and Dr. Yinhua Zhou for work function measurements. I acknowledge Prof. Seth Marder and Sergio Paniagua for providing phosphonic acid samples (PAs). I also must extend my gratitude to Prof. Seth Marder for allowing me to use his lab's UV Vis Spectroscopy tool at an early stage of my research.

I acknowledge the Materials Research Science & Engineering Centers (MRSEC) at the Georgia Institute of Technology and National Science Foundation (NSF) Grant No. 0927736 as funding providers.

TABLE OF CONTENTS

ACKNOWLEDGEMENTS iv

LIST OF TABLES xiii

LIST OF FIGURES xiv

LIST OF SYMBOLS AND ABBREVIATIONS xxiv

SUMMARY xxxi

CHAPTER

1 INTRODUCTION AND MOTIVATION 1

1.1. Background 1

1.2. Goals of the Research 8

2 RELEVANT BACKGROUND AND LITERATURE REVIEW 10

2.1. PYSICAL PROPERTIES OF GRAPHENE 10

2.2. Electronic structure of graphene 12

2.3. Raman spectroscopy in graphene 14

2.4. Review of graphene synthesis 18

2.4.1. Mechanical Exfoliation 18

2.4.2. Epitaxial Growth 19

2.4.2.1. Epitaxial growth on silicon carbide 19

2.4.2.2. Epitaxial growth on metals 22

2.4.3. Reduction methods 22

2.4.3.1. Reduced graphene oxide (RGO) 23

2.4.3.2. Hydrazine reduction 23

2.4.3.3. Sodium reduction of ethanol 24

2.4.4. Chemical vapor deposition (CVD): synthesis and transfer 25

2.4.4.1. Introduction 25

2.4.4.2. CVD on Ni 26

2.4.4.3. CVD on Cu 31

2.4.4.4. CVD using solid carbon source 36

2.5. Review of graphene unintentional doping 38

2.6. Review of Intentional Graphene Doping and Interface Modification 41

2.6.1. Graphene p-doping for transparent conductive electrode applications 41

2.6.2. Graphene n-doping for field effect transistor (FET) applications 43

2.6.3. Graphene interface modification 46

2.7. Review of graphene p-n junctions 49

2.8. Research objectives 52

3 SYNTHESIS, TRANSFER, AND CHARACTERIZATION OF CVD GRAPHENE FILMS 54

3.1. Introduction 54

3.2. Synthesis of CVD graphene films 56

3.3. Transfer of CVD graphene films 59

3.4. Characterization of the CVD Graphene Films 62

3.4.1. Raman spectroscopy in Graphene 62

3.4.2. X-ray photo electron spectroscopy (XPS) 64

3.4.3. Thickness measurement and refractive index of graphene 67

3.4.4. Imaging the graphene film 71

3.4.5. Optical transmittance 73

3.4.6. Mobility measurement 74

3.4.7. Sheet resistance measurement 78

3.4.8. Figure of merit 81

3.5. Conclusion 83

4 THE IMPACT OF POST-GROWTH THERMAL ANNEALING AND ENVIRONMENTAL EXPOSURE ON THE UNINTENTIONAL DOPING OF CVD GRAPHENE FILMS 85

4.1. Introduction 85

4.2. In-situ Raman study of CVD graphene films 87

4.2.1. Measurement set up 87

4.2.2. Raman results and discussion 89

4.3. X-ray photo electron spectroscopy (XPS) of CVD graphene films before and after vacuum annealing and re-exposure to air 96

4.3.1. Methods 96

4.3.2. XPS results and discussion 97

4.4. Carrier concentration and mobility studies 99

4.5. Work function measurements 103

4.6. Conclusions 104

5 GRAPHENE DOPING/INTERFACE MODIFICATION USING SELF ASSEMBLED MONOLAYERS (SAMS) 106

5.1. Introduction 106

5.2. Graphene doping/interface modification using SAMs 108

5.2.1. Interface modification using SAMs containing silane group 108

5.2.1.1. Introduction 108

5.2.1.2 Methods 108

5.2.1.3 Verification of SAMs contain silane group on the substrate 111

5.2.1.4 Doping verification using In-situ Raman spectra 114

5.2.1.5 Graphene FET device using SAMs contain silane group 117

5.2.2. Interface modification using phosphonic acids (PAs) 125

5.2.2.1. Introduction 125

5.2.2.2. Methods 126

5.2.2.3. Verification of PAs on the substrate 128

5.2.2.4. Electrical data measurements on back-gated FET functionalized with PAs 131

5.3. Graphene p-n junction using SAMs 132

5.3.1. Introduction 132

5.3.2. P-N junction through intentionally n- and p-doped graphene 133

5.3.2.1 Fabrication method 133

5.3.2.2 Characterization 134

5.3.2.3 Electrical data measurements 135

5.3.3. p-n junction with intentionally n-doped and intrinsically p-doped graphene 136

5.3.3.1 Fabrication method 136

5.3.3.2 Characterization 137

5.3.3.3 Electrical data measurements 138

5.4 Conclusion 140

6 TRANSFER-FREE SYNTHESIS OF GRAPHENE ON DIELECTRIC SUBSTRATES 142

6.1. Introduction 142

6.2. Synthesis of graphene using solid carbon source 144

6.2.1. Introduction 144

6.2.2. Methods 145

6.2.3. Graphene synthesis on quartz 146

6.2.4. Graphene synthesis on SiO_2 148

6.2.5. Substrate effect 149

6.2.6. Growth condition/evolution effect 150

6.2.6.1. Growth evolution on SiO2 150

6.2.6.2. Growth evolution on quartz 152

6.2.6.3. Effect of growth parameters 154

6.2.7. Removing residual Cu 156

6.3. Synthesis of graphene using trace carbon dissolved in metals 158

6.3.1. Introduction 158

6.3.2. Methods 158

6.3.3. Characterization of metal sources 161

6.3.4. Characterization of synthesized graphene 163

6.3.5. Etching residual metal 166

6.3.6. Patterned synthesis 168

6.4. Conclusion 169

7 CONCLUSIONS AND FUTURE OUTLOOK 171

7.1. Conclusions 171

7.2. Future work 174

7.2.1. Improvement in the electrical properties of CVD graphene films 174

7.2.2. Integration of CVD graphene films in OPV and OLED devices 175

7.2.3. Low temperature and transfer-free synthesis of graphene on dielectric substrates 178

REFERENCES 180

LIST OF TABLES

Table 3.1. Shows transmittance, sheet resistance, and FoM for layer-by-layer graphene. 82

Table 4.1. Atomic % of different peaks assigned to C1s before and after vacuum annealing followed by exposure to air. 99

LIST OF FIGURES

Figure 1.1. Formation of 0-D (buckminster fullerenes), 1-D (carbon nanotubes), and 3-D (graphite) from graphene. Picture taken from [1]. 1

Figure 1.2. (Left) Schematic view of a top-gated graphene transistor on diamond-like carbon substrate. (Right) This graphene wafer contains more than 22,000 field effect transistor (FET) devices and test structures. Pictures taken from [9]. 2

Figure 1.3. (Left) assembled graphene/PET panel showing outstanding flexibility. (Right) A graphene-based touch-screen panel connected to a computer. Picture taken from [11]. 3

Figure 1.4. Schematic diagram of the photovoltaic device structure with multi-layer graphene (MLG) electrodes and a hole-blocking TiO_X layer. Picture taken from [13]. 3

Figure 1.5. (Left) Micro hot plate (MHP) sensor showing interdigitated electrodes layered over heated leads. (Right) Four-point interdigitated electrode sensor. 4

Figure 1.6. Schematic of graphene integrated circuit (complementary inverter). Picture taken from [32]. 6

Figure 1.7. (Top) Device structure for flexible OLEDs. (Bottom) Optical image of light emission from a flexible fluorescent green OLED. Picture taken from [33]. 8

Figure 2.1. Sp^2 hybridization in carbon. (a) and (b) show formation of strong $\sigma$and π bonds in graphene, respectively. 10

Figure 2.2. Honeycomb lattice and its Brillouin zone. (Left) Lattice structure of graphene, made out of two interpeneterating lattices: a_1 and a_2 are the lattice unit vectors, and $\delta i, i = 1,2,3$ are the nearest-neighbor vectors. (Right) corresponding Brillouin zone. The Dirac cones are located at the K and K' points. Picture taken from [37]. 12

Figure 2.3. Electronic dispersion in the honeycomb lattice. (Left) Energy spectrum (in units of t) for finite values of t and t', with t=2.7 eV and t'=-0.2t. (Right) Inset of the energy bands close to one of the Dirac points. Picture taken from [37]. 14

Figure 2.4. Phonon dispersion of graphene showing LO, TO, ZO, LA, TA, and ZA phonon branches along the high symmetry direction ΓM and ΓK in the BZ. Picture taken from [43]. 16

Figure 2.5. Raman spectra of graphene, showing the main Raman features, the D, G, G' (2D). 17

Figure 2.6. (Left) First-order G-band process and (Center) one-phonon second-order DR process for the D-band (intervalley process) (top) and for the D0-band (intravalley process) (bottom) and (Right) two-phonon second-order resonance Raman spectral

processes (top) for the doubleresonance G0 process, and (bottom) for the triple resonance G0 band process (TR) for monolayer graphene. Picture taken from [38]. 17

Figure 2.7. Single flakes of graphene have been isolated and transferred from highly oriented pyrolytic graphite (HOPG) to other substrates using micromechanical exfoliation. 18

Figure 2.8. The confinement controlled sublimation (CCS) method. (A) SiC wafer in UHV: Sublimed silicon is not confined, causing rapid, nonequilibrium graphene growth. (B) The CCS method: sublimed Si gas is confined in a graphite enclosure so that growth occurs in near thermodynamic equilibrium. Growth rate is controlled by the enclosure aperture (leak), and the background gaspressure. (C) Photograph of the induction furnace. (D) Under CCS conditions few layer graphite (FLG, from 1 to 10 layers) grows on the Si terminated face, and multilayer epitaxial graphene (MEG, from 1 to 100 layers) grows on the C terminated face. Picture taken from [57]. 20

Figure 2.9. Image of devices fabricated on a 2-inch graphene wafer and schematic cross-sectional view of a top-gated graphene FET. Picture taken from [59]. 21

Figure 2.10. Morphology of epitaxial graphene on Ru(0001). (Left) UHV-SEM image of a large area of the Ru(0001) surface after first-layer graphene growth. (Right) UHV-SEM image of a group of second-layer graphene islands. Picture taken from [55]. 23

Figure 2.11. (Left) SEM image of aggregated reduced GO sheets. (Right) A platelet having an upper bound thickness at a fold of ~2 nm. Picture taken from [64]. 24

Figure 2.12. Photographs of 15 mg of graphite oxide (GO) paper in a glass vial (a) and the resultant hydrazinium graphene (HG) dispersion after addition of hydrazine. Picture taken from [61]. 25

Figure 2.13. Example of the bulk quantity of graphene product. The image consists of approximately 2 g of sample. Picture taken from [66]. 25

Figure 2.14. Illustration of carbon segregation at metal surface. Picture taken from [39]. 27

Figure 2.15. Raman spectra of segregated carbon at Ni surface with different cooling rates. Picture taken from [39]. 28

Figure 2.16. Photograph of a 4 in by 4 in CVD graphene film (a) coated with PMMA and floating on liquid after etching off the Cu substrate and (b) transferred on a Si wafer, with PMMA removed (arrow marks the edge of graphene and thick black lines on the wafer are room ceiling reflections). (c) Representative Raman spectra (c, offset for clarity) measured (with a 532nm laser) in a CVD graphene film transferred to SiO_2/Si. The 2D band can all be fitted by a single Lorentzian, with center ~2680 cm^{-1} and FWHM ~34 cm^{-1}. (d) Raman map of I_{2D}/I_G over a 200 μm ×200 μm area, most (99%) of which can be associated with monolayer (I_{2D}/I_G>2). Picture taken from [70]. 30

Figure 2.17. Synthesis, etching, and transfer process for large scale and patterned graphene films. Picture taken from [28]. 32

Figure 2.18. Time dependence of experimental parameters: temperature, pressure, and gas composition/flow rate. Picture taken from [29]. 33

Figure 2.19. SEM image of graphene on a copper foil with a growth time of 30 min. (B) High-resolution SEM image showing a Cu grain boundary and steps, two- and three-layer graphene flakes, and graphene wrinkles. (C and D) Graphene films transferred onto a SiO_2/Si substrate and a glass plate, respectively. Picture taken from [29]. 34

Figure 2.20. Schematic of the roll-based production of graphene films grown on a copper foil and its transfer to flexible substrate. Picture taken from [11]. 35

Figure 2.21. (Left) Photographs of the roll-based production of graphene films. Copper foil wrapping around a 7.5-inch quartz tube to be inserted into an 8-inch quartz reactor. The lower image shows the stage in which the copper foil reacts with CH_4 and H_2 gases at high temperatures. (Right) A transparent ultralarge-area graphene film transferred on a 35-inch PET sheet. Picture taken from [11]. 35

Figure 2.22. Monolayer graphene is derived from solid PMMA films on Cu substrates by heating in an H_2/Ar atmosphere at 800 °C or higher (up to 1,000 °C). Picture taken from [78]. 36

Figure 2.23 Schematic shows formation of graphene from C60 and its transfer to SiO_2 substrate. Picture taken from [76]. 37

Figure 2.24. Changes in resistivity by graphene exposure to different gases. Picture taken from [82]. 39

Figure 2.25. Thermal annealing removes resist residue on graphene surfaces and brings it into close contact with SiO_2, inducing increased coupling between them. Picture taken from [91]. 40

Figure 2.26. Schematic of graphene transfer, chemical doping, and device fabrication process. Picture taken from [96]. 42

Figure 2.27. The schematic of the layer-by-layer doping CVD graphene with $AuCl_3$. Picture taken from [97]. 43

Figure 2.28. FET device e-annealed under high current in NH_3 atmosphere indicates reaction of GNRs with ammonia. Picture taken from [100]. 44

Figure 2.29. (Left) XPS N 1s spectrum of the n-doped graphene. (Right) Schematic representation of the n-doped graphene. The blue, red, green, and yellow spheres represent the C, "graphitic" N, "pyridinic" N, and "pyrrolic" N atoms in the n-doped graphene, respectively. Picture taken from [92]. 45

Figure 2.30. Raman spectra of graphene shows presence of defect. Picture taken from [92]. 45

Figure 2.31. Schematic transfer process of monolayer graphene on patterned self-assembled monolayer (SAM)-modified SiO_2 substrate. (b) Molecular structure of amine (NH_2)- functionalized SAMs on SiO_2/Si substrate. (c) Optical microscope image of patterned NH_2 SAMs on SiO_2/Si substrate. Picture taken from [114]. 47

Figure 2.32. (Top) A general bottom-gated graphene FET structure with phenyl-SAM interface engineering. (Bottom) Illustration of the physical mechanisms for the hysteresis behavior of graphene FETs. Picture taken from [115]. 48

Figure 2.33. (Left) Schematic illustration of the chemical modification of substrates. (Right) Work function of graphene on various substrates as a function of graphene thickness. Picture taken from [120]. 49

Figure 2.34. (Left) Schematic of graphene FET device. (Right) Resistance vs. gate voltage indicate formation of graphene p-n junction as two separate Dirac points were observed. Picture adapted from [125]. 51

Figure 2.35. Schematic of the experimental set-up showing the top- and back-gate arrangement. Raman spectra of graphene showing its characteristic bilayer mode. Picture adapted from [129]. 51

Figure 3.1. Schematic of a 25 µm roll of Cu foil used for synthesis of CVD graphene. 57

Figure 3.2. Photograph of low pressure graphene growth set up. 57

Figure 3.3. (a) Photo of Cu foil covered with graphene. (b) Optical image of graphene on Cu foil. (c) Micro Raman Spectroscopy (532-nm laser wavelength) data taken of CVD-grown graphene films on a 25 µm Cu substrate at 1000˚C. Data show prominent graphitic (G) and 2D bands and the lack of any detectable defect peak (D). These results indicate high quality graphene grown on Cu. The scale bare in A is 50 µm. 58

Figure 3.4. Transfer process of CVD graphene films. 60

Figure 3.5. Photograph of a graphene film transferred onto a field effect transistor (FET) device with 300 nm thick oxide coated on a Si wafer. 61

Figure 3.6. Bilayer PMMA/graphene transferred onto a flexible PET substrate. 62

Figure 3.7. Shows Raman spectra of graphene after transfer to SiO_2/Si substrate. 62

Figure 3.8. (Left) Raman map of 2D peak from 2670 to 2710 cm^{-1}. (Right) Raman map of G peak from 1580 to 1590 cm^{-1}. 63

Figure 3.9. I_{2D}/I_G (Top) and I_G/I_D (Bottom) collected from Raman mapping date over a 30 µm by 30 µm area. 63

Figure 3.10. XPS survey spectra of graphene without HCl treatment from 0-1300 eV indicates presence of Fe and Cl. 64

Figure 3.11. XPS survey spectra of graphene with HCl treatment from 0-1300 eV indicates lack of any peak associated with Fe or Cl. 65

Figure 3.12. Fe 2p core level spectra of graphene with and without HCl treatment. 66

Figure 3.13. Optical image of graphene shows the presence of cracks in the transferred film on SiO_2. 68

Figure 3.14. Spectroscopic data for graphene and Silicon dioxide. 69

Figure 3.15. Optical constants of graphene (n, k) at different wavelengths. 69

Figure 3.16. Graphene thickness contour plot over 4 mm by 4 mm area. 70

Figure 3.17. AFM image shows graphene film covering grain boundaries of Cu. 71

Figure 3.18. SEM image of graphene transferred on SiO_2 substrates shows the presence of wrinkles and small graphene flakes. 72

Figure 3.19. (Left) TEM image of graphene with a small crack. (Right) Diffraction pattern of graphene showing presence of monolayer film. 73

Figure 3.20. Optical transmittance of graphene film as a function of wavelength. 74

Figure 3.21. Schematic of a back-gated graphene field effect transistor fabricated using lithography for mobility measurement. 75

Figure 3.22. Photo of a graphene FET device shows source, drain, and the channel. 76

Figure 3.23. $I_{D/S}$ vs. V_G of a graphene FET device shows presence of electrons and hole carriers. 77

Figure 3.24. Schematic of circuit diagram for two point probe electrical measurements. 79

Figure 3.25. Schematic of circuit diagram for four point probe measurements shows that resistance of graphene film can be measured without excluding contact measurements. 79

Figure 3.26. Geometry of a rectangular thin film with uniform thickness. 80

Figure 3.27. Photo of a four point probe device for sheet resistance measurements of graphene. 80

Figure 3.28. FoM of layer-by-layer graphene compared with the data obtained from literature. 83

Figure 4.1. Schematic of chemical desorption by vacuum annealing and atmospheric adsorption upon exposure to air. 87

Figure 4.2. Photo of In-situ Raman measurement set up with heating, cooling, vacuum, and gas delivery capabilities. Thermal stage has gas inlet, vacuum outlet, and water cooling system. 88

Figure 4.3. Graphitic peaks (G and 2D) positions under controlled environment conditions. (a) Temperature dependence of G peak with ~ 12 cm^{-1} blue shift due to vacuum annealing and re-exposure to air. (b) Temperature dependence of 2D peak with ~ 9 cm^{-1} blue shift due to vacuum annealing and re-exposure to air. A hysteresis was observed during heat up and cool down cycles. 90

Figure 4.4. Oxygen and water vapor doping reversibility study. (a) Variation in G peak position of sample #1 as it undergoes annealing and gas/air exposure steps. (a) Variation in G peak position of sample #2 as it undergoes annealing and gas/air exposure steps. (c) Variation in FWHM (G) peak of sample #3 as it undergoes annealing and gas/air exposure steps. (d) Variation in FWHM (G) peak of sample #3 as it undergoes annealing and gas/air exposure steps. 94

Figure 4.5. Raman spectra of graphene before and after annealing and re-exposure to air. There is a stronger dependence of the 2D mode intensity to annealing than for the G mode. 95

Figure 4.6. O1s binding energy before and after annealing and re-exposure to air. O1 s BE was used for calibration purposes and the XPS scans were charge shifted to bring the O1s peak from SiO_2 to B.E. of 533 eV. 98

Figure 4.7. Core-level X-ray photoelectron spectroscopy (XPS) peaks showing typical shift and broadening caused by vacuum annealing and exposure to air. 98

Figure 4.8. Illustration of change in atmospheric dopants with vacuum annealing and re-exposure to air on graphene FET device. 100

Figure 4.9. IV curve showing p-doping of graphene after annealing and re-exposure to air. 101

Figure 4.10. De-doping of graphene due to heating in vacuum over time. 102

Figure 4.11. Schematic of a change in the work function of graphene due to annealing and re-exposure to air. Work function (WF) measurements were obtained using Kelvin Probe (Besocke Delta Phi). 103

Figure 5.1. Schematic of APTES and PFES containing amine and fluorine groups, respectively. 109

Figure 5.2. Schematic of (Left) APTES treated (Right) PFES treated SiO_2 substrate on highly doped Si for graphene FET device applications. 110

Figure 5.3. Survey XPS spectra for graphene (black), graphene/PFES (red) and graphene/APTES (green). 111

Figure 5.4. XPS spectra representing N 1s binding energy for graphene/ SiO_2 (black) and graphene /SAMs (red). 112

Figure 5.5. C 1s core level XPS spectra for graphene (black), graphene/PFES (red) and graphene/APTES (green). 113

Figure 5.6. (a) Raman spectra of graphene (black), graphene/APTES (green), and graphene/PFES (red) after annealing at 200°C under nitrogen atmosphere for 3 hours. (b) G peaks position (c) FWHM (G) (d) $I_{2D/G}$ as a function of annealing time under nitrogen atmosphere for graphene (black), graphene/APTES (green), and graphene/PFES (red). 116

Figure 5.7. Schematic of back-gated APTES and PFES-treated devices. 118

Figure 5.8. Schematic of atmospheric p-dopants removal shows unmasking of n-doped graphene FET device induced by APTES. 119

Figure 5.9. Schematic of atmospheric p-dopants removal shows unmasking of p-doped graphene FET device induced by PFES. 120

Figure 5.10. Source-drain current versus gate voltage for different device heating times at 200°C for simple graphene FET devices fabricated using an APTES coated gate dielectric. 121

Figure 5.11. Source-drain current versus gate voltage for different device heating times at 200°C for simple graphene FET devices fabricated using a PFES coated gate dielectric. 121

Figure 5.12. Source-drain current versus gate voltage for different device heating times at 200°C for simple graphene FET devices fabricated using a simple SiO_2 gate dielectric. 122

Figure 5.13. shows source-drain current versus gate voltage as a function of heat treatment and pump down time; this indicates no significant change in the neutrality point even after 7 days without having SAMs. 123

Figure 5.14. Dopant concentration and Nitrogen/silicon (N/Si) ratio versus APTES deposition time. 124

Figure 5.15. Drain-source current versus gate voltage as function of different APTES treatment times. 125

Figure 5.16. Schematic of (Left) 4-trifluoromethylbenzylphosphonic acid (pCF3BPA) phosphonic acids (PAs) with fluorine orientation looking up and (Right) 2,6-difluorobenzylphosphonic acid (oF2BPA) with fluorine orientation looking down. 127

Figure 5.17. Schematic of a back-gated graphene FET device functionalized by (Left) OF_2BPA and (Right) PCF_3BPA before transfer of CVD graphene. 128

Figure 5.18. XPS survey spectra that show the presence of F 1s indicative of successful treatment with OF_2BPA and PCF_3BPA. 129

Figure 5.19. Core level (Top) C 1s spectra and (Bottom) F 1s spectra acquired on bare Al_2O_3, and OF_2BPA and PCF_3BPA treated Al_2O_3. 130

Figure 5.20. Source-drain current versus gate voltage heated at 200°C for 12 hours as a function of gate voltage for graphene, graphene/OF_2BPA, and graphene/PCF_3BPA FET. 131

Figure 5.21. Schematic of the graphene p-n junction fabrication steps using APTES and PFES. 134

Figure 5.22. (Left) N1s binding energy centered at 400.1 eV and (Middle) F1s binding energy centered at 689.3 eV. (Right) C1s binding energy centered at 285.3 eV. 134

Figure 5.23. Drain-source current versus gate voltage for a graphene p-n junction measured after different annealing time. Both APES and PFES were used for surface modification. 135

Figure 5.24. Schematic showing the process used to fabricate the graphene p-n junction using only APTES without PFES modification. 137

Figure 5.25. XPS mapping of the graphene p-n junction using APTES and intrinsically p-doped graphene for the (Left) C1s intensity at a binding energy of ~ 285 eV (Right) N 1s intensity at a binding energy of 399.9 eV. 138

Figure 5.26. Source-drain current versus gate voltage as a function of heating times at 200°C for a graphene p-n junction using APTES and intrinsically p-doped film. 139

Figure 6.1. Different images showing the presence of cracks, voids, and contamination in transferred CVD graphene when care was not taken during the transfer. (Top left) AFM image (Top right) SEM image of transferred graphene with cracks. (Bottom) Optical image with contamination. 143

Figure 6.2. Schematic of graphene synthesis using solid carbon source on dielectric substrate. 146

Figure 6.3. (a) Optical microscope image and (e) SEM image of a graphene sample grown on quartz after 40 min. The images reveal the incomplete removal of Cu through evaporation during the growth process. (b) Raman spectra from metal-free areas (red and blue lines) and Cu regions (black line) showing full coverage of graphene on the sample. Mapping of I_{2D}/I_G and FWHM(2D) of the same area in (a), respectively. 148

Figure 6.4. (a) Optical microscope image of a graphene sample grown on SiO_2/Si after 20 min of growth. The image shows graphene directly on the SiO_2 surface as well as residual copper with less than 15% surface coverage. (b) Raman spectra from metal-free regions (red and blue lines) and Cu regions (black line) show the presence of graphene everywhere on the sample. 149

Figure 6.5. (a-d) Optical microscope images of graphene samples grown on quartz, SiO_2, AlN, and sapphire, respectively. (e) Representative Raman spectra from the metal-free regions on each substrate showing the presence of graphitic peaks. 150

Figure 6.6. (a-f) Optical microscope images showing the residual copper coverage on SiO_2/Si substrates as a function of synthesis time for 1.5, 3, 10, 20, 40, and 60 minutes, respectively. (g) The dependence of the Raman spectra (I_{2D}/I_G and I_D/I_G) collected from samples shown in (a-f). The data suggests a maximum in the layer thickness (highest I_{2D}/I_G ratio) and a minimum in the defects in the graphene (lowest I_D/I_G ratio) after 20 minutes of growth. 151

Figure 6.7. (a-f) Optical microscope images of the residual copper coverage on quartz substrates after 1, 10, 20, 40, 60, and 90 minutes growth, respectively. (g) Raman spectra collected from the samples in (a-f). The data suggests a maximum in the layer thickness (highest I_{2D}/I_G ratio) and a minimum in the defects in the graphene (lowest I_D/I_G ratio) after 40 minutes of growth. 153

Figure 6.8. Optical microscope images showing the residual copper coverage after 20 minutes of growth on SiO_2/Si with H_2 flow rate (sccm)/Ar flow rate (sccm)/pressure (mTorr) as (a) 100/500/1500, (b) 3/50/9, (c)50/500/1000, (d)100/50/1350, (e)50/50/450, and (f) 20/50/220. (g,h) Average I_{2D}/I_G and I_D/I_G collected from the samples in (a-f). 155

Figure 6.9. (a,b) Optical microscope images of graphene before and after acid treatment. (c) SEM image of the sample grown on quartz after acid treatment. (d) Raman spectra from two different points on the sample in (b) after acid treatment. (e) X-ray photo electron spectroscopy of the sample after acid treatment indicates the presence of C1s binding energy without any peaks for copper or Fe. 157

Figure 6.10. Schematic of graphene synthesis using trace carbon dissolved in metals. 159

Figure 6.11. Graphene on SiO_2/Si (100 mm wafer) after 30 minutes of growth. 160

Figure 6.12. (Top) Schematic shows SIMS operation. (Bottom) SIMS results show the intensity of detected ions versus sputtering time, indicative of 2 orders of magnitude higher C solubility in Ni compared to Cu. 162

Figure 6.13. (a) and (b) Optical microscope image of graphene before and after acid treatment. (c) Raman spectra from Ni (black line) and Cu regions (blue line) showing full coverage of graphene on the sample. (d) Raman spectra from SiO_2 showing the presence of graphene after etching metals. (e) Secondary-electron SEM image of a graphene sample grown on Ni before etching. (f) In-lens SEM image of graphene on SiO_2 after

etching Ni and residual Cu showing presence of wrinkles. (g) and (h) EDX pattern of the same area in (e). 164

Figure 6.14. I_{2D}/I_G and I_D/I_G ratios as functions of Ni thickness. 166

Figure 6.15. (a) Core level Ni XPS spectra shows removal of Ni after acid treatment. (b) Survey spectra collected randomly indicate the presence of C1s binding energy without any peaks for copper or Ni after acid treatment. (c) Average UV Vis spectra indicates the synthesized graphene in primarily bilayer showing ~95 % transmittance at 550 nm. 167

Figure 6.16. (a) Photograph of a typical patterned sample. (b) and (d) SEM images of a channel before and after acid treatment. (c) SEM image of a graphene sample showing wrinkles. (e) Optical image of a channel after growth, showing presence of Cu dots. (f) Representative Raman spectra show the presence of graphene on the areas where Ni and Cu were patterned. No graphitic peaks were observed at other areas (in the channel). 169

Figure 7.1. Schematic of decrease in work function of graphene after PEIE deposition. 176

Figure 7.2. I-V characteristic curve for PEIE/graphene before and after heat treatment. Inset shows schematic of a back-gated graphene device with a thin layer of PEIE deposited on top. 177

Figure 7.3. Schematic of an organic inverted-structure solar cell using graphene as electrode functionalized with PEIE for improved electron collection. 178

LIST OF SYMBOLS AND ABBREVIATIONS

0-D	zero-dimensional
1-D	one-dimensional
3-D	three-dimensional
2D	2D or G' peak in Raman spectra of graphene
a_1, a_2	graphene lattice vectors
$a_{j,\sigma}$ ($a^*_{i,\sigma}$)	creates an electron with spin σ on site R_i on sublattice A
A	acoustic branches in phonon dispersion of graphene
AFM	atomic force microscopy
Al	aluminum
Al_2O_3	aluminum oxide
ALD	atomic layer deposition
AlN	aluminum nitride
Ar	argon
Au	gold
$AuCl_3$	gold (III) chloride
A_c	cross-sectional area of the thin film
APTES	3-Aminopropyltriethoxysilane
$b_{i,\sigma}$ ($b^*_{i,\sigma}$)	creates an electron with spin σ on site R_i on sublattice B
B.E	binding energy
BOE	Buffered oxide etch
BZ	Brillouin zone
C	carbon
C1s	core level carbon binding energy

C60	buckminsterfullerene (or buckyball) fullerene
C70	C70 fullerene
C=O	carbonyl group
C-OH	carboxyl group
CH_4	methane
C_g	gate capacitance
CMOS	complementary metal–oxide–semiconductor (CMOS
Cu	copper
Co	cobalt
CO	carbon monoxide
CVD	chemical vapor deposition
D-band	D peak in Raman spectra of graphene
DI water	deionized water
DR	double resonance Raman process
e	electron charge
E_{laser}	laser energy
E_{phonon}	phonon energy
EDX	energy-dispersive X-ray spectroscopy
F1s	core level fluorine binding energy
FET	field effect transistor
Fe 2p	iron core level binding energy
$FeCl_3$	iron chloride
$Fe(NO_3)_3$	iron nitride
FLG	few layer graphene
FoM	figure of merit
FWHM	Full width at half maximum

G	G peak in Raman spectra of graphene
GNRs	graphene nanoribbons
GO	graphene oxide
G'	G' or 2D peak in Raman spectra of graphene
G^*	D+G peak in Raman spectra
H	Hamiltonian
H_2	hydrogen
hBN	hexagonal boron nitride
HCl	hydrochloric acid
HF	hydrofluoric acid
HG	hydrazinium graphene
HNO_3	nitric acid
HOPG	highly oriented pyrolytic graphite
I_{C-}/I_{Cu-}	carbon to copper ion intensity ratio in SIMS measurements
I_{C-}/I_{Ni-}	carbon to nickel ion intensity ratio in SIMS measurements
ID	inner diameter
Ir	iridium
I_{2D}/I_G	2D over G peak intensity ratio
I_G/I_D	G over D peak intensity ratio
$I_{D/S}$	drain-to-source current
IPA	isopropanol
I-V	drain-to-source current vs. gate voltage
K, K′	Dirac cones in graphene Brillouin zone
L	longitudinal branches in phonon dispersion of graphene
L_{ch}	channel length
LA	longitudinal acoustic branches in phonon dispersion of graphene

LEDs	light emitting devices
LO	longitudinal optical branches in phonon dispersion of graphene
M point	located midway between points K and K' along the zone boundary
MEG	multi-layer epitaxial graphene
MHP	micro hot plate
MLG	multi-layer graphene
$-NH_3^+$	protonated or hydrogen bonded amine
$-NH_2$	free amine
n, k	Optical constants of graphene
N 1s	core level nitrogen binding energy
n	negative
N_2	nitrogen
N1s	nitrogen binding energy
$(NH_4)_2S_2O_8$	ammonium persulphate
NH_3	amonia
NN	nearest-neighbor
NMP	N-methylpyrrolidone
Ni	nickel
NO_2	nitrogen dioxide
O	optical branches in phonon dispersion of graphene
O_2	oxygen
O 1s	core level oxygen binding energy
-OH	hydroxyl
oF2BPA	2,6-difluorobenzylphosphonic acid
OFETs	organic field effect transistors
OLEDs	organic light-emitting diodes

OPVs	organic photovoltaic cells
p	positive
PAs	phosphonic acids
PCE	power conversion efficiency
pCF3BPA	4-trifluoromethylbenzylphosphonic
PDMS	polydimethylsiloxane
PEIE	polyethylenimine ethoxylated
PET	polyethylene terephthalate
PFES	1H,1H,2H,2H-Perfluorooctyltriethoxysilane
PMMA	Poly(methyl methacrylate)
R	bulk resistance
RCE	rotating compensator ellipsometer
RGO	reduced graphene oxide
R_P , R_S	Fresnel reflection coefficients
R_{sh}	sheet resistance
Ru	rodinium
S_1, S_2, S_3	electrical probes
SAMs	self assembled monolayers
SEM	secondary electron spectroscopy
Si	silicon
SiC	silicon carbide
SiO_2	silicon dioxide
SIMS	secondary ion mass spectroscopy
SKPM	scanning Kelvin probe microscope
sp^2	sp^2 orbital hybridization
t	thin film thickness

T	transmittance
T	transverse branches in phonon dispersion of graphene
TA	transverse acoustic branches in phonon dispersion of graphene
TEM	transmission electron microscopy
TO	transverse optical branches in phonon dispersion of graphene
TiO_X	Titanium dioxide
UHV	ultra high vacuum
$V_{D/S}$	drain-to-source voltage
V_G	gate voltage
V_{NP}	voltage at neutrality point
W_{ch}	channel width
WF	work function
XPS	X-ray photoelectron spectroscopy
Z	out-of-plane branches in phonon dispersion of graphene
ZA	out-of-plane acoustic branches in phonon dispersion of graphene
ZO	out-of-plane optical branches in phonon dispersion of graphene
+	upper band
-	lower band
$\delta_1, \delta_2, \delta_3$	three nearest-neighbor (NN) vectors in real space of graphene
ρ	electrical resistivity
σ	in-plane covalent band
σ_{DC}	direct current conductivity
σ_{Op}	optical conductivity
π	out-of-plane bond
ϑ_F	Fermi velocity of the carriers in graphene
Γ	Brillouin zone center in graphene lattice

$\omega_{G'}$	the frequency in which G' or 2D peak occurs
ω_D	the frequency in which D peak occurs
μ_n	electron mobility
μ_p	hole mobility
μ_0	permeability of free space
ϵ_0	permittivity of free space

SUMMARY

Graphene, a two-dimensional counterpart of three-dimensional graphite, has attracted significant interest, due to its distinctive electrical and mechanical properties, for developing electronic, optoelectronic, and sensor technologies. In general, doping of graphene is important, as it gives rise to p-type and n-type materials, and it adjusts the work function of the graphene. This adjustment is necessary in order to control charge injection and collection in devices such as solar cells and light emitting devices. Current methods for graphene doping involve high temperature process or interactions with chemicals that are not stable. Moreover, the process of transferring graphene from its growth substrate and its exposure to the environment results in a host of chemical groups that can become attached to the film and alter its electronic properties by accepting or donating electrons/holes. Intentional and controllable doping of the graphene, however, requires a deeper understanding of the impact of these groups. The proposed research will attempt to clarify the unintentional doping mechanism in graphene through adsorption or desorption of gas/vapor molecules found in standard environments. A low temperature, controllable and defect-free method for doping graphene layers will also be studied through modifying the interface of graphene and its support substrate with self-assembled monolayers (SAMs) which changes the work function and charge carriers in the graphene layer. Furthermore, current methods of chemical vapor deposition synthesis of graphene requires the film to be transferred onto a second substrate when the metal layer used for growth is not compatible with device fabrication or operation. To address this issue, the proposed work will investigate a new method for wafer scale, transfer-free synthesis of graphene on dielectric substrates using new carbon sources. This technique allows patterned synthesis on the target substrate and is compatible with standard device

fabrication technologies; hence, it opens a new pathway for low cost, large area synthesis of graphene films.

CHAPTER 1

INTRODUCTION AND MOTIVATION

1.1. Background

Graphene [1-2] is a flat monolayer of carbon atoms arranged into a 2 dimensional honeycomb lattice, and is the building block for various forms of carbon materials ranging from 0-D fullerenes (C60, C70) to commonplace 3-D graphite (pencil lead). The concept of a graphene sheet rolled into 1D carbon nanotubes has attracted vast interest in material science and nanoelectronics in the last two decades [3]. Figure 1.1 shows the formation of various graphitic structures from graphene.

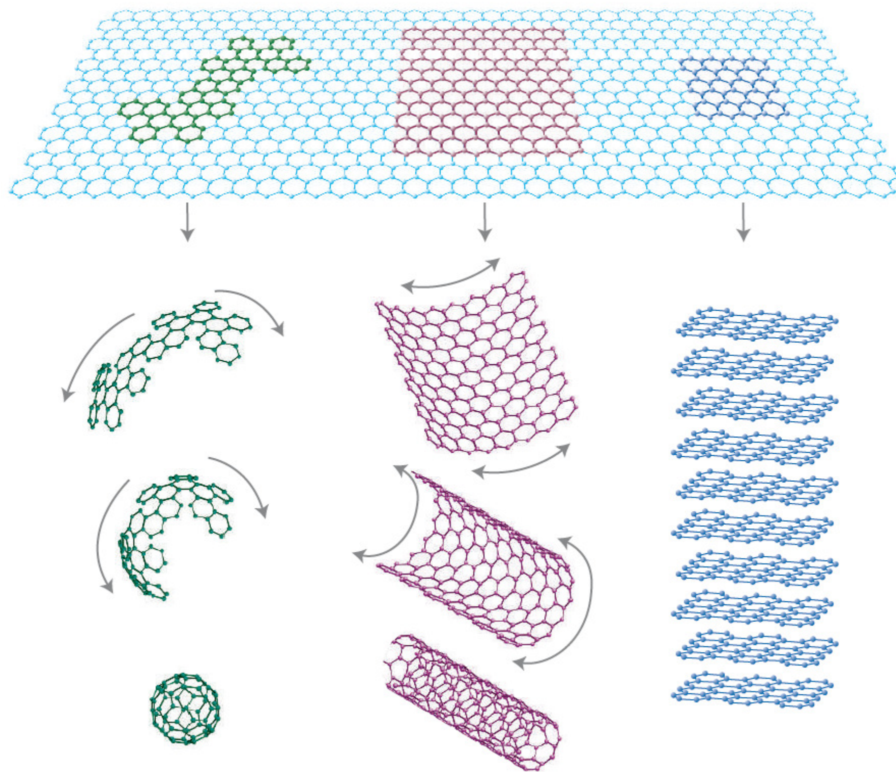

Figure 1.1. Formation of 0-D (buckminster fullerenes), 1-D (carbon nanotubes), and 3-D (graphite) from graphene. Picture taken from [1].

Graphene has distinctive electrical properties that make it a very powerful material for electronic device applications [1, 4-6]. Graphene is a zero-gap semiconductor with zero effective mass for electrons and holes. Very low scattering of charge carriers and relative temperature independence, even up to room temperature, results in high carrier mobility on the order of 200,000 cm^2/Vs [7] in graphene. Furthermore, graphene can carry an exceptionally large current densities. The breakdown current density of some graphene nanoribbon devices is in the range of 108 A/cm^2 [8]. These electrical properties enabled graphene-based field effect transistors (FETs) to operate in the 155 GHz regime, showing its potential to be used in integrated circuits [9].

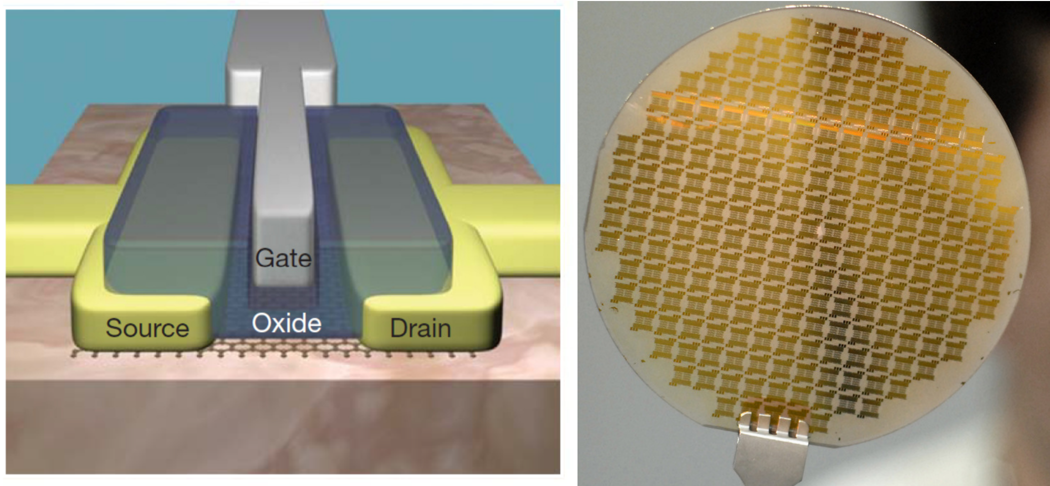

Figure 1.2. (Left) Schematic view of a top-gated graphene transistor on diamond-like carbon substrate. (Right) This graphene wafer contains more than 22,000 field effect transistor (FET) devices and test structures. Pictures taken from [9].

Graphene is highly transparent; it absorbs 2.3% of white light. Falkovsky [10] showed that reflectance from the monolayer is determined for the infrared region by the intraband Drude-Boltzmann conductivity and for higher frequencies by the interband absorption. At low temperatures and high carrier densities, the reflectance from multilayers has a sharp downfall with a subsequent plateau. These features are caused by

the excitations of weakly damped waves in conditions of direct interband electron transitions [6].

High electrical conductivity, low sheet resistance, and good transparency make graphene a potential candidate for primary transparent conductive electrodes in applications such as touch screens, [11] liquid crystal displays, [12] organic photovoltaic cells (OPVs), [13-14] and organic light-emitting diodes (OLEDs), [15] or as an interface modifier to improve charge injection or collection in devices [16-17]. Figure 1.3 shows a graphene-based touch-screen panel. Multi-layer graphene (MLG) films were applied as transparent conductive electrodes in organic photovoltaic devices (OPVs), and this resulted in a power conversion efficiency (PCE) of ~ 1.3%. The PCE was further enhanced when a hole-blocking TiO_X layer was inserted in the device as shown in Figure 1.4.

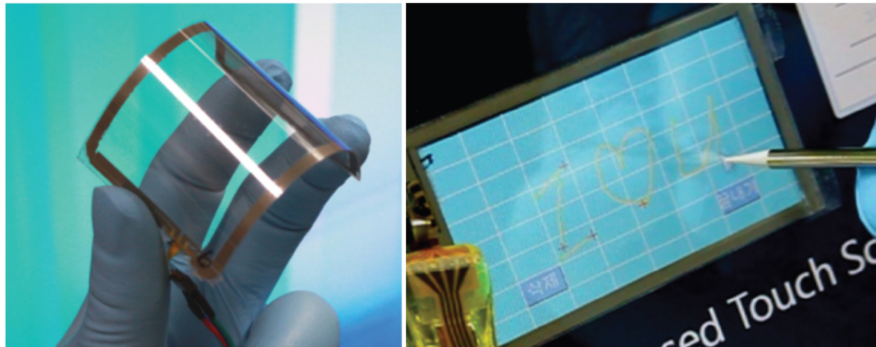

Figure 1.3. (Left) assembled graphene/PET panel showing outstanding flexibility. (Right) A graphene-based touch-screen panel connected to a computer. Picture taken from [11].

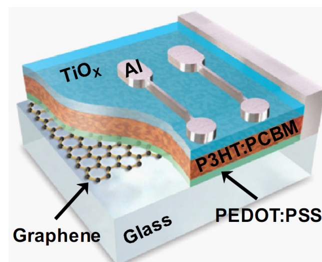

Figure 1.4. Schematic diagram of the photovoltaic device structure with multi-layer graphene (MLG) electrodes and a hole-blocking TiO_X layer. Picture taken from [13].

The electrical properties of graphene are also sensitive to the adsorption and desorption of gas molecutles, making it very attractive as a detector material for gas sensors [18-20]. Improvements in the effectiveness of reduction methods to form graphene layers from graphite oxide opened a door to a wide range of possible application, one of which is for chemical sensors. Due to high conductivity in single layer graphene, any adsorption of gas molecules is detectable through measuring the change in resistance; this change is detectable at room temperature. Jesse Fowler et al. [21] reported on the development of a new graphene-based chemical sensor. Figure 1.5. shows an interdigitated planar electrode array in which graphene is produced using spin coating of hydrazine dispersions. The sensor response is consistent with a charge transfer mechanism between the analyte and graphene with a limited role for the electrical contacts, as shown in Figure 1.5. However, these sensitivity of graphene to the exposure of gas species normally found in the environment also make the control of electrical properties more difficult due to potential variability with changes in the surrounding environment.

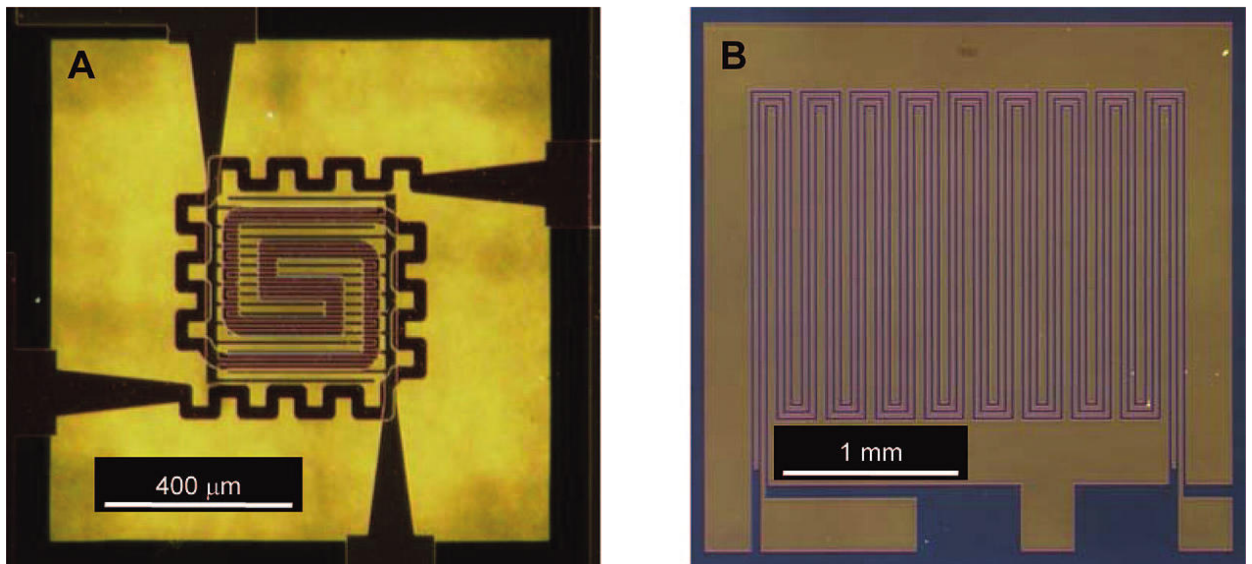

Figure 1.5. (Left) Micro hot plate (MHP) sensor showing interdigitated electrodes layered over heated leads. (Right) Four-point interdigitated electrode sensor.

Graphene sheets have been produced mainly by exfoliating graphene flakes from bulk graphite and depositing them on the SiO_2/Si substrate [1-2]. However, the size, deposition, and crystalline quality of graphene are not easily controlled. Professor Walter de Heer's group at Georgia Institute of Technology has grown epitaxially graphene sheets on SiC(0001) for the first time [22-23]. However the graphene layers have had wide variation in thickness, and it is challenging to detach them from the expensive SiC substrate. Solution based synthesis of graphene has been developed to produce large-scale films [24-26]. However, the quality of the graphene synthesized in this way is low compared to other methods. To address issues for synthesis of large scale and high quality graphene, the chemical vapor deposition (CVD) method has been introduced to grow films on transition metals [27-28]. Current techniques for the CVD synthesis of graphene often utilize metal substrates such as copper, [29] nickel, [30] iridium, [31] along with gaseous hydrocarbon sources, to form graphene at high temperatures. While highly scalable, this methodology has a drawback in that the graphene film needs to be transferred onto a different substrate after synthesis, because the metal films used in the synthesis are not compatible with the operation of most optoelectronic or electronic devices. In addition, polymers and many low cost glass substrates are not compatible with the growth temperature of the graphene. In practice, it is difficult to transfer a pristine sheet of large area graphene without leaving significant wrinkles, cracks, and voids. Thus, routes that can directly synthesize large area graphene films on dielectric substrates in a manner that mitigates these challenges are needed.

Moreover, the process of transferring graphene from one substrate to another often involves exposing the graphene to both aqueous and atmospheric gas environments, where a host of chemical groups can become attached to the graphene. These groups have the ability to unintentionally dope the graphene and alter the electronic properties that are important for most sensor and transistor applications. The variation in mobility and charge carrier concentration depends on the donor or acceptor nature of the chemical

groups. Controlling the exposure of graphene to these groups provides the opportunity to further tailor its electronic structure by altering their concentration. Therefore, understanding the mechanism by which CVD graphene is doped with adsorbed oxygen and moisture, which are byproducts of the transfer process, is required in order to develop appropriate post-transfer treatments for adjusting the presence of these groups on the graphene surface to obtain desired electrical properties for the film.

As mentioned earlier, due to its peculiar electronic properties, graphene has been proposed as a candidate for CMOS and post-CMOS electronics. These remarkable electronic properties and the compatibility of graphene with Si lithographic techniques promise to simplify the transition to graphene-based electronics. However, in order to make electronic applications of graphene realistic, one has to necessarily tune its electronic properties, so that, for example, a band gap is introduced. The realization of a proper band gap is critical for device performance. In addition, intentional doping of the graphene is important, as it gives rise to p- and n-type materials that are important for field effect transistor applications. Traversi et al. developed the first integrated circuit (a complementary inverter) on graphene as shown in Figure 1.6 [32].

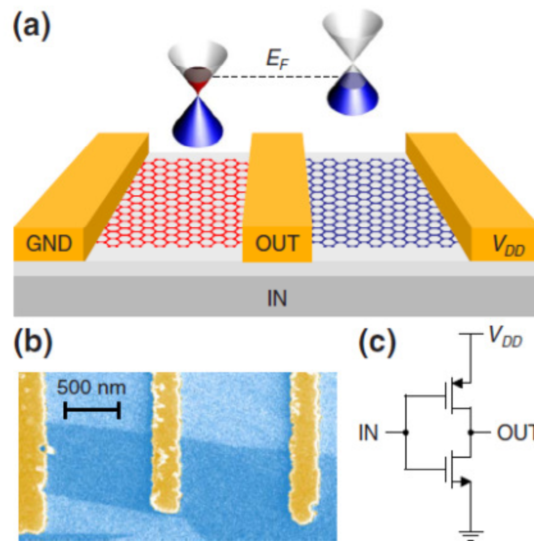

Figure 1.6. Schematic of graphene integrated circuit (complementary inverter). Picture taken from [32].

The key to obtaining a functional integrated circuit using graphene was to change the type of one of the transistors from p-type to n-type by Joule heating. An ideal graphene transistor is n-type, meaning that electrons pass current, when a positive voltage is applied to the gate, but it is p-type when a negative voltage is applied. As explained earlier, oxygen and moisture in the air unintentionally dope graphene, making p-type transistors. Joule heating was utilized to remove these contaminants from one side of the circuit and therefore restore n-type behavior. In this way, two transistors of opposite type were integrated on the same graphene sheet. This pair of transistors forms a digital logic inverter, a basic building block of CMOS.

With respect to optoelectronic device performance, the most attractive features of graphene sheets are their high transparency in the visible-light range and their low resistivity; these qualities makes graphene an ideal candidate to explore further its potential as a transparent electrode. To this end, adjustment in the work function of the graphene is necessary to control charge injection and collection in devices such as solar cells and light emitting devices. Han et al. have developed extremely efficient flexible organic light-emitting diodes (OLEDs) by improving the work function and reducing the sheet resistance of graphene films to the level required for electrodes [33]. They demonstrated a method to increase the surface work function (WF) using conductive polymer compositions. This enhanced WF enabled holes to be injected easily into the organic material despite the high hole-injection barrier at the interface between the graphene anode and the organic layer.

Overall, the doping of graphene films has been studied through electrostatic gating, [34] interaction with chemical species, [11, 35] and intercalation methods, [36] showing that the variation in mobility and charge carrier concentration depends on the donor or acceptor nature of the chemical. However, these methods are not stable and usually introduce defects in graphene structure that negatively impact its electronic

properties. Therefore, a defect-free and stable method to create p- and n-type graphene without degrading the performance of the device is required.

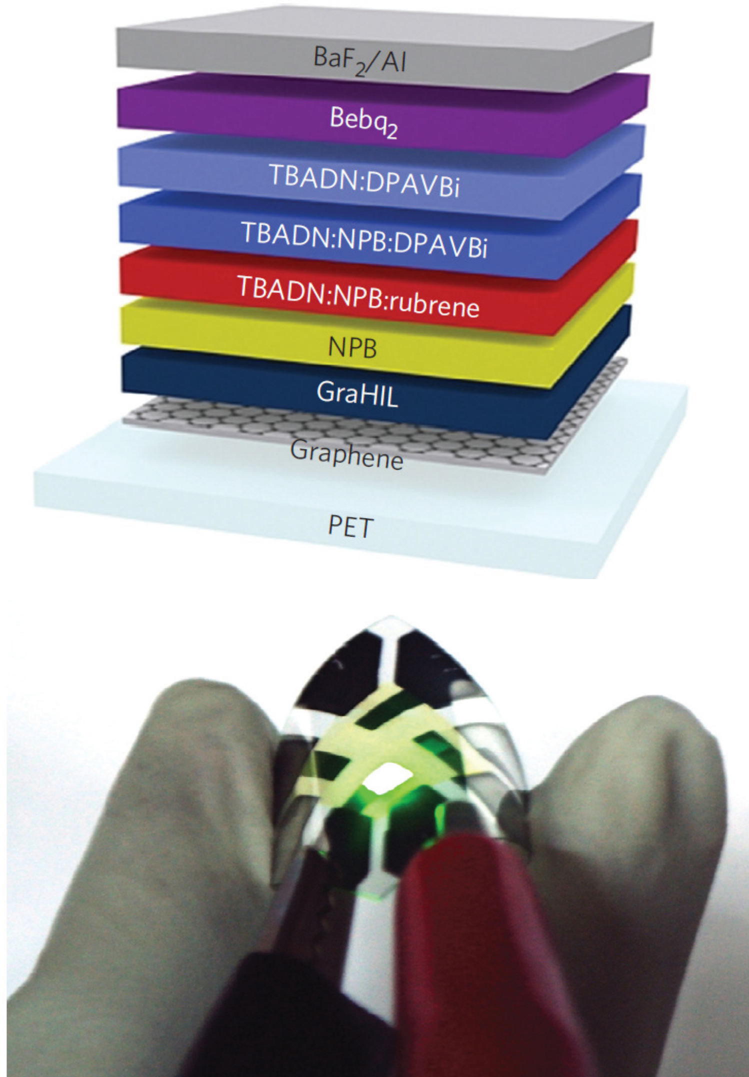

Figure 1.7. (Top) Device structure for flexible OLEDs. (Bottom) Optical image of light emission from a flexible fluorescent green OLED. Picture taken from [33].

1.2. Goals of the Research

The objectives of this study are two folds. First, the goal is to develop a method to directly synthesize graphene on a target substrate without requiring a transfer step. This

method should be easy to perform, scalable, and allow for uniform or patterned graphene films to be formed on the substrate with limited processing subsequent to the synthesis step. Secondly, a new approach to modify the interface between graphene and the target substrate will be utilized towards the formation of n-type and p-type graphene; the new approach will show improved performance over current approaches. This method aims to provide a systematic approach to tailor the electronic properties of graphene for p- and n-type field effect transistors through a defect-free, low temperature process. However, intentional and controllable modification of the graphene requires a deeper understanding of the impact of chemical groups on its electronic properties induced by the transfer process. A vacuum annealing study will be proposed to understand the adsorption and desorption of functional groups/molecules on the surface of graphene, and controlled gas exposures will be used to reconstitute their makeup on the graphene surface. This will give insight into the environmental stability of the doping of graphene layers used in electronic applications. The dissertation format will be as follows. Chapter 2 will give background information and theory necessary for Chapters 3-6. Chapter 3 will summarize the growth and transfer process of CVD graphene films used in this study and the corresponding characteristics study before and after transfer of CVD graphene. Chapter 4 will demonstrate a comprehensive study of the impact of environmental exposure on the electronic properties of graphene films. Chapter 5 will elucidate the doping process of graphene films and the formation of graphene-based p-n junctions. Chapter 6 will present new routes for the synthesis of graphene films using solid carbon source and trace carbon dissolved in metals. Finally, Chapter 7 will give a comprehensive conclusion and propose future works.

CHAPTER 2

RELEVANT BACKGROUND AND LITERATURE REVIEW

2.1. PYSICAL PROPERTIES OF GRAPHENE

Graphene is a single layer of carbon atoms arranged in a honeycomb structure. The s orbital and two of the p orbitals from the second energy level of carbon are hybridized to form three hybrid orbitals. This kind of hybridization is called sp^2 hybridization. It has three hybrid orbitals as well as an unchanged p orbital called $2p_z$. The geometric arrangement of these three sp^2 hybrid orbitals is in a flat plane with 120 degree angles between them. The leftover $2p_z$ orbital lies at a 90 degree angle to the hybrid orbitals. This kind of hybridization occurs when a carbon atom is bonded to three other atoms. All sp^2 orbitals form σ-bonds with the sp^2 orbitals of the neighboring carbon atoms in a single layer graphene. The bonding orbital associated with each σ-bond is occupied by two electrons (spin-up and spin-down). The $2p_z$ orbital sticks out of the plane and forms π-bonds with neighboring $2p_z$ orbitals. Figure 2.1 shows the hybridization of carbon atoms in a graphene structure and the formation of σ and π bonds.

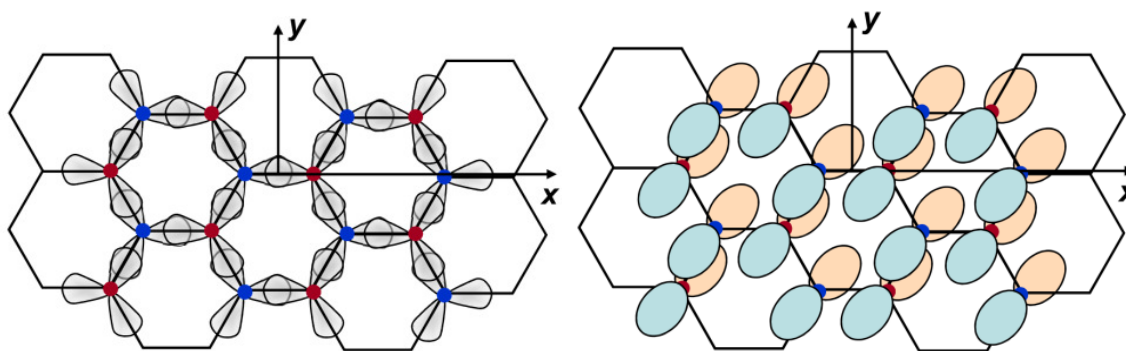

Figure 2.1. Sp^2 hybridization in carbon. (a) and (b) show formation of strong $\sigma$and π bonds in graphene, respectively.

The crystal structure of graphene in Figure 2.2 shows that graphene is made of carbon atoms arranged in a hexagonal honeycomb-like structure. It can be imaged as a triangular lattice with a basis of two atoms that are shown as red and blue solid dots. The two lattice vectors can be written as:

$$a_1 = \frac{a}{2}\left(3, \sqrt{3}\right) \quad , \quad a_2 = \frac{a}{2}\left(3, -\sqrt{3}\right) \qquad \text{2-1}$$

where a ~1:42 Å is the carbon-carbon distance.

In the Brillouin zone (BZ), the Dirac cones are located at two corners *K* and *K′*, which are of particular importance. Their positions in the reciprocal space are:

$$K = \left(\frac{2\pi}{3a}, \frac{2\pi}{3\sqrt{3}a}\right) \quad , \quad K' = \left(\frac{2\pi}{3a}, -\frac{2\pi}{3\sqrt{3}a}\right) \qquad \text{2-2}$$

and the three nearest-neighbor (NN) vectors in real space are:

$$\delta_1 = \frac{a}{2}\left(1, \sqrt{3}\right), \delta_2 = \frac{a}{2}\left(1, -\sqrt{3}\right), \delta_3 = -a(1,0) \qquad \text{2-3}$$

From these vectors, we can construct the Brillouin zone (BZ) by forming perpendicular bisectors of these reciprocal lattice vectors. This construction is shown in Figure 2.2, and gives a hexagonal BZ, with a few key high symmetry points. The Γ point is at the zone center, and there are two inequivalent points at the corners of the zone, labeled by *K* and *K′*. As will be shown later, these points give rise to the intriguing electronic behavior of graphene. The last interesting point is the M point, located midway between points *K* and *K*' along the zone boundary.

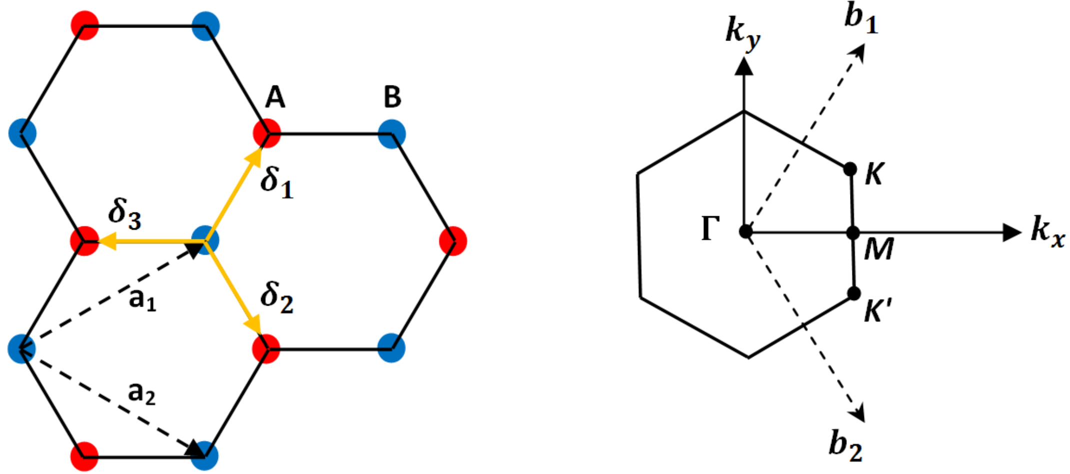

Figure 2.2. Honeycomb lattice and its Brillouin zone. (Left) Lattice structure of graphene, made out of two interpeneterating lattices: a_1 and a_2 are the lattice unit vectors, and $\delta_i, i = 1,2,3$ are the nearest-neighbor vectors. (Right) corresponding Brillouin zone. The Dirac cones are located at the K and K' points. Picture taken from [37].

2.2. Electronic structure of graphene

P.R. Wallace first calculated the band dispersion of graphene using a tight-binding method [4]. The Hamiltonian in second quantization form is given by:

$$H = -t_1 \sum_{\langle i,j \rangle,\sigma} \left(a_{i,\sigma}^* b_{j,\sigma} + h.c. \right) - t_2 \sum_{\langle <i,j> \rangle,\sigma} \left(a_{i,\sigma}^* a_{j,\sigma} + b_{i,\sigma}^* b_{j,\sigma} + h.c. \right) \quad 2\text{-}4$$

where $a_{j,\sigma}$ ($a_{i,\sigma}^*$) creates an electron with spin σ on site R_i on sublattice A, $b_{i,\sigma}$ ($b_{i,\sigma}^*$) creates an electron with spin σ on site R_i on sublattice B, t_1 is the NN hopping amplitude, and t_2 is the NNN hopping amplitude.

Making a Fourier transformation of H results in the Hamiltonian in momentum space [37], which is given by:

$$H = \sum_{\vec{k},\sigma}\left(T_1 a^*_{\vec{k},\sigma} b_{\vec{k},\sigma} + T_2 b^*_{\vec{k},\sigma} a_{\vec{k},\sigma} + T_3 (a^*_{\vec{k},\sigma} a_{\vec{k},\sigma} + b^*_{\vec{k},\sigma} b_{\vec{k},\sigma})\right) \quad \text{2-5}$$

where the coefficients are defined as:

$$\mathbf{T_1 = -t_1 \left(2e^{i\frac{a}{2}k_x} \cos\left(\frac{\sqrt{3}}{2} ak_y\right) + e^{-iak_x}\right)} \quad \text{2-6}$$

$$T_2 = -T_1 \left(2e^{-i\frac{a}{2}k_x} \cos\left(\frac{\sqrt{3}}{2} AK_Y\right) + e^{iak_x}\right) \quad \text{2-7}$$

$$T_3 = -t_2 \left(4\, cos\left(\frac{3}{2} ak_x\right) cos\left(\frac{\sqrt{3}}{2} ak_y\right) + 2cos(\sqrt{3}ak_y)\right) \text{8-2}$$

This Hamiltonian can be represented by a 2 by 2 matrix and the diagonalization of this matrix gives the band dispersion as:

$$E_{\pm}(\vec{K}) = +T_1 \sqrt{3 + F(\vec{K})} - T_2 F(\vec{K}), \quad \text{2-9}$$

$$F(\vec{K}) = 4\cos\left(\frac{3}{2} AK_X\right) \cos\left(\frac{\sqrt{3}}{2} AK_Y\right) + 2\cos(\sqrt{3} AK_Y) \quad \text{2-10}$$

where "+" applies to the upper band while "-" applies to the lower band. From Eq. 2-9, the band structure is symmetric around zero energy if $t_2 = 0$, but the electron-hole symmetry is broken and the upper and lower bands become asymmetric for finite t_2.

The whole band dispersion of graphene is shown in Figure 2.3 with finite t_1 and t_2. The bands near one of the Dirac cones are also shown in the inset in Figure 2.3. This dispersion can be obtained by expanding Eq. 2-9 aound the K point, as $\vec{k} = \vec{K} + \vec{q}$ (the vector K is given by Eq. 2-2) with $|\vec{q}| \ll \vec{K}$ and ignoring the t_2 term, since t_2 is small enough. This approximation results in:

$$E_{\pm}(\vec{Q}) \approx \pm T_1\sqrt{\left(\frac{3A}{2}Q_X\right)^2 + \left(\frac{3A}{2}Q_Y\right)^2 + O(Q_X^3) + O(Q_Y^3)} 11\text{-}2$$

$$= \pm v_F|\vec{q}| + O[q^2] \qquad \text{2-12}$$

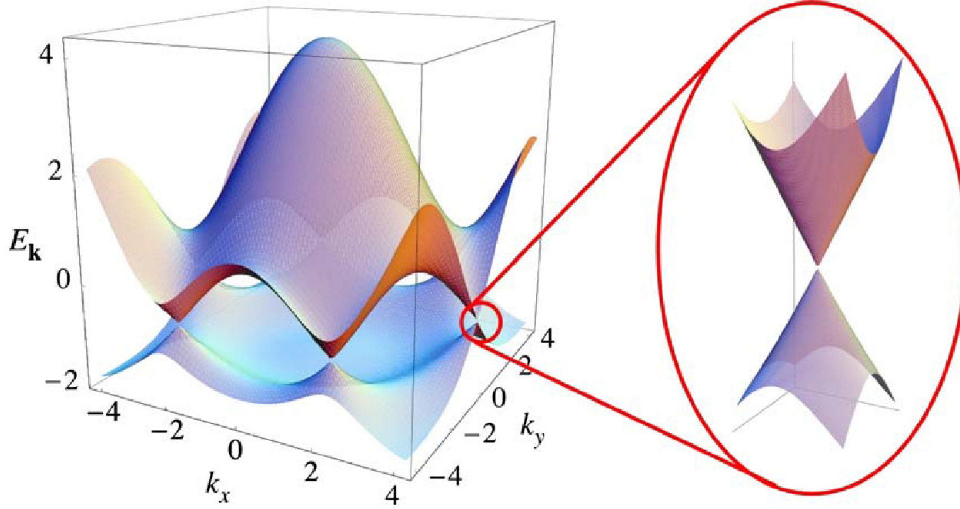

Figure 2.3. Electronic dispersion in the honeycomb lattice. (Left) Energy spectrum (in units of t) for finite values of t and t', with t=2.7 eV and t'=-0.2t. (Right) Inset of the energy bands close to one of the Dirac points. Picture taken from [37].

Equation (2-12) gives the Fermi velocity of the carriers in graphene with a value $v_F = \frac{3at_1}{2} \cong 1 \times 10^6\, m/s$. Graphene electronic dispersion in Figure 2.3 shows that the carriers in graphene are Dirac fermions, which should be described by the Dirac relativistic equation.

2.3. Raman spectroscopy in graphene

Raman spectroscopy is a spectroscopic technique used to study vibrational, rotational, and other low-frequency modes in a system. It relies on inelastic or Raman scattering of monochromatic light, usually from a laser in the visible, near infrared, or near ultraviolet range. The laser light interacts with phonons through the excitation and relaxation of charge carriers in the system, resulting in the energy of the scattered

photons being shifted to higher or lower energies. The shift in the energy of the photons is related to the energy of the zone center optical phonon modes in the system. An understanding of the phonon dispersion is essential to interpret the Raman spectra. Since there are two carbon atoms, A and B, in the unit cell of graphene as illustrated in Figure 2.2, one must consider 6 coordinates to interpret phonons once they are considered as mechanical vibrations in the system. The secular equation to be solved is thus a dynamical matrix of rank 6, such that 6 phonon branches are achieved. The phonon dispersion relation of the graphene comprises three acoustic (A) branches and three optical (O) branches. The modes are associated with out-of-plane (Z), in-plane longitudinal (L), and in-plane transverse (T) atomic motions [38].

Figure 2.4 shows the phonon dispersion branches of graphene. The three phonon dispersion branches, which originate from the Γ-point of the Brillouin zone, correspond to acoustic modes: an out-of plane mode (ZA), an in-plane transverse mode (TA), and in-plane longitudinal (LA), listed in order of increasing energy. The remaining three branches correspond to optical modes: one out-of plane mode (ZO), and two in-plane modes (TO) and (LO). While the TA and LA modes display the normal linear dispersion around the Γ-point, the ZA mode shows a q^2 energy dispersion as a consequence of the D_{6h} point-group symmetry of graphene [38]. Another consequence of the symmetry are the linear crossings of the ZA/ZO and the LA/LO modes at the K-point.

Near the zone center (Γ point), the in-plane TO and LO optic modes correspond to the vibrations of the sublattice A against the sublattice B, and these modes are degenerate at the Γ point. The degenerate zone-center LO and TO phonon modes belong to the two-dimensional E_{2g} representation and, therefore, they are Raman active modes [39-40]. The phonon modes around the K point are especially important, since the D-band and G'-band are related to phonon modes in the vicinity of the K point. The LO and LA phonon branches meet each other at the K point giving rise to a doubly degenerate phonon [38, 41-42].

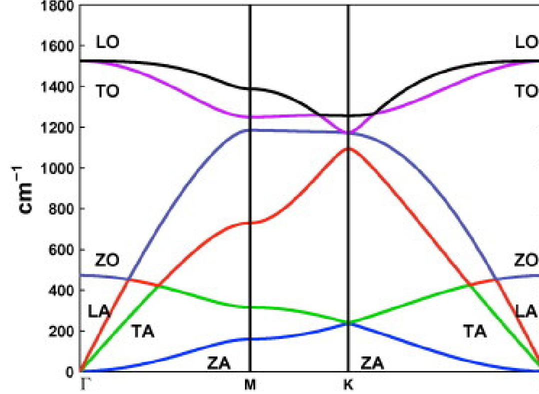

Figure 2.4. Phonon dispersion of graphene showing LO, TO, ZO, LA, TA, and ZA phonon branches along the high symmetry direction ΓM and ΓK in the BZ. Picture taken from [43].

The most prominent features in the Raman spectra of monolayer graphene are the so-called G band appearing at 1582 cm^{-1} and the G' band at 2700 cm^{-1} using laser excitation at 2.41 eV[38]. The G-peak (~ 1585 cm^{-1}) is due to first-order Raman scattering by the doubly degenerate zone center optical phonon mode, and the G'-peak (2680-2700 cm^{-1}) is associated with second-order scattering by zone-boundary phonons.[38, 44-46] In defective graphite, the D-peak (1345-1350 cm^{-1}) is due to first-order scattering by zone-boundary phonons. Since the G' peak approximately occurs in a frequency that is twice that of the D peak, $\omega_{G'} \sim 2\omega_D$, sometimes it is referred as the 2D peak. There are two less important peaks called G^* at 2450 cm^{-1} and D+G at ~ 2940cm^{-1} as shown in Figure 2.5. The D and 2D peak positions vary with changes in the energy of the incident laser. This is due to so-called double resonance (DR) Raman process that results in a dispersive behavior in the frequencies of D and 2D peaks.

The double-resonance (DR) process shown in the center and right side of Figure 2.6 begins with an electron of wave-vector **k** around K absorbing a photon of energy E_{laser}. The electron is inelastically scattered by a phonon or a defect of wavevector **q** and energy E_{phonon} to a point belonging to a circle around the K' point, with wavevector **k+q**, where the K' point is relatedto K by time reversal symmetry [36]. The electron is then

scattered back to a **k** state, and emits a photon by recombining with a hole at a **k** state. In the case of the D band, the two scattering processes consist of one elastic scattering event due to the defects of the crystal and one inelastic scattering event due to emitting or absorbing a phonon, as shown in Figure 2.6.

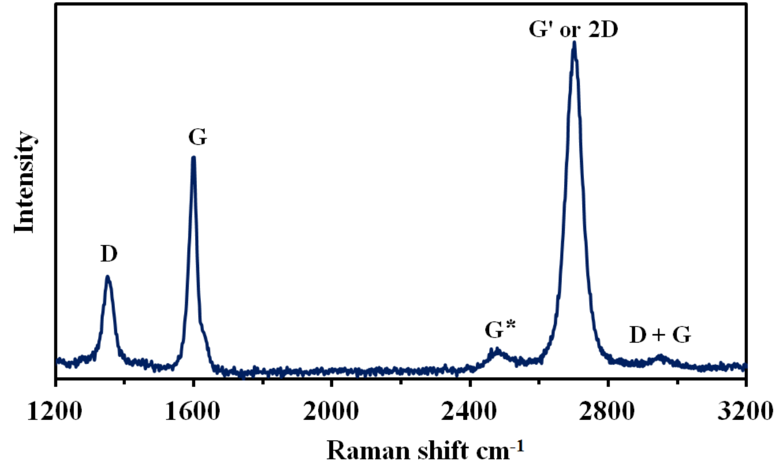

Figure 2.5. Raman spectra of graphene, showing the main Raman features, the D, G, G' (2D).

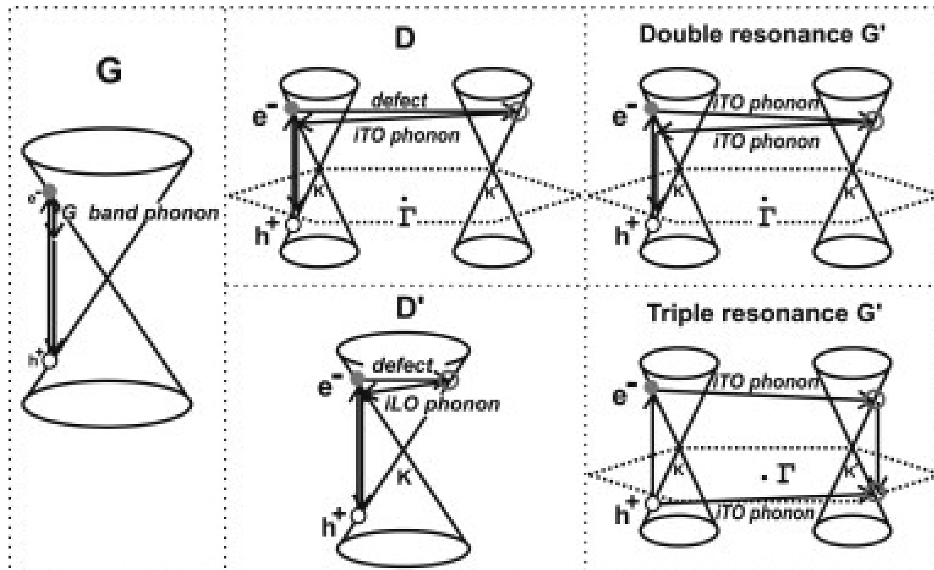

Figure 2.6. (Left) First-order G-band process and (Center) one-phonon second-order DR process for the D-band (intervalley process) (top) and for the D0-band (intravalley process) (bottom) and (Right) two-phonon second-order resonance Raman spectral processes (top) for the doubleresonance G0 process, and (bottom) for the triple resonance G0 band process (TR) for monolayer graphene. Picture taken from [38].

2.4. Review of graphene synthesis

2.4.1. Mechanical Exfoliation

Graphene has been synthesized on metal surfaces under ultra high vacuum conditions for many years and has been investigated in a series of studies to yield insight into its formation [47-52]. More recently, single flakes of graphene have been isolated and transferred from highly oriented pyrolytic graphite (HOPG) to other substrates using micromechanical exfoliation. Through repeated peeling of 3-D graphite crystals, British researchers, Andre Geim and Konstantin Novoselov, obtained relatively large graphene crystals [1-2, 53]. The interlayer spacing in graphite is 3.35 Å. It is reported that the exfoliation energy for pyrolytic graphite is 61 meV/C atom [54]. It has been estimated that a 1-nm square of graphene contains about 38 carbon atoms and the separation energy of two 1 nm squares of graphene is over 2 eV. A top-down approach using a micromechanical cleavage technique is applied to overcome this energy. Peeling small masses of HOPG makes a fresh surface of layered crystal which, when rubbed against another surface, leaves a variety of flakes attached to it. Within this process, unexpectedly, a single layer was found using an adhesive tape applied to the graphite as shown in Figure 2.7.

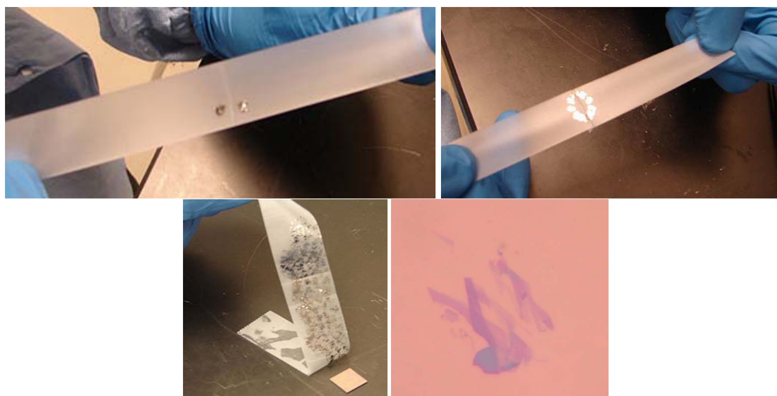

Figure 2.7. Single flakes of graphene have been isolated and transferred from highly oriented pyrolytic graphite (HOPG) to other substrates using micromechanical exfoliation.

Graphene mechanical exfoliation has sparked significant research interest due to the distinctive electronic structure and physical properties observed [1-2, 53]. However, this method of obtaining graphene leads to a random deposition of small graphene flakes with both low surface coverage and low reproducibility. Many applications require the synthesis of large area graphene films on insulating substrates, and this has motivated the search for other techniques.

2.4.2. Epitaxial Growth

2.4.2.1. Epitaxial growth on silicon carbide

Considerable efforts to synthesize large-area high quality graphene films have been made in recent years. Epitaxial growth from single crystal SiC has been the target of intense research due to the high quality of the graphene films that form on SiC substrates for electronics applications. A SiC substrate can be reduced to graphene through heating at high temperatures, usually more than 1100℃ [22-23]. This system is composed of several graphene layers, of which the first layer is electron doped, due to the built-in electric field at the SiC-graphene interface, and the other layers are essentially undoped [22-23, 55-56]. Epitaxial graphene shows quasi-ballistic transport and long coherence lengths. In contrast to exfoliated graphene, the quantum Hall effect is not observed in high mobility epitaxial graphene. It appears that the effect is suppressed due to the absence of localized states in the bulk of the material [2, 22]. Epitaxial graphene can be patterned using standard lithography methods and characterized using a wide array of techniques [22-23]. These favorable features indicate that interconnected room temperature ballistic devices may be feasible for low dissipation high-speed nano-electronics. Ultrathin epitaxial graphene is synthesized on the silicon-terminated face of single-crystal 6H-SiC by thermal desorption of Si as shown in Figure 2.8.

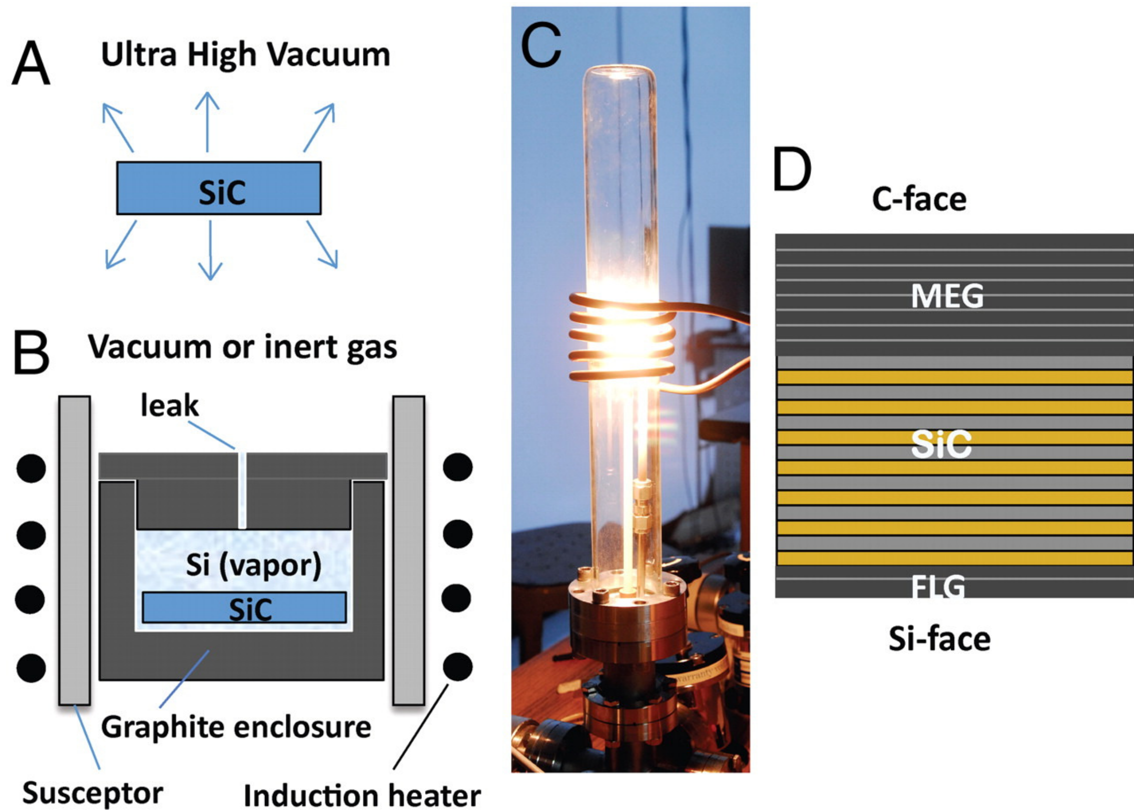

Figure 2.8. The confinement controlled sublimation (CCS) method. (A) SiC wafer in UHV: Sublimed silicon is not confined, causing rapid, nonequilibrium graphene growth. (B) The CCS method: sublimed Si gas is confined in a graphite enclosure so that growth occurs in near thermodynamic equilibrium. Growth rate is controlled by the enclosure aperture (leak), and the background gaspressure. (C) Photograph of the induction furnace. (D) Under CCS conditions few layer graphite (FLG, from 1 to 10 layers) grows on the Si terminated face, and multilayer epitaxial graphene (MEG, from 1 to 100 layers) grows on the C terminated face. Picture taken from [57].

First, SiC substrate was treated by oxidation or H_2 etching. Then, samples were heated up to 1000°C by electron bombardment in ultrahigh vacuum to remove the oxide. Finally the sample was heated up to 1250°C to 1450°C for 1-20 minutes [22]. Monolayer and bilayer graphene on the Si-terminated face, and multilayer graphene on the carbon face, have been synthesized [57-58]. Electron mobility on the order of 15000 cm^2/Vs has been obtained in FETs using epitaxial graphene grown on SiC substrates [23].

Researchers at IBM have made a transistor with a cut-off frequency of 100 GHz using epitaxial graphene [59].

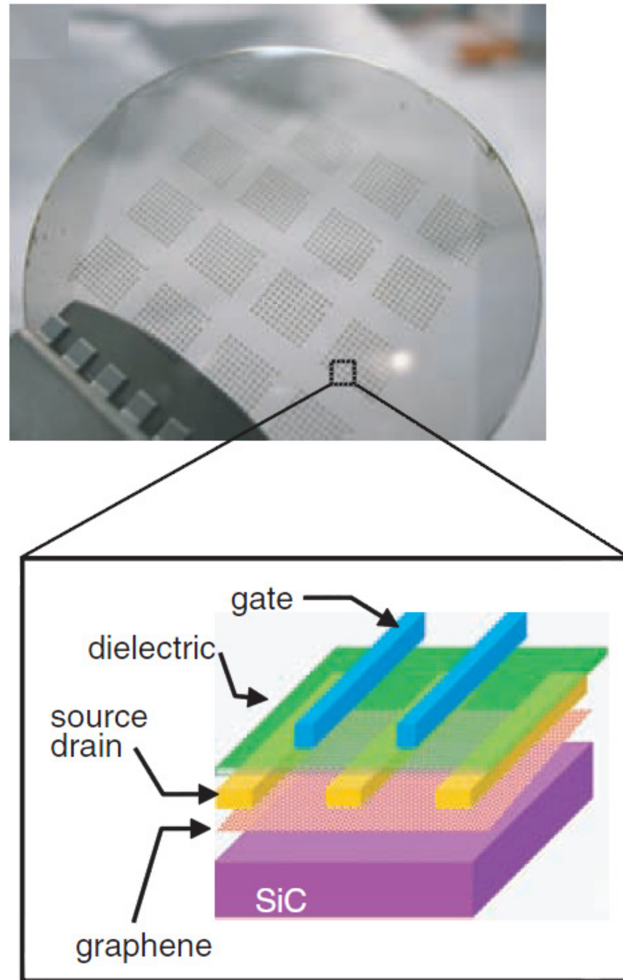

Figure 2.9. Image of devices fabricated on a 2-inch graphene wafer and schematic cross-sectional view of a top-gated graphene FET. Picture taken from [59].

It is believed that the device can be further miniaturized and optimized so that it could soon outperform conventional devices made from silicon. Figure 2.9 shows an image of devices fabricated on a 2-inch graphene wafer and a schematic cross-sectional view of a top-gated graphene FET. The transistor could find application in microwave communications and imaging systems. However, this method is limited in terms of the production of large area graphene films due to the expense and the limited size of SiC substrates. In addition, this method is not amenable to the production of graphene for use

on other substrates, since it is challenging to detach graphene from the SiC [23, 55, 58]. Furthermore, the bonding between the bottom graphene and the substrate affects the properties of carbon layers.

2.4.2.2. Epitaxial growth on metals

Sutter et al. [55] developed a method based on the epitaxial technique to overcome the shortcoming of epitaxial method on SiC which produces arrays of macroscopic single-crystalline graphene on ruthenium (0001). In this way, while the bottom graphene layer interacts strongly with the surface, the layer up is strongly detached and only a weak electronic coupling exists there. This allows graphene to have free-standing behavior. In this method, carbon atoms are absorbed within the ruthenium by heating the entire sample up to 1150°C. Then, the sample is cooled down to 850°C causing some of the absorbed carbon atoms to rise up to surface. Islands of about 100 micrometers formed dotting the entire surface. Finally, these islands grow to cover the entire surface and the second layer forms after reaching 80 percent coverage. Later iridium is used as another substrate to form graphene. Although, the graphene grown on iridium was uniform in thickness and can be made to be highly ordered, it is slightly rippled which may result in the generation of minigaps in the electronic band-structure. Figure 2.10 shows the morphology of epitaxial graphene on Ru (0001).

2.4.3. Reduction methods

To address the shortcomings with epitaxial and exfoliation methods, several techniques have been developed to deposit graphene films onto a variety of substrates, including the chemical reduction of solution deposited graphite oxide (GO) films [25, 60-63] and liquid phase exfoliation and solution deposition of graphite [24, 26, 56].

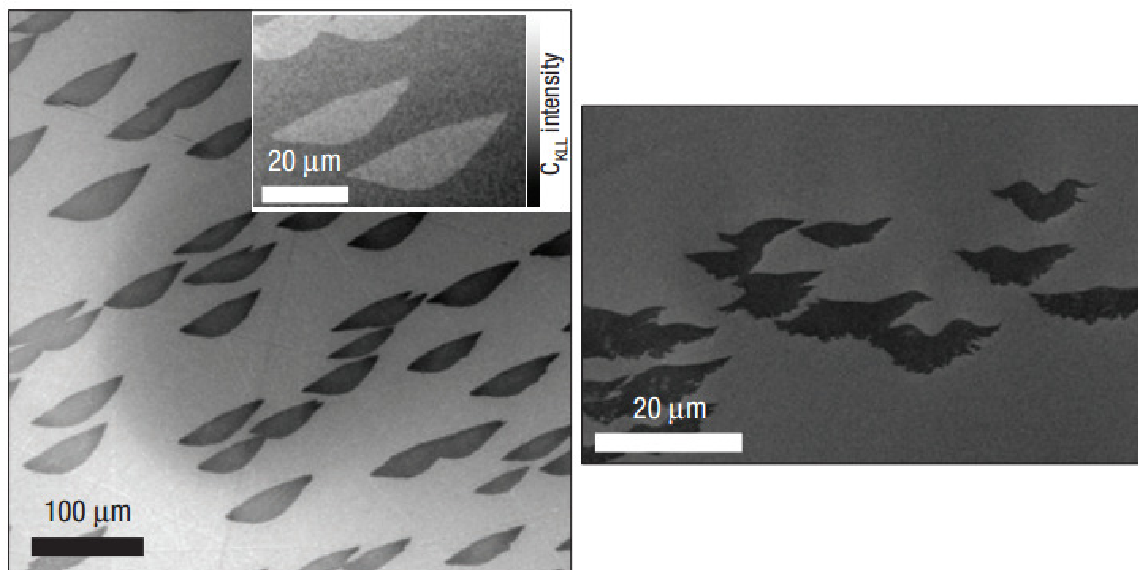

Figure 2.10. Morphology of epitaxial graphene on Ru(0001). (Left) UHV-SEM image of a large area of the Ru(0001) surface after first-layer graphene growth. (Right) UHV-SEM image of a group of second-layer graphene islands. Picture taken from [55].

2.4.3.1. Reduced graphene oxide (RGO)

Stankovich et al. [64] focused more on characteristics of traditional hydrazine-reduced graphene oxide (GO). After oxidizing using the Hummer's method in sulfuric acid/potassium permanganate solution and reducing with hydrazine, the researchers characterized the before-and-after transformation with SEM to show crumpled up sheets of the reduced GO [64]. Figure 2.11 shows secondary electron mass spectroscopy (SEM) images of reduced GO sheets.

2.4.3.2. Hydrazine reduction

Yang et al. [65] proposed a method for mass production of graphene. They developed a method of placing graphite oxide paper in a solution of pure hydrazine, composed of nitrogen and hydrogen, which reduces the graphite oxide paper into single layer graphene. The coverage of graphene can be controlled by altering the composition

of the hydrazine solution. Tung et al. [61] reported a versatile solution-based process for large scale production of single layer chemically converted graphene over the entire area of a Si/SiO_2 wafer. They removed oxygen functionalities and restored the planar single sheets by dispersing graphite oxide paper on pure hydrazine. Figure 2.12 shows graphite oxide (GO) paper in a glass vial and the resultant hydrazinium graphene (HG) dispersion after addition of hydrazine.

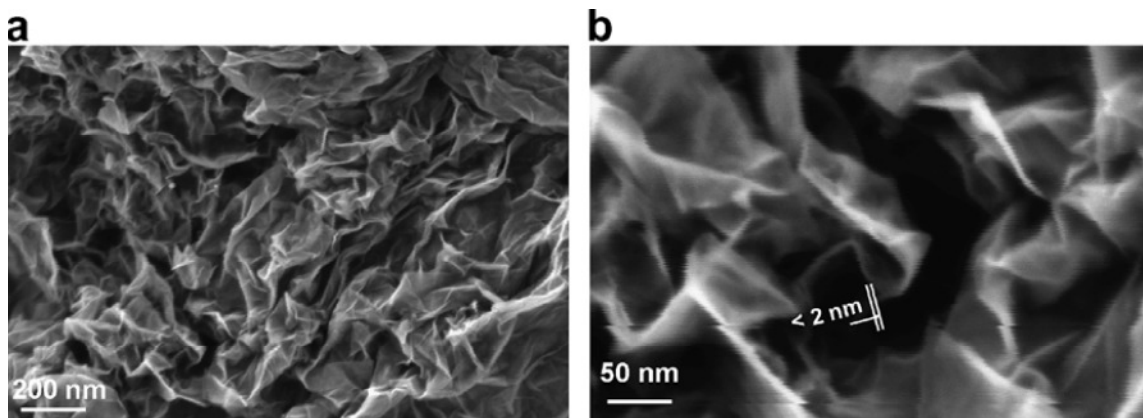

Figure 2.11. (Left) SEM image of aggregated reduced GO sheets. (Right) A platelet having an upper bound thickness at a fold of ~2 nm. Picture taken from [64].

2.4.3.3. Sodium reduction of ethanol

Choucair et al. [66] reported the direct chemical synthesis of carbon nanosheets in gram-scale quantities in a bottom-up approach. They utilized sodium metal for reduction of ethanol and then pyrolized it. Sodium salts were removed through washing with water. The ability to produce bulk graphene samples from non-graphitic precursors with a scalable, low-cost approach should take us a step closer to real-world applications of graphene. An example of the bulk quantity of graphene product is shown in Figure 2.13.

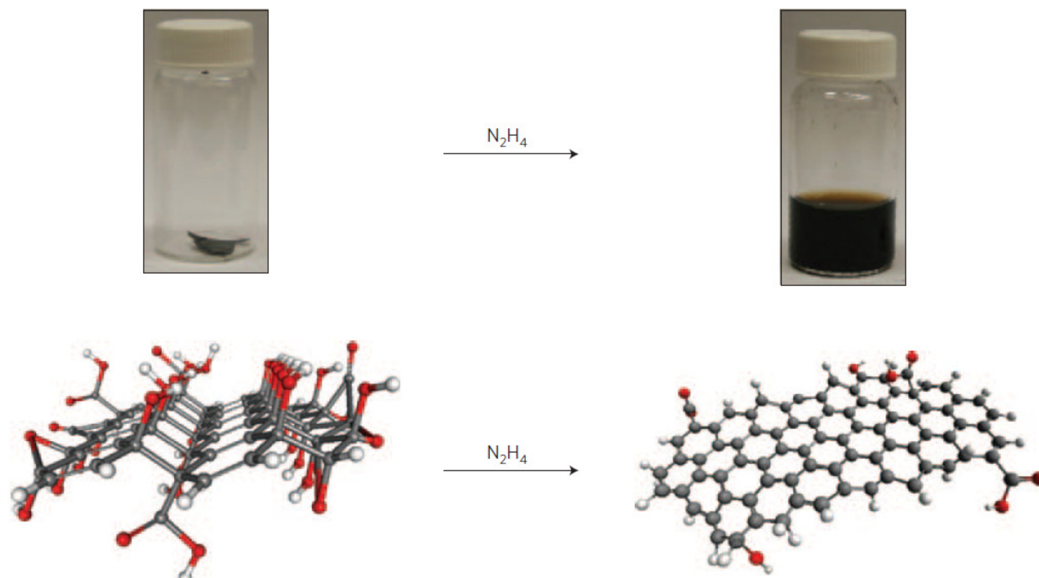

Figure 2.12. Photographs of 15 mg of graphite oxide (GO) paper in a glass vial (a) and the resultant hydrazinium graphene (HG) dispersion after addition of hydrazine. Picture taken from [61].

Figure 2.13. Example of the bulk quantity of graphene product. The image consists of approximately 2 g of sample. Picture taken from [66].

2.4.4. Chemical vapor deposition (CVD): synthesis and transfer

2.4.4.1. Introduction

CVD is one of the easiest methods for the fabrication of large area graphene sheets [28, 30, 39]. The key feature of such fabrication is the solubility of carbon in

transitional metals such as Ni, Co, Pt, Ir, Ru, and Cu at the typical synthesis temperature for graphene (~900 - 1000°C) [28, 30]. Rapid advances in CVD graphene on Ni and Cu polycrystalline films have been achieved recently, which have stimulated various applications owing to scalability and transferability. In a typical CVD method, a hydrocarbon gas such as methane, [29] acetylene, [67] or ethylene [68] was passed through the catalyst surface under high temperature, causing the nucleation and growth of graphene. Under these conditions, hydrocarbon decomposes and provides carbon atoms that diffuse rapidly into the nickel at the growth temperature, and later precipitate to the surface to form a graphene layer during the cool down phase of the CVD growth cycle. A mixture of various layers has been grown, which can be ascribed to the nonequilibrium precipitation of carbon from a Ni substrate, especially at grain boundaries [30].

2.4.4.2. CVD on Ni

Yu et al. [39] reported an approach to synthesize high quality graphene through a segregation process followed by transfer to an insulator substrate. The idea was pioneered by Hayes et al. [69] in the 1930s, where they studied graphite segregation at the surfaces and grain boundaries of metals. They conducted segregation at high temperatures in an equilibrium process. However, during the cool down stage the number of carbon layers cannot be preserved at ambient temperature. Therefore, controlling the synthesis parameters, especially the cooling rate, is critical to produce thin film graphenes. Figure 2.14 demonstrates the steps for synthesis of graphene on Ni substrates reported in [39]. As the first step Ni foils with thickness of 0.5 mm and purity of > 99 %, from Alfa Aesar, were cut into 5×5 mm^2 pieces and were then mechanically polished. The samples were placed in a chamber with protection gas flow, H_2 at 100 sccm, for an hour at high temperature. In the second step of carbon dissolution, precursor gases CH_4:H_2:Ar = 0.15: 1: 2 with a total gas flow rate of 315 sccm were introduced at ambient pressure. Under

these conditions, hydrogen molecules decompose at the Ni surface and carbon atoms diffuse into the metal.

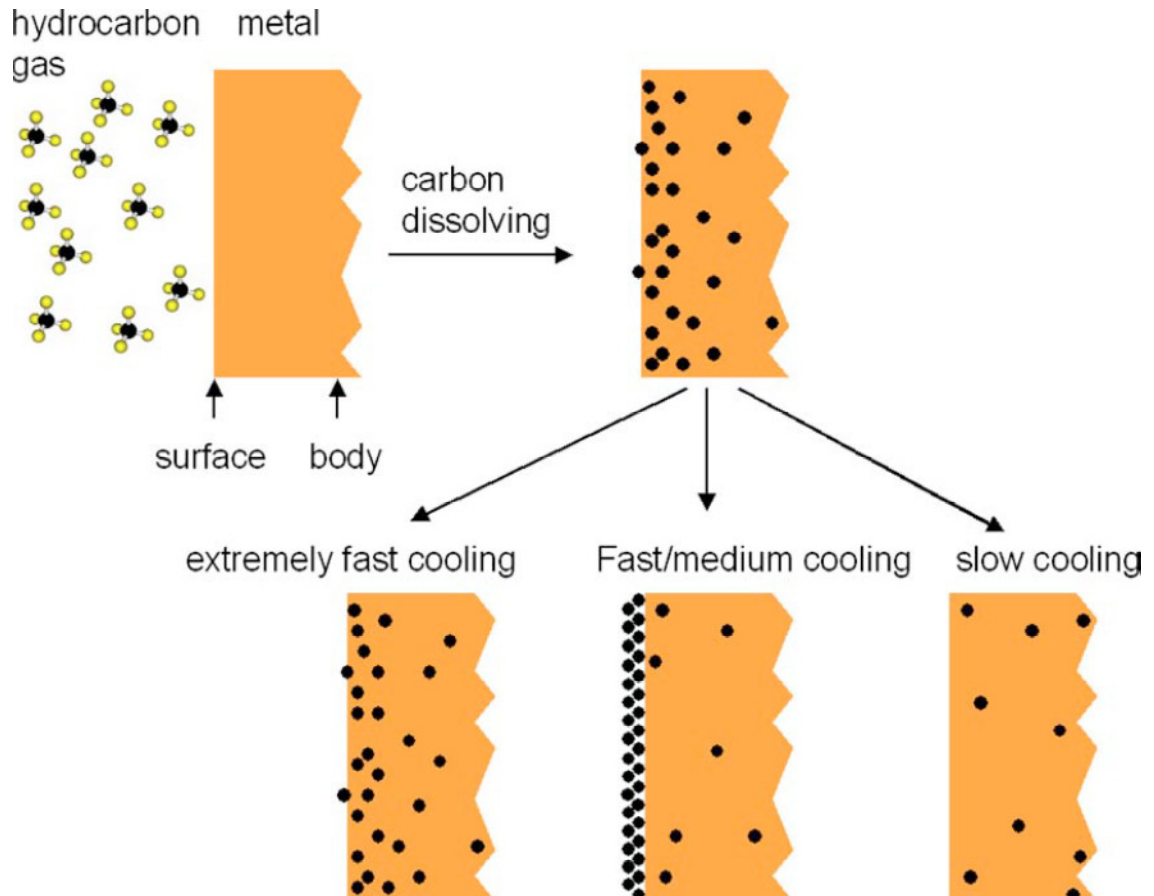

Figure 2.14. Illustration of carbon segregation at metal surface. Picture taken from [39].

The carbon concentration decreases exponentially from surface to bulk material. This step takes usually 20 minutes at 1000°C. In the last step, carbon segregation, the sample was cooled down mechanically, pushing the sample holder to a low temperature area in the presence of an Ar atmosphere. The cooling rate was found to be important in the characteristics of graphene formed on Ni substrates. Using Raman spectroscopy this difference in carbon characteristics was made clear. Figure 2.15 shows the Raman spectra of segregated carbon on a Ni surface with different cooling rates.

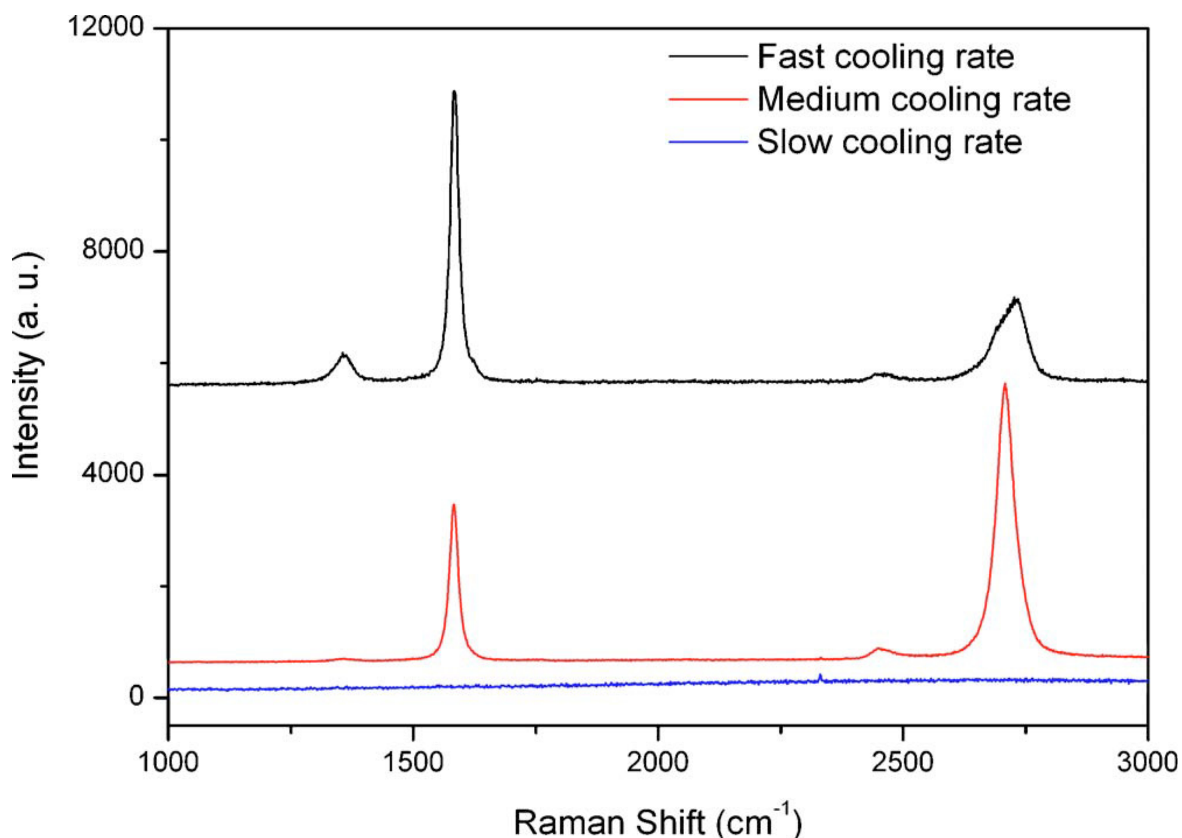

Figure 2.15. Raman spectra of segregated carbon at Ni surface with different cooling rates. Picture taken from [39].

Another challenge for graphene synthesis using CVD is the ability to transfer it from the growth substrate to other substrates of technical importance. Yu et al. [39] employed a wet etching technique to transfer the grown film to an insulating substrate by detaching the graphene films from the Ni in HNO_3 solution. The process was performed using copper grids and was followed by rinsing with deionized water. Another technique for transferring graphene films is to use silicon rubber. After growth of graphene on Ni layer, a thin layer of silicon rubber was applied on the surface, which was then covered by a glass substrate to form a four layer sandwich structure (Ni/Graphen/silicone/glass). After curing overnight, the metal substrate was etched away with a diluted HNO_3 solution. Cao et al. [70] utilized the same procedure to synthesize graphene and transfer it to insulators for electronic applications. They reported carrier mobility reaching 2000

cm^2/Vs and phase coherence length over 0.2 μm. This opened many application possibilities for carbon-based electronics. Films as thin as ~2 layers and as thick as tens of layers of graphene in the sample were reported. The transfer process was conducted without any auxiliary or supportive material. A photograph of large-scale graphene films transferred to an insulating substrate is shown in Figure 2.16. Changing the growth parameters to investigate its influence on the characteristics of CVD-grown graphene indicated that medium cooling rates have a high quality crystal structure. Higher intensity in the Raman 2-D vs. G peak occurs in graphene having a few (less than four) layers. Higher cooling rates result in more layers with defects, and more graphene (less than four layers) can be synthesized on smoother Ni substrates.

Reina et al. [30] presented a low cost technique via ambient pressure chemical vapor deposition (CVD) on Ni substrate. Thin films were e-beam evaporated onto SiO_2/Si substrates and thermally annealed up to 900-1000°C in the presence of H_2 (500 sccm) and Ar (600 sccm) gases for 10-20 minutes. During this process Ni grains with flat surfaces and sizes of 1-20 μm formed. During the CVD growth constant temperature was maintained; CH_4 and H_2 were maintained, with the flow rate of 5-25 sccm and 1500 sccm, respectively, for 5 to 10 minutes. Finally, the system cooled down. The transfer of graphene films onto a substrate was enabled by the wet-etching process. The film was exposed to an aqueous HCl solution after applying a supportive material, for example PMMA, on the synthesized graphene. After etching the metal away, PMMA/graphene floated over the solution. Finally, PMMA/graphene transferred to desired substrate and PMMA was dissolved with acetone to leave graphene film on the substrate. The size and the shape of the transferred graphene film depended on the Ni sample size.

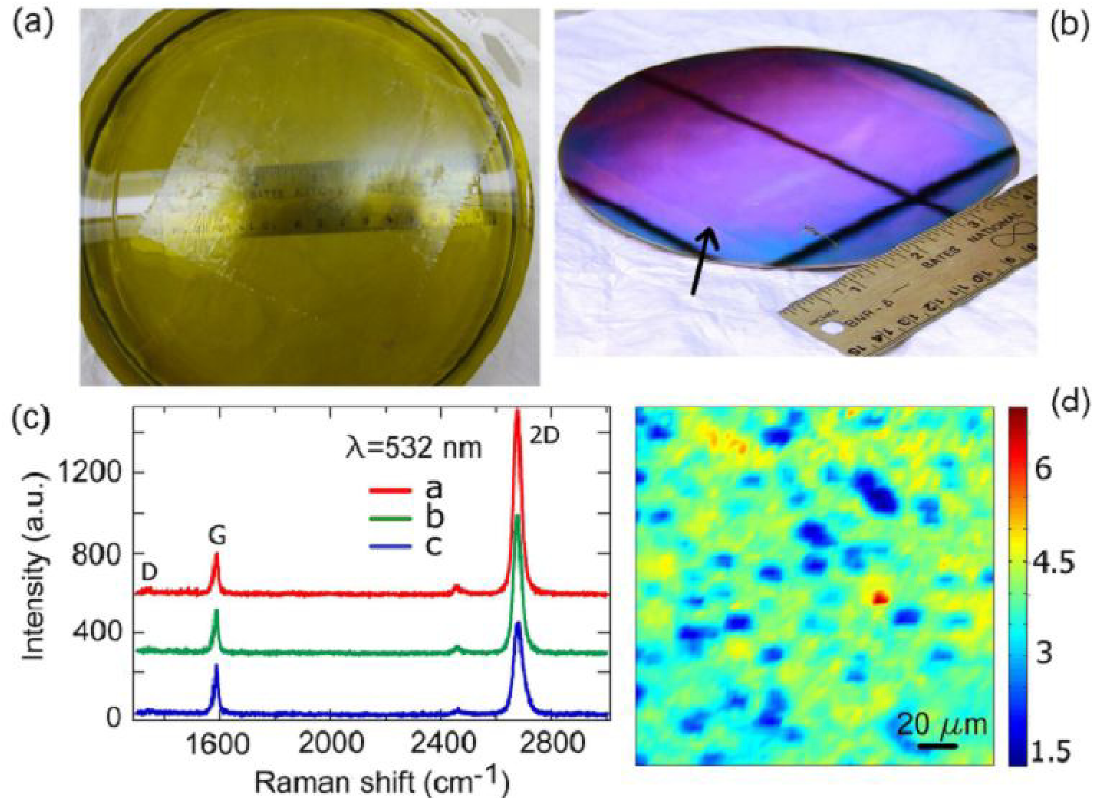

Figure 2.16. Photograph of a 4 in by 4 in CVD graphene film (a) coated with PMMA and floating on liquid after etching off the Cu substrate and (b) transferred on a Si wafer, with PMMA removed (arrow marks the edge of graphene and thick black lines on the wafer are room ceiling reflections). (c) Representative Raman spectra (c, offset for clarity) measured (with a 532nm laser) in a CVD graphene film transferred to SiO_2/Si. The 2D band can all be fitted by a single Lorentzian, with center ~2680 cm^{-1} and FWHM ~34 cm^{-1}. (d) Raman map of I_{2D}/I_G over a 200 μm ×200 μm area, most (99%) of which can be associated with monolayer (I_{2D}/I_G>2). Picture taken from [70].

Kim et al. [28] reported the direct synthesis of large-scale graphene films using chemical vapor deposition on thin nickel layers. They presented two different methods of patterning the films and transferring them to arbitrary substrates. The growth recipe is the same as presented in the literature with some minor changes. The substrate was Ni/SiO_2/Si with Ni having less than 300 nm thickness. The growth was conducted in an

Ar atmosphere at 1000 °C inside a quartz tube chamber. The precursor gases were H_2, CH_4, and Ar with 65, 50, and 200 sccm, respectively. The growth lasted for 7 minutes. After growth, the system was cooled down rapidly by flowing Ar at ambient pressure to maintain a cooling rate 10 °C/s for better graphene formation. Graphene transfer was conducted in two different methods. In a much easier method, a solution of HF and buffered oxide etchant (BOE) was applied to graphene/Ni/SiO_2/Si for a short period of time; this resulted in separating graphene/Ni from the Si substrate; then, in the second stage the graphene/Ni was again exposed to the same solution, causing the graphene film to float on the solution. This process can be performed for a long period of time to detach Ni/SiO_2/Si at once from graphene film. Then, the floating graphene film can be transferred by direct contact with substrates.

In the second method, a layer of PDMS as a supportive material was deposited on graphene/Ni/SiO_2/Si. Then, the five layer sandwich structured was exposed to a $FeCl_3$ solution (1 M) to etch the Ni. The remaining PDMS/graphene was stamped on a substrate. Figure 2.17 illustrates the growth and transfer process on Ni/SiO_2/Si substrate.

2.4.4.3. CVD on Cu

Cu is a favorable substrate for synthesis of uniform graphene. A large area of monolayer graphene, with less than 5% of that having bi or tri-layers, has been produced by CVD process on Cu substrate [29]. Graphene was continuous across copper surface steps and grain boundaries. It has been reported that the growth of the second layer would stop once the catalytic Cu surface was fully covered by one-layer graphene; this would be an instance of the so-called self-limiting effect [29, 71]. However, the self-limiting effect has not been repeated and is yet not confirmed in the scientific community. Different Cu thicknesses were tried and better results were obtained using a 25 μm thick Cu foil. The samples were placed in a 22 mm ID fused silica tube heated in a split tube furnace.

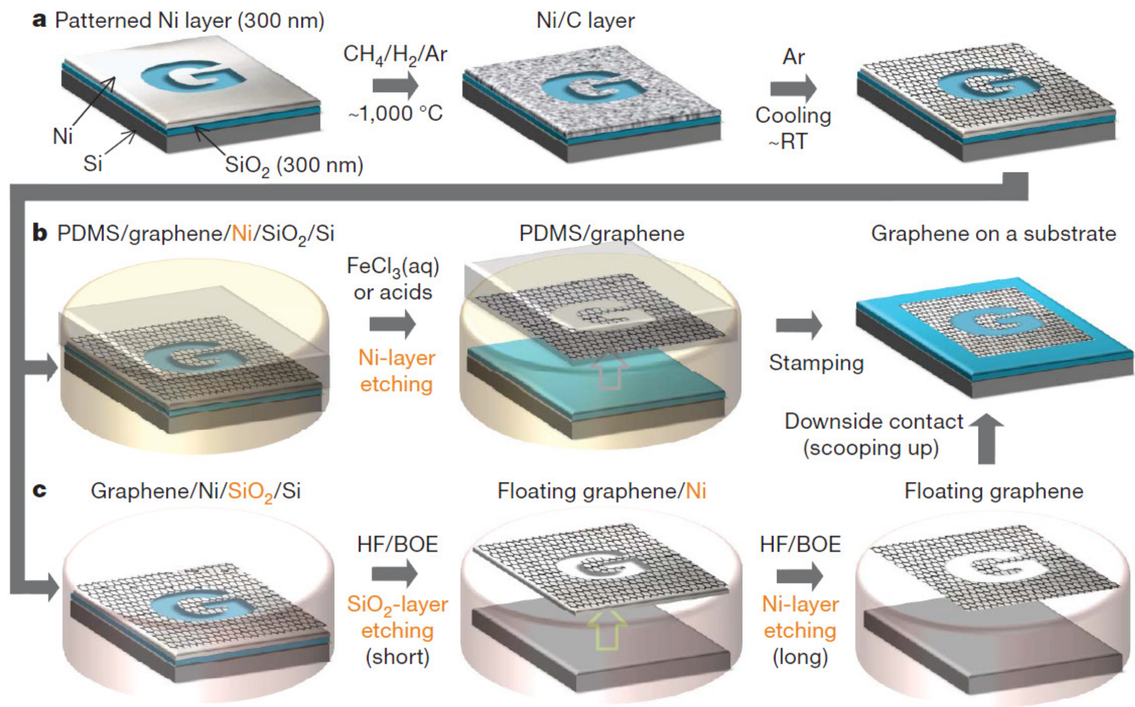

Figure 2.17. Synthesis, etching, and transfer process for large scale and patterned graphene films. Picture taken from [28].

Unlike other CVD recipes, growth was conducted under vacuum pressure in this method. First, the system was evacuated and back filled with hydrogen. Then it was heated up to 1000°C maintaining a H_2(g) pressure of 40 mTorr under a 2 sccm flow rate. During growth, after stabilizing the temperature at the same temperature, CH_4(g) with the flow rate of 35 sccm was introduced for a desired period of time at total pressure of 500 mTorr. Finally, the furnace was cooled down to room temperature. This recipe is depicted in Figure 2.18.

Graphene films were removed through two methods. In the first method, graphene was placed in a $Fe(NO_3)_3$ solution, with 0.05 g/ml iron nitrate, overnight, which caused Cu to be dissolved. In the second method, a layer of PDMS was applied on graphene as an auxiliary layer to form a three layer sandwich structure: PDMS/graphene/Cu. Then, the sample was placed in $Fe(NO_3)_3$ solution to remove Cu. PDMS was lifted from the graphene using methods similar to those described in the literature. The graphene films

were easily transferred using the second method with fewer holes or cracks. Figure 2.19 shows an SEM image of graphene films grown on Cu and the graphene films transferred onto Si/SiO_2 and glass substrates.

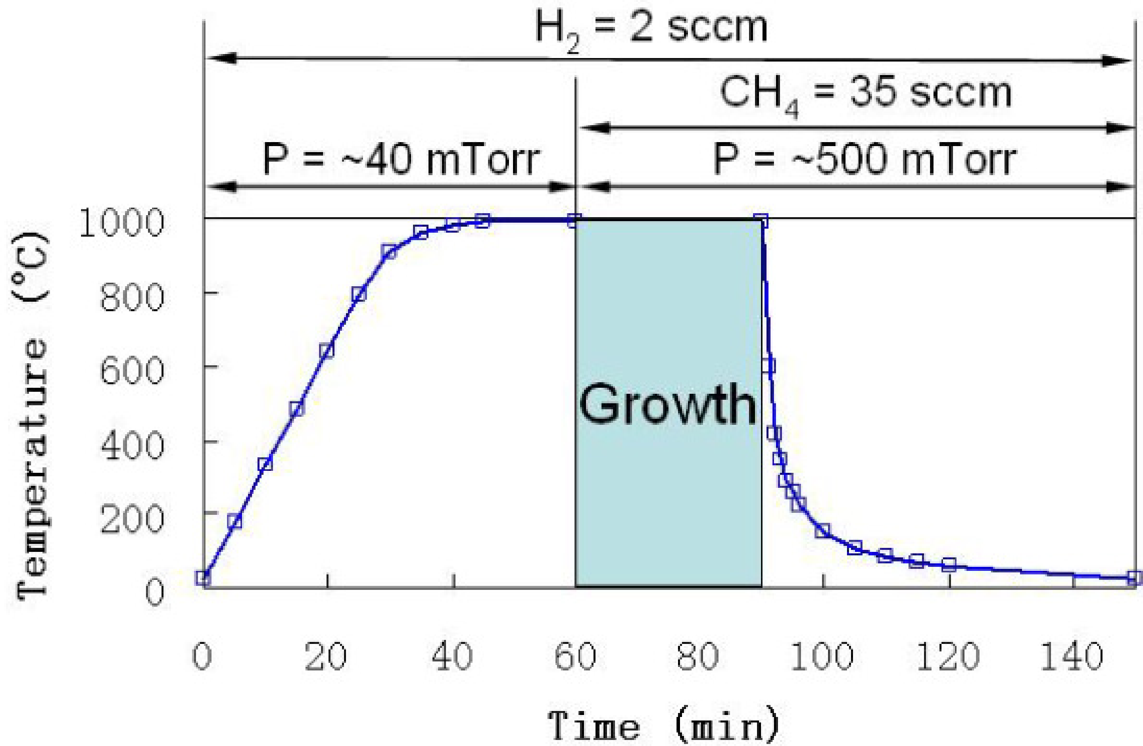

Figure 2.18. Time dependence of experimental parameters: temperature, pressure, and gas composition/flow rate. Picture taken from [29].

The CVD method allows large-scale production of high quality graphene films on flexible copper substrates that can be used in the form of roll-type substrates fitting inside a tubular furnace to maximize the scale and homogeneity of the produced films. Bae and colleagues [11] reported a cost- and time-effective method to produce 30 inch graphene films for transparent electrode applications. They utilized a multiple roll-to-roll transfer and wet chemical doping to enhance the electrical properties of the graphene films. Figure 2.20 shows the three step transfer of graphene from Cu foil onto a flexible transparent substrate. First, graphene was attached to a thin polymer coated with an thermal adhesive layer through passing between two rollers. Then, Cu was etched in

aqueous 0.1 M ammonium persulphate solution $(NH_4)_2S_2O_8$. Finally, graphene was transferred to target substrate through removing adhesive force by heating. Figure 2.21 presents photographs of the roll-based synthesis and transfer process. An 8-inch-wide tubular quartz reactor was used in the CVD system, allowing a monolayer graphene film to be synthesized on a roll of copper foil with dimensions as large as 30 inches in the diagonal direction.

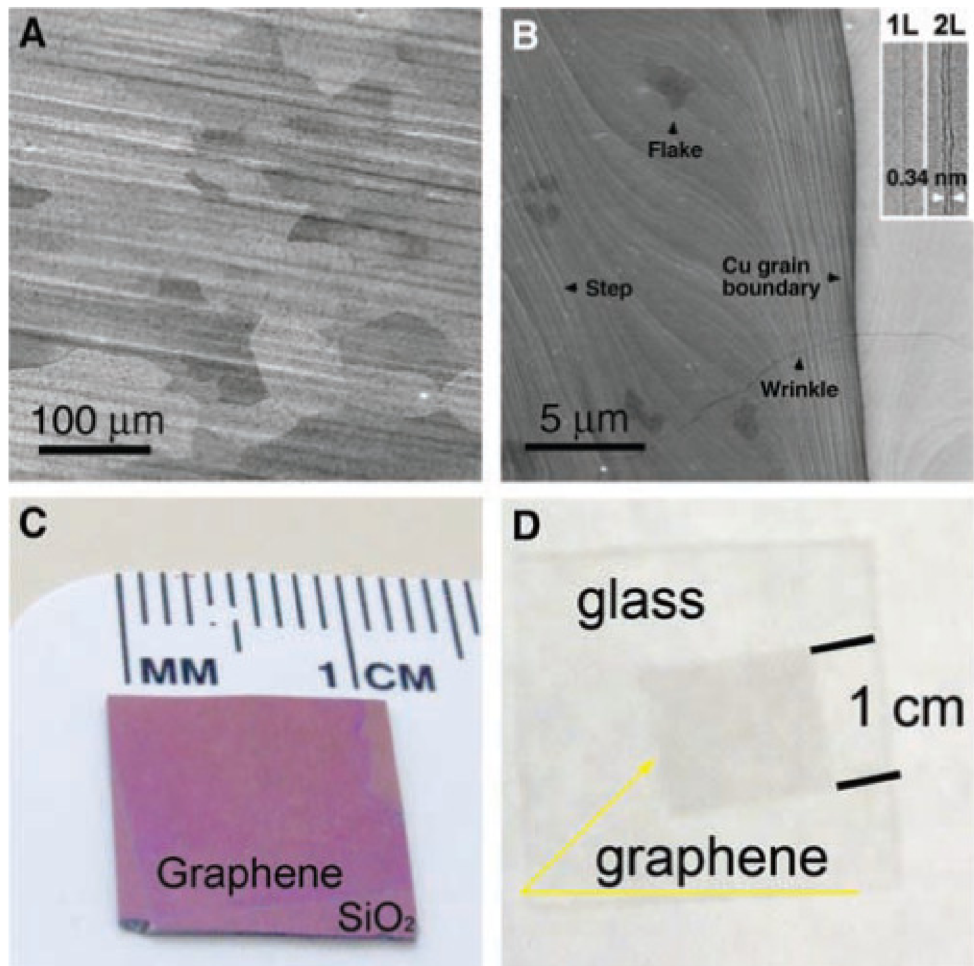

Figure 2.19. SEM image of graphene on a copper foil with a growth time of 30 min. (B) High-resolution SEM image showing a Cu grain boundary and steps, two- and three-layer graphene flakes, and graphene wrinkles. (C and D) Graphene films transferred onto a SiO_2/Si substrate and a glass plate, respectively. Picture taken from [29].

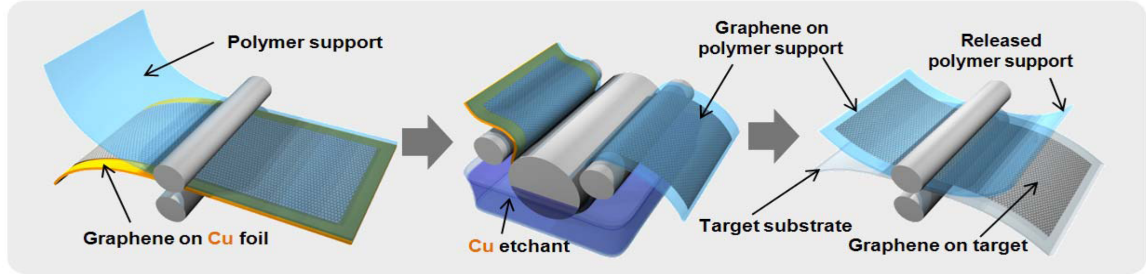

Figure 2.20. Schematic of the roll-based production of graphene films grown on a copper foil and its transfer to flexible substrate. Picture taken from [11].

The saturated solubilities of carbon species at high temperature in Cu and Ni are significantly different, with Cu having small solubility with a maximum of ~ 0.04%, while Ni has a moderate solubility of carbon close to 2.7%., which may lead to their distinct CVD performances for graphene growth [72].

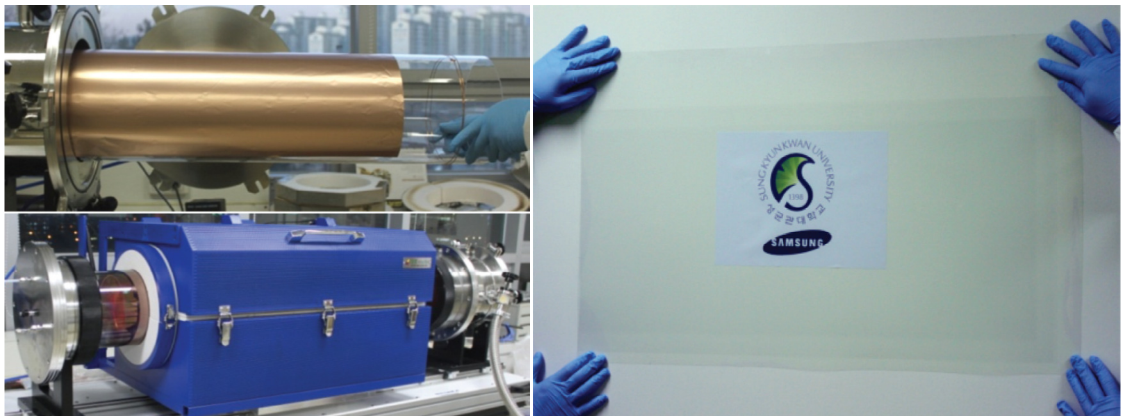

Figure 2.21. (Left) Photographs of the roll-based production of graphene films. Copper foil wrapping around a 7.5-inch quartz tube to be inserted into an 8-inch quartz reactor. The lower image shows the stage in which the copper foil reacts with CH_4 and H_2 gases at high temperatures. (Right) A transparent ultralarge-area graphene film transferred on a 35-inch PET sheet. Picture taken from [11].

Overall, the quality of graphene synthesized using CVD is lower than that of graphene grown on SiC through the epitaxial method. For example, the highest mobility

measured in CVD graphene transferred on SiO_2 substrate without surface treatment is 3000-4000 cm^2/Vs [27], which is an order of magnitude less than that obtained with the epitaxial method. However, recent reports indicate the possibility of improvement in the properties of CVD graphene through synthesis of large-grain graphene [73].

2.4.4.4. CVD using solid carbon source

In addition, carbon atoms can also be supplied by the decomposition of a carbon containing material, [74] single crystal diamond, [75] C_{60}, [76] or HOPG, [77] in contact with the transitional metal catalyst film. Graphene synthesis using a solid carbon source, such as a polymer film or small molecules deposited on a metal catalyst substrate, provides flexibility in the control of layers that are produced [78-80]. In addition, the CVD method is limited to flammable gases, which are difficult to handle and apply the technology to the variety of potential feedstocks [78]. The key feature in this method is decomposition of polymers upon heating, which provides a carbon source to the catalyst through diffusion process. This method has the lowest quality compared to CVD and epitaxial methods; however, it is a simple, inexpensive, and safe process. In addition, polymers can be easily deposited on any substrate and can be patterned using simple lithography.

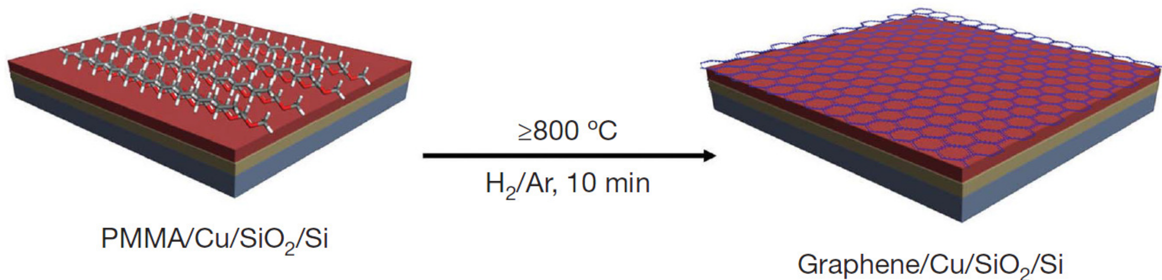

Figure 2.22. Monolayer graphene is derived from solid PMMA films on Cu substrates by heating in an H_2/Ar atmosphere at 800 °C or higher (up to 1,000 °C). Picture taken from [78].

Sun et al. [78] reported the growth of monolayer graphene from solid poly(methyl methacrylate) (PMMA) film 100nm thick that was spin-coated on Cu as metal catalyst substrate. Graphene synthesis was performed under H_2/Ar flow rate and low pressure atmosphere at a temperature range of 800 °C to 1000 °C as shown in Figure 2.22.

In a similar study Perdigao et al. [76] reported formation of graphene through the thermally induced decomposition of C_{60} in combination with a Ni thin film as depicted in Figure 2.23. For buried films the graphene thickness is shown to depend on the fullerene dosage, with evidence of domain growth from nucleation sites separated by tens of micrometers.

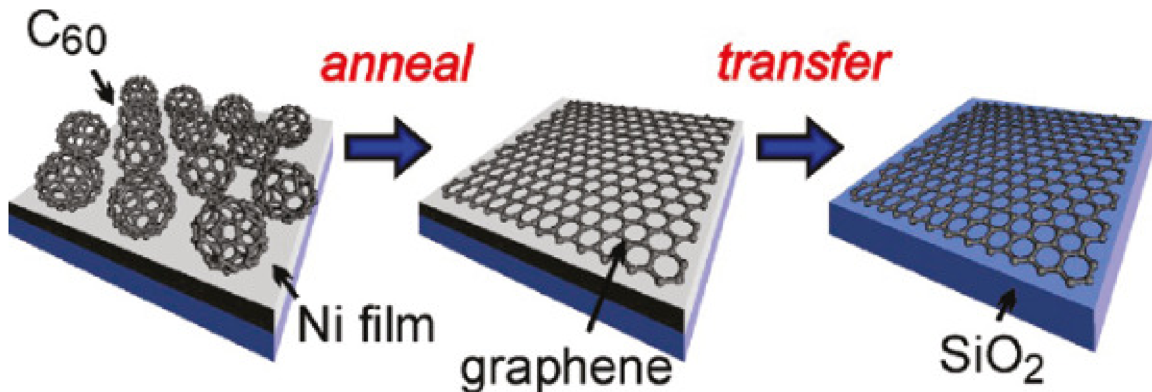

Figure 2.23. Schematic shows formation of graphene from C60 and its transfer to SiO_2 substrate. Picture taken from [76].

Recently, the synthesis of graphene films on dielectrics has been demonstrated through the surface catalytic decomposition of hydrocarbon precursors on thin copper films in which the copper evaporated away during synthesis [81]. However, this technique has been used primarily with hydrocarbon gases as a carbon source over small samples. The extension of this approach to include solid carbon sources, which provide greater flexibility in graphene synthesis, has yet to be demonstrated. Trace amounts of carbon dissolved in metals can be another source for graphene synthesis. In a controlled environment graphene films can be formed directly on dielectric substrates through a

segregation process. This method allows synthesis of patterned graphene for a variety of applications.

2.5. Review of graphene unintentional doping

The large surface-to-volume ratio makes graphene extremely sensitive to the environment. The adsorption of chemical groups on the surface of graphene has the ability to inject or withdraw electrons, creating n-type or p-type doping. These molecules, which are adsorbed on the surface, must be controlled in order to create material with a specific type of doping. Most importantly, the nature of the adsorption (e.g., chemisorbed or physisorbed) will impact the stability of graphene doping. Previous research has shown that the doping level in graphene can be modified through adsorption or desorption of gas/vapor molecules (e.g., H_2O, CO, NH_3, etc) [82]. Attachment/detachment of molecules changes the local carrier concentration in graphene that leads to step-like changes in the resistance. Figure 2.24 shows the response of zero-field resistivity, $\rho = \frac{1}{\sigma}$, to NO_2, NH_3, H_2O and CO in concentrations, C, of 1 part per million (p.p.m.). Hall measurements on graphene revealed that H_2O molecules acted as acceptors, whereas CO molecules acted as donors.

In addition, contamination and adsorbed molecules from the ambient air plays a significant role in imperfections and large variance in the mobility of graphene-based field effect transistors [83]. To achieve desired functionalities, a deeper understanding of graphene surface chemistry is required. Moreover, controlled tuning of the Fermi level in graphene would be highly desirable in view of the use of graphene in realistic microelectronics. The functional groups can also be introduced in the process of fabricating graphene-based devices due to exposure to chemicals or any heat treatment process. Therefore, understanding their effects on the properties of graphene will help researchers to reconsider the device fabrication process.

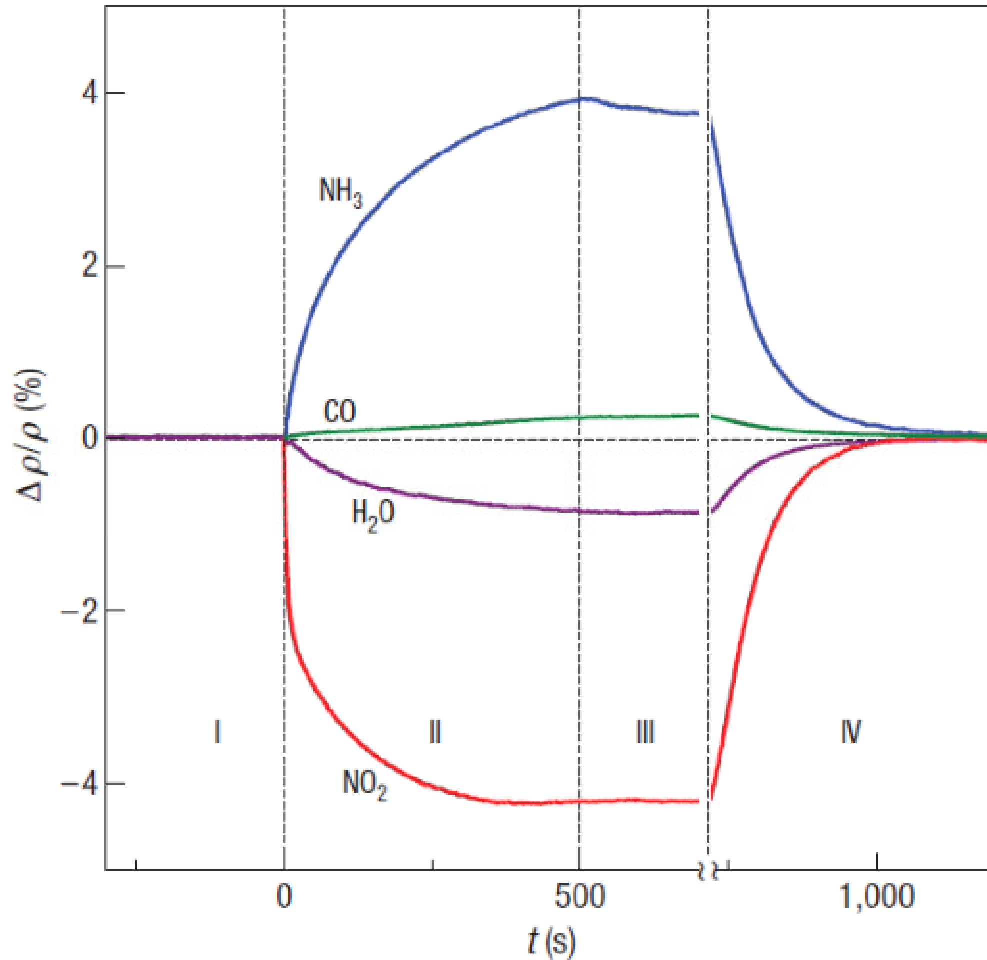

Figure 2.24. Changes in resistivity by graphene exposure to different gases. Picture taken from [82].

As explained earlier, high quality CVD graphene enables the preparation of large area films from which transparent electrodes, transistors, and other electronic devices can be developed [28-29, 39]. However, the synthesis of CVD graphene often involves the removal of the graphene from its metal growth substrate, followed by transfer to a target substrate for device fabrication. This process involves exposing the grapehene to both aqueous and atmospheric gas environments [71], resulting in the attachment of a host of chemical groups to the graphene. These groups can dope the graphene and alter its electronic properties. This process is called unintentional doping, as it is a byproduct of

the transfer process and exposure to the environment and the doping level is neither controlled or is it the main focus of the process.

Oxygen molecules exhibit a variety of chemical reactions with aromatic molecules [84-85] and carbon nanotubes [86]. The adsorbed oxygen is a well-known hole dopant for carbon nanotubes [87]. In a recent experiment O_2 trapped between graphene and a SiO_2 substrate induced hole-doping [88]. This doping effect can be enhanced in the presence of moisture. A common method for desorption of chemical groups, oxygen, and moisture from graphene through heat treatment. To this end, thermal annealing has been investigated extensively to eliminate contamination and alter the electronic properties of graphene [89-90]. Cheng et al. reported that annealing at high temperature brings graphene in close contact with the SiO_2 substrate it was deposited on and induces increased coupling between them [91]. Figure 2.25 shows the schematic of resist removal from a graphene surface using vacuum annealing.

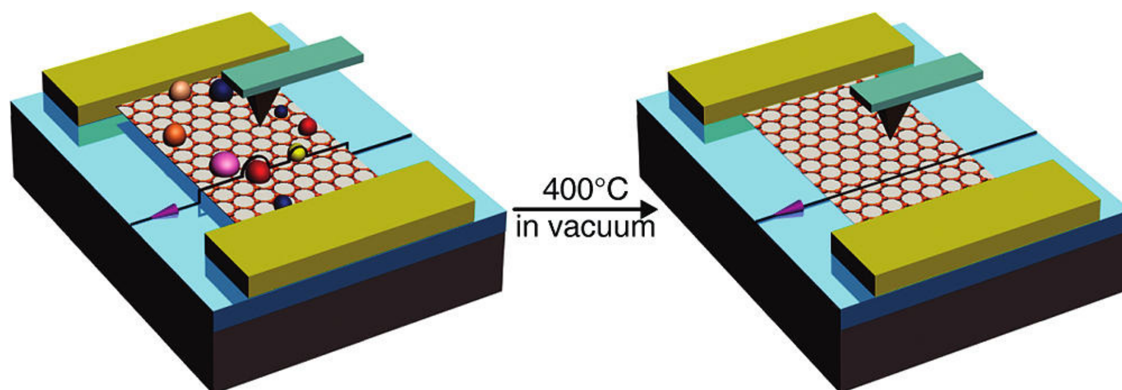

Figure 2.25. Thermal annealing removes resist residue on graphene surfaces and brings it into close contact with SiO_2, inducing increased coupling between them. Picture taken from [91].

Thermal annealing has activated the ability of diatomic oxygen to accept charges from graphene. However, this method induced a pronounced structural distortion due to the close coupling of graphene to the SiO_2 substrate [88]. Tailoring the electronic properties of graphene was performed through controlled heat treatment without

degrading its structural properties. The basic cause of these changes is uncertain, and a systematic study to understand the mechanisms behind the interaction between graphene and the chemical groups bounded to its surface is still lacking and highly desired. Furthermore, the variation in mobility and charge carrier concentration in CVD-graphene depends on the donor or acceptor nature of the chemical. Therefore, a controlled environment for graphene provides the opportunity to further tailor the electronic structure by altering the concentration of different dopants.

2.6. Review of Intentional Graphene Doping and Interface Modification

2.6.1. Graphene p-doping for transparent conductive electrode applications

The extremely high mobility of graphene suggests great potential to be exploited for applications in next-generation microelectronics. Control of the carrier density towards n- and p-type conductive channels is of importance in fabricating logic devices. The conventional ion implantation technique in silicon based FETs induces damage in the structure of graphene. In addition, graphene's zero bandgap raises difficulties for controlling electrical conductivity as compared to conventional semiconductors [2]. Substituting carbon atoms with foreign molecules showed that it is possible to open the bandgap and modulate the carrier types and concentration to make p- and n-type FETs [92-95]. In general, doping adjusts the work function of the graphene, which is necessary to control charge injection and collection in devices such as solar cells and light emitting devices. Shi et al. [96] demonstrated that the work function of graphene synthesized by CVD method can be tuned up to 0.5 eV by immersing the films into $AuCl_3$ solution. The photovoltaic device based on graphene as an electrode showed 40 times greater maximum power conversion efficiency (PCE) due to chemical doping of graphene film. A schematic of the graphene transfer, chemical doping, and device fabrication process is depicted in Figure 2.26.

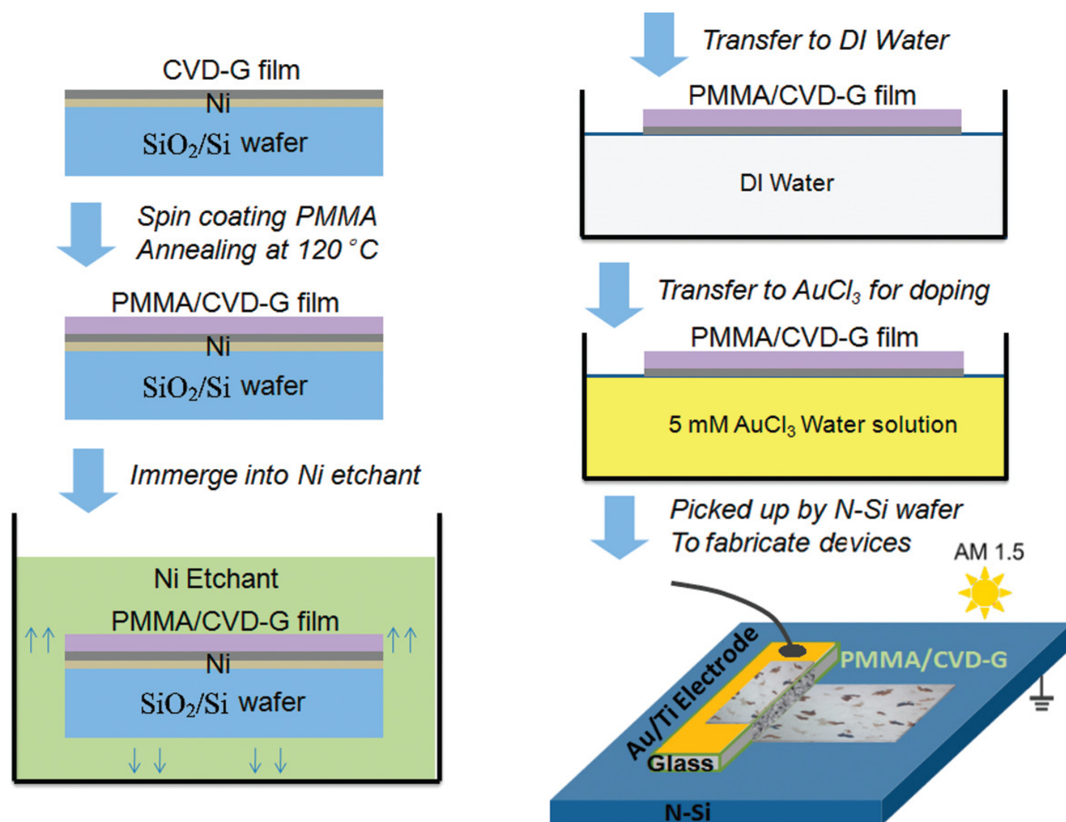

Figure 2.26. Schematic of graphene transfer, chemical doping, and device fabrication process. Picture taken from [96].

In addition, chemical doping can further increase the conductivity of graphene for transparent conductive electrode applications [11, 97-98]. Gunes et al. [97] proposed a new method of layer-by-layer doping of graphene films using $AuCl_3$, as depicted in Figure 2.27. Using this method, the sheet resistance of the film decreased up to ~80% with little sacrifice in transmittance. This method also resulted in better environmental stability for the film due to presence of dominant Au atoms between layers of graphene.

The best transparent conductive electrode was obtained by Bae et al. [11] where they used HNO_3 (70%) to dope CVD graphene films. However, this doping is not stable upon exposure to air, and the performance of the electrode will degrade over the time. Furthermore, graphene can be readily p-doped through adsorbents from air like oxygen and moisture [88-90, 99].

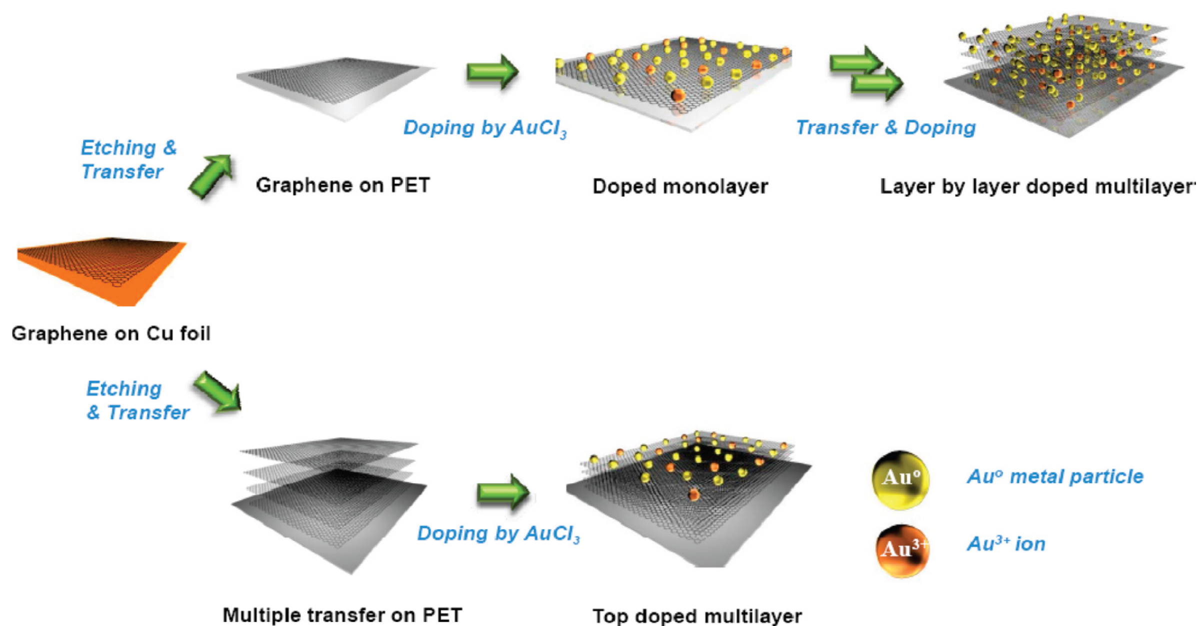

Figure 2.27. The schematic of the layer-by-layer doping CVD graphene with $AuCl_3$. Picture taken from [97].

2.6.2. Graphene n-doping for field effect transistor (FET) applications

For n-doping, nitrogen is considered to be an excellent element for the chemical doping of carbon materials because it is of comparable atomic size and contains five valence electrons available to form strong valence bonds with carbon atoms. Dai and coworkers [95] functionalized graphene nanoribbons (GNRs) by nitrogen species through high-power electrical joule heating in ammonia gas. The formation of carbon-nitrogen bonds confirmed the n-type electronic doping consistent with theory. An n-type field effect transistor (FET) device that operates at room temperature was fabricated using this method as shown in Figure 2.28.

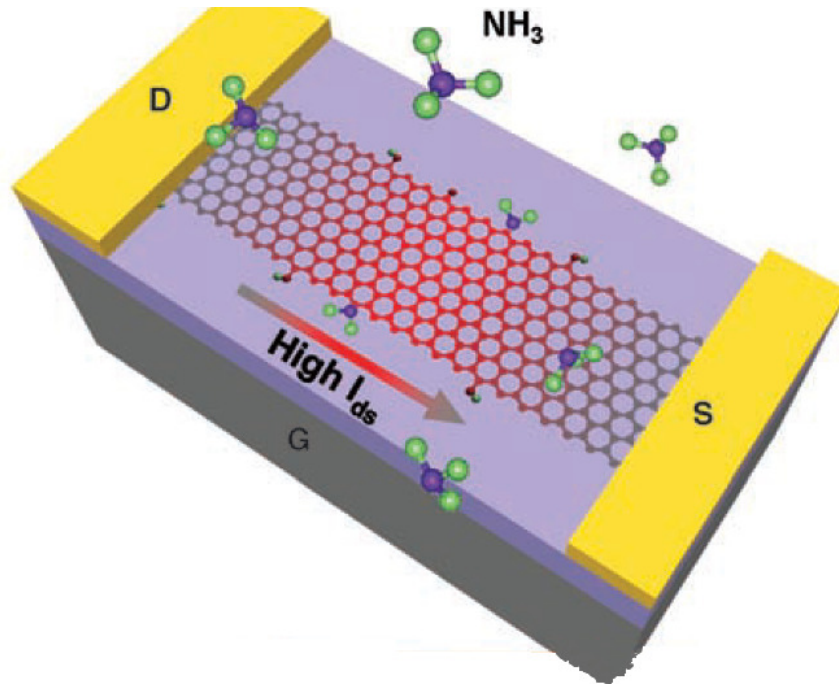

Figure 2.28. FET device e-annealed under high current in NH_3 atmosphere indicates reaction of GNRs with ammonia. Picture taken from [100].

N-doped graphene has been created through chemical vapor deposition (CVD) using ammonia [92] and Pyride [101] as nitrogen-doping sources. In a typical CVD growth, NH_3 (gas) was introduced into the flow as a nitrogen source. Nitrogen atoms substantially doped into the graphene lattice when recombination of carbon atoms occurred in the CVD process. X-ray photoelectron spectroscopy (XPS) was utilized to indicate the presence of nitrogen atoms in the graphene lattice and to establish their bonding state. As shown in Figure 2.29, appearance of an N1s peak in the core level spectra confirms the presence of nitrogen embedded in the graphene lattice. However, this method of n-doping graphene resulted in formation of defects in the lattice, as a significant D peak was observed in the measured Raman spectra, as shown in Figure 2.30. Ammonia plasma [102] and N+ Ion irradiation followed by annealing in ammonia and nitrogen environments [94] have been used to modulate the doping concentration in graphene flakes.

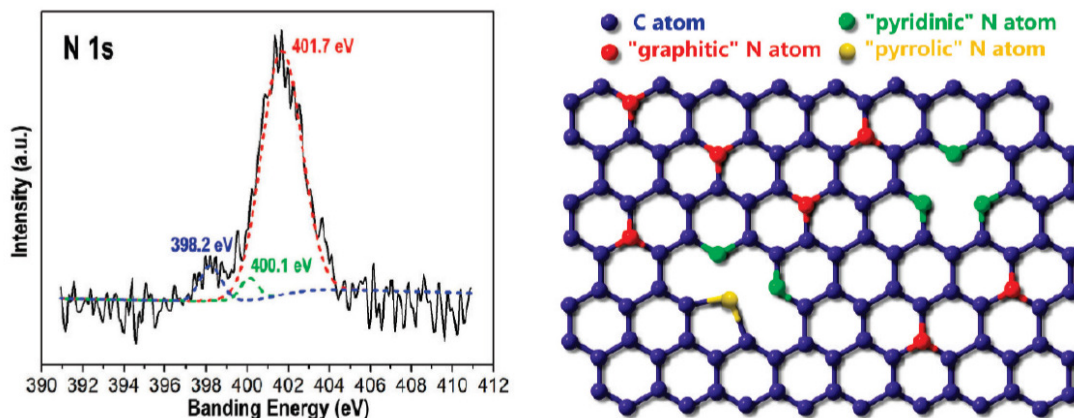

Figure 2.29. (Left) XPS N 1s spectrum of the n-doped graphene. (Right) Schematic representation of the n-doped graphene. The blue, red, green, and yellow spheres represent the C, "graphitic" N, "pyridinic" N, and "pyrrolic" N atoms in the n-doped graphene, respectively. Picture taken from [92].

Furthermore, a segregation phenomenon was utilized to turn the trace amounts of carbon and nitrogen dissolved in bulk materials to synthesize nitrogen doped graphene [103]. However, these processes were performed at high temperatures to "drive-in" the dopants. Moreover, doping through chemical treatments is unstable, as physically adsorbed molecules will be desorbed under heat or vacuum, as described in the previous section [104-105]. Therefore, a low-temperature, defect-free, and controllable method of doping of graphene is greatly needed.

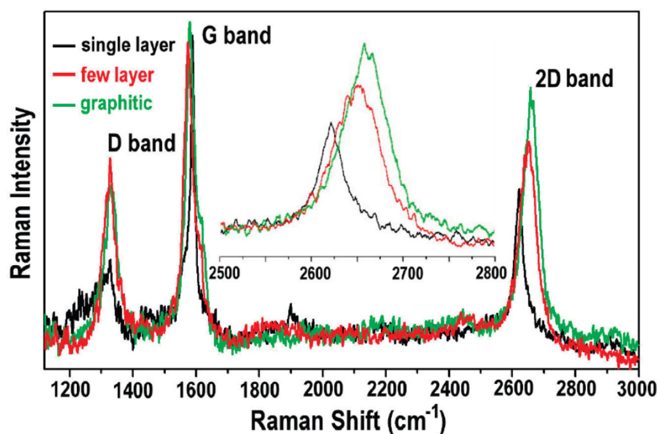

Figure 2.30. Raman spectra of graphene shows presence of defect. Picture taken from [92].

2.6.3. Graphene interface modification

The ease of fabrication and optical contrast has made SiO_2 a potential dielectric substrate for graphene-based FET devices. However, the performance of these devices is limited through charge transfer, adsorbates, and electron phonon scattering. A variety of scattering and trapping effects from the substrate can affect the carrier type and density in graphene. Therefore, further investigation of a graphene/dielectric interface that ensures stable electrical performance of graphene devices is needed [106-108]. In a recent study, a hexagonal boron nitride substrate has been used for high quality graphene electronics where mobilities as high as 37 000 cm^2/Vs were observed which are an order of magnitude higher than those of devices based on SiO_2 [109]. This suggests that the interface between the graphene layer and the substrate is a primary factor in the performance of devices made from graphene. Thus, interface modification through the use of self assembled monolayers (SAMs) may be a potential method to overcome these performance limits on a wider array of substrates and may result in p- and n- type graphene. SAMs have been extensively used to enhance the mobility of organic thin film transistors and to eliminate the Schottky barrier at the metal semiconductor interface [110-113]. It is believed that the ordering of SAMs molecules with molecular dipoles produces a built-in electric field on the thin film transistor device, which is superimposed on the externally applied gate field. SAMs with fluorine and amine groups have been shown to accumulate holes and electrons, respectively, in the transistor channel: These properties are understood in terms of the effects of electric dipoles of the SAMs molecules, and weak charge transfer between organic films and SAMs [110-113]. A buffer layer has been provided between graphene and SiO_2 to reduce charged impurity scattering and environmentally adsorbed doping effects [114]. This was done by controlling the work function of graphene electrodes in the organic field effect transistors (OFETs) through functionalizing the surface of the SiO_2 substrate with SAMs. NH_2-terminated SAMs induce n-doping while CH_3-terminated SAMs neutralize the p-doping

affect of SiO_2 substrate. Patternability of SAMs provides more flexibility in utilizing this idea. Figure 2.31 shows the schematic of patterned SAMs on the SiO_2 substrate where a silane group is key in binding SAMs to the substrate.

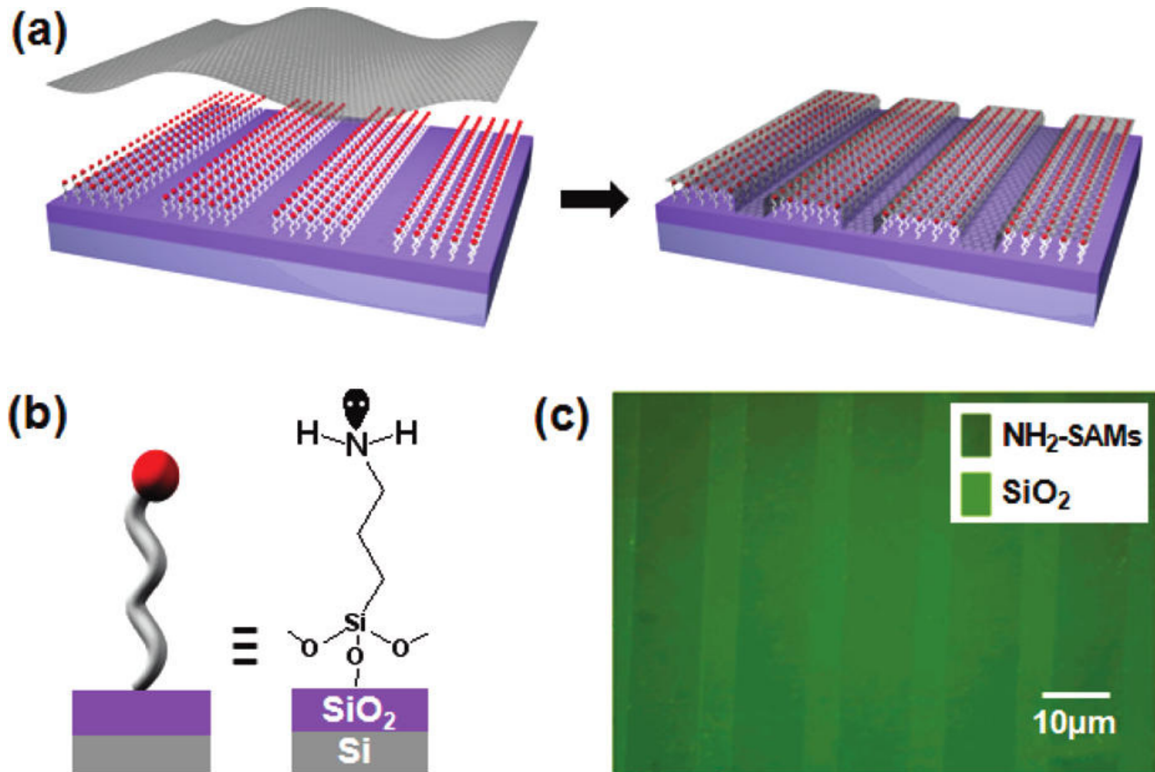

Figure 2.31. Schematic transfer process of monolayer graphene on patterned self-assembled monolayer (SAM)-modified SiO_2 substrate. (b) Molecular structure of amine (NH_2)- functionalized SAMs on SiO_2/Si substrate. (c) Optical microscope image of patterned NH_2 SAMs on SiO_2/Si substrate. Picture taken from [114].

Liu et al. showed that phenyl-alkyl-terminated self-assembled monolayers (SAM) on SiO_2 improves the CVD graphene FET mobility, hysteresis, and bias stress stability [115]. The field-effect mobility of graphene transistors on phenyl-SAM modified substrate is ~ 2500 cm^2/Vs, which is considerably higher than that of transistors without SAM. Charge injection from graphene to the dielectric/graphene interface is the dominant reason for the observed hysteresis effect in graphene-based FETs. Applying a SAM

between the graphene and the dielectric modifies the interface in such a way that charge injection from graphene to the SAM interface will be mostly suppressed. Figure 2.32 shows the schematic of modified SiO_2 in graphene-based FET using phenyl-alkyl-SAM. The mechanism of charge injection is illustrated in the bottom left, through the enhanced dipole effect induced by SAMs.

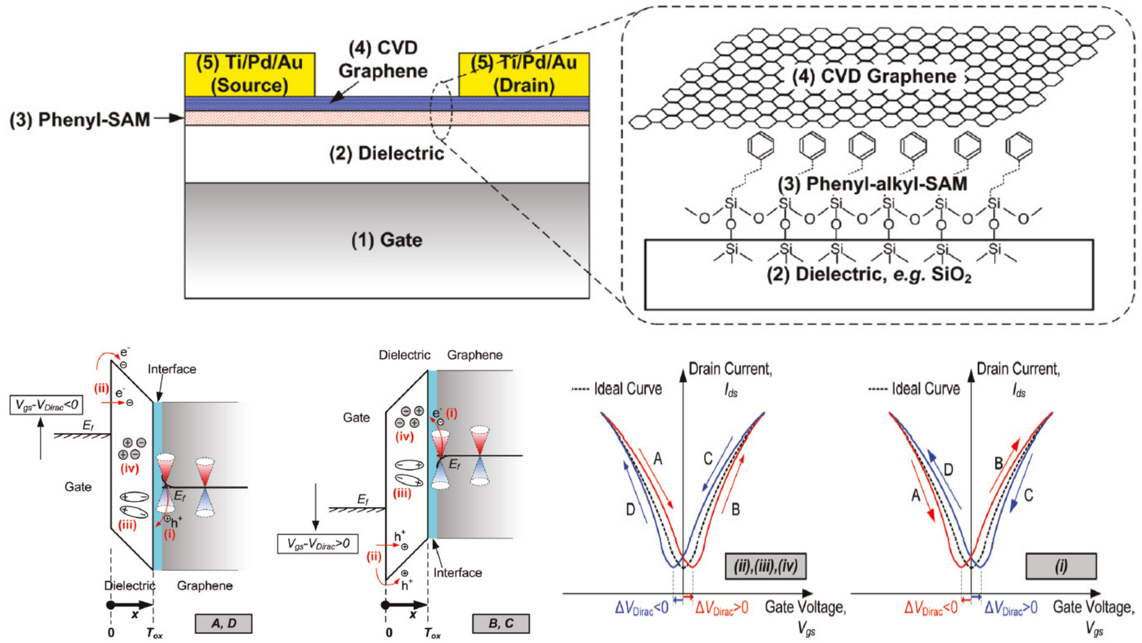

Figure 2.32. (Top) A general bottom-gated graphene FET structure with phenyl-SAM interface engineering. (Bottom) Illustration of the physical mechanisms for the hysteresis behavior of graphene FETs. Picture taken from [115].

These methods illustrate that the chemical reactivity of a graphene surface can be easily tuned by attaching functional groups via SAMs through the formation of dipoles at the interface [116-119]. Wang et al. [120] modified the substrate of graphene to adjust its work function from -130 to 90 mV with respect to the Dirac point. This corresponds to a doped carrier concentration up to 1012 cm^{-2}. Figure 2.33 shows a schematic of graphene on bare SiO_2, PMMA, and SAMs and the corresponding change in the work function as the number of graphene layers changes.

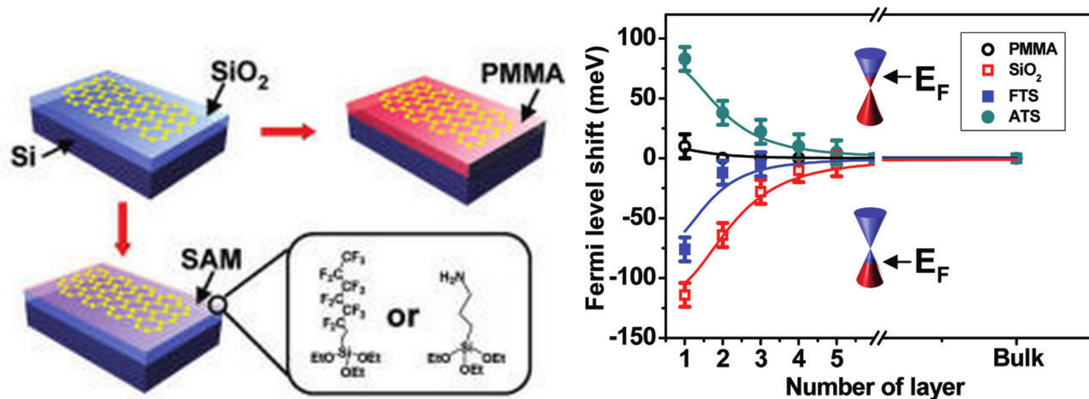

Figure 2.33. (Left) Schematic illustration of the chemical modification of substrates. (Right) Work function of graphene on various substrates as a function of graphene thickness. Picture taken from [120].

However, limited research has been done on controlling charge carrier and concentration towards n and p-type graphene FETs through functionalizing substrates with SAMs. This needs a systematic study to reveal the mechanism by which the electrical properties of graphene FETs are affected. Understanding this mechanism together with the unintentional doping will help us to propose an easy approach for the fabrication of graphene p-n junctions.

2.7. Review of graphene p-n junctions

P-N junctions are the elementary building blocks of most semiconductor electronic devices such as diodes, transistors, solar cells, light emitting devices (LEDs), and integrated circuits; they are the active sites where the electronic action of the devices take place. Due to the zero-gap in single-layer graphene, both carrier type and concentration can be controlled through an electrostatic gate, making graphene a promising material for semiconductor applications [2, 108]. This electrostatic gating allows the development of graphene-based bipolar devices where a junction between hole-rich and electron-rich regions, or a p-n junction, can be formed [121-122]. Graphene

p-n junctions have already displayed new and exciting phenomena such as Klein tunneling [123], where electrons traveling perpendicular to the junction experience zero resistance and fractional quantum Hall transport [122]. Such junctions are predicted to produce lensing effects for coherent electrons, so called Veselago lensing, where diverging electron waves are refocused by the junction [124]. Most graphene junctions to date have been fabricated using multiple electrostatic gates, [122] electrical stress-induced doping, [125] chemical treatment by gas exposure, [126] molecular modifications on top of the graphene, [127-128] and modification of the substrate by changing the local electrostatic potential in the vicinity of one of the contacts [34]. Yu et al. [125] demonstrated doping in graphene through electrical stressing. This doping was tunable from n-type to p-type as the electrical stressing level increases. They showed formation of p-n junctions on graphene through doping based on locally applied electrical stressing. Figure 2.34 shows the schematic structure of a graphene FET device. Resistance measurement as a function of gate voltage indicates superposition of two separate Dirac points that confirm an energy separation of neutrality points within the complementary regions.

Chakraborty et al. [129] showed simultaneous p- and n- type carrier concentration in a bilayer graphene by varying the longitudinal bias across the channel and the top-gate voltage. The gate was applied electrochemically using solid polymer electrolyte. Unlike single layer graphene, the drain-source current does not saturate on varying the drain-source bias voltage. Figure 2.35 shows the schematic of the structure with both top- and back- gates. Raman spectra of the bilayer graphene shows characteristics of a 2D peak, as four lorentzian curves were fitted to the peak at ~ 2700 cm^{-1}.

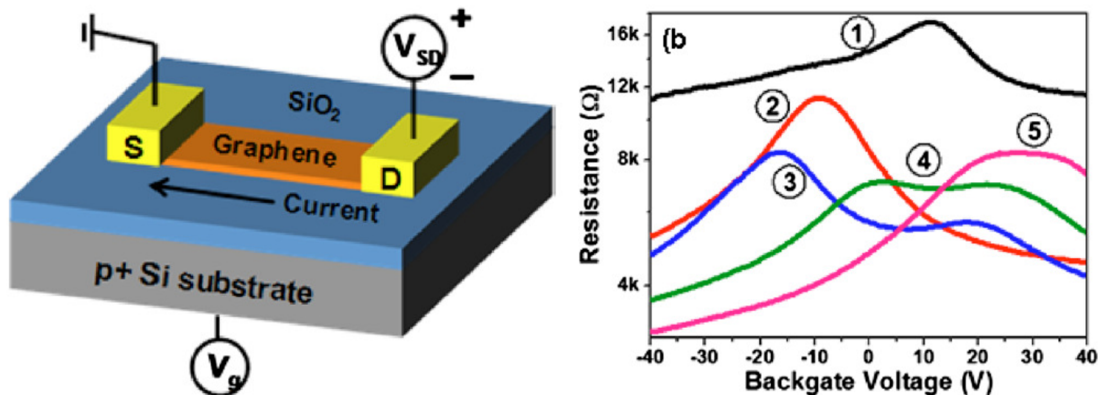

Figure 2.34. (Left) Schematic of graphene FET device. (Right) Resistance vs. gate voltage indicate formation of graphene p-n junction as two separate Dirac points were observed. Picture adapted from [125].

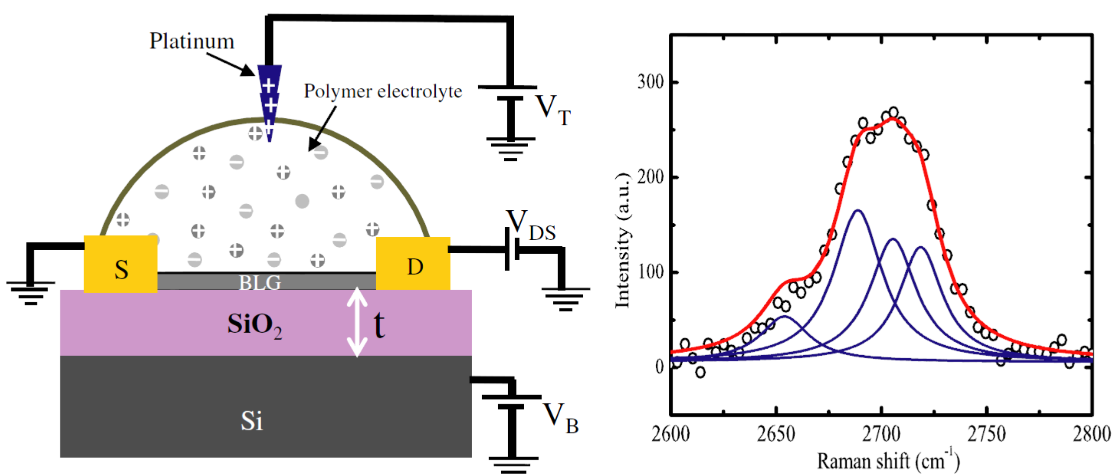

Figure 2.35. Schematic of the experimental set-up showing the top- and back-gate arrangement. Raman spectra of graphene showing its characteristic bilayer mode. Picture adapted from [129].

However, current methods for electrostatic gating require a number of fabrication steps that are complex and not easily scalable. In addition, chemical/molecular doping of graphene can degrade the carrier mobility through the introduction of defects, and physisorbed molecules may not be stable and may desorb during annealing or environmental exposure.

2.8. RESEARCH OBJECTIVES

It can be concluded from the above literature review that the current methods for graphene synthesis have the shortcoming that the films need to be transferred onto an appropriate substrate for device applications. The transfer process can introduce defects into the graphene that result in a negative impact on its electrical conductivity. The reduction of these defects is a key issue that must be solved in order to further develop this technology for scaling to large areas with low sheet resistance and high carrier mobilities. Therefore, a simple, inexpensive, transfer-free method for graphene synthesis is much needed. Such a technique can potentially lead to a large area transfer free method to produce graphene on a wide range of dielectric substrates that mitigates the aforementioned challenges associated with the transfer of CVD graphene.

In addition, this transfer process involves attachment of chemical groups on graphene that can unintentionally tailor its electronic properties. A comprehensive thermal annealing study to understand the mechanism behind this doping is needed. In this proposal, we study the effects of vacuum annealing and re-exposure to air on CVD graphene grown on copper foils and subsequently transferred onto insulating substrates. This study will also elucidate the mechanism for intentional doping of graphene films. A number of studies have reported the control of carrier density towards n- and p-type conductive channels. However, current methods are not stable and lead to a decrease in the carrier mobility of graphene, as they introduce defects to graphene structure. Hence, a low temperature, scalable and defect-free technique of doping graphene is of great interest in order to pave the road towards graphene-based integrated circuits. A facile approach to p- and n-doped large area CVD graphene will be proposed through a thin layer of different SAMs. Upon heating under an inert atmosphere, the adsorbed molecules and atmospheric dopants will be removed; under these circumstances the electron rich SAM allows the carrier concentration to be controlled by varying the amount of molecules available in the surface. This can be observed though electrical

measurement data and various characterizations. A graphene p-n junction will be obtained by patterning both modifiers on the same dielectric and will be verified through the creation of a field effect transistor (FET).

This research aims to fill in the gaps in existing knowledge by: 1) Understanding the doping mechanism of CVD graphene through adsorbed oxygen and moisture, 2) Providing a defect-free, controllable, and stable p- and n- doping of CVD graphene through an interface modification, 3) Developing a new method for wafer scale, transfer-free, and patterned synthesis of graphene on dielectric substrates.

CHAPTER 3

SYNTHESIS, TRANSFER, AND CHARACERIZATION OF CVD GRAPHENE FILMS

3.1. Introduction

Chapter 2 provided a review of graphene films that exhibited excellent electrical, thermal, and mechanical properties. These properties suggest graphene as a potential candidate for a number of electronic applications for example radio frequency (RF) transistors. Chapter 2 also provided a review on different routes for synthesis of graphene, the impact of heat treatment, and unintentional doping of the graphene films. In addition, it posited important questions remaining in the graphene research community regarding: (1) the impact of post-growth thermal annealing and environmental exposure on the unintentional doping of CVD graphene films, (2) the new techniques for defect-free and stable doping of graphene films for transistor applications, and (3) the new routes for transfer-free large scale synthesis of graphene film. These questions will be addressed by the research contribution of this dissertation in Chapters 4 – 6. However, this chapter will first provide a technical basis upon which subsequent chapters can build. In particular, this chapter will present the methodology used to synthesize and transfer the CVD graphene films that will be investigated later. Also, the baseline characteristics and properties of graphene films will be evaluated, providing a general methodology to evaluate the performance of these films under the various heat and chemical treatments that will be discussed in further details in Chapters 4 –6. Section 3.2 explains how the large-area uniform graphene films are synthesized on thin Cu foils and describes some of their characteristics before their transfer.

As explained earlier, graphene films need to be transferred from their growth substrate to a targeted substrate for electronic device applications. Details of the transfer

process will be explained in section 3.3. Once transferred, graphene films need to be characterized to ensure the presence of large-scale, high quality films on the target substrate. Section 3.4 covers various characteristic studies performed on graphene and their experimental methods. In section 3.4.1, Raman spectroscopy will be used as a powerful technique to identify the number of graphene layers and their quality by examining graphitic peak positions. The transfer process typically leaves a number of chemical groups and other contamination on the surface of the graphene film. Understanding the extent of these chemical groups, their impact on the properties of graphene, and the methods to remove them is important for the application of graphene.

Additional treatments during transfer and post-transfer will be performed, and their effectiveness will be explored using X-ray photo electron spectroscopy, explained in section 3.4.2. In section 3.4.3, ellipsometery will be used to measure the overall thickness of the graphene film in large scales. It also will provide the refractive index of graphene as another parameter of interest. Imaging of graphene films is essential to understand the structure of the film and the presence of possible cracks and voids, particularly after transfer. To this end, atomic force microscopy (AFM), secondary electron microscopy (SEM), and transmission electron microscopy (TEM) will be utilized in section 3.4.3. UV Vis spectroscopy will be performed in section 3.4.5 as another method for understating the thickness of the film, as transmittance of a single-layer graphene is known.

The electrical properties of graphene are among the main interests in this miracle material. The mobility of graphene will be measured using a back-gated field effect transistor device in section 3.4.6. The same device structure will be used in the next chapters for study of unintentional and intentional doping of graphene in Chapters 4 and 5, respectively. Graphene is a potential material for transparent conductive electrodes, as explained in Chapter 2. To this end the sheet resistance of the film will be measured using the four point probe method in section 3.4.7, and in conjunction with transmittance measurements in section 3.4.5, the figure of merit (FoM) for graphene films will be

calculated in section 3.4.8. These are essential steps in this thesis and will be referred to many times in the next chapters.

3.2. Synthesis of CVD graphene films

The first step in this thesis is to synthesize graphene films. As explained in Chapter 2, various methods can be used for this purpose. Chemical vapor deposition (CVD) on Cu foil has been shown to be a promising method for large-area synthesis [29]. Similar to the method explained in [29] with some modifications graphene was grown on a 25 µm thick Cu foil (Alfa Aesar, item No. 14482, cut to pieces in arbitrary size) in a low pressure environment using chemical vapor deposition (CVD). Figure 3.1 shows a photo of a sample of Cu foil used for the synthesis of graphene. Care must be taken while cutting the Cu foil to avoid folding the foil and to have a smooth substrate for growth. In a typical synthesis process, the Cu foil was loaded into a quartz tube and heated in a furnace to 1000°C. The annealing process was carried out under 20 sccm H_2 and 50 sccm Ar atmosphere at vacuum pressure ~800 mTorr for 30 minutes. This helps to remove oxide from the Cu foil and to increase the grain size of the Cu, as this is critical for large area and uniform synthesis of graphene films. In the growth step, 35 sccm CH_4 was introduced for 20 minutes maintaining the same H_2 and Ar gas flow rate. Then, the furnace was shut down and the quartz tube dragged out of the hot area to allow rapid cool down to room temperature under the same gas flow rate. It typically took 30 minutes to reach room temperature before taking the samples out. Figure 3.2 shows a photo of the CVD set up used for synthesis. The quartz tube in the set up was 45" long with a outer diameter of 1.5". Thermolyne 59300 high temperature tube furnace was used in this set up that can go to temperatures up to 1700°C. A DTC-531-115-BX, ditgital thermocouple readout and gauge tube was used to measure the pressure and was placed in the set up before the tube. Stainless steel tubing 1/4" diameter was used to direct the gases from mass the flow controllers to the tube. The distance between the mass flow controllers and

the tube is ~ 100". A Leybold D40BCS vacuum pump was used to lower the pressure during growth and was found to be critical for growing large area uniform graphene. Fomblin oil was used in the vacuum pump for safety issues, as graphene synthesis involves flowing hydrocarbons and hydrogen gases. A LNTA6150K 6" Right Angle liquid nitrogen (LN_2) Trap, NW40, 2 Liter Reservoir was used to cool the hydrocarbons gases and trap them before they entered the vacuum pump. This is important for the life time of the pump and general safety of the system.

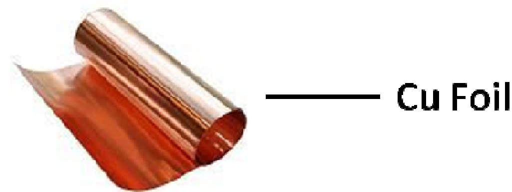

Figure 3.1. Schematic of a 25 μm roll of Cu foil used for synthesis of CVD graphene.

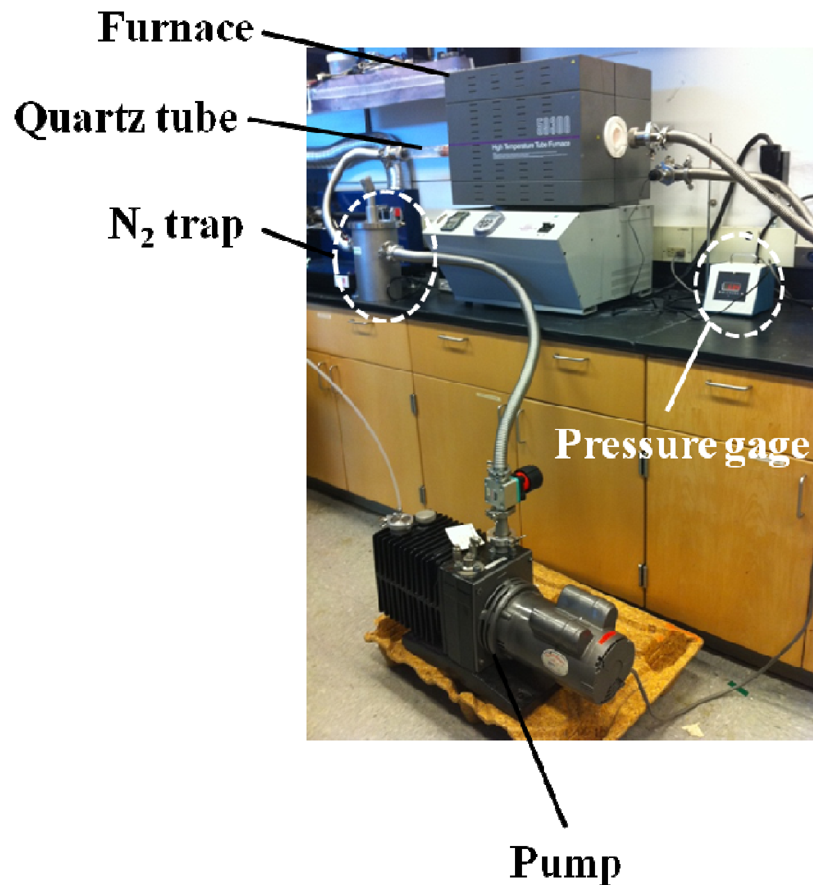

Figure 3.2. Photograph of low pressure graphene growth set up.

Figure 3.3 (a) shows a photo of a Cu foil covered with graphene that has a shiny surface. It is important to note that graphene was synthesized on both sides of the foil. An optical image of the graphene shows a large area film covering the entire Cu foil uniformly as shown in Figure 3.3 (b). The sample was characterized using a variety of optical and surface science methods to quantify the quality and doping state of the graphene. For a baseline, Raman spectroscopy was performed with an excitation wavelength of 532 nm and collected in the backscattering configuration. Laser power was kept below 0.5 mW to avoid laser-induced heating. A 50X objective lens was used to focus the laser on the graphene samples during the Raman measurements.

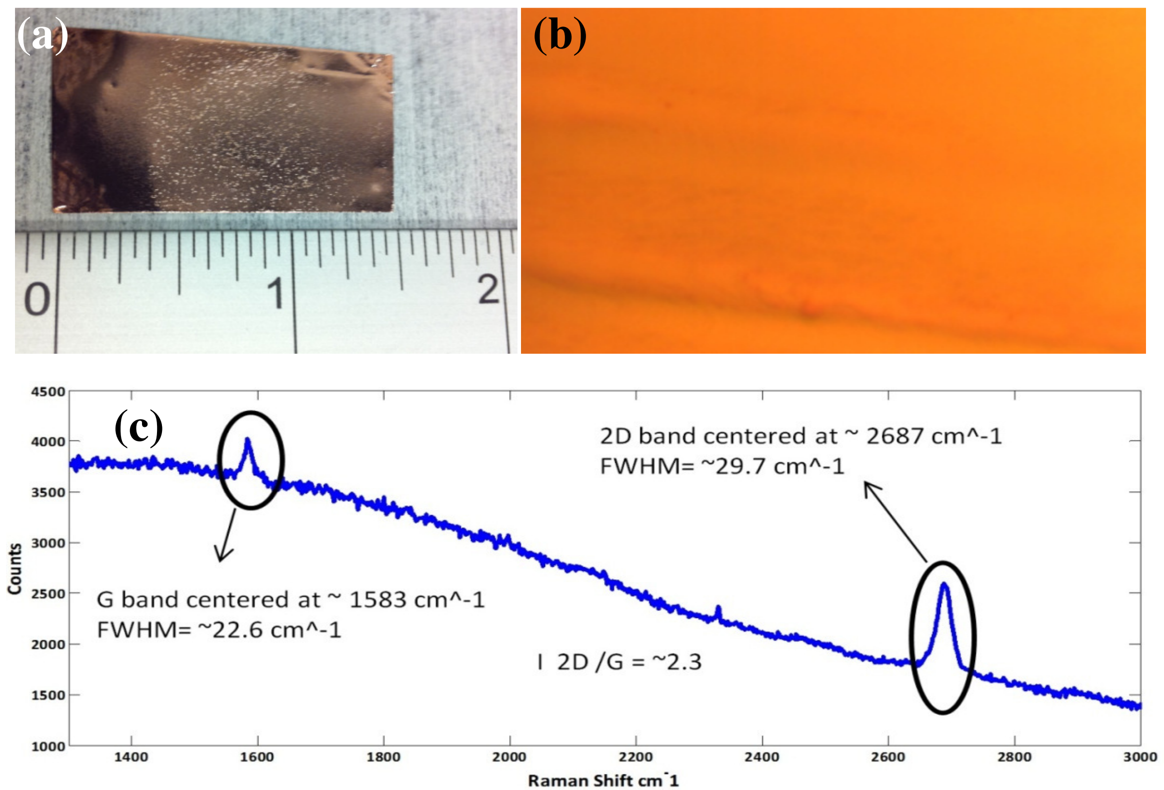

Figure 3.3. (a) Photo of Cu foil covered with graphene. (b) Optical image of graphene on Cu foil. (c) Micro Raman Spectroscopy (532-nm laser wavelength) data taken of CVD-grown graphene films on a 25 μm Cu substrate at 1000˚C. Data show prominent graphitic (G) and 2D bands and the lack of any detectable defect peak (D). These results indicate high quality graphene grown on Cu. The scale bare in A is 50 μm.

Figure 3.3 (c) shows a representative Raman spectroscopy measurement that shows prominent graphitic (G) and (2D) bands and the lack of any detectable defect peak (D) on synthesized graphene films. The background in the Raman spectra on which graphitic peaks were observed is due to presence of graphene on Cu foil, the so-called fluorescence effect. This background should not be observed after transfer of graphene off the Cu foil to another substrate. As explained in Chapter 2, the G-peak (~ 1585 cm^{-1}) is due to first-order Raman scattering by the doubly degenerate zone center optical phonon mode, and the 2D-peak (2680-2700 cm^{-1}) is associated with second-order scattering by zone-boundary phonons [38, 44-46]. In first-order Raman scattering, the observation of zone boundary phonons is inhibited by selection rules. However, in defective graphite, the so-called D-peak (1345-1350 cm^{-1}) is due to first-order scattering by zone-boundary phonons. The Raman fingerprint for CVD graphene, however, was confirmed by using the 2D- and G-peaks' intensity ratio (I_{2D}/I_G), [29, 45] and the width of the 2D-peak [38, 45, 130]. The 2D to G band intensity ratios, I_{2D}/I_G, of the samples synthesized were higher than 2.3, and the full width at half maximum (FWHM) of the 2D band was around 30 cm^{-1}, which was typical of these films and is indicative of monolayer CVD graphene.

3.3. Transfer of CVD graphene films

After synthesis, graphene needs to be transferred onto another substrate for device application. However, the transfer process can leave various chemical groups on graphene films that affect its electrical properties. In addition, the transfer process may result in the formation of cracks and voids in graphene films that are detrimental to the performance of such devices. Therefore, a defect-free method needs to be utilized to minimize the impact of the transfer process on the graphene film. To this end, the same process reported in [27] with some modifications will be utilized. First a layer of PMMA (9% volume dissolved in anisole) was deposited on the graphene by spin coating. It is

important to prevent any bending or folding of Cu foil during the spin-coating process; it must be smooth. A high vacuum in the spin-coating tool usually induces folding in the Cu foil. A reduced vacuum pressure was achieved to avoid folding by using a rubber support disc on the spin-coating stage. Depends on the sample size, droplets of PMMA used to cover the Cu foil. Spin coating was performed at 1500 rpm for 1 minute. After spin coating a razor blade was used to remove thin Cu foil from the stage of the spinner without leaving folds in the film. PMMA was cured at 150-180°C for ~ 5 minutes in a box furnace, and then the sample was cooled to room temperature gradually. The Cu foil was then etched with 30 vol. % $FeCl_3$ aqueous solution overnight. (The $Fe(NO_3)_3$ solution can be used for a faster etching rate as well). Then the PMMA/graphene film was washed in DI water two times; it was then treated with 10 vol. % HCl solution for 10 min to remove any $FeCl_3$ residue. The sample was washed again in deionized (DI) water several times to remove residual HCl and any contaminants bound to the graphene. For all these washing and acid treatments, a piece of clean glass slide was used to transfer bilayer PMMA/graphene from one batch to another to reduce any folding or mechanical force on the film.

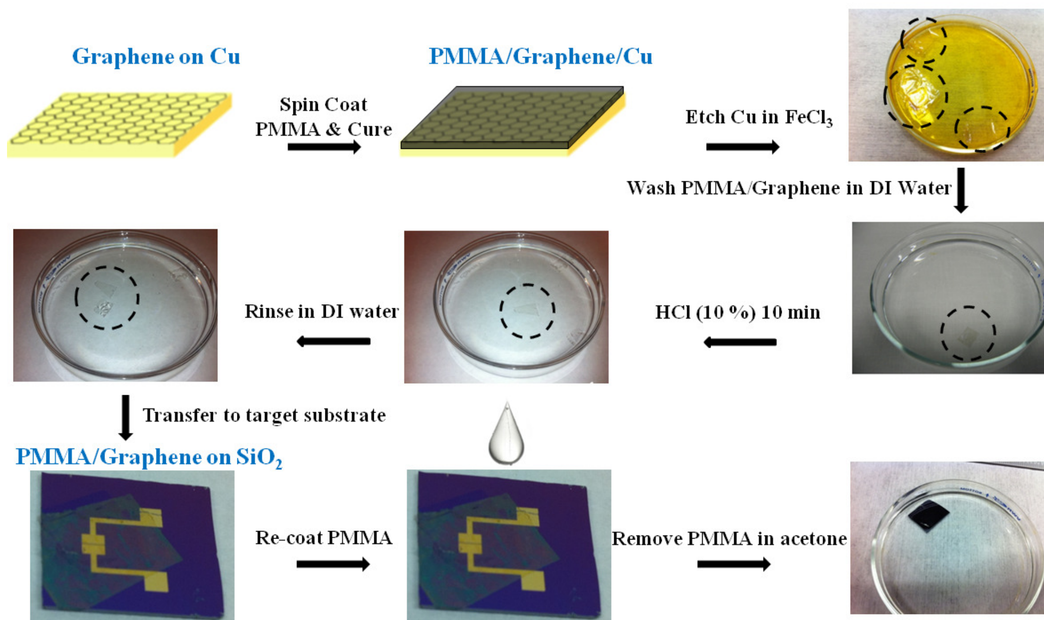

Figure 3.4. Transfer process of CVD graphene films.

The bilayer PMMA/graphene sample was then placed on the desired substrate by scooping it out from the DI water on which it was floating. The substrate was cleaned with acetone, methanol, isopropanol (IPA), and DI water and dried with air or with a nitrogen gun before transfer of the bilayer PMMA/graphene. The substrate was placed inside a petri dish and heated to 70°C gradually on a hotplate to evaporate water trapped between the film and the substrate. This helps better adhesion of the film to the substrate and improves the transfer quality. Usually 5-10 minutes of heating was enough for this step. Then, the sample was cooled down to room temperature. A droplet of diluted PMMA (4% volume dissolved in anisole) was placed on the bilayer PMMA/graphene and cured at room temperature for an hour. The sample inside the petri dish was placed on a hot plate at 50°C and the PMMA was removed using acetone. Washing in acetone can be repeated multiple times for better removal of PMMA. Without loss of generality, the films can be transferred onto any substrates compatible with this processing method (e.g., silicon dioxide, plastics, glass, quartz, etc.). Figure 3.4. shows the schematic for transfer of CVD graphene films.

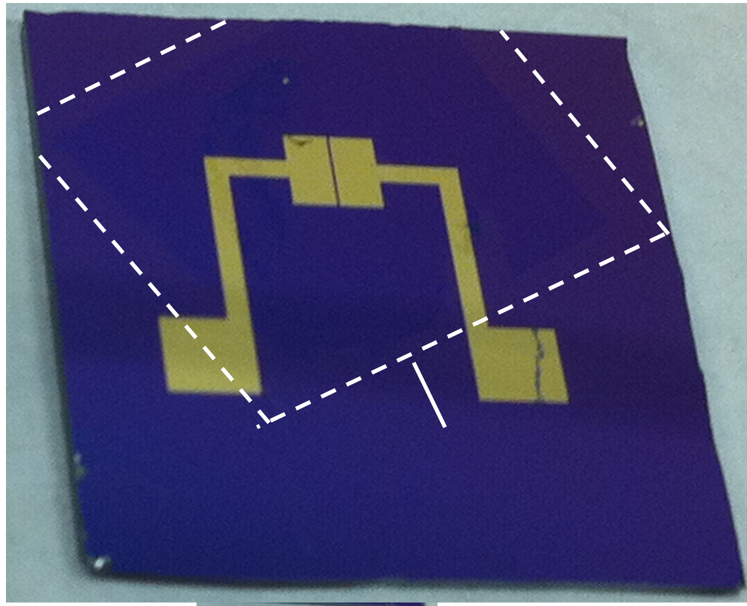

Figure 3.5. Photograph of a graphene film transferred onto a field effect transistor (FET) device with 300 nm thick oxide coated on a Si wafer.

Monolayer graphene films transferred onto a SiO2 coated (300 nm) Si wafer can be observed by the color contrast (purple-to-violet in color) under the white light due to light interference effect. Figure 3.5 shows graphene transferred onto SiO2 (300 nm)/Si substrate that is visible under the white light. The dashed arrows in the figure are plotted at the border of the graphene film. Figure 3.6 shows a photo of bilayer PMMA/graphene transferred onto a flexible PET substrate.

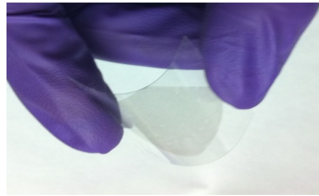

Figure 3.6. Bilayer PMMA/graphene transferred onto a flexible PET substrate.

3.4. Characterization of the CVD Graphene Films

3.4.1. Raman spectroscopy in Graphene

The quality and number of graphene layers were identified through various characterization methods. Raman spectroscopy was employed to ensure the presence of graphene films after the transfer process according to the method explained in section 3.3. Figure 3.7 shows the Raman spectra of graphene transferred onto SiO_2/Si substrate with dominant G and 2D peaks and lack of detectable D peak. This indicates that the transfer process did not induce any defects on the graphene films.

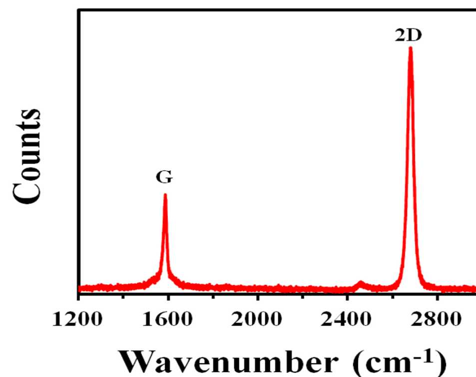

Figure 3.7. Shows Raman spectra of graphene after transfer to SiO_2/Si substrate.

Figure 3.8 shows Raman mapping of the 2D and G peaks over a 30 μm by 50 μm.

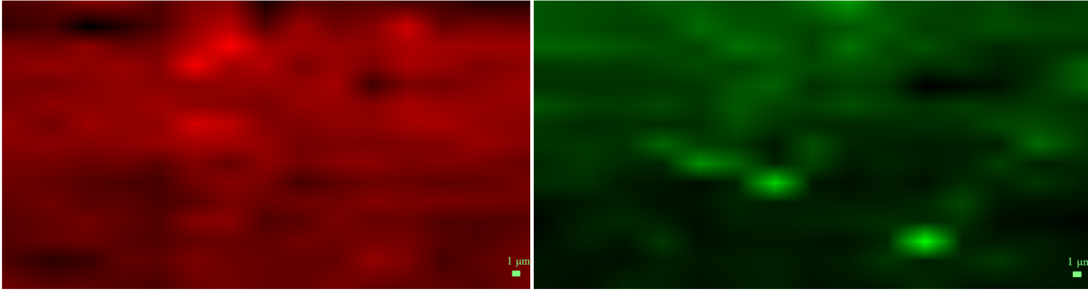

Figure 3.8. (Left) Raman map of 2D peak from 2670 to 2710 cm^{-1}. (Right) Raman map of G peak from 1580 to 1590 cm^{-1}.

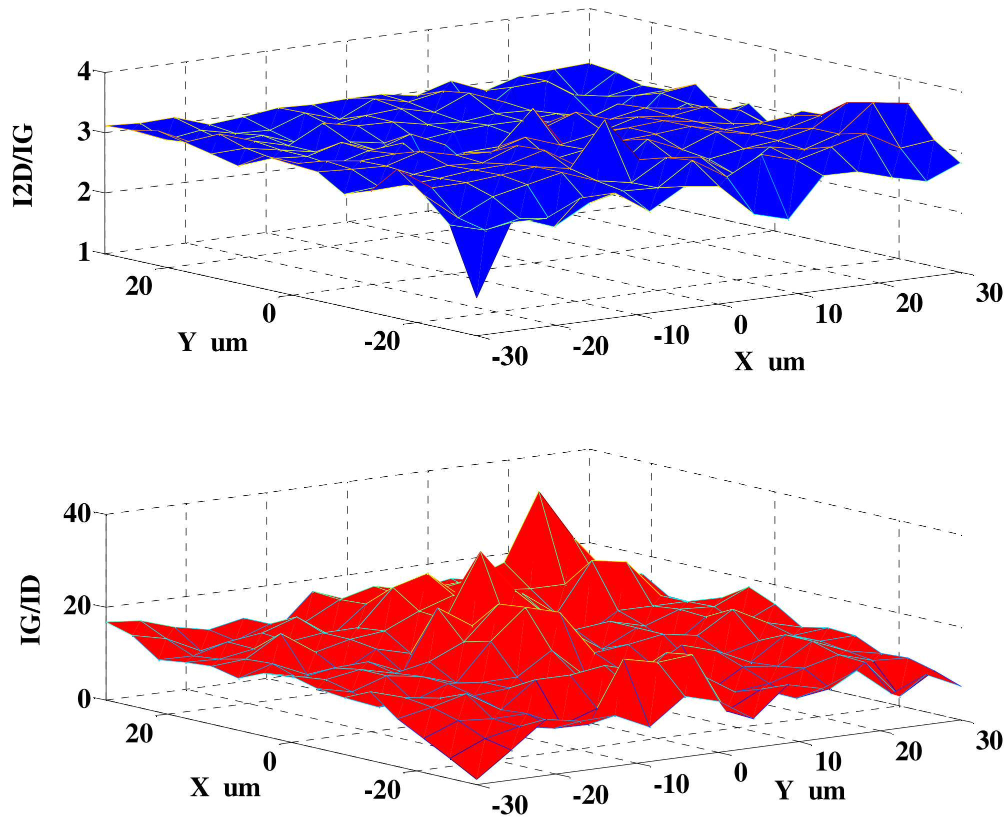

Figure 3.9. I_{2D}/I_G (Top) and $I_{G/D}$ (Bottom) collected from Raman mapping date over a 30 μm by 30 μm area.

The intensity of D, G, and 2D peaks were collected from Raman mapping data, and I_{2D}/I_G and I_G/I_D were plotted over a 30 μm by 30 μm area as shown in Figure 3.9.

I_{2D}/I_G ~3 is indicative of monolayer graphene and I_G/I_D between 10-40 is indicative of less defects induced to the film due to transfer process.

3.4.2. X-ray photo electron spectroscopy (XPS)

As explained earlier, the transfer of CVD graphene can leave a number of chemical groups on the surface of the film that impact its electrical properties. Some of these groups can unintentionally dope the film, as will be explained in further detail in Chapter 4. Intentional doping of graphene by chemical dopants and various self-assembled monolayers can be confirmed through X-ray Photoelectron Spectroscopy (XPS) as well. Therefore, a XPS study of graphene films is of importance before utilizing it in device applications. XPS was employed to identify the elements present on the sample surface after the transfer process. XPS detection limits for most of the elements are in the parts per thousand range. Detection limits of parts per million (ppm) are possible, but require special conditions: concentration at top surface or very long collection time (overnight).

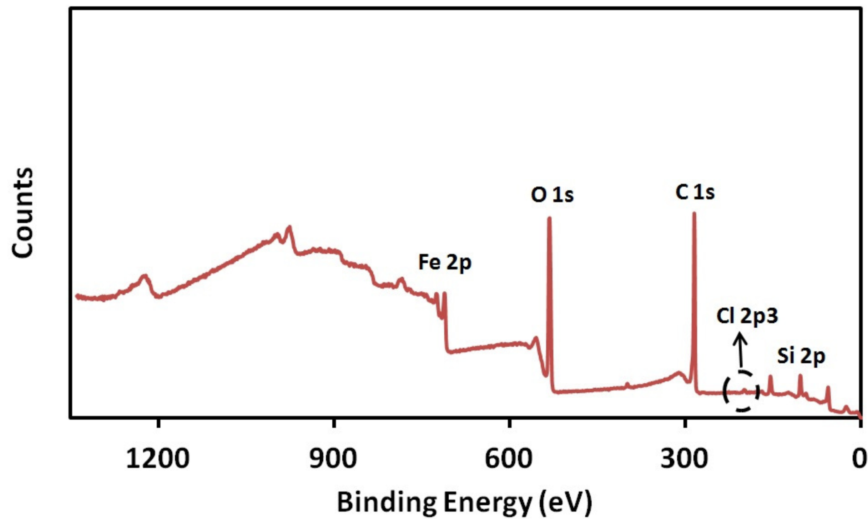

Figure 3.10. XPS survey spectra of graphene without HCl treatment from 0-1300 eV indicates presence of Fe and Cl.

XPS data were acquired using a spectrophotometer (VG Scientific ESCALAB 210) with an Al $K\alpha$ X-ray source ($h\upsilon = 1486.68$ eV). XPS measurements were first conducted on a SiO2 substrate that had been taken through the same graphene transfer process. This initial test was designed to determine the baseline of any residual elements and chemical groups on the substrate. Next, CVD graphene films transferred onto SiO2 substrates and measurements were repeated on graphene film. The survey scan spectra were collected randomly at several points at the binding energy (B.E.) of 0-1300 eV with a step size of 1 eV and a spot size of 400 µm as shown in Figure 3.10.

This scan showed the most prominent peaks to be C1s and O1s. Oxygen was abundant on the surface of the carbon as well as from the SiO_2 substrate. However, there are two peaks at binding energy of 195 eV and 700 eV that are corresponding to Cl and Fe. Peak table analysis indicates the presence of 1.1% and 2.13% of Cl and Fe in the sample. As explained earlier, $FeCl_3$ was used to etch the Cu foil in the transfer of CVD graphene.

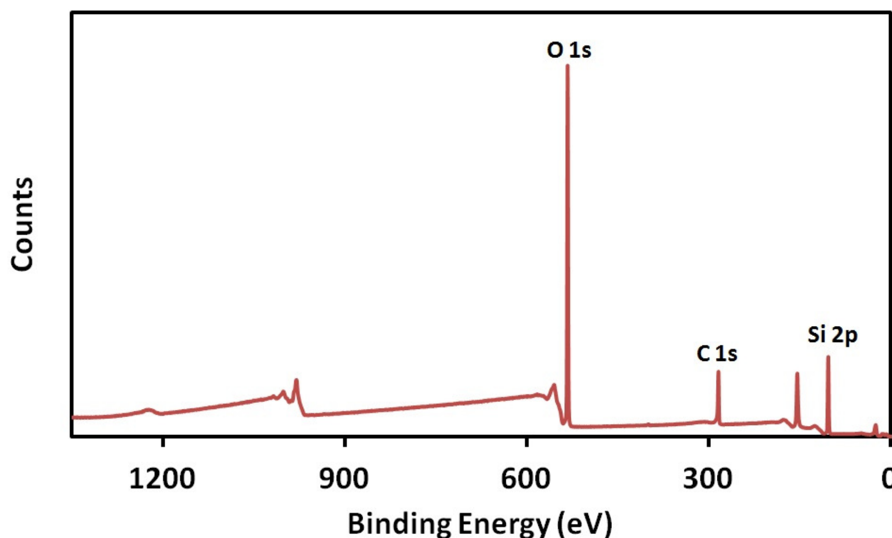

Figure 3.11. XPS survey spectra of graphene with HCl treatment from 0-1300 eV indicates lack of any peak associated with Fe or Cl.

The presence of Fe and Cl in the XPS survey of transferred CVD graphene indicates that multiple washings in DI water does not clean the sample of $FeCl_3$ completely. Therefore, another acid treatment step was utilized to treat the sample with HCl before transfer to the desired substrate; this assures complete removal of $FeCl_3$. Figure 3.11 shows the XPS survey spectra of graphene films after HCl treatment. The survey spectra prominently showed the C1s and O1s peaks and the lack of any peak associated with Fe or Cl (Figure 3.11).

A high resolution XPS spectrum of the Fe 2p peak was also acquired over 690-730 eV with the same spot size and the step size of 0.1 eV (Figure 3.12). Comparison of the Fe 2p core level spectra before and after HCl treatment, shown in Figure 3.12, suggests that the acid treatment effectively removed all $FeCl_3$ from the graphene film below the detection limit of Fe 2p in XPS (~0.008%).

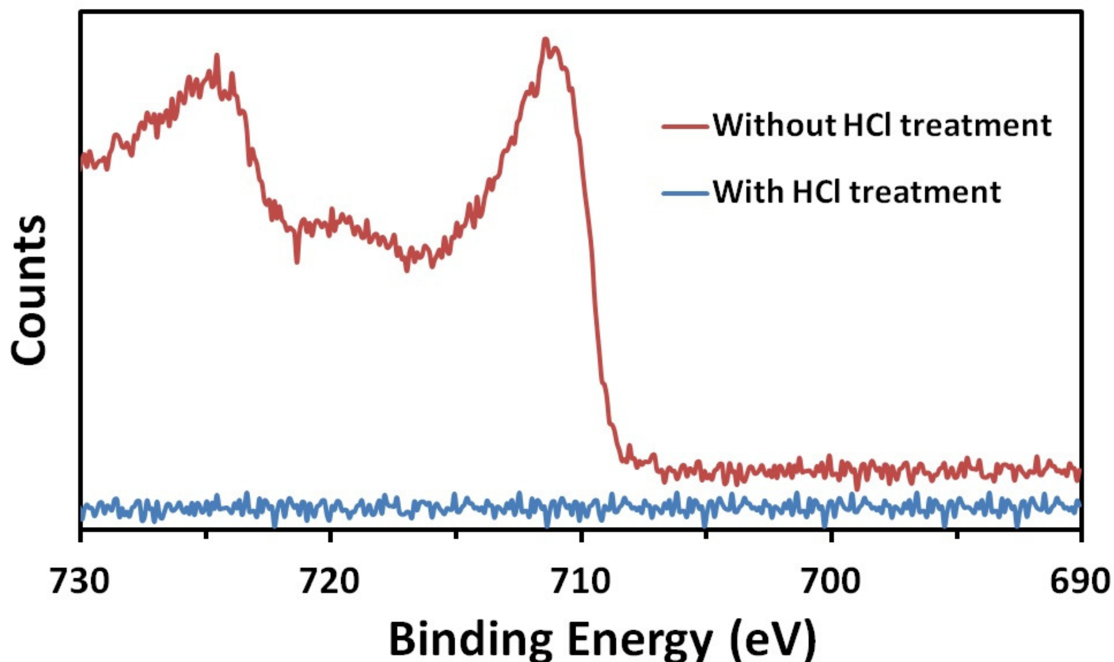

Figure 3.12. Fe 2p core level spectra of graphene with and without HCl treatment.

3.4.3. Thickness measurement and refractive index of graphene

The importance of graphene synthesis on Cu foil using CVD technique is that this produces large area films that are uniform. To investigate the thickness uniformity in the microscale range, Raman mapping was utilized, where the intensity ratio of the 2D over G peak was employed to confirm the presence of monolayer graphene. However, graphene films can be synthesized on the macroscale (from a centimeter to couple of meters scale) on Cu foil. To investigate the thickness uniformity over large scale, ellipsometry was used. The film thickness and refractive index were measured using an M-2000 Woollam spectroscopic ellipsometer over the wavelength range of 192-1698 nm. The M-2000 utilizes CCD array detection in which all wavelengths are simultaneously measured. This provides up to 700 wavelengths in a few seconds. It uses a rotating compensator ellipsometer (RCE) configuration for fast, accurate measurements. Ellipsometry uses polarized light to characterize thin film and bulk materials. A change in polarization is measured after reflecting light from the surface. This measurement is expressed as two values, Psi and Delta, which are related to the ratio of Fresnel reflection coefficients, R_P and R_S, for p- and s- polarized light, respectively.

$$\rho = \frac{R_P}{R_S} = \tan(\Psi)\, e^{i\Delta} \qquad \text{3-1}$$

The Psi-Delta data are analyzed using regression methods (see flowchart) to determine properties of the sample of interest. These properties can include film thickness and layer optical constants.

A high resolution, 18,000 point ellipsometric scan of a graphene coated sample was conducted. The data were analyzed and the graphene thickness was determined using recently published values of graphene's optical properties [131]. Figures 3.13-3.16 on the next few pages will help describe the analysis. When modeling the thermal oxide and

graphing the fit quality over the entire sample, the mean square error (MSE) was found to be drastically higher in areas outside of the cracks in the graphene. This gives us confidence that the measurements are highly sensitive to the very thin layer of graphene.

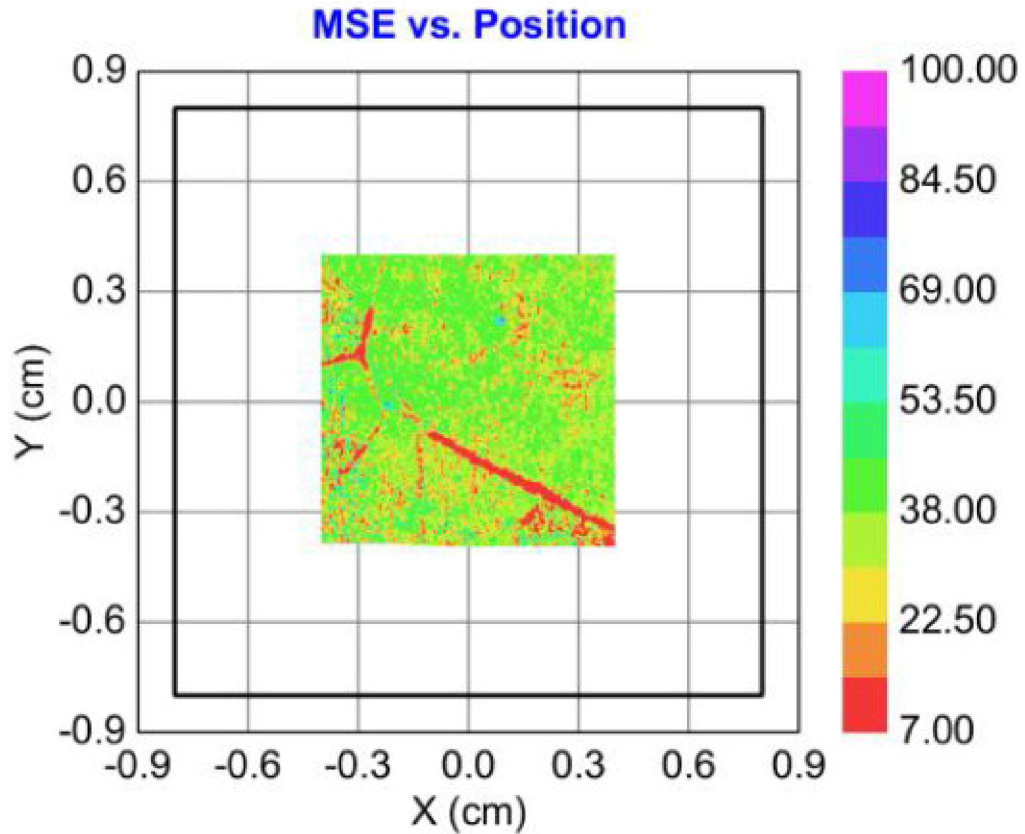

Figure 3.13. Optical image of graphene shows the presence of cracks in the transferred film on SiO_2.

The ellipsometric data measured in the cracked region of the graphene film was found to be quite different than the data measured outside of the cracks. An example of the ellipsometric data for the graphene is shown in Figure 3.14 in comparison to the bare thermal oxide surface found within the cracks. The uniformity of the thermal oxide is unknown; therefore, the thermal oxide thickness was allowed to vary. Since the measurement was highly sensitive to the thin graphene layer, correlation was avoided.

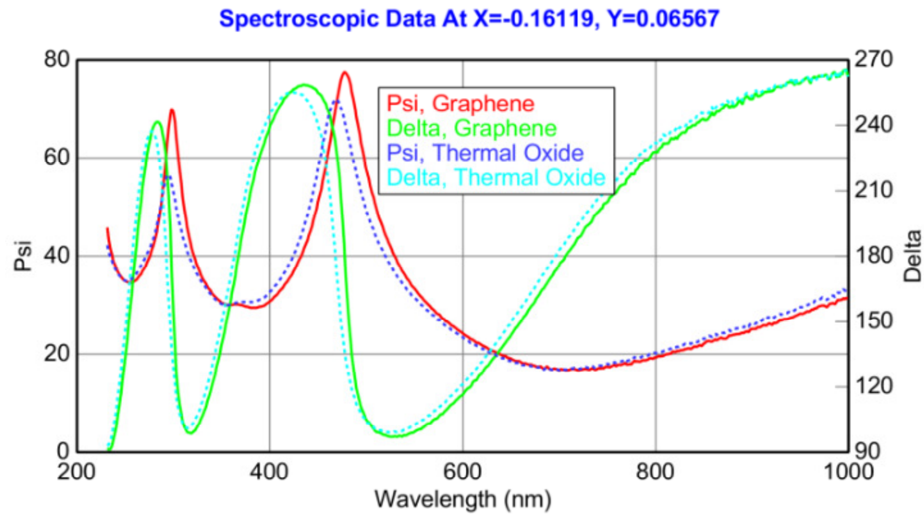

Figure 3.14. Spectroscopic data for graphene and Silicon dioxide.

As previously discussed, an 18,000 point ellipsometric measurement was conducted. The refractive index of graphene was taken from published values and held fixed. The thickness of both the graphene and silicon thermal oxide were allowed to vary. Ellipsometric data from one of the many measured graphene locations is shown in Figure 3.15. The optical constants are taken from Weber, et al. [131].

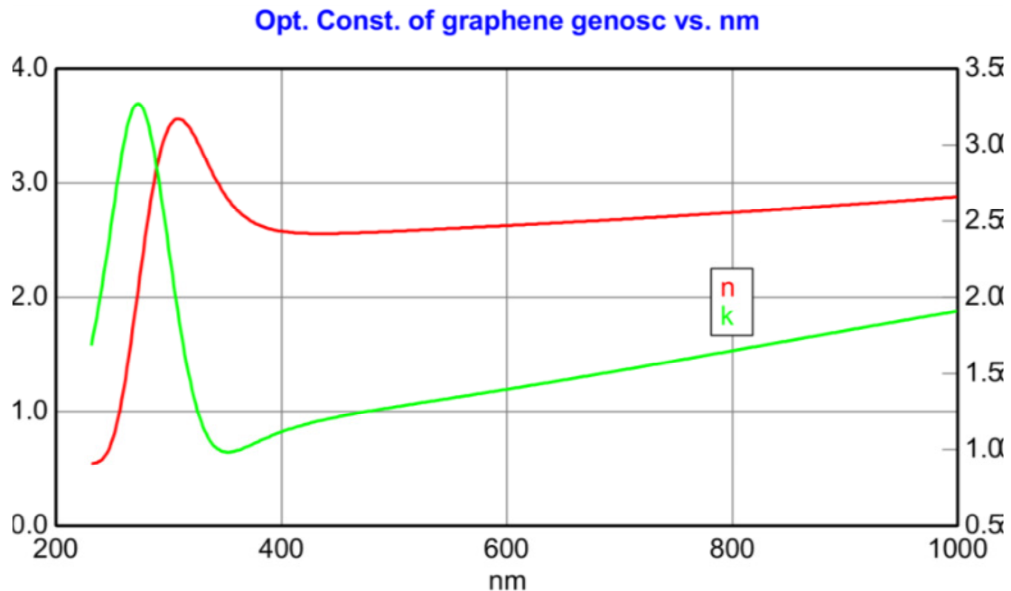

Figure 3.15. Optical constants of graphene (n, k) at different wavelengths.

The average thickness of the graphene layer was found to be 2.25Å (see Figure 3.16). The typical thickness of a monolayer graphene film is about 3.35Å [132]. The slight difference should be mostly attributed to the discontinuities in the graphene film. The red areas in the figure indicate that graphene is not present. This is verified by the very noticeable 'cracks' in the graphene, due to the transfer process, that are even visible to the eye. The density of the red spots will lower the 'average' thickness of the graphene film. Visual inspection of the figure reveals that the dense graphene areas are about 3Å in thickness, which confirms the presence of monolayer graphene [133].

Figure 3.16. Graphene thickness contour plot over 4 mm by 4 mm area.

3.4.4. Imaging the graphene film

Cu foil as growth substrate for graphene has microscale nonuniformities in thickness. In addition, the grain size of the Cu foil is of importance for synthesis of large grain size graphene. Imaging of graphene on Cu foil before transfer is important to ensure the presence of high quality films, as cracks and voids might be introduced during the transfer process. Furthermore, some contamination on the graphene surface can be seen using various imaging techniques. These methods are key to assuring quality before utilizing graphene for any device applications; they are employed on the graphene samples used for various unintentional and intentional dopings that will be studied in Chapters 4 and 5.

Atomic force microscopy (AFM, Dimension 3100 MultiMode AFM, NanoScope III controller, Veeco) measurements were done on graphene on Cu substrates as shown in Figure 3.17. The image shows Cu grain covered with graphene film. The waviness on the Cu foil in microscale can results in formation of wrinkles on graphene after transfer to another substrate.

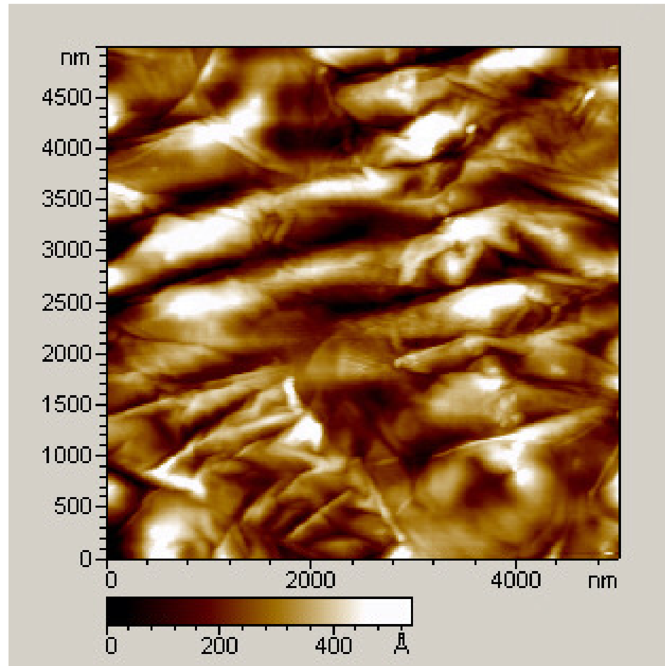

Figure 3.17. AFM image shows graphene film covering grain boundaries of Cu.

A Zeiss Ultra60 scanning electron microscope was also used to image graphene. Figure 3.18 presents a representative SEM image of the transferred graphene film on a SiO_2 substrate that reveals wrinkles and a few small flakes. It is believed that these wrinkles are due to folding of graphene films in transfer and parts of the films that are grown on the grain boundaries of graphene. As explained earlier, graphene was grown on both sides of the Cu. In the transfer process the graphene on the bottom face of the Cu, which is not covered with PMMA, was detached from the Cu foil and floating in the etchant solution. Sometimes, small flakes of floating graphene became attached to the bilayer graphene/PMMA. These flakes can be observed in the SEM image as shown in Figure 3.18.

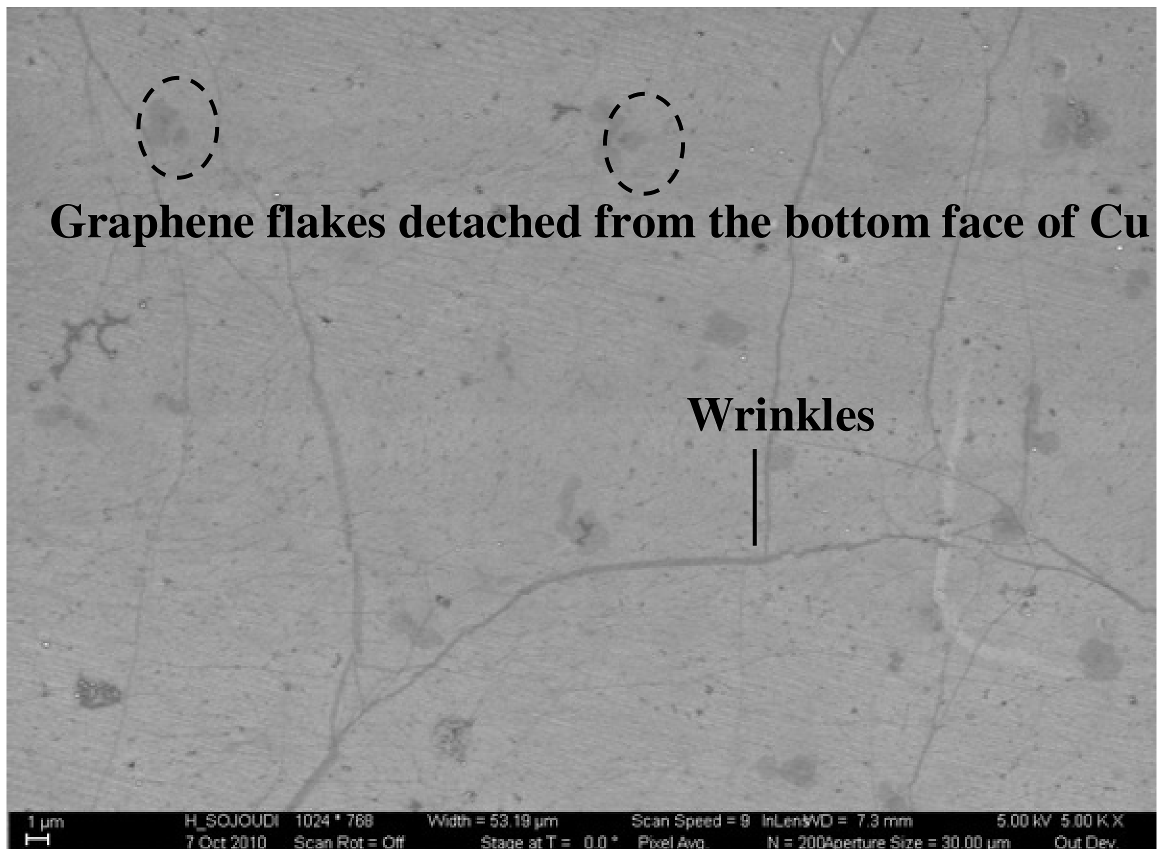

Figure 3.18. SEM image of graphene transferred on SiO_2 substrates shows the presence of wrinkles and small graphene flakes.

Transmission electron microscopy was also used to characterize the graphene film. To this end, graphene was transferred to a TEM grid using a procedure similar to the method explained in section 3.3. The only difference is that PMMA was removed by holding the TEM grid with bilayer graphene/PMMA above acetone vapor rather than placing it inside the acetone bath. This prevented any damage to the TEM grid and allowed better transfer quality. Figure 3.19 shows a TEM image of a graphene section that has a small crack. Diffraction pattern TEM indicates the presence of a monolayer film as shown in Figure 3.19 (Left).

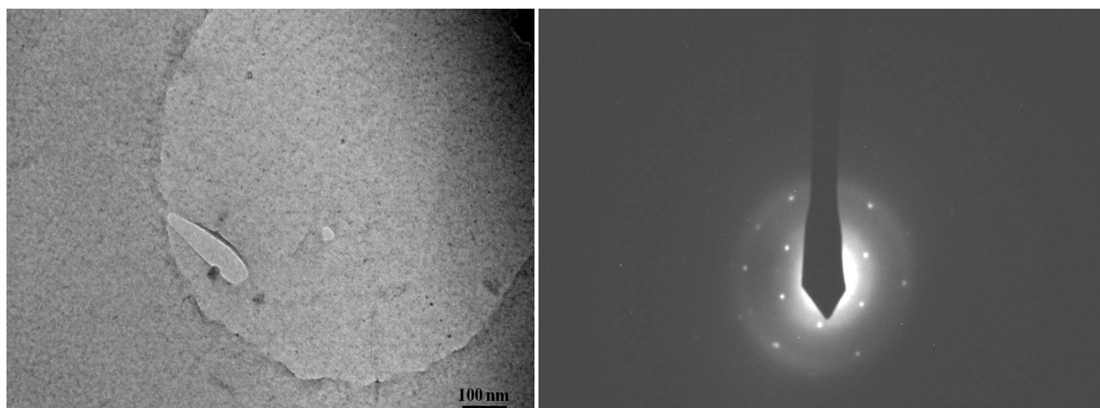

Figure 3.19. (Left) TEM image of graphene with a small crack. (Right) Diffraction pattern of graphene showing presence of monolayer film.

3.4.5. Optical transmittance

As explained in Chapter 2, graphene is highly transparent with ~ 2.5 % adsorption of light in the visible range (550 nm wavelength) [132]. This is very important, as it makes graphene a potential material for transparent conductive electrode applications. In addition, with a well known transmittance of monolayer graphene, this is yet another technique to ensure the presence of monolayer graphene on large scale areas. For calculating the figure of merit (FoM) for graphene films, explained later in this chapter, optical transmittance measurement is required.

The optical transmittance of the graphene was measured using a Cary 5E UV-Vis-NIR dual-beam spectrophotometer. To this end, graphene was transferred onto a quartz substrate using a process similar to the method explained earlier. Pieces of the same quartz substrate were used as a baseline to obtain the transmittance of the monolayer graphene film. The graphene film has shown ~97.5% transmittance at 550 nm, averaging data taken for a minimum of three different points per sample (Figure 3.20) [132]. This indicate that graphene can be a potential material for transparent conductive electrode applications.

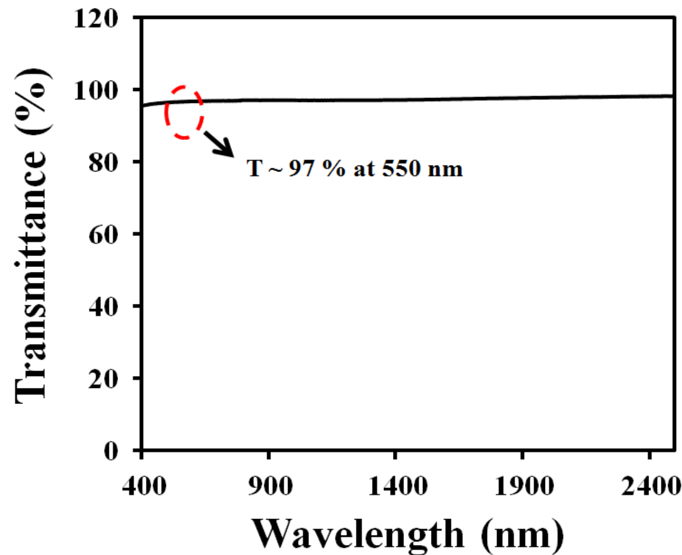

Figure 3.20. Optical transmittance of graphene film as a function of wavelength.

3.4.6. Mobility measurement

The electrical properties of graphene are of significant importance for transistor and transparent conductive electrode applications. Carrier mobilities in pristine graphene have been estimated to be as large as 200,000 cm^2/Vs, which are several orders of magnitude larger than is the case of silicon. Silicon possesses maximum carrier mobilities of approximately 1450 cm^2/Vs [134]. In comparison to other organic semiconductors, graphene's mobility is far superior since the best organic semiconductors have mobilities that are only on the order of 1 to 15 cm^2/Vs [135]. These electrical properties have

spurred research directed at developing graphene for use in a variety of electronic, optoelectronic, and sensor technologies [136-137].

To measure carrier mobilities in graphene, back-gated CVD graphene field effect transistors were fabricated using standard lithography and metallization techniques in conjunction with a solution based transfer of CVD grown graphene. A highly p-doped Si wafer was used as a gate, with a 300 nm thick thermally grown silicon dioxide layer as the gate dielectric. Au was used as source and drain contact. A schematic of a graphene FET device was shown in Figure 3.21.

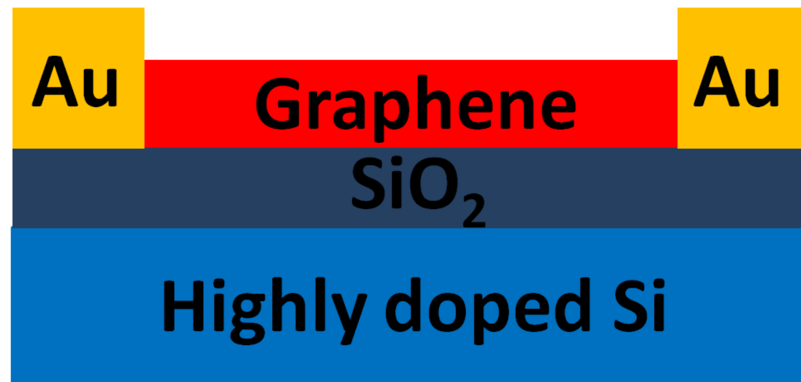

Figure 3.21. Schematic of a back-gated graphene field effect transistor fabricated using lithography for mobility measurement.

A photo of a graphene FET device is shown in Figure 3.22. The channel size used was 50 µm by 2 mm. The size of the channel affects the mobility of graphene as with an increase in the channel size the carrier mobility decreases. This is due to possibly increased presence of cracks and voids in the graphene film within the channel that present resistance to the flow of charge carriers.

A constant voltage applied between drain-to-source, $V_{D/S}$, and current from drain-to-source, $I_{D/S}$, was measured with a change in the voltage across the gate, V_G . Figure 3.23 shows measurements of the $I_{D/S}$ vs V_G of a graphene FET device. The gate voltage at which $I_{D/S}$ is minimum is called V_{NP} or "voltage at neutrality point". A V_{NP} value close to zero is indicative of graphene with equal presence of electron and hole carriers. It is

important to note that as-made CVD graphene is intrinsically p-doped because the transfer process produces an excess amount of p-dopant, as V_{NP} is a positive value. Figure 3.23 shows the I-V curve of an FET device after vacuum annealing that resulted in removal of atmospheric p-dopants resulting in V_{NP} being close to zero.

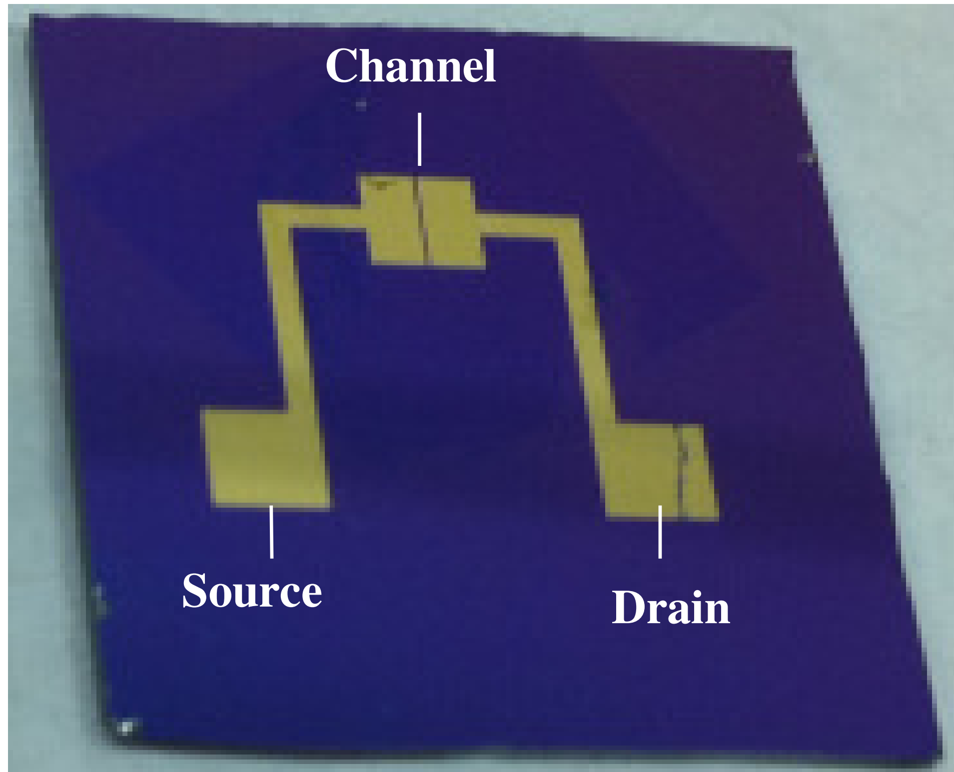

Figure 3.22. Photo of a graphene FET device shows source, drain, and the channel.

The field-effect mobility for both of the devices was ~ 600 ±100 cm^2/Vs (hole and electron mobility); it was extracted using equation 3-2, [138]:

$$\mu_{n/p} = L_{ch} g_m / W_{ch} V_{DS} C_g \qquad 3\text{-}2$$

where μ_n is electron mobility and μ_p is hole mobility, L_{ch}= 2 mm, $g_m = dI_D/dV_G$, W_{ch}= 50 μm , V_{DS}= 0.1 V and Cg=115 aF/μm^2. For electron mobility, $g_m = dI_D/dV_G$ is the slope of

the I-V curve at the right hand side of V_{NP}, and for hole mobility it is the slope of the I-V curve at the left hand side of V_{NP}. It is important to note that the calculated carrier mobilities will have two components: one is due to long-range disorder and another one due to short-range scatterers. Therefore, the values will be reported in this thesis for carrier mobilities are overall field effect mobilities and they are not intrinsic mobilities of graphene within a single domain. To this end, peak g_m values are used for all of the mobility calculations.

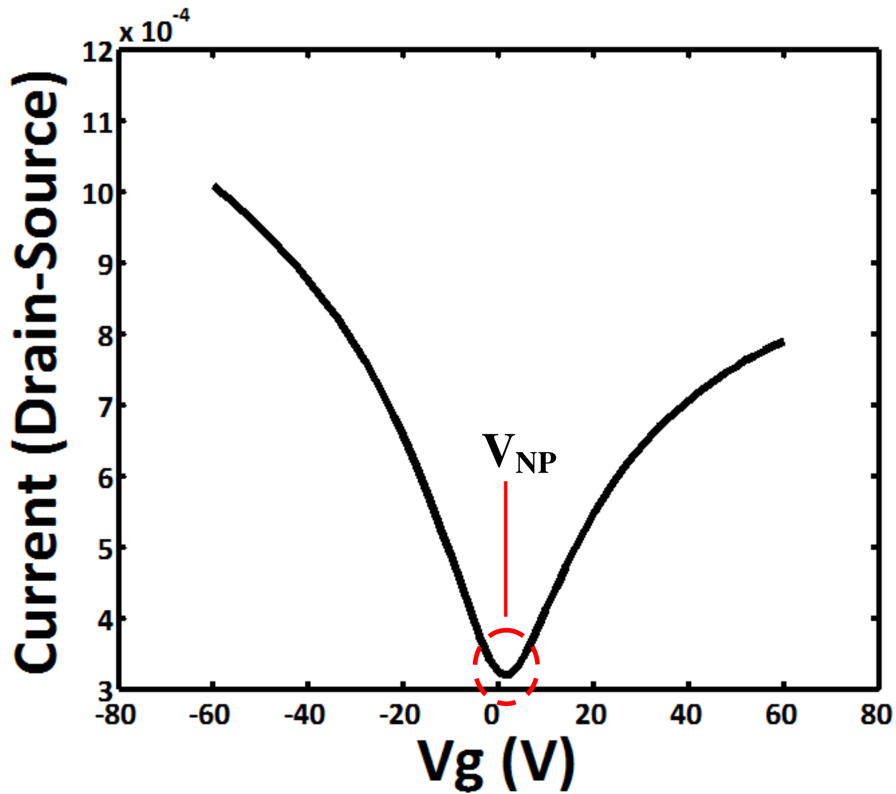

Figure 3.23. $I_{D/S}$ vs. V_G of a graphene FET device shows presence of electrons and hole carriers.

The electron (n) and hole (p) concentrations of graphene can be calculated using following equation, [90, 139]:

$$n/p = C_g V_{NP}/e \quad \text{3-3}$$

where e is the charge of the electron, and V_{NP} is the voltage at the charge neutrality point.

3.4.7. Sheet resistance measurement

The significance of the mobility of the electron carrier, μ_n, and the hole carrier, μ_p, is that they have a direct impact on the direct current conductivity, σ_{DC} , for graphene film as shown in equation 3-4.

$$\sigma_{DC} = e(n\mu_n + p\mu_p) \qquad 3\text{-}4$$

Therefore, the conductivity can be increased with an increase in the carriers (electrons/holes) mobilities or their concentration. The carrier mobilities are intrinsic properties of the material that depend on the grain size and the quality of the film. However, they can be enhanced through optimizing the substrate as well. The carrier concentration can be increased via doping of the films. These methods and their impact on the electrical properties of the graphene will be discussed in detail in Chapter 5.

According to equation 3-4, the resistivity can be expressed as equation 3-5:

$$\rho = \frac{1}{\sigma_{DC}} \qquad 3\text{-}5$$

The resistance of thin films that are nominally uniform in thickness, also called sheet resistance (R_{sh}), can be obtained from equation 3-5 as follows:

$$R_{sh} = \frac{\rho}{t} \qquad 3\text{-}6$$

Therefore, the sheet resistance of graphene can be obtained from the mobility data measurements presented in the previous section. However, this is a very crude method of measuring the sheet resistance, as it utilizes two probes for applying voltage and measuring current. This method of measurements results in total resistance that includes both sheet resistance of the graphene and resistance of graphene and metallic contact as depicted in Figure 3.24.

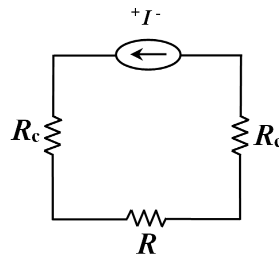

Figure 3.24. Schematic of circuit diagram for two point probe electrical measurements.

The four-point probe method avoids the issue of contact resistance in sheet resistance measurements and was first developed by Kelvin [140]. In this method a constant current source is applied to the outer probes and a voltmeter is connected to the inner probes to measure the voltage drop. A four-point probe schematic and electrical circuit diagram are shown below in Figure 3.25, where electrical probes S_1, S_2, S_3 are equally spaced from one another, at a distance equal to *S*.

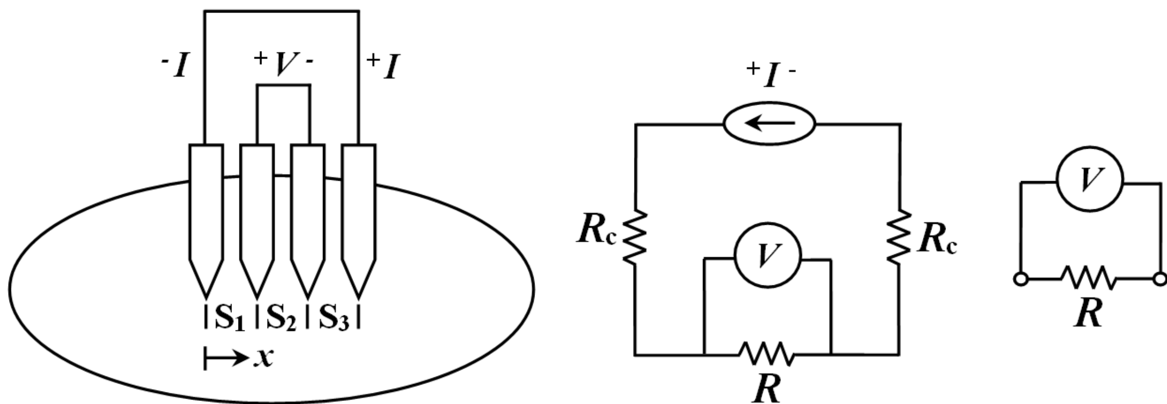

Figure 3.25. Schematic of circuit diagram for four point probe measurements shows that resistance of graphene film can be measured without excluding contact measurements.

Once the bulk resistance, *R,* is obtained, the resistivity of the thin film as shown in Figure 3.26 can be rewritten as:

$$R = \rho \frac{L}{A_c} \quad 3\text{-}7$$

where A_c is the cross-sectional area of the thin film and is defined in equation 3.3, and L is the length of the thin film.

$$A_c = Wt \quad 3\text{-}8$$

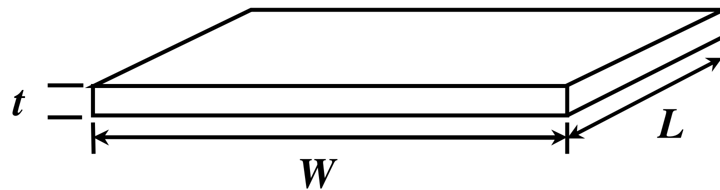

Figure 3.26. Geometry of a rectangular thin film with uniform thickness.

Substituting equation 3-8 in equation 3-7 and considering equation 3-6, the resistance of the film can be written as a function of sheet resistance:

$$\boldsymbol{R = \frac{\rho}{t}\frac{L}{W} = R_s \frac{L}{W}} \quad 3\text{-}9$$

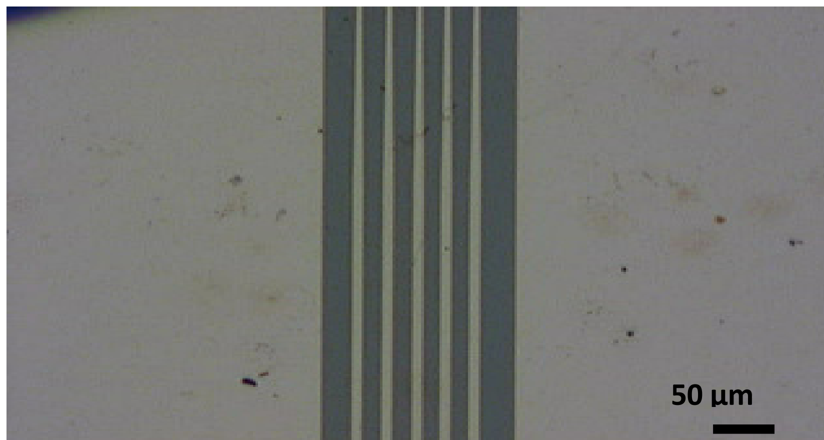

Figure 3.27. Photo of a four point probe device for sheet resistance measurements of graphene.

A four point-probe device was fabricated using a standard lithography and metallization technique similar to the method used for mobility measurements; this probe was used to obtain the bulk resistivity of graphene films without inclusion of contact resistance. A schematic of this device is shown in Figure 3.27 where L is 30 µm and W is 1 mm. The resistivity for several as-made graphene devices is 4.5 ± 0.5 Ω, and the calculated sheet resistance is 150 ± 16 Ω/sq.

3.4.8. Figure of merit

As explained in Chapter 2, one of the applications of large-area graphene films is in transparent conductive electrodes devices like touch screens, flat panel displays, OLEDs, and OPVs. For enhanced performance both higher transparency and higher conductivity (lower sheet resistance) are desired for transparent conductive electrodes. The performance of thin films can be further understood by relating sheet resistance to optical transmittance. To do this, consider the definition of the two-dimensional sheet resistance, R_{sh}, as shown in equation 3-6. Recalling that the σ_{DC} , is simply $1/\rho$ from equation 3-5, the thickness of thin film t can be written as a function of σ_{DC}. The transmittance, T, of a thin film can be related by the optical conductivity, σ_{Op}, as is shown in [141-142],

$$T = \left[1 + \frac{Z_0}{2R_{sh}} \sigma_{Op} t\right]^{-2} \qquad Z_0 = \sqrt{\frac{\mu_0}{\epsilon_0}} \tag{3-10}$$

where the impedance of free space, Z_0, is related to the permeability of free space, μ_0 , and the permittivity of free space, ϵ_0. Replacing t as a function of σ_{DC} in equation 3-10 results in the conductivity ratio, σ_{DC}/σ_{Op}, which correlates the transmittance and the sheet resistance.

$$T = \left[1 + \frac{Z_0}{2R_{sh}} \frac{\sigma_{Op}}{\sigma_{DC}}\right]^{-2} \qquad \mathrm{FoM} = \sigma_{DC}/\sigma_{Op} = \frac{Z_0}{2R_{sh}(T^{-0.5}-1)} \tag{3-11}$$

As explained earlier, the transmittance of graphene films at 550 nm wave length is ~ 97.5%. Substituting this transmittance and the sheet resistance values obtained in the previous section, FoM for monolayer CVD graphene will be 81 ± 7. To maximize the conductivity ratio it is desired to obtain a relatively large σ_{DC} and a relatively small σ_{Op}. To this end, a layer-by-layer approach was utilized to obtain improved conductivity in the films with a minimum sacrifice in the transmittance; the method is similar to that used in [11, 97]. The transfer process for each layer is similar to the transfer of CVD graphene film that was explained in detail earlier in section 3.3. After adding each layer of graphene, the resistance of the film and its transmittance were measured; Table 3-1 shows the measured transmittance and sheet resistance for layer-by-layer graphene and the corresponding FoM.

Table 3.1. Shows transmittance, sheet resistance, and FoM for layer-by-layer graphene.

	1-layer	2-layers	3-layers	4-layers
Transmittance (%)	~97.5	~95	~92.5	~90
Sheet resistance (Ω/sq)	150	70	50	40
FoM	81	103	95	87

Transmittance of the film decreased ~ 2.5% by adding each layer of graphene, which is in accord with the previously reported value for absorption of light in monolayer graphene film [132]. The sheet resistance drops by adding each layer, as this process provides excess paths for travel of electrons and holes within the film. However, the FoM has the highest value for 2-layer graphene film. This means that the decrease in the sheet resistance is not enough to compensate the decrease in the transmittance that is obtained by adding layers 3 and 4. The FoM calculated from layer-by-layer CVD graphene is compared with other carbon based composite (graphene and carbon nano tube) and doped

graphene films. The layer-by-layer graphene film resulted in sheet resistance of 30 Ω/sq with 90% transmittance. However, these films were doped with HNO_3 towards improved conductivity. It has been shown that the improvement by doping with HNO_3 is not stable in the air, and the conductivity of these samples degrades. Therefore, FoM for our CVD graphene samples in this work is outstanding.

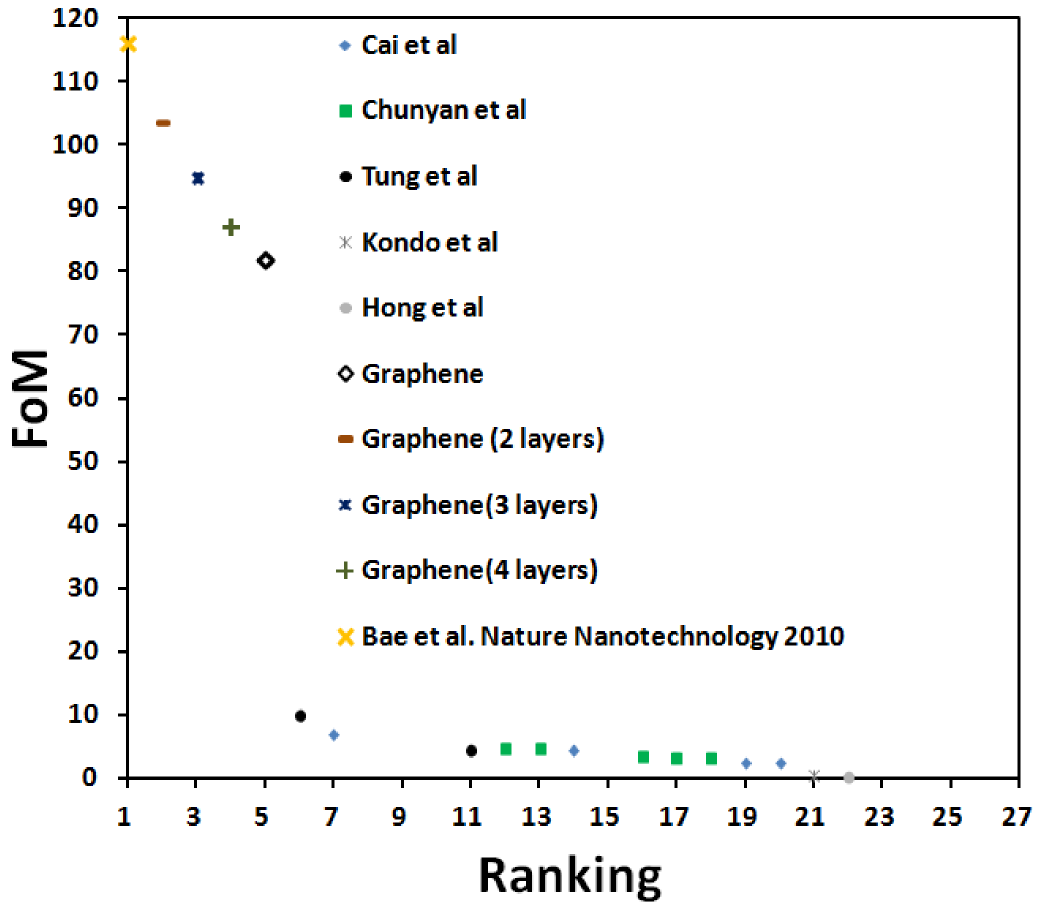

Figure 3.28. FoM of layer-by-layer graphene compared with the data obtained from literature.

3.5. Conclusion

This chapter describes the process used to synthesize, transfer, and characterize CVD graphene films. An optimized transfer process was employed towards a clean

graphene film with fewer defect sites. Different characteristic methods were applied to ensure the presence of high quality, large-scale monolayer graphene films. Field effect mobility measurements, in conjunction with sheet resistance data, are indicative of outstanding electrical properties for CVD graphene films that can be potentially used in next generation transistors. A figure of merit (FoM) ~ 103 obtained using layer-by-layer transfer of monolayer graphene suggests that our CVD graphene can be a potential candidate for transparent conductive electrode applications that are stable upon exposure to air. Therefore, the CVD graphene films discussed in this chapter provide a good reference point for subsequent chapters (Chapters 4 – 6) that will enhance the current understanding of graphene with regard to their application in FET devices.

CHAPTER 4

THE IMPACT OF POST-GROWTH THERMAL ANNEALING AND ENVIRONMENTAL EXPOSURE ON THE UNINTENTIONAL DOPING OF CVD GRAPHENE FILMS

4.1. Introduction

As explained in Chapter 3, CVD graphene must be removed from its metal growth substrate in order to be integrated into electronic devices. This process often involves exposure of the graphene to a range of aqueous solutions as well as the atmospheric environment, [71] resulting in a host of chemical groups that are attached to the graphene once it is transferred to the target substrate. The impact of these chemical species on single layer graphene is of significant importance in controlling the electronic properties, as molecules adsorbed on the surface may change the level and nature of doping in the graphene in a way that is often not the intent of the process (referred to as unintentional doping) [143]. Previous research has shown that the doping level in graphene can be modified through adsorption or desorption of gas/vapor molecules (e.g., H_2O, CO, NH_3, etc.) [82]. This effect has been explored in order to develop graphene for environmental and biological sensor applications [18, 20-21, 62, 144]. Other examples of such graphene-based devices include ultrafast sensors made using positively gated reduced graphene oxide field effect transistors (FETs) [145] and low cost, miniaturized graphene pH sensors [146].

Thermal annealing has been investigated as a method to change the interaction of graphene with molecules adsorbed from the environment, thereby affecting its electrical properties [88-91, 99]. However, it is still unclear as to which mechanisms or functional groups are responsible for this unintentional doping in graphene, and how the attachment of the functional groups correlates to shifts in the p-doping level and charge mobility of graphene. Therefore, additional work is needed to better understand this environmentally-induced unintentional doping effect and the degree to which it can be controlled or manipulated.

In this chapter, we present a study of the effects on unintentional doping levels of graphene exposed to vacuum annealing followed by exposure to controlled environmental conditions. CVD graphene films were grown on copper foils and subsequently transferred onto insulating substrates using a process similar to the method explained in Chapter 3. The graphene films were characterized in an environmental chamber using in-situ Raman spectroscopy and ex-situ X-ray photoelectron spectroscopy, Kelvin probe measurements, and using back gated field effect transistor structures before and after annealing. The goal of this chapter is to indicate how the vacuum annealing process alters the electronic properties of CVD graphene films. Figure 4.1 shows a schematic of chemical desorption by vacuum annealing and adsorption upon subsequent exposure to air. Results demonstrated that the desorption process leaves active sites for the oxygen and water vapor molecules from the environment to be re-adsorbed on graphene resulting in a more highly p-doped film. This is a complex process and shows the importance of the thermal and environmental history on the unintentional doping of graphene films.

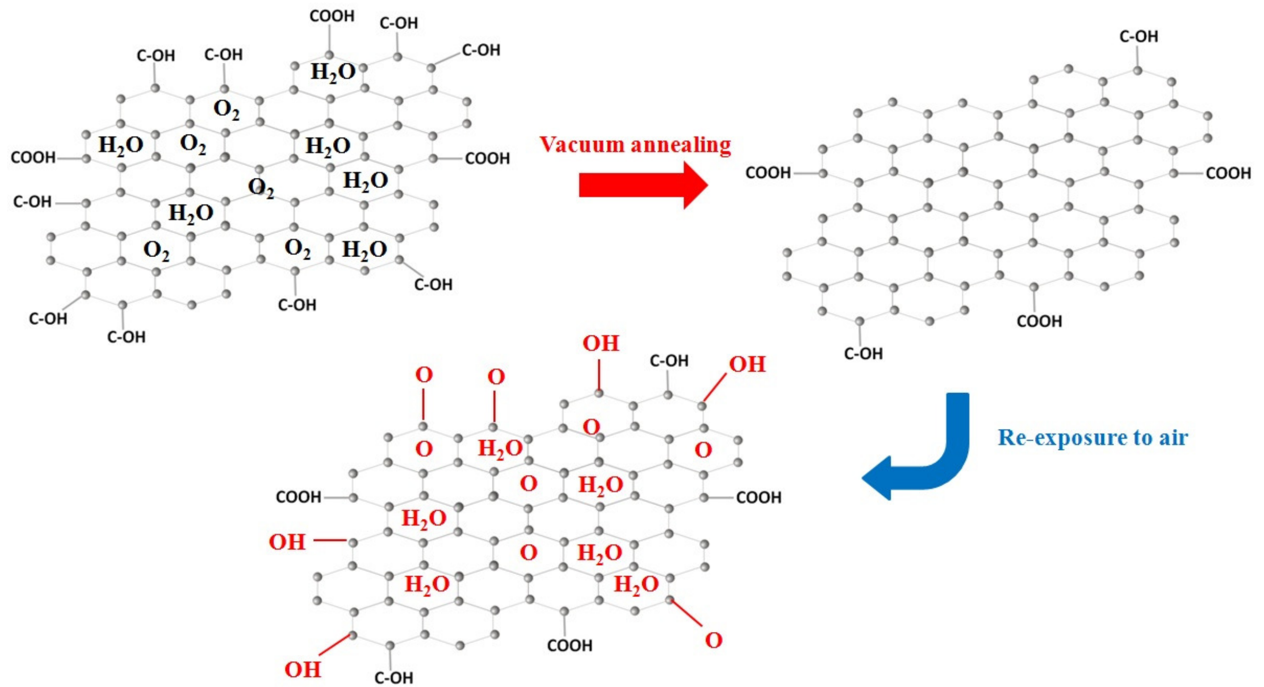

Figure 4.1. Schematic of chemical desorption by vacuum annealing and atmospheric adsorption upon exposure to air.

4.2. In-situ Raman study of CVD graphene films

4.2.1. Measurement set up

As explained in Chapter 2, Raman spectroscopy is a powerful tool for identifying the number of graphene layers by examining their graphitic peak (D, G, and 2D) intensity ratios/linewidth and their doping state through the position and linewidth of these peaks. To this end, graphene films were synthesized and transferred onto a SiO_2 substrate as explained in Chapter 3 [29, 147]. After their transfer onto the SiO_2 substrate, Raman spectroscopy was utilized to investigate the quality of the as-transferred graphene by examining the D, G, and 2D bands. All spectra were excited with visible (532 nm) laser

light and collected in the backscattering configuration with a laser power below 0.5 mW to avoid laser-induced heating [89]. A 50X objective lens was used to focus the laser on the graphene samples during the Raman measurements. The samples were placed inside an environmentally controlled microscope stage with heating, vacuum, and gas delivery capability (Linkam TS 1500) for in-situ Raman measurements. The thermal stage was mounted onto a X-Y-Z micropositioning stage to control focusing and the measurement position. A quartz window was used to allow optical access to the sample, while a vacuum pump was used to evacuate the pressure down to 1mTorr. The temperature was controlled between room temperature and 500°C. The drift of the laser spot on the graphene due to thermal expansion was minimized before all measurements.

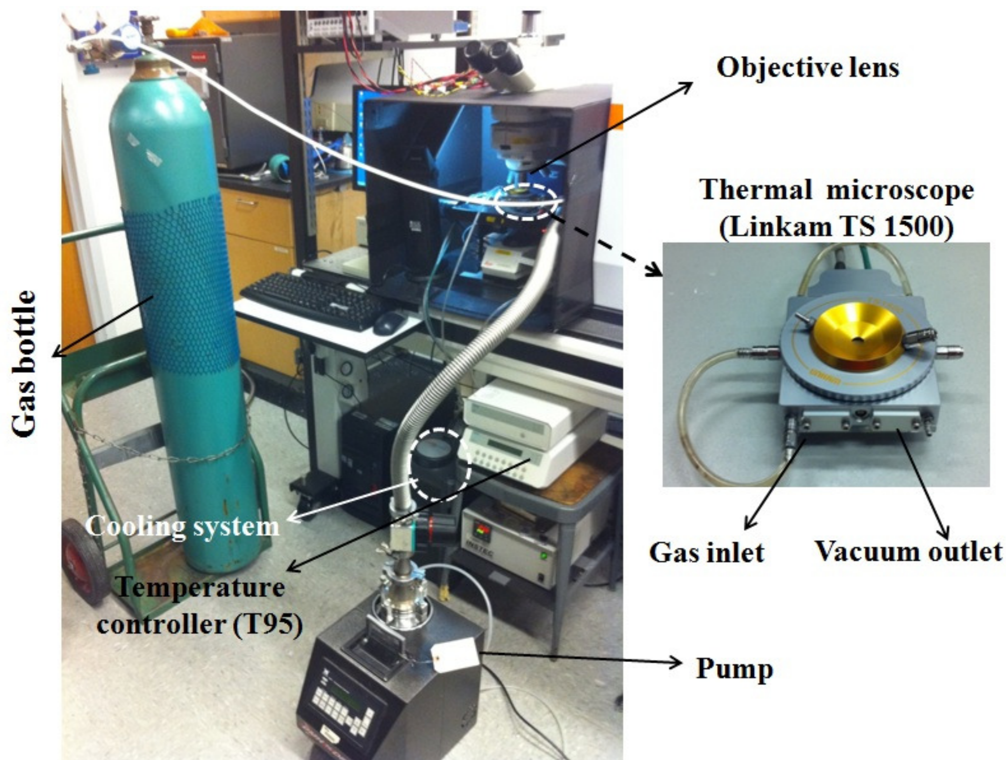

Figure 4.2. Photo of In-situ Raman measurement set up with heating, cooling, vacuum, and gas delivery capabilities. Thermal stage has gas inlet, vacuum outlet, and water cooling system.

The sample was heated up to each set point temperature and held for 15 min to ensure temperature stability and to allow for desorption of surface functional groups bonded to the sample. Raman measurements were performed at each temperature set point both on heat up and cool down at several different spots on the surface of the graphene to verify reproducibility. After cool down, the sample was exposed to N_2, O_2, and air while Raman measurements were repeated on the same measurement locations using the micropositioning stage. All Raman peaks were fitted with Gauss-Lorentzian lineshapes to determine the peak position, line width and intensity of the D, G, and 2D Raman peaks.

4.2.2. Raman results and discussion

Figure 4.3 shows the graphitic peak position measured under controlled environmental conditions. Red and blue data indicate the measurement results during the heat up and cool down process of each graphene film, respectively. The G and 2D peak positions shifted to lower wave numbers as the temperature increased, as previously observed [148-149]. This is partially attributed both to a temperature effect and to thermal expansion of graphene at high temperatures. The intrinsic temperature effect depends on the anharmonic potential constant as well as on the phonon occupation number. As the Debye temperature of carbon materials is ~2800°K, the anharmonic contribution can be ignored [89]. Therefore, direct coupling of the phonon modes and thermal expansion induced volume change both contribute to the resulting temperature dependence of Raman spectra. In addition, vacuum annealing at elevated temperature can cause desorption of oxygen groups and moisture, which results in de-doping of graphene.

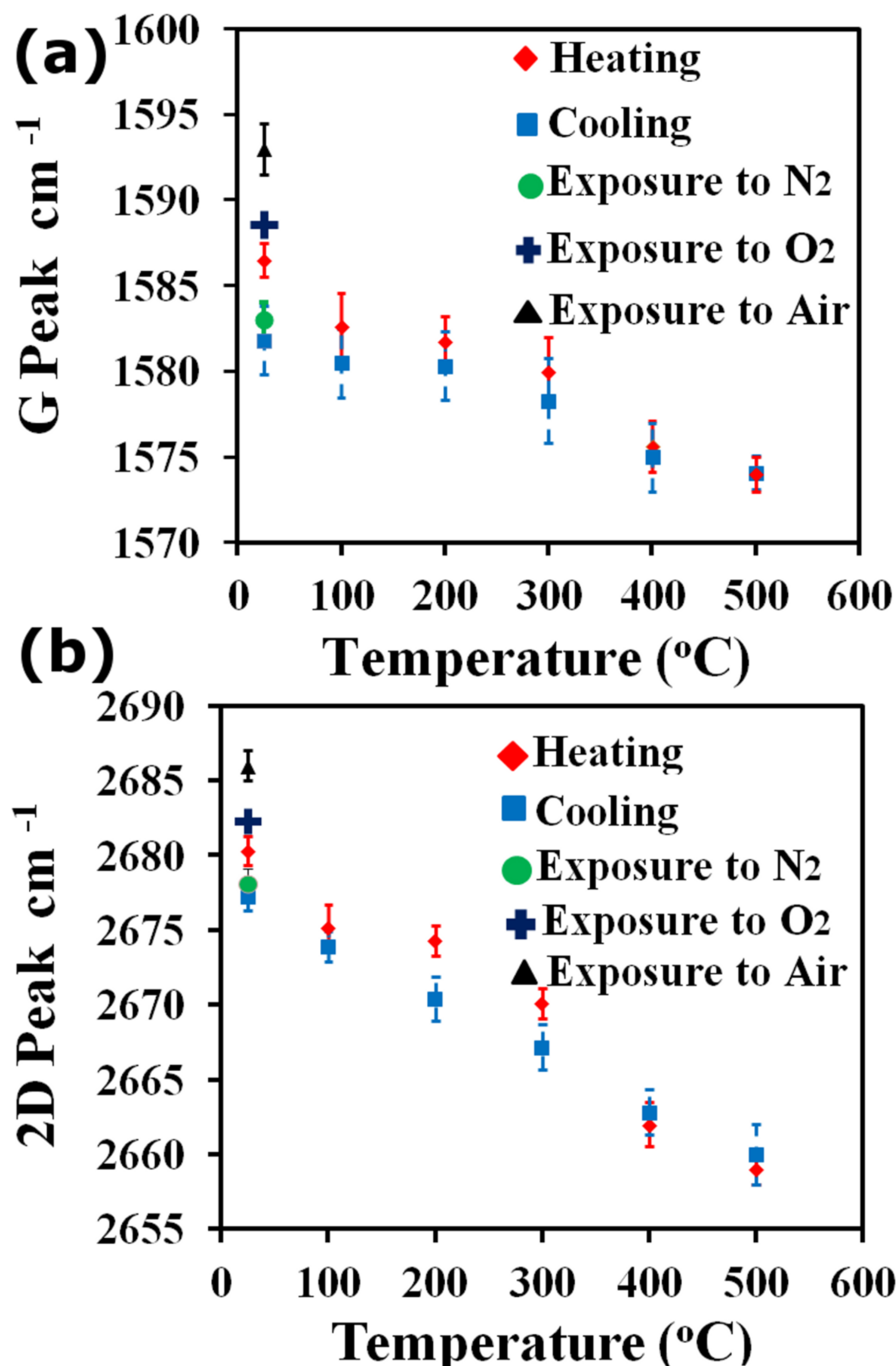

Figure 4.3. Graphitic peaks (G and 2D) positions under controlled environment conditions. (a) Temperature dependence of G peak with ~ 12 cm^{-1} blue shift due to vacuum annealing and re-exposure to air. (b) Temperature dependence of 2D peak with ~ 9 cm^{-1} blue shift due to vacuum annealing and re-exposure to air. A hysteresis was observed during heat up and cool down cycles.

A decrease in Raman graphitic peak position due to the de-doping process may also occur. A sudden drop in the G and 2D peak positions measured after vacuum annealing at 100°C indicates possible evaporation of moisture of the substrate. A hysteresis effect observed in the G and 2D peak positions measured during the heat up and cool down process confirms that the desorption of oxygen groups and moisture during vacuum annealing has some impact on the Raman peak position. This is in contrast with the previously observed temperature dependence of exfoliated graphene [89, 149-150], where the G and 2D peaks showed a red shift of ~5 cm^{-1} and ~3 cm^{-1} due to vacuum annealing, respectively. The temperature coefficient for the shift in the G and 2D bands in CVD-grown graphene was measured as 0.024 $cm^{-1}{}^{\circ}C^{-1}$and 0.044 $cm^{-1}{}^{\circ}C^{-1}$, respectively. This indicates the higher sensitivity of the 2D peak to temperature change, as the 2D peak is a second-order phonon peak, and the shift is enhanced for the second harmonic.

After vacuum annealing and cool down, the sample was exposed to N_2 gas in the Linkham stage and the Raman measurements were repeated after 30 minutes as a control. The peak positions did not experience a significant change, as expected. Next, O_2 was introduced inside of the Linkham stage, and the samples were exposed to it for periods varying from 5-60 minutes. Under these conditions, in-situ Raman measurements showed a significant increase in the G and 2D peak positions. It is important to note that a saturation in the oxygen adsorption was observed, as further increase in exposure to O_2 gas did not result in an additional shift in the peak position [88]. Following oxygen exposure, the sample was exposed to air, resulting in a further increase in the Raman peak positions, indicative of additional doping through the adsoption of water vapor to

the edges and defect sites of the graphene [89]. Figure 4.3 shows the blue shift in the G peak position up to ~12 cm^{-1}, which is in accordance with other reported doping effects by air exposure [151-152]. The 2D peak position is known to increase with hole doping and to decrease with electron doping [151]. In our analysis, the 2D peak position shifted ~9 cm^{-1} through O_2 exposure followed by air exposure. The observed shift in the 2D peak position induced by atmospheric p-dopants is similar to that reported after graphene p-doping by electrostatic gating [89, 151].

Since it is believed that the oxygen containing groups responsible for the p-doping are physisorbed to the graphene, their attachment and detachment may be reversible, depending on changes in the environmental conditions. To explore this, another set of measurements was performed to investigate the reversibility of the doping process through O_2 gas and air exposure. Figure 4.4 shows the in-situ Raman G peak position of graphene samples that have undergone various annealing and gas/air exposure steps. First, sample #1 was placed inside of the Linkham stage and heated in vacuum to 500°C, resulting in a decrease in G peak position from 1587 cm^{-1} down to 1574 cm^{-1}. Upon cooling to room temperature, the peak position increased, but remained at a reduced value of 1581 cm^{-1} corresponding to the de-doping of the graphene film.

Next, an N_2 exposure resulted in no significant change in the Raman peak position. After the N_2 exposure, a 5 minute O_2 exposure resulted in a significant shift in the G peak position to 1585 cm^{-1}, while further exposure from 30-60 minutes caused a slight change to 1587 cm^{-1}. This indicates that the O_2 absorption is a fast process and that it saturates before an hour of exposure [88]. Re-exposure of the sample to an N_2 environment for 30 minutes resulted in a decrease in the peak position back to 1581 cm^{-1},

showing the reversibility of the doping process by O_2 absorption. Subsequent exposure to oxygen resulted in the G peak shifting back to its saturated O_2 doped position of 1587 cm^{-1}. This is in accordance with the reversibility of doping with dry O_2, reported for exfoliated graphene [88]. Subsequent exposure to air resulted in a significant increase in the G peak position to 1594 cm^{-1}, as shown in Figure 4.4. In Figure 4.4 sample # 2 was subjected to a similar heating and cooling cycle, but was exposed to air directly rather than having an intermediate O_2 exposure step.

As expected, a significant blue shift was observed in Raman G peak position, increasing from 1581 cm^{-1} after vacuum annealing to 1594 cm^{-1}. However, in contrast to doping with dry O_2, exposure of the sample to an N_2 environment did not shift the peak position back to its initial position of 1581 cm^{-1}, but 1589 cm^{-1}. It should be noted that the sample exposed to air could be doped by water vapor as well as O_2 and other oxygen containing molecules. The decrease in the doping level during the exposure to dry N_2 may be a result of the removal of molecules, such as O_2, that are weakly absorbed to the graphene. However, other molecules such as water have much stronger bonds to the graphene and do not readily desorb in the dry N_2 environment. Next, the sample was vacuum annealed in the Linkham stage at temperatures up to 500°C to determine if the adsorbed molecules could be removed. The data show that after heating to 500°C and cooling back to room temperature, the Raman peak position returned to 1581 cm^{-1}. Again, another exposure to air resulted in an increase in the Raman peak position to 1594 cm^{-1} demonstrating the reversibility of the process. Additional O_2 gas followed by air-exposure did not result in a significant shift in the peak position.

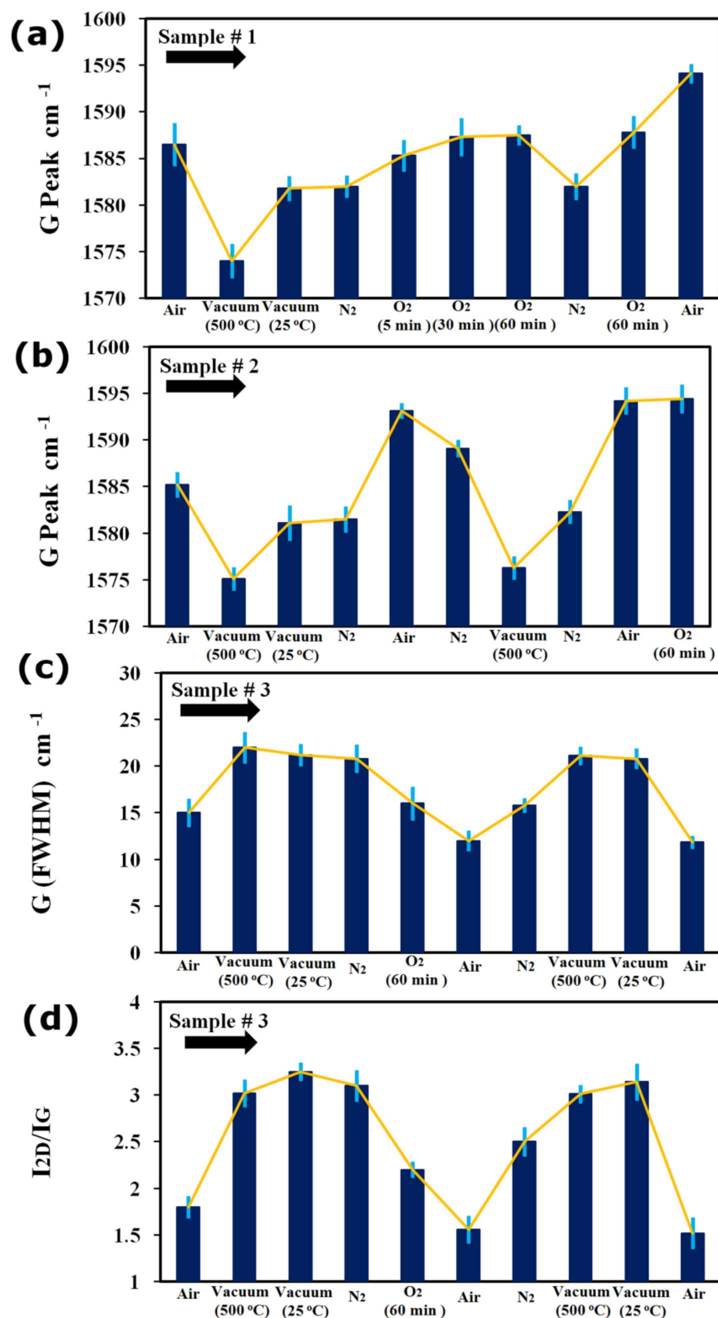

Figure 4.4. Oxygen and water vapor doping reversibility study. (a) Variation in G peak position of sample #1 as it undergoes annealing and gas/air exposure steps. (a) Variation in G peak position of sample #2 as it undergoes annealing and gas/air exposure steps. (c) Variation in FWHM (G) peak of sample #3 as it undergoes annealing and gas/air exposure steps. (d) Variation in FWHM (G) peak of sample #3 as it undergoes annealing and gas/air exposure steps.

Figure 4.4. illustrates the variation of the FWHM of G peak and the intensity ratio of the 2D and G peak (I_{2D}/I_G) of sample #3 before and after vacuum annealing followed by controlled exposure to different gas/air environments. The significant difference of the intensity ratio while heating and cooling is an indication of a change in the electronic structure of CVD graphene due to annealing in vacuum and before exposure to air. A sharpening of ~3 cm^{-1} in the G peak with a 0.5 decrease in the I_{2D}/I_G observed. The change in the FWHM of the G peak and the I_{2D}/I_G ratio for both samples that underwent N_2, O_2, and air exposure cycles is consistent with the shift in the G and 2D peak positions, indicative of de-doping and p-doping processes. However, the FWHM of the G peak experienced a temperature dependence which is in contrast with the previous report [149].

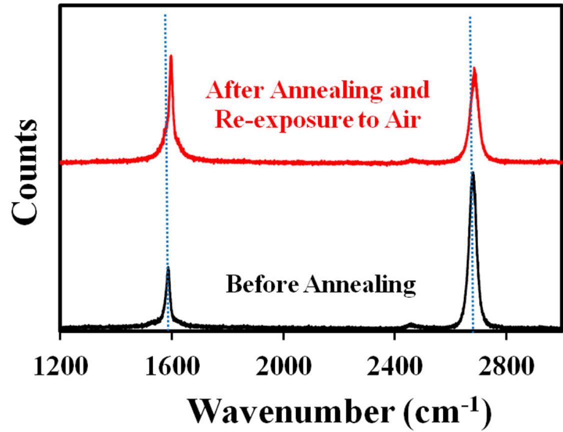

Figure 4.5. Raman spectra of graphene before and after annealing and re-exposure to air. There is a stronger dependence of the 2D mode intensity to annealing than for the G mode.

It is important to note that this vacuum annealing and re-exposure to air process does not induce defects to the structure of the graphene. Figure 4.5 shows Raman spectra of graphene after undergoing vacuum annealing, cooling, and air/gas exposure cycles.

4.3. X-ray photo electron spectroscopy (XPS) of CVD graphene films before and after vacuum annealing and re-exposure to air

4.3.1. Methods

To investigate the effect of the thermal annealing of CVD graphene and re-exposure to air on its chemical composition, X-ray photoelectron spectroscopy was utilized. XPS data were acquired using a spectrophotometer (VG Scientific ESCALAB 210) with an Al $K\alpha$ X-ray source ($h\upsilon = 1486.68$ eV) using a process similar to the method explained in Chapter 3. Each surface was examined in at least three spots. XPS measurements were first conducted on a SiO_2 substrate that had been taken through the same graphene transfer process. This initial test was designed to determine the baseline of any residual elements and chemical groups on the substrate. Next, CVD graphene films that had been transferred onto SiO_2 substrates were measured before as well as after vacuum annealing followed by re-exposure to air. The survey scan spectra were collected over the binding energy (B.E.) range of 0-1100 eV with a step size of 1 eV at a pass energy of 200 eV and a spot size of 400 µm. This scan showed the most prominent peaks to be C1s and O1s, as explained in Chapter 3. Oxygen was abundant on the surface, as the graphene had been transferred to a substrate of SiO_2. Consequently it was not easy to detect changes in the oxygen peak in samples that were evaluated before and after the heat treatment. Therefore, only high resolution XPS spectra of C1s B.E. acquired over 282-293 eV with 400 µm spot size, 0.1 eV step size and 50 eV pass energy were used for analysis. Thermo Avantage v4.54 Build 02750 was utilized for analysis of the collected spectra, where a shirley-type background was subtracted and 70% Gaussian-30%

Lorentzian curve fitting was performed. O1s was utilized for calibration purposes through charge shifting the O1s peak from SiO_2 to B.E. of 533 eV [153].

4.3.2. XPS results and discussion

Figure 4.6 shows O1s B.E. before and after vacuum annealing and re-exposure to air. A slight change in the shoulder of O 1s B. E. can be due to removal of oxygen containing groups by vacuum annealing. In order to deconvolute, the C1s B.E. corresponding to carbon was set at 284.6 eV, and the peak-fitting procedure was repeated until an acceptable peak was obtained. A line-shape analysis revealed four main components centered at binding energies of 284.6, 285.4, 286.1, and 287.8 eV. In agreement with results published elsewhere, the peak at 284.6 ev is assigned to the C-C (sp^2) , while the 285.4, 286.1, and 287.8 eV are attributed to defect (sp^3), C-OH, and C=O, respectively. These peaks verify the presence of surface functional groups on CVD graphene due to the process it undergoes in growth and in transfer onto insulator substrates.

The atomic concentration of different peaks assigned to C1s was compared before and after vacuum annealing followed by exposure to air (Table 4-1). Hydroxyl (-OH) and carbonyl (C=O) groups are the most dominant groups that decrease after vacuum annealing and re-exposure to air. This decrease provides more room for oxygen and water vapor to be adsorbed on graphene upon exposure to dry gas or air, resulting in an additional p-doping of graphene.

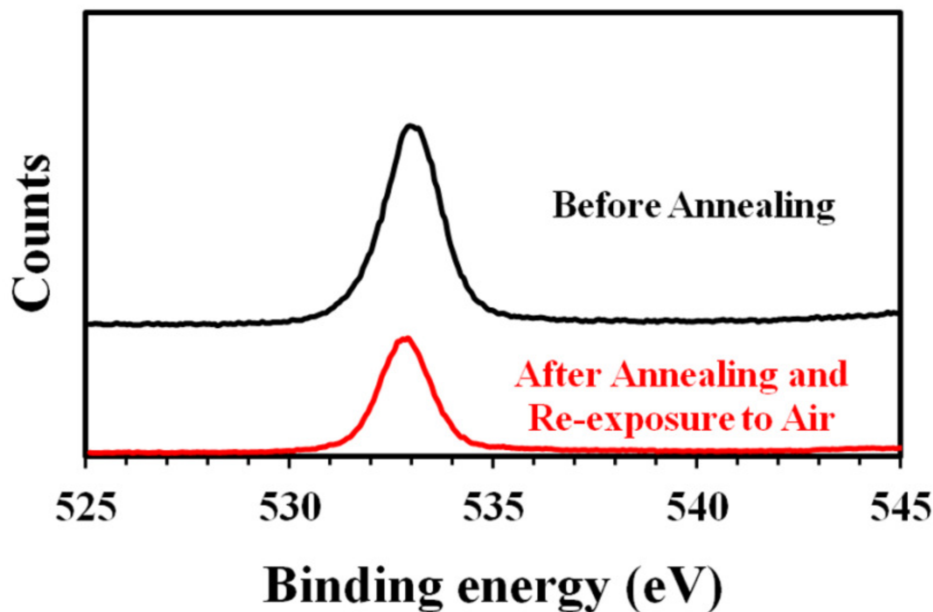

Figure 4.6. O1s binding energy before and after annealing and re-exposure to air. O1 s BE was used for calibration purposes and the XPS scans were charge shifted to bring the O1s peak from SiO_2 to B.E. of 533 eV.

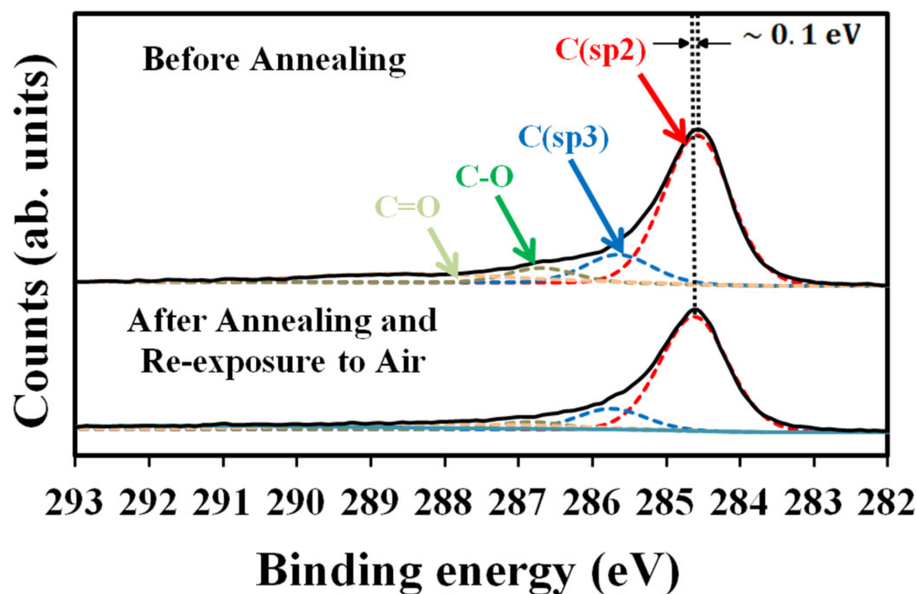

Figure 4.7. Core-level X-ray photoelectron spectroscopy (XPS) peaks showing typical shift and broadening caused by vacuum annealing and exposure to air.

The energy position of the C 1s core level peak shifts is indicated by the dashed line in Figure 4.7, and is in accordance with previous reports of graphene p-doping though chemical treatment [11]. As explained earlier, oxygen and water vapor are well-known electron acceptors. Therefore, addition of these species on graphene makes electron ejection harder, which translates to higher C1s B.E. Table 4-1 summarizes those changes in the atomic percentages before and after annealing and re-exposure to air.

Table 4.1. Atomic % of different peaks assigned to C1s before and after vacuum annealing followed by exposure to air.

	Before Annealing (At. %)	After Annealing (At. %)
C (sp^2) 284.6 eV	61.2	68.5
C (sp^3) 285.4 eV	12.5	14
C-OH 286.1 eV	14.1	5.7
C=O 287.8 eV	12.2	11.8

4.4. Carrier concentration and mobility studies

To further investigate the p-doping in graphene due to annealing followed by air exposure and to corroborate the results of XPS and Raman spectroscopy measurements, electrical characterization using field effect transistors was performed. A back-gated field effect transistor (FET) was fabricated by transferring CVD graphene onto heavily doped Si with a 300 nm thick thermal oxide layer; this step was followed by lithography, plasma etching, and Cr/Au metallization with a FET channel size of 50 µm wide and 2 mm length, as explained in detail in Chapter 3. Figure 4.8 shows a schematic of the change in

atmospheric dopants by vacuum annealing and re-exposure to air. As stated earlier, vacuum annealing removes contamination and provides more room for the atmospheric dopants to be adsorbed.

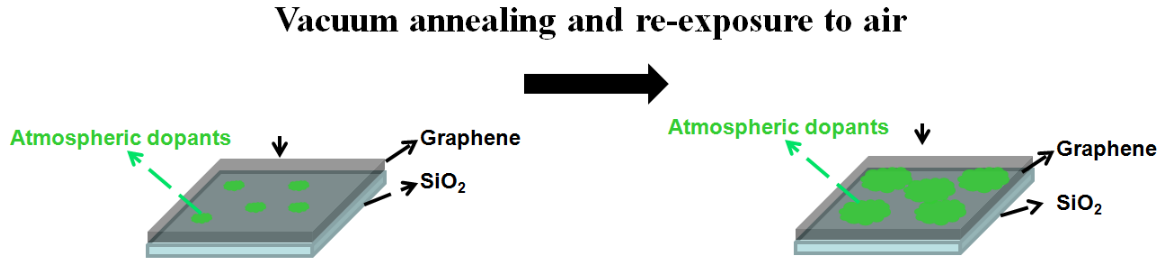

Figure 4.8. Illustration of change in atmospheric dopants with vacuum annealing and re-exposure to air on graphene FET device.

Figure 4.9 shows source-drain current (I_{DS}) vs gate voltage (Vg) of a graphene-based FET device as transferred and then after annealing and re-exposure to air. A positive neutrality point voltage (V_{NP}) on the order of 20V demonstrates p-doped characteristics, which are attributed to chemical groups bounded to graphene due the transfer process. The electron and hole mobility for the as-made device is ~108 ±50 cm^2/Vs and ~217±50 cm^2/Vs. Annealing at 200 ^oC results in a decrease in V_{NP} close to zero and an increase in electron and hole mobility up to ~217±50 cm^2/Vs and ~434±50 cm^2/Vs, respectively. This is due to removal of p-dopants by annealing, which leads to graphene with higher mobilities. After annealing and re-exposure to air, an increase in the V_{NP} to values higher than 60V was observed. This confirms an increase in accumulation of p-dopants due to annealing and re-exposure to air. A dopant concentration of 1 E 13 cm^{-2} was calculated for the device after annealing and re exposure to air, with a hole mobility of 65 ±35 cm^2/Vs. Figure 4.10 shows the I_{DS} vs V_g measured on the same

sample after annealing. An increase in annealing time and temperature showed a decrease in V_{NP} corresponding to the de-doping process. This confirm the removal of p-dopants due to annealing, as the V_{NP} shifted to zero voltage after 3 hours annealing, indicative of very little doping in the graphene sample.

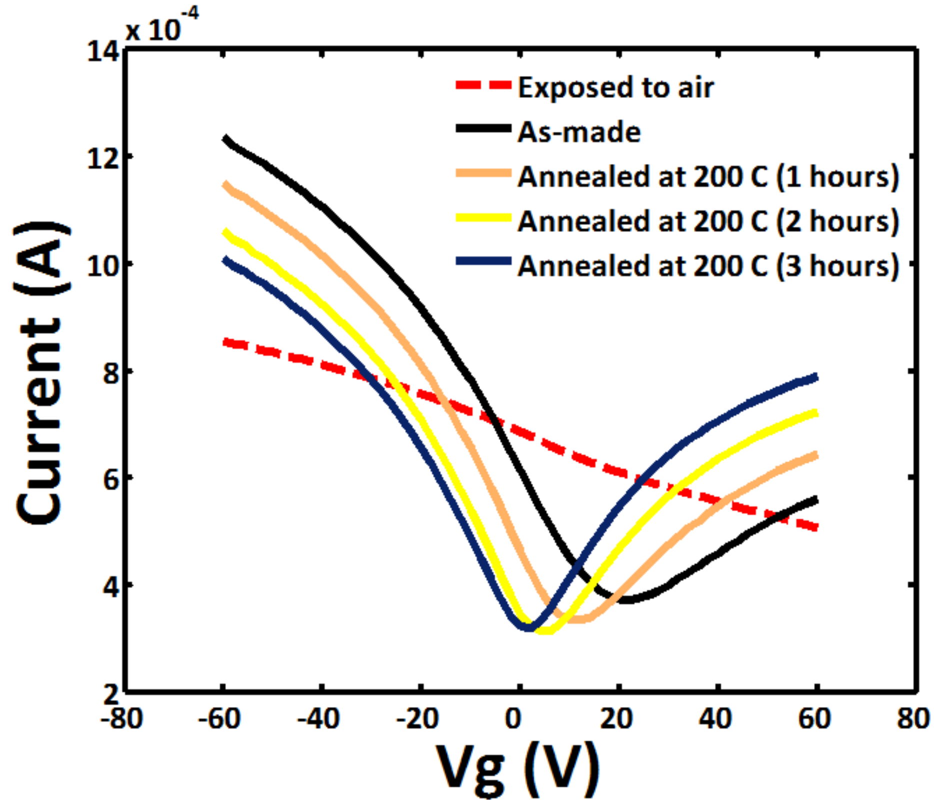

Figure 4.9. IV curve showing p-doping of graphene after annealing and re-exposure to air.

The stability and reversibility of atmospheric doping were also investigated. To this end, the sample was annealed at 200°C for 3 hours and then exposed to air for one hour. For this case V_{NP} is shifted from zero to more than 10 V, indicative of p-doping, and electron and hole mobility decreased ca. 130±50 cm^2/Vs and ca. 220±50 cm^2/Vs,

respectively. The sample underwent the same heat treatment cycle, and as a result V_{NP} shifted back to zero and electron and hole mobility shifted back to their initial values. (~217±50 cm^2/Vs for electrons and ~434±50 cm^2/Vs for holes). However, the inert N_2 environment resulted in no change in the V_{NP}. The observed atmospheric doping effect was reversible by heat treatment and irreversible by N_2 environment, as is consistent with the Raman measurements.

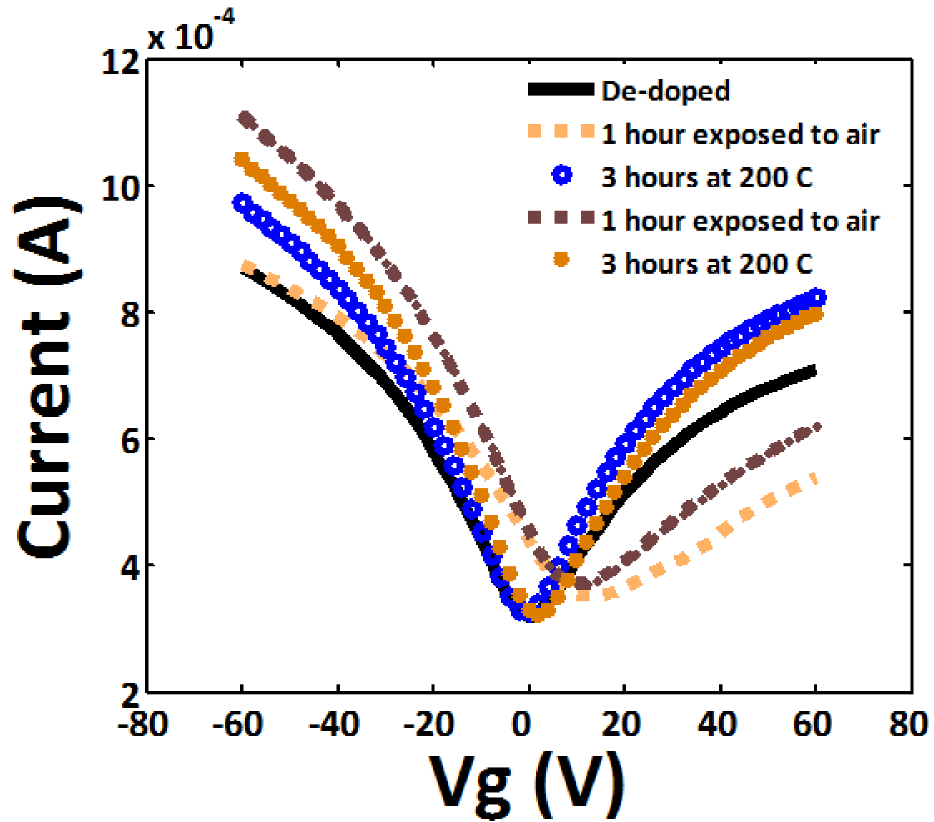

Figure 4.10. De-doping of graphene due to heating in vacuum over time.

4.5. Work function measurements

The work function of graphene before and after vacuum annealing and environmental exposure were measured by Kelvin Probe (Besocke Delta Phi) [154-155]. Kelvin Probe work function measurements were averaged over three locations on each substrate. A highly ordered pyrolytic graphite (HOPG) sample with a work function of 4.5 eV was used as the reference sample. The measurement results are shown in Table 4-1. The work function measured on as-transferred CVD graphene was ~5 eV, which is higher than the value obtained for pristine graphene, ~ 4.7 eV, and is indicative of an intrinsically p-doped sample. Kelvin probe measurements were repeated on transferred CVD graphene after vacuum annealing and re-exposure to air. An increase in the work function after annealing and re-exposure to air up to 0.2 eV was observed, indicative of further adsorption of atmospheric p-dopants. A higher annealing temperature results in heavier p-doping, which translates to more shift in the Fermi energy level. This increase is considered to provide direct evidence for chemical/molecular desorption/adsorption of O_2, H_2O, and chemical groups on the graphene surface.

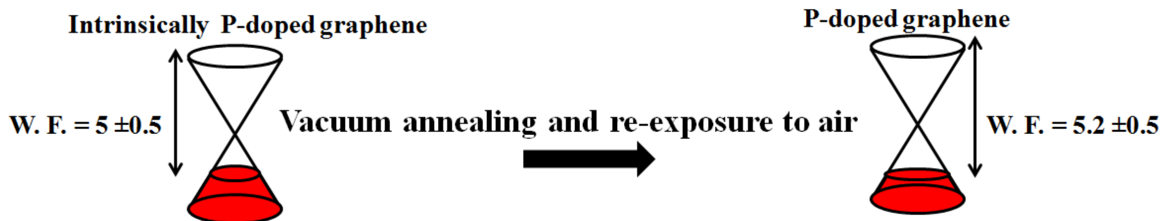

Figure 4.11. Schematic of a change in the work function of graphene due to annealing and re-exposure to air. Work function (WF) measurements were obtained using Kelvin Probe (Besocke Delta Phi).

4.6. Conclusions

The goal of this chapter was to demonstrate that a change in the oxygen containing groups on the graphene film, induced by both annealing and re-exposure to air, results in a p-doping on graphene samples. CVD graphene samples were cycled between room temperature and 500°C in vacuum while in-situ Raman measurements were recorded. During the heating and cooling cycle, a hysteresis in the Raman response due to the desorption of p-dopants was observed. Upon exposure to O_2 gas or air, a blue shift in the Raman response with respect to the as grown film was observed, which was due to increased adsorption of p-dopants on the sample. Experiments showed that a water vapor and oxygen combination is more effective at p-doping the samples than oxygen alone, and that the doping effects are reversible in both cases.

Electrical measurements performed on back-gated field effect graphene devices indicate that shifts in the Dirac point correlate well to the shift in the Raman peak positions. XPS measurements revealed the change in chemical species on graphene, resulting a p-doping. The change in the Fermi energy level was confirmed by work function measurements before and after annealing and exposure to air. The ability to use vacuum annealing to systematically tailor the surface potential of CVD graphene makes it a potential material for device applications.

The results of this chapter suggest that vacuum annealing is an effective method to remove contaminants and other atmospheric dopants from a graphene surface. It also improves the mobility of graphene film, which is of importance for FET device applications. Controlled exposure to O_2 and water vapor can result in a graphene film

with controlled work function, which is important for graphene application as transparent conductive electrodes.

This chapter highlighted the impact of post-growth thermal annealing and environmental exposure on the unintentional doping of CVD graphene films. Understanding the mechanism of unintentional doping and its impact on the electrical properties of graphene provides a great foundation for intentional doping of such films. Therefore, this chapter provides essential knowledge about intentional doping of graphene films that will be discussed in Chapter 5.

CHAPTER 5

GRAPHENE DOPING/INTERFACE MODIFICATION USING SELF ASSEMBLED MONOLAYERS (SAMS)

5.1. Introduction

Graphene has many unique electrical properties, including its nearly linear energy dispersion relation, which results in electric field induced generation of electrons and holes in the material; these electrons theoretically travel as massless Dirac fermions with very high velocities [2, 108, 156]. Nevertheless, there are many challenges that must be overcome before viable graphene-based devices can be created. In its pristine state, graphene is metallic [2]. Although graphene may be useful as a conductor in electronic devices, much of the current interest is in utilizing it in a semiconducting form. Therefore, introduction and control of a bandgap in graphene is crucial. Methods to open a bandgap in graphene have been reviewed in Chapter 2. For example, substitution of carbon atoms in the graphene lattice with atoms such as nitrogen [157-158], substrate induced band-gap opening, [159] and lateral confinement of charge carriers to a quasi-one-dimensional (1D) system through formation of graphene nanoribbons have been shown to create an energy gap near the charge neutrality point [160].

A second and equally important challenge is to develop methods for controllably doping graphene, since such methods potentially give access to both p-type and n-type materials and can allow for adjustment of the work function of graphene [35]. Graphene doping been performed primarily through electrostatic gating, [161] chemical interactions, [162] and intercalation methods [35, 163-164]. However, most graphene samples obtained in these ways are composed of multilayer films with significant

numbers of defects that reduce carrier mobilities significantly. Therefore, due to both the complexity and lack of control of some of these doping processes and the resulting high defect levels reported for many of these doping techniques, this chapter will focus on developing a low temperature, scalable technique for doping graphene with minimal introduction of defects.

Chapter 4 demonstrated the unintentional mechanism of graphene doping through adsorbates from the ambient environment. In this chapter, surface interactions of graphene monolayers with self assembled monolayers (SAMs) on SiO_2 substrates will be explained to intentionally dope graphene films. As explained in Chapter 2, SAMs have been recently used to modify graphene and dielectric interfaces by reducing charged impurity scattering and the effects of environmentally induced doping on graphene; [114-115] SAMs have also been used to control charge carrier and concentration in order to create n- and p-type graphene field effect transistors (FETs) [116-119]. Unlike chemical doping, this method uses SAMs that covalently bond to the substrate rather than to graphene; this results in thermally stable doping and, unlike electrostatic gating, it is independent of dielectric material and thickness. The unintentional doping described in Chapter 4 will assist in the development of methods for stable and intentional doping of the films using SAMs. First, p- and n-type doping through SAMs will be explained, where various characterization methods will be utilized to identify and validate the extent of achieved doping. Next, this method of doping will be extended to form controllable graphene p-n junctions.

5.2. Graphene doping/interface modification using SAMs

5.2.1. Interface modification using SAMs containing silane group

5.2.1.1. Introduction

In this section, a facile, defect-free, and low temperature approach was utilized to intentionally dope CVD grown graphene films. To this end, 3-Aminopropyltriethoxysilane (APTES) and 1H,1H,2H,2H-Perfluorooctyltriethoxysilane (PFES) were used to modify the interface between transferred CVD graphene films and their supporting dielectric to create n-type and p-type graphene, respectively. APTES contains an amine functional group with a basic nitrogen atom having a lone electron pair. The electron-rich amine group donates an electron to the carbon atoms in graphene, causing n-doping. In contrast, fluorine is a well-known electron acceptor. Thus, adding a layer of PFES results in the transfer of an electron from the graphene creating p-type film. The purpose of the silane group is to create a strong covalent bond to the oxide dielectric support, such as SiO_2, thereby anchoring the APTES and PFES; this induces thermal stability of the modified interface and the doped graphene layer. X-ray photoelectron spectroscopy (XPS) and micro-Raman spectroscopy will be utilized to confirm that the obtained graphene is defect-free and that the dopant concentrations are indeed modulated by the APTES concentration on the substrate as well as the concentration of the adsorbed molecules and atmospheric dopants on the graphene. Figure 5.1 shows a schematic of APTES and PFES that contain amine and fluorine functional groups, respectively.

5.2.1.2 Methods

To functionalize the substrate with SAMs, a highly p-doped Si wafer with a 300 nm thick thermally grown layer of silicon dioxide was used. The reason for this is that a similar substrate will be used for the fabrication of back-gated graphene FET device.

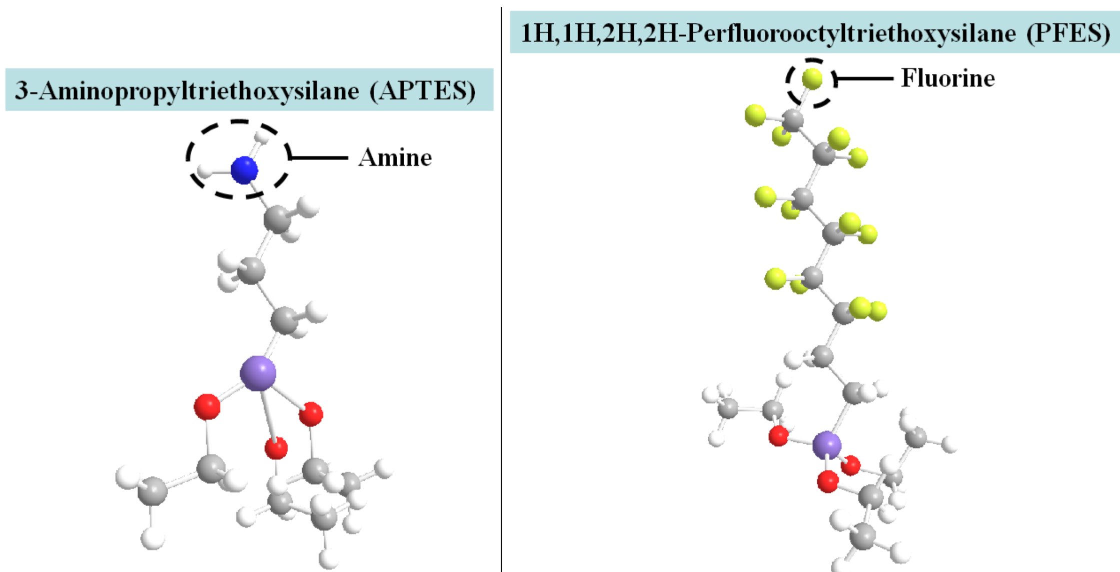

Figure 5.1. Schematic of APTES and PFES containing amine and fluorine groups, respectively.

For the APTES layer deposition, the substrate was first cleaned and pre-treated by UV ozone for 15 min in order to produce a hydroxyl-terminated substrate, known to react efficiently with silane-coupling agents such as APTES. Immediately after cleaning, the substrate was immersed in a 1%(v/v) solution of anhydrous toluene and APTES for three hours. The substrate was removed from solution, sonicated for 15 min in pure toluene, and dried under flowing nitrogen or argon. For PFES deposition, another device was used with a similar procedure. The only difference is that the treatment was performed for one hour with 10 microliters of PFES dissolved in 10 ml of toluene 1 %(v/v). The deposition of the SAMs was confirmed by contact angle measurements using a VCA 2000 goniometry system similar to the one explained in Chapter 3. The APTES coated surface had a measured contact angle with deionized (DI) water of ~ 60° [165] as compared to <10° contact angle measured immediately after the UV ozone cleaning treatment, indicative of coupling of the APTES monolayer to the surface.

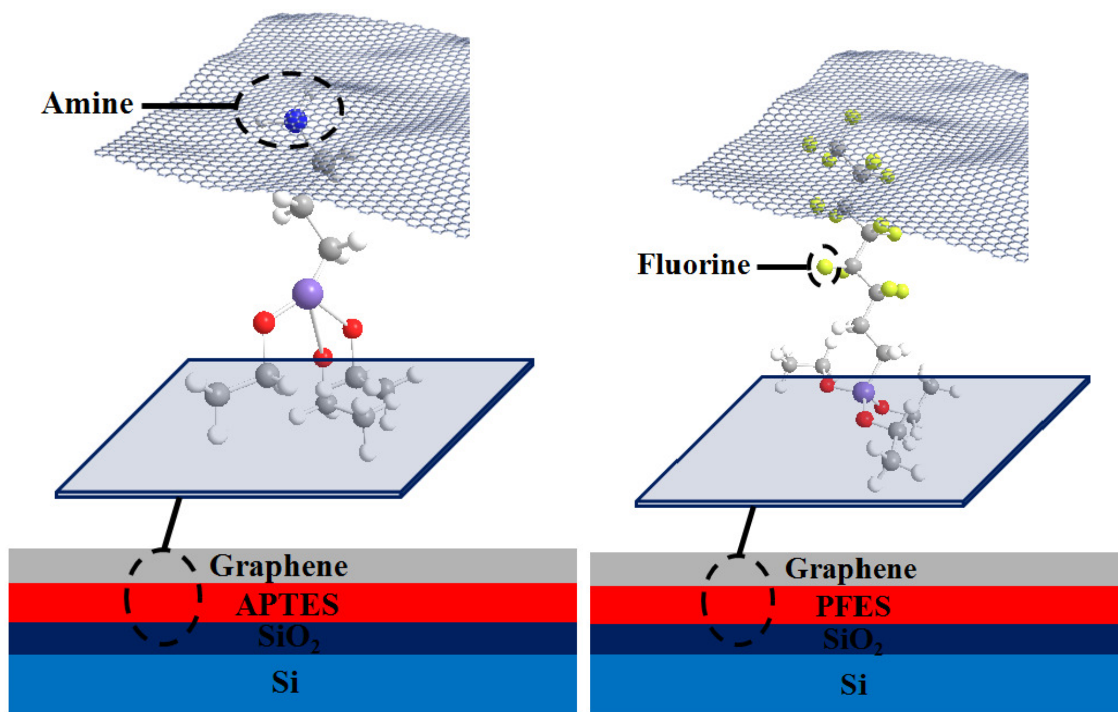

Figure 5.2. Schematic of (Left) APTES treated (Right) PFES treated SiO_2 substrate on highly doped Si for graphene FET device applications.

The measured contact angle for the PFES-treated substrate was c.a. 110°, indicative of a hydrophobic surface. Finally, CVD grown graphene was transferred on top of the pre-treated substrates containing SAMs (APTES or PFES) using a method similar to that explained in Chapter 3. In addition to SAMs treated substrates, control samples were also fabricated, consisting of CVD graphene transferred onto the cleaned SiO_2 coated silicon substrate. These control samples were utilized for collection of reference XPS and Raman spectra. Figure 5.2 shows a schematic of a highly p-doped Si/SiO_2 functionalized with APTES and PFES.

5.2.1.3 Verification of SAMs contain silane group on the substrate

X-ray photoelectron spectroscopy was employed to identify the surface functionalization present on graphene, graphene on the APTES treated substrate, and graphene on the PFES treated substrate, using a method similar to that explained in Chapter 3.

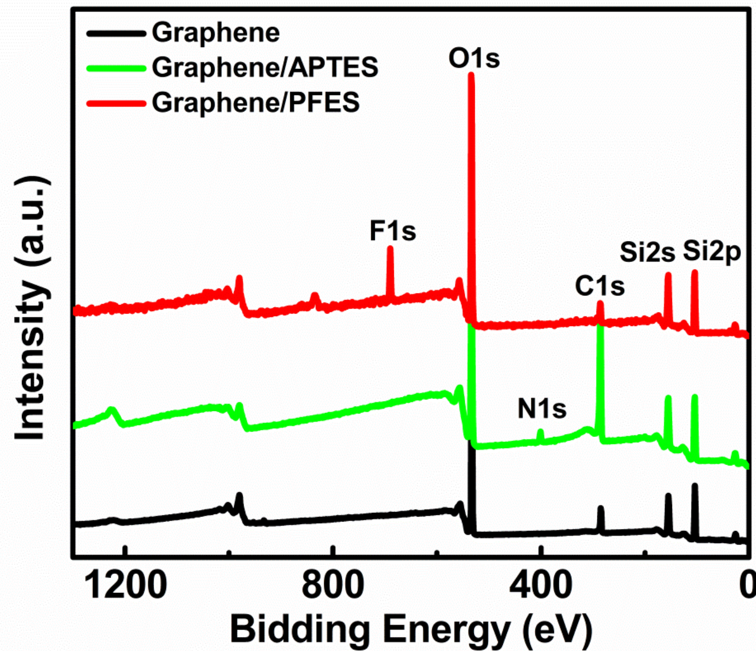

Figure 5.3. Survey XPS spectra for graphene (black), graphene/PFES (red) and graphene/APTES (green).

XPS data were acquired using a Thermo K-Alpha XPS (Thermoscientific) operating under ultra-high vacuum conditions with an Al Kα micro-focused monochromator. The survey scan spectra were collected at the binding energy (B.E.) of 0-1300 eV, with a step size of 1 eV and a spot size of 400 μm. Figure 5.3 shows survey scan spectra randomly collected from as-transferred graphene, functionalized with APTES, and with PFES. The scan showed the most prominent peaks to be C1s and O1s on all spectra. The appearance of a N1s peak centered at 399 eV and a F1s peak centered at 689 eV in the survey spectra confirms the presence of APTES and PFES underneath

the graphene, respectively. Lack of these peaks considering detection limit of F 1s (0.025%) and N 1s (0.06%) in XPS in the graphene without SAMs supports the conclusion that the APTES and PFES SAMs were successfully deposited onto the SiO_2 substrate.

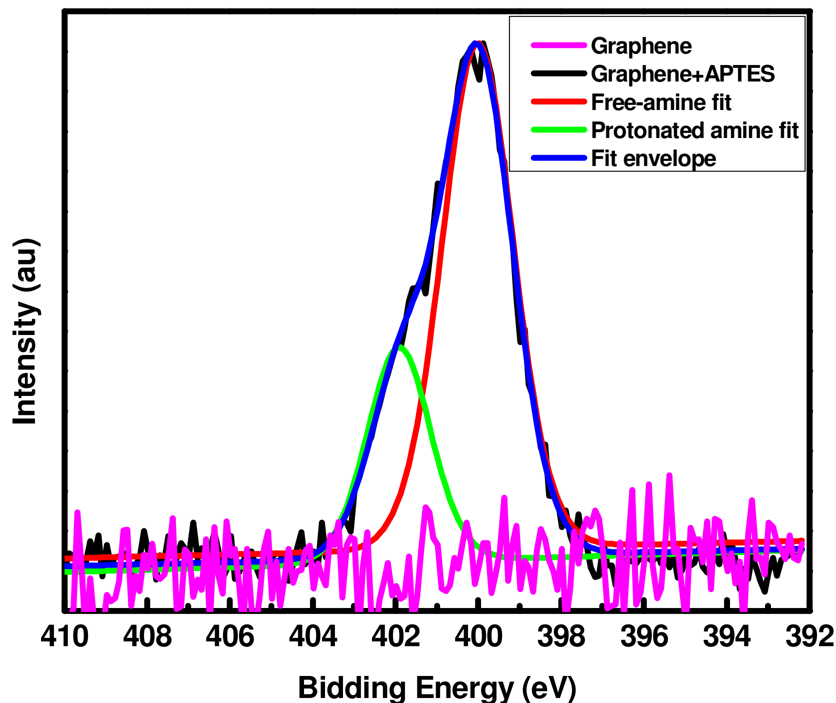

Figure 5.4. XPS spectra representing N 1s binding energy for graphene/ SiO_2 (black) and graphene /SAMs (red).

The N1s high resolution spectrum (see Figure 5.4) for regions containing APTES can be deconvoluted and fit with two peaks centered at 400 eV (representing 77% of the total N1s peak area) and 401.9 eV (representing 23% of the total N1s peak area), which can be assigned to free amine ($-NH_2$) and either a protonated ($-NH_3^+$) or hydrogen bonded amine, respectively [166-167]. The small amount of the nitrogen XPS signal assigned to the peak at 401.9 eV is likely due to protonated amine that results from the graphene

transfer process (e.g. from exposure to acid). According to N/Si peak intesity, surface coverage of APTES is ~ 95% with ~ 80% of the surface covered with free amine and the rest with protonated amine.

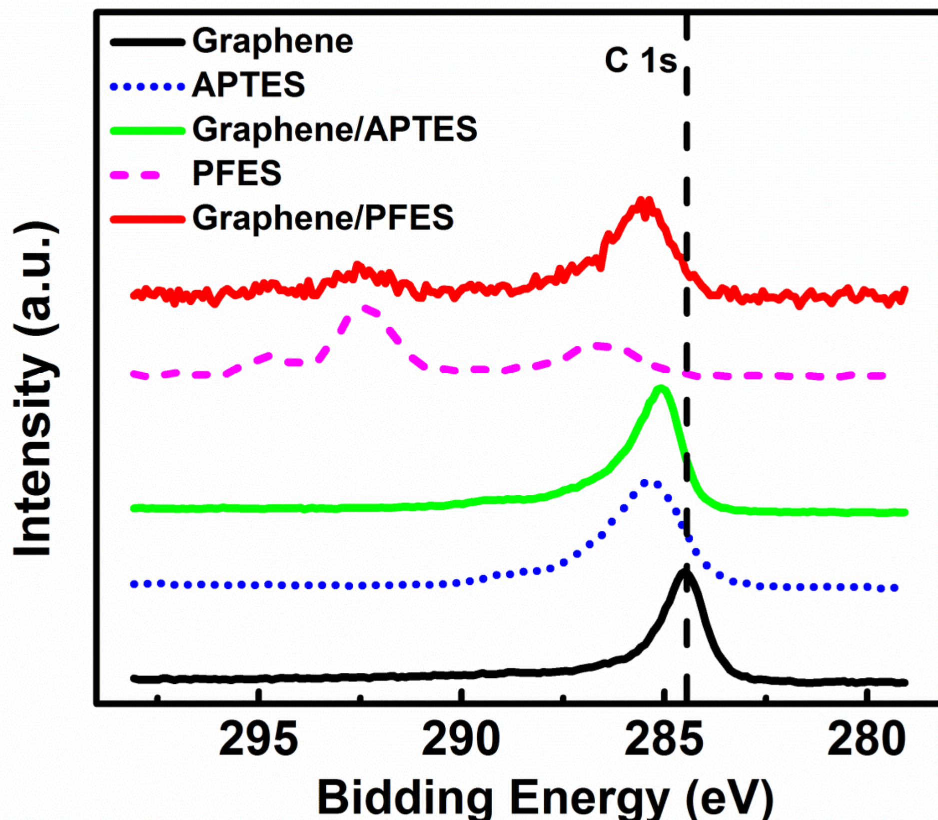

Figure 5.5. C 1s core level XPS spectra for graphene (black), graphene/PFES (red) and graphene/APTES (green).

High resolution XPS spectra of the C1s binding energy was also acquired over 282-293 eV with a step size of 0.1 eV. Figure 5.5 shows the chemical shifts in the high resolution C1s spectra for graphene (black), APTES (dark blue), and PFES (light blue) on bare SiO_2 as well as graphene on APTES (green) and PFES (red) treated SiO_2 substrates. We observe that for the APTES control sample the C1s peak maximum is found to be at a binding energy of 285.3eV. The shift in the C1s peak binding energy in the case of the

APTES layer away from that for simple hydrocarbons (i.e. simple hydrocarbon C1s peak locations are approximately 284.5 eV is attributed to the inductive effect of nitrogen atoms present in the APTES layer [168] and is in accord with previously reported data [169]. The C1s peak location for graphene on the oxide surface is at a binding energy of 284.5 eV and is typical of graphene measurements. The C1s peak in the graphene samples deposited onto the APTES coated oxide films (Graphene/APTES) is observed to reach its maximum at a binding energy of 285.1 eV, and appears to simply be the result of the superposition of the graphene and APTES C1s XPS spectra. Overall, the appearance of a shoulder and a shift in the C1s peak position of functionalized graphene also verified the presence of APTES and PFES on the substrate.

5.2.1.4 Doping verification using In-situ Raman spectra

As explained in Chapter 3, environmentally-induced water vapor and oxygen bound to the graphene are electron acceptors [82] that play an important role in the unintentional p-doping of graphene films. This unintentional doping of the graphene had to be removed in order to fully reveal the effects of the APTES and PFES on the graphene. To remove this unintentional doping effect, the samples were heat treated under vacuum or inert atmosphere to unmask the intentional doping effects of the APTES and the PFES underlying layer [89]. To this end, the samples were heated up to 200°C under nitrogen atmosphere between 5 and 180 minutes. In-situ Raman spectroscopy was utilized to investigate the quality of the graphene and its doping state by examining the D, G, and 2D bands and their positions. All spectra were excited with visible (532 nm) laser light and collected in the backscattering configuration with a laser power below 0.5 mW to avoid laser-induced heating [89]. A 50X objective lens was used to focus the laser on the graphene samples during the Raman measurements. The samples were placed inside

an environmentally controlled microscope stage with heating, vacuum, and gas delivery capability (Linkam TS 1500) for in-situ Raman measurements. The sample was heated up to 200°C under nitrogen atmosphere and held between 5-180 min to allow for desorption of atmospheric p-dopants bonded to the sample. Raman measurements were performed before and after the vacuum annealing step. Figure 5.6 (a) shows the Raman spectra of as transferred, APTES treated, and PFES treated graphene after 3 hours of vacuum annealing at 200°C. The difference in the G and 2D peak width, position, and intensity ratio for each sample is indicative of various doping states. A critical observation is that no increase on the D band was observed during any of the annealing steps; hence successful doping of the graphene monolayer without significant damage to the lattice structure was achieved [19, 169]. Monitoring of the G peak position with increase in heating time, its full width at half maximum FWHM(G), and intensity ratio of 2D over G peak (I_{2D}/I_G) reveal the changes in electronic state of various devices. A decrease in the G peak position of as-transferred graphene was observed after annealing for only 5 minutes. Further annealing resulted in a greater decrease in the peak position, leading to 1588 cm^{-1} after 3 hours of annealing. This indicates the de-doping process induced by the removal of the environmentally induced dopants through annealing [151]. An increase in FWHM(G) from 17 to 23 and I_{2D}/I_G from 1.685 to 1.7 confirms the removal of atmospheric p-dopant, leading to de-doped graphene after 3 hours of heat treatment. The G peak position of as-transferred graphene functionalized with APTES was 1590 cm^{-1}, and FWHM (G) was 14 cm^{-1}. FWHM(G) and I_{2D}/I_G values for graphene functionalized with APTES are lower than the corresponding values for graphene and this is indicative

of a reduction in p-doping state. The change in the G peak position is due to competing effects between n-doping induced by APTES and p-doping by water vapor and oxygen.

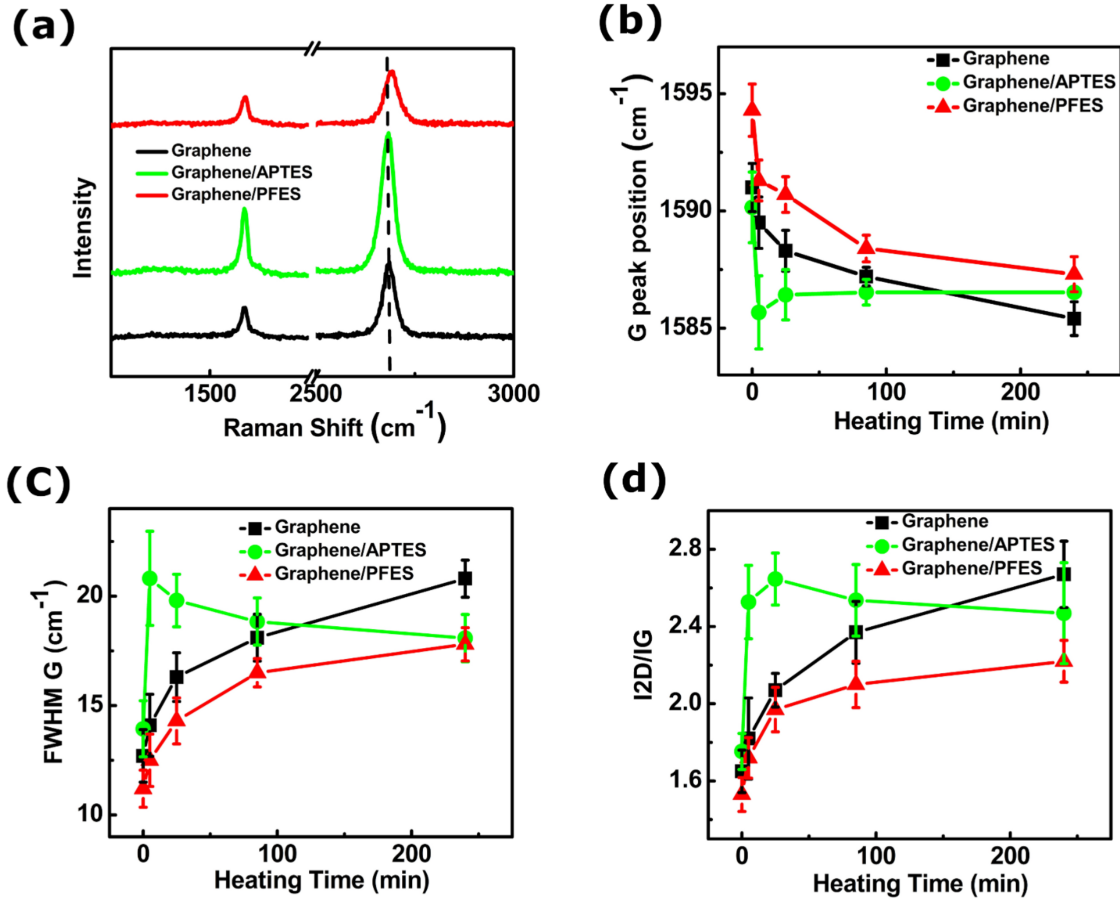

Figure 5.6. (a) Raman spectra of graphene (black), graphene/APTES (green), and graphene/PFES (red) after annealing at 200°C under nitrogen atmosphere for 3 hours. (b) G peaks position (c) FWHM (G) (d) $I_{2D/G}$ as a function of annealing time under nitrogen atmosphere for graphene (black), graphene/APTES (green), and graphene/PFES (red).

Similar to as-transferred graphene, heat treatment for 5 minutes resulted in the removal of p-dopants, leading to a decrease in G peak position down to 1585.5 cm^{-1}, and an increase in FWHM (G) to 21 and I_{2D}/I_G to 2.65. These values are similar to those measured for de-doped graphene. However, further heat treatment resulted in the removal of additional p-

dopants, causing the n-doping effect to become dominant. This led to an increase in the G peak position to 1586.5 cm^{-1} and a decrease in FWHM (Γ) to 20 and I_{2D}/I_G to 2.3, which is in accord with observed Raman characteristics for n-doped graphene.

The trend in Raman characteristics for PFES functionalized graphene is similar to that obtained with as-transferred graphene. A heavily p-doped characteristic before heat treatment is due to the presence of both PFES and atmospheric dopants from water vapor and oxygen. However, removal of atmospheric dopants by heat treatment for 3 hours results in lowering the p-doping level in the graphene with a 7 cm^{-1} decrease in the G peak position, 6 cm^{-1} increase in FWHM (G), and 0.7 increase in I_{2D}/I_G. The shift in the position of the G peak is indicative of induced doping by SAMs without a change in the structure of graphene.

5.2.1.5 Graphene FET device using SAMs contain silane group

To further demonstrate the n-type and p-type characteristics induced by APTES and PFES respectively in graphene, back-gated FET devices were fabricated on SAM treated SiO_2/highly doped Si as shown in Figure 5.2. Back-gated CVD graphene field effect transistors were fabricated using standard lithography and metallization techniques in conjunction with a solution-based self-assembled monolayer coating technique and a solution based transfer of CVD grown graphene. Another set of devices was fabricated without SAMs as control devices. Transport in the APTES- and PFES-treated graphene devices as well as the devices without SAMs was measured using a probe station equipped with an HP 4156 semiconductor parameter analyzer under a nitrogen atmosphere. The measurements were performed, on as-made devices and again after heat treatment in the inert atmosphere, to verify the de-doping through removal of

atmospheric dopants and n- and p-doping through APTES and PFES modifications. Figure 5.8 and Figure 5.9 show the schematic of de-doping by heat treatment and unmasking the n- and p- doping effect induced by APTES and PFES, respectively. All as-made devices demonstrated p-type characteristics, due to the dominant p-doping effect caused by unintentional p-dopants from air exposure. A gradual decrease in the charge neutrality point was observed in the device without SAMs modification, due to heat treatment up to 200°C under the nitrogen atmosphere. After 3 hours of annealing, the charge neutrality was around zero volts, indicative of de-doped graphene.

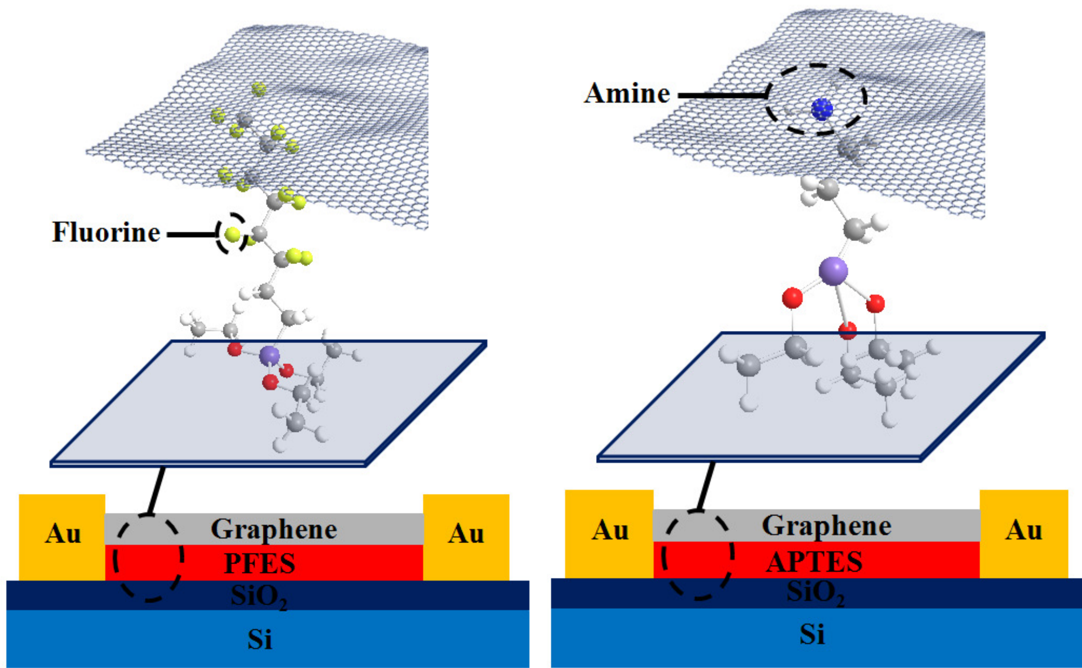

Figure 5.7. Schematic of back-gated APTES and PFES-treated devices.

For the APTES treated device, n-doping characteristics were observed with the charge neutrality point (CNP) stably forming at c.a. -20 V after 3 hours of heat treatment at 200°C (see Figure 5.10). On the other hand, for the PFES treated device, p-type behavior was observed with the charge neutrality point stabilizing at c.a. 22 V after 3 hours of annealing at the same environment (see Figure 5.11)

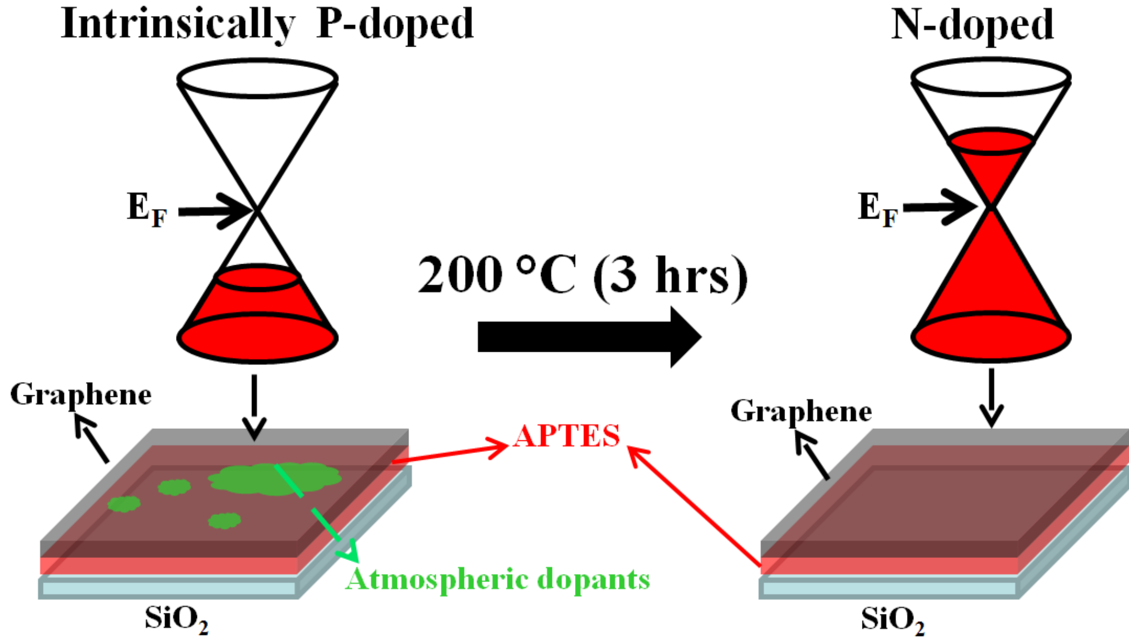

Figure 5.8. Schematic of atmospheric p-dopants removal shows unmasking of n-doped graphene FET device induced by APTES.

Several APTES and PFES-treated devices were fabricated, and similar results were obtained for each set of devices. Unlike the sample without SAMs, intentional doping by APTES and PFES was shown to be thermally stable, as there was no change in the neutrality point after removal of the atmospheric dopants via thermal annealing in nitrogen. The electron and hole concentration of the APTES and PFES-treated graphene after annealing was approximately 2×10^{12} cm^{-2} for both devices. These values were calculated using a method similar to that explained in Chapter 4 using the equation, $n = C_g V_{NP}/e$ [90, 139], where $C_g = 115$ $aF/\mu m^2$, [139] e is the charge of the electron and V_{NP} is the voltage at the charge neutrality point.

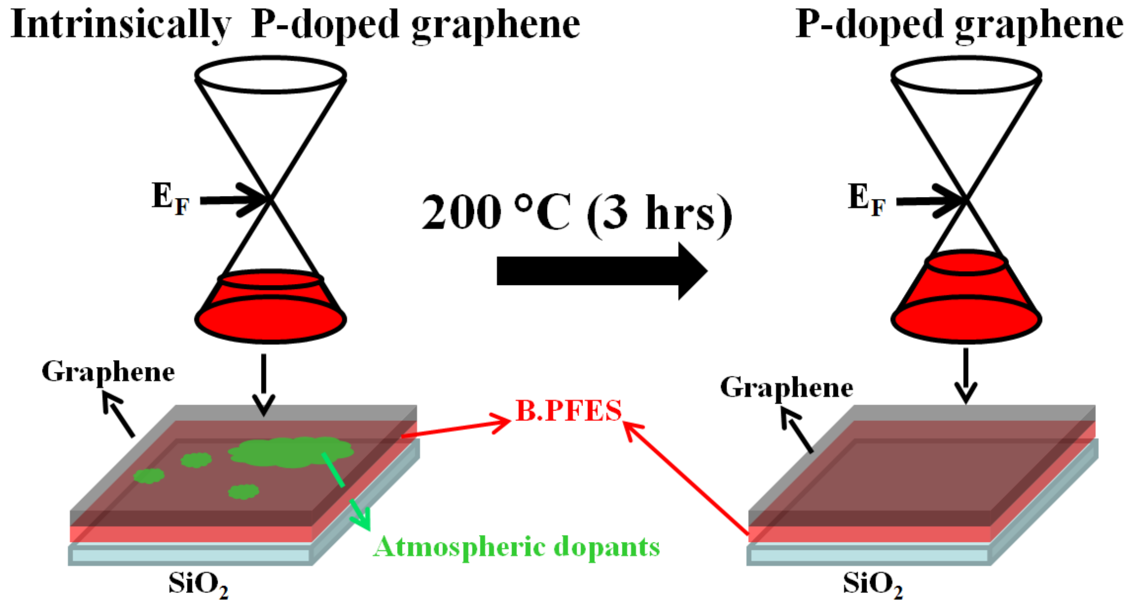

Figure 5.9. Schematic of atmospheric p-dopants removal shows unmasking of p-doped graphene FET device induced by PFES.

Both electron and hole field-effect mobilities for the APTES and PFES-treated graphene after annealing were approximately 217 cm^2/Vs and 412 cm^2/Vs, respectively. The electron and hole mobilities for graphene devices without SAMs are of the same order of magnitude. These values are extracted using the relation $\mu_{FE} = L_{ch}g_m/W_{ch}V_{D/s}C_g$, where L_{ch}= 2000μm, g_m=dI_D/dV_{GS} , W_{ch}= 50μm , $V_{D/S}$= .1V and Cg=115 aF/μm2, [89] indicating that the SAMs has no effect on the mobility of graphene devices [117, 162, 170]. The slight difference in the mobility and the minimum current of APTES and PFES-treated devices can be due to the differences in the transferred graphene that originate in varying grain size or in the transfer process of CVD graphene.

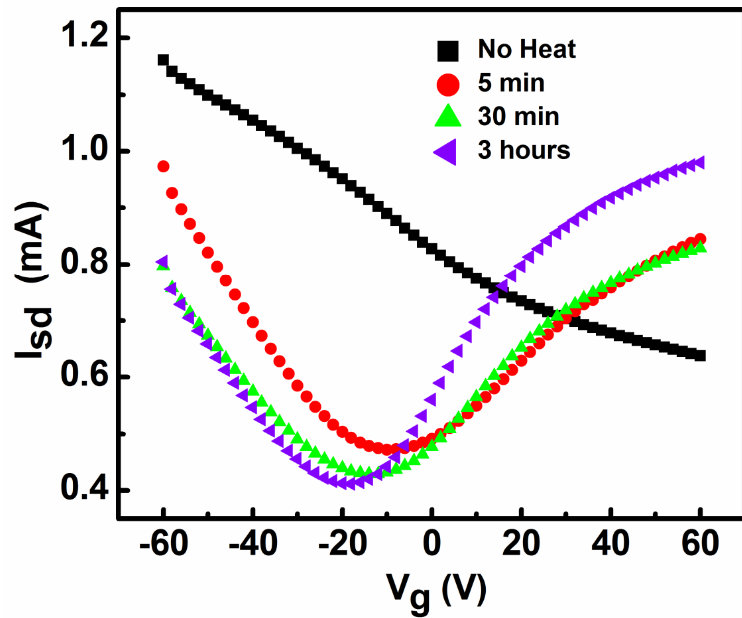

Figure 5.10. Source-drain current versus gate voltage for different device heating times at 200°C for simple graphene FET devices fabricated using an APTES coated gate dielectric.

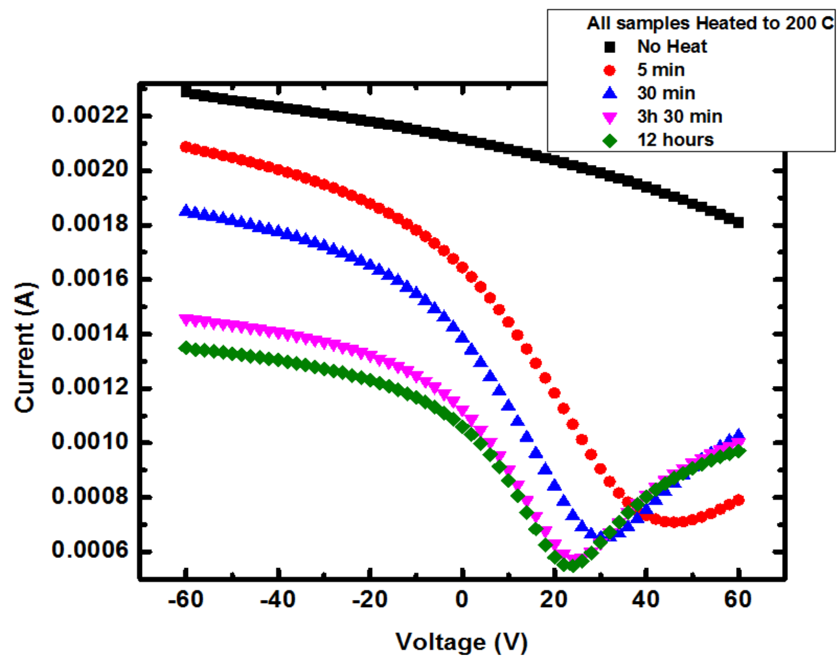

Figure 5.11. Source-drain current versus gate voltage for different device heating times at 200°C for simple graphene FET devices fabricated using a PFES coated gate dielectric.

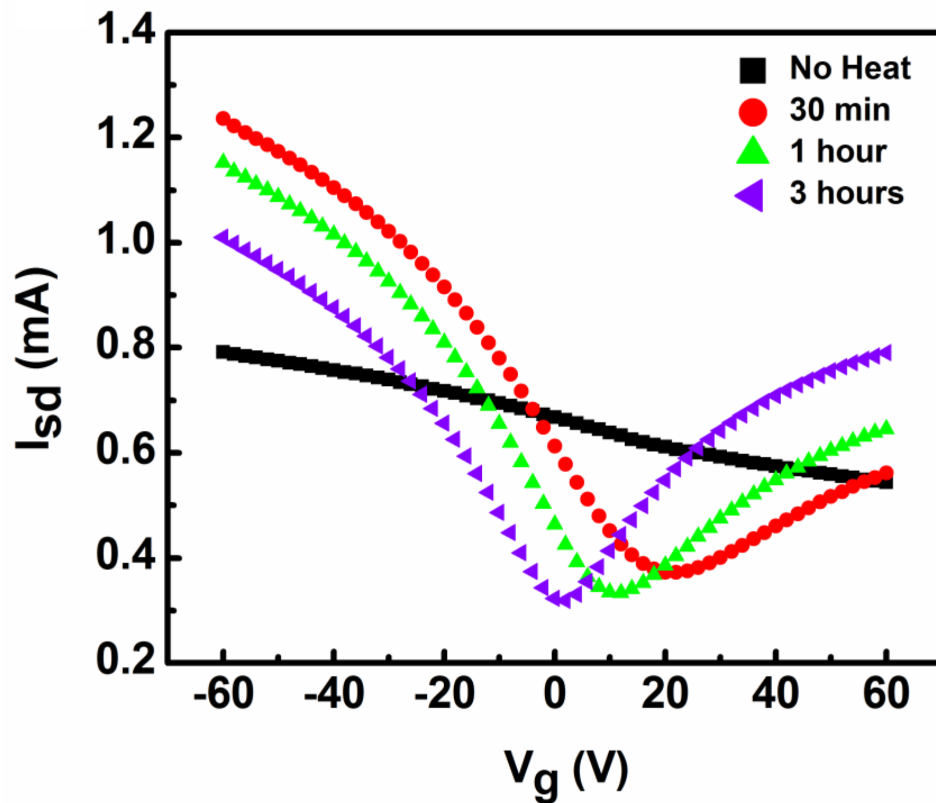

Figure 5.12. Source-drain current versus gate voltage for different device heating times at 200°C for simple graphene FET devices fabricated using a simple SiO_2 gate dielectric.

It is noteworthy that further annealing for up to 7 days did not cause a change in the neutrality point. This is in contrast with the observed n-type characteristic of graphene due to annealing in a nitrogen atmosphere, as we saw no evidence of n-type doping in these samples [171]. In addition to using this strategy of depositing the amine layer to introduce controlled modulation of the doping profile in the device channel, it is also of course possible to modulate the amount of free amine on the substrate by changing the time or solution concentration conditions used to deposit the amine. This modulation of the amount of APTES on the dielectric surface can in turn be used to modulate the doping level in the devices.

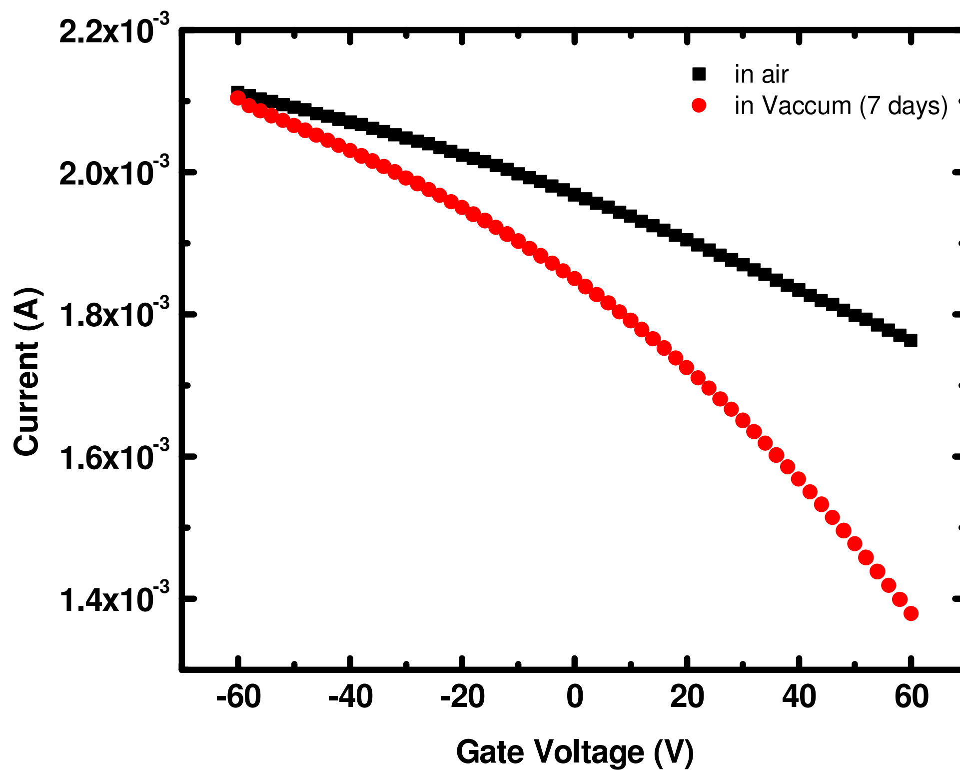

Figure 5.13. Shows source-drain current versus gate voltage as a function of heat treatment and pump down time; this indicates no significant change in the neutrality point even after 7 days without having SAMs.

To demonstrate this, the APTES deposition time was varied between 1 and 7 hours for devices made with the unpatterend APTES layer covering the entire device channel. Figure 5.14 shows the carrier concentration measured in the graphene devices along with the nitrogen to silicon ratio (N/Si) obtained by XPS in each of these samples as a function of APTES deposition time.

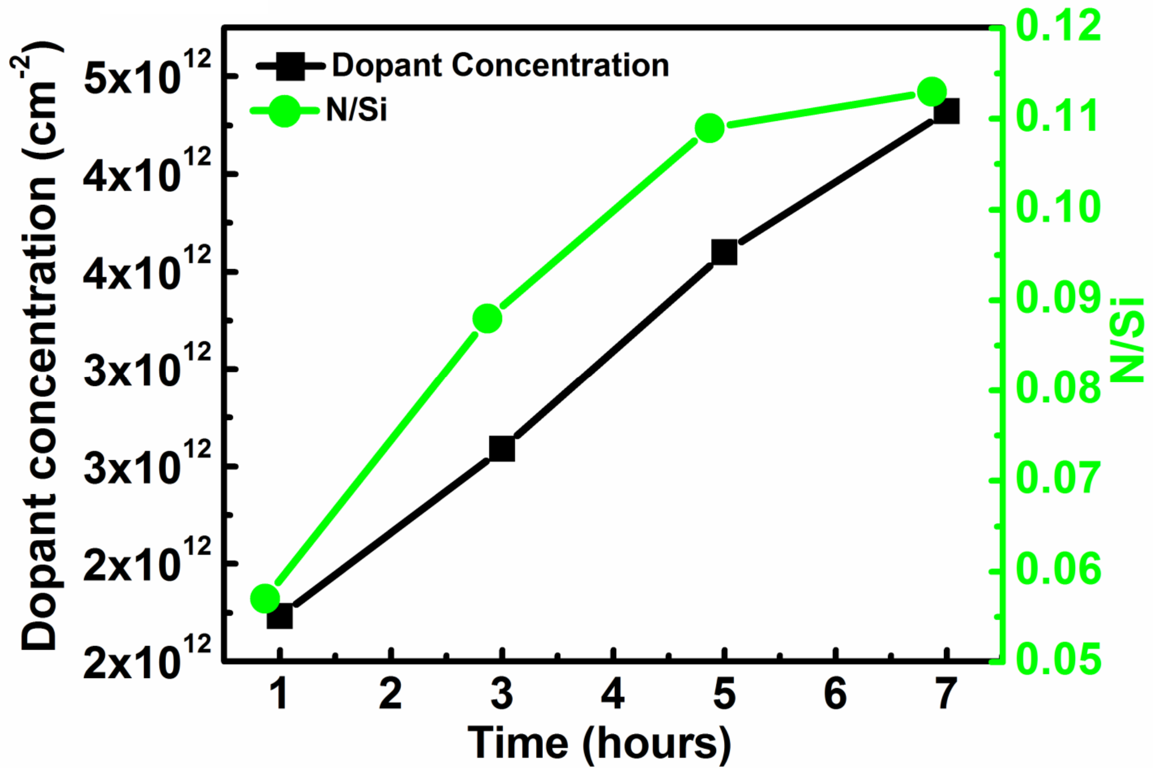

Figure 5.14. Dopant concentration and Nitrogen/silicon (N/Si) ratio versus APTES deposition time.

Clearly the carrier concentration is observed to scale roughly with APTES deposition time over the range of APTES deposition times measured. One would expect this behavior to saturate at some point once a sufficiently dense and thick enough APTES layer is formed such that no further electronic influence on the graphene film is observed by further deposition of APTES. Carrier concentrations in excess of 4.5×10^{12} cm^{-2} were observed in the devices measured, corresponding to a CNP change above -60 V (see Figure 5.15).

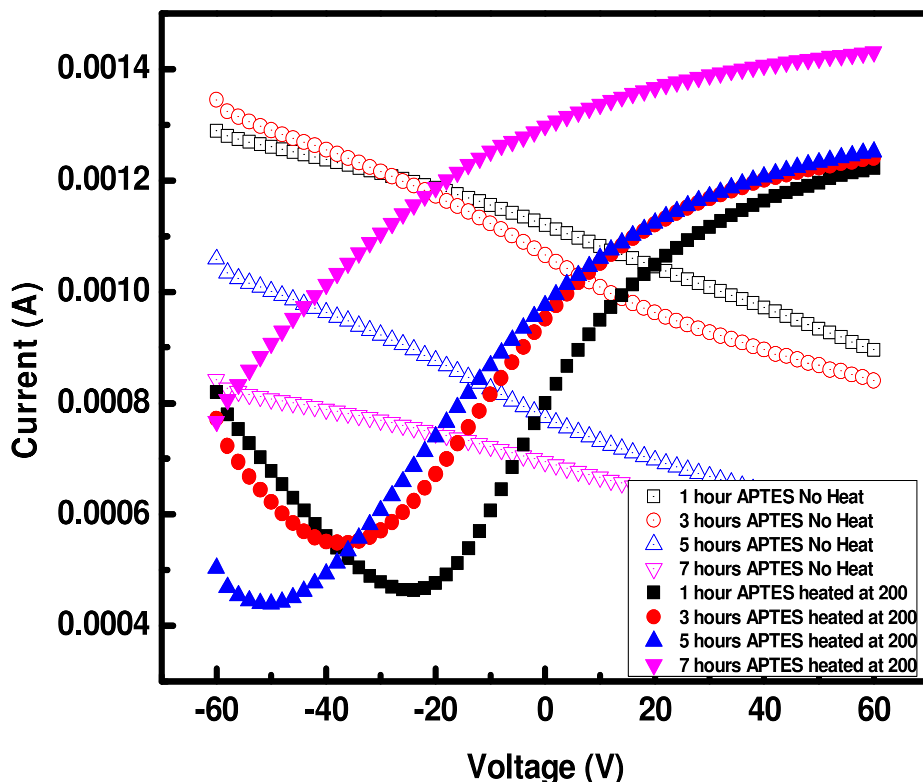

Figure 5.15. Drain-source current versus gate voltage as function of different APTES treatment times.

5.2.2. Interface modification using phosphonic acids (PAs)

5.2.2.1. Introduction

A variety of applications of SAMs to electronic devices have been investigated [172-173]. Of particular interest among their findings is that the dipoles of SAMs molecules change the Schottky barriers between metals and organic semiconductors [174-175]. The dipole alignment of the SAM molecules is thought to produce a built-in electric field and thereby modify the carrier [110, 112]. Kobayashi et al. demonstrated that by changing the SAMs molecules, the channel carrier density in the organic field-

effect transistors can be controlled by effects of molecular dipoles and weak charge transfer. In this section, we attempt to utilize phosphonic acids (PAs) with a different dipole alignment as interface layer between graphene and the substrate to modulate the work function of the film. The existence of a large dipole in the phosphonic acids (PAs) should result in a p- and n- type graphene FET. 2,6-difluorobenzylphosphonic acid (oF2BPA) and 4-trifluoromethylbenzylphosphonic acid (pCF3BPA) were used for this purpose. The fluorination pattern is a key in the expected dipole effect on the substrate. Both pCF3BPA and oF2BPA have fluorine as electronegative groups that result in an overall charge on the phosphonic acids. The fluorine groups are away from the substrate in pCF3BPA; this creates a positive charge close to the substrate and a negative charge away from the substrate. Therefore, it will be hard to inject the electrons from the substrate. However, in oF2BPA fluorine groups are close to the surface and result in negative charge on the surface, leading to an easier injection of electrons off the substrate. Figure 5.21 shows the schematic of various PAs with different dipole alignments.

5.2.2.2. Methods

Treatment of the surface with PAs was performed in a fashion similar to the methods explained in the literature [176]. Briefly, 1.0 mM phosphonic acid solution was prepared freshly in ethanol, and stored in amber bottles. The substrates were immersed in the solutions at room temperature. After couple of hours, the samples were removed, immediately rinsed with ethanol and were then sonicated for 10 min in triethylamine 5%v/v in ethanol. Then, samples were rinsed with ethanol and blown dry with nitrogen as the last step. The process of functionalizing the substrate with PAs was characterized with XPS similar to the method explained earlier in section 5.2.1.3.

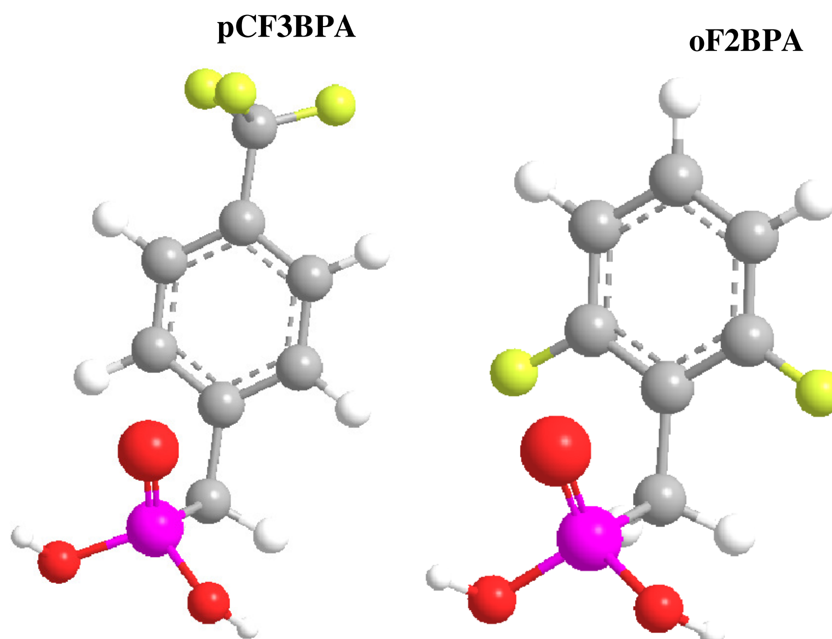

Figure 5.16. Schematic of (Left) 4-trifluoromethylbenzylphosphonic acid (pCF3BPA) phosphonic acids (PAs) with fluorine orientation looking up and (Right) 2,6-difluorobenzylphosphonic acid (oF2BPA) with fluorine orientation looking down.

Similar to APTES and PFES treatment, a graphene-based back-gated FET device was fabricated to test for a p- and n-type behavior. Unlike APTES and PFES, Al_2O_3 was used as a dielectric for back-gated FET device. This is because PAs bond better to the phosphonic acids (PAs). To this end, highly doped Si wafer was coated with 2 nm thick layer of Aluminum using E-Beam evaporation at vacuum pressure of 10^{-6} Torr. This thin layer of Al oxidized upon exposure to air, which enhances bonding sites on the substrate for improved quality of Al_2O_3 deposition using Atomic Layer Deposition (ALD) tool. The Cambridge Fiji Plasma Thermal ALD system was used for this purpose to deposit pin-hole free films in ultra-high aspect ratio features. Film thickness was c.a. 200 nm and deposition was performed at 250°C. Figure 5.17 shows a schematic of the back-gated FET device functionalized with PAs, where a 200 nm thick layer of Al_2O_3 was used as the gate dielectric.

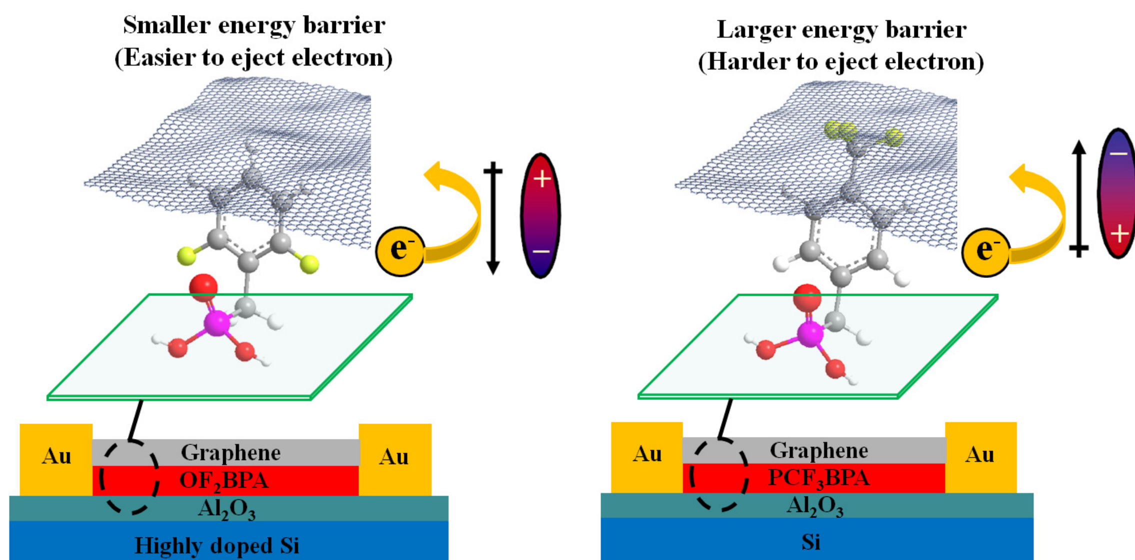

Figure 5.17. Schematic of a back-gated graphene FET device functionalized by (Left) oF_2BPA and (Right) pCF_3BPA before transfer of CVD graphene.

5.2.2.3. Verification of PAs on the substrate

To verify the presence of phosphonic acids on the substrate, X-ray photoelectron spectroscopy (XPS) was utilized. XPS data were acquired using a spectrophotometer (VG Scientific ESCALAB 210) with an Al $K\alpha$ X-ray source ($h\upsilon = 1486.68\,eV$). The measurements were examined on multiple spots on each sample. XPS measurements were conducted on a bare Al_2O_3 substrate that had been taken through the graphene transfer process and on Al_2O_3 substrates that were treated with PCF_3BPA and OF_2BPA. The survey scan spectra were collected over the binding energy (B.E.) range of 0-750 eV with a step size of 1 eV at a pass energy of 200 eV and a spot size of 400 μm. Figure 5.18 shows survey scan spectra of the PAs treated Al_2O_3 substrate. The major peaks are corresponding to C1s and O1s that are indicative of graphene and oxide substrate. A clear presence of F 1s peak on OF_2BPA and PCF_3BPA is indicative of successful treatment with these groups.

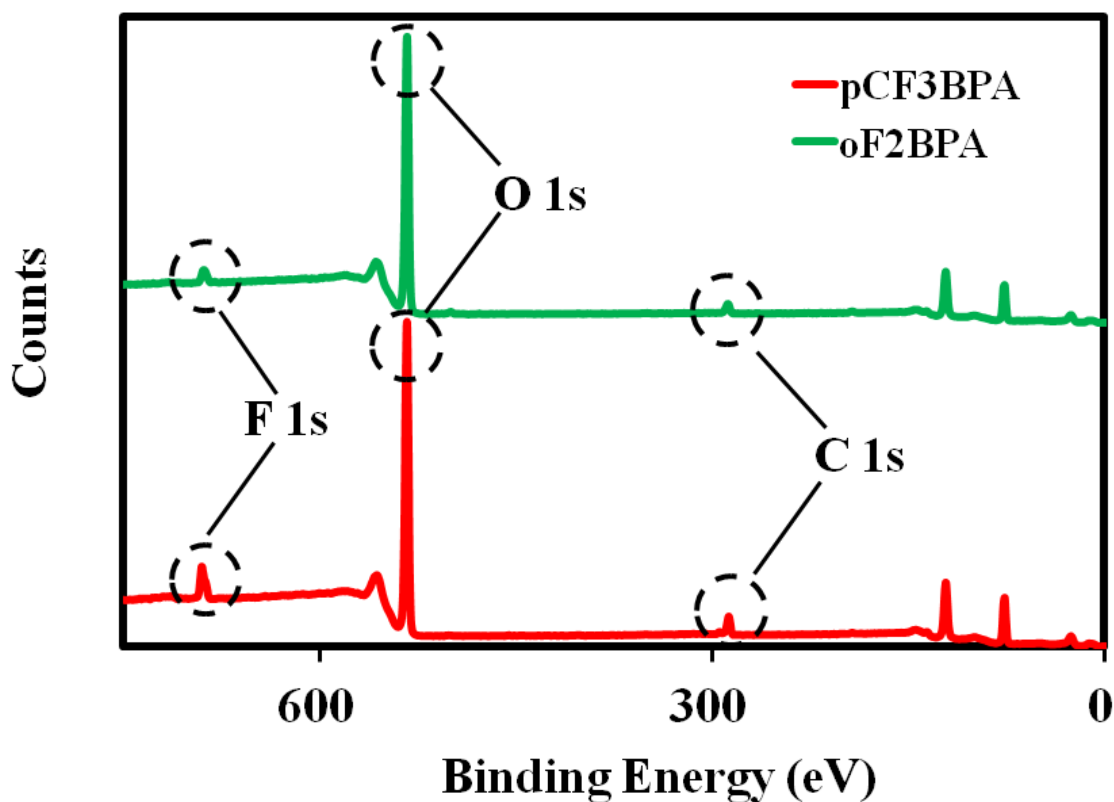

Figure 5.18. XPS survey spectra that show the presence of F 1s indicative of successful treatment with OF_2BPA and PCF_3BPA.

Core level spectra were acquired to further analyze various chemical groups on the substrate. Figure 5.19 (Top) shows a core level C1s peak acquired on bare Al_2O_3, and oF_2BPA and pCF_3BPA treated Al_2O_3. The appearance of a shoulder in the C1s peak for core oF_2BPA and for pCF_3BPA treated Al_2O_3 is indicative of the presence of fluorine on the substrate. Comparison of the core level F1s peak on oF_2BPA and pCF_3BPA treated Al_2O_3 with bare Al_2O_3 confirm the presence of fluorine on the functionalized substrates.

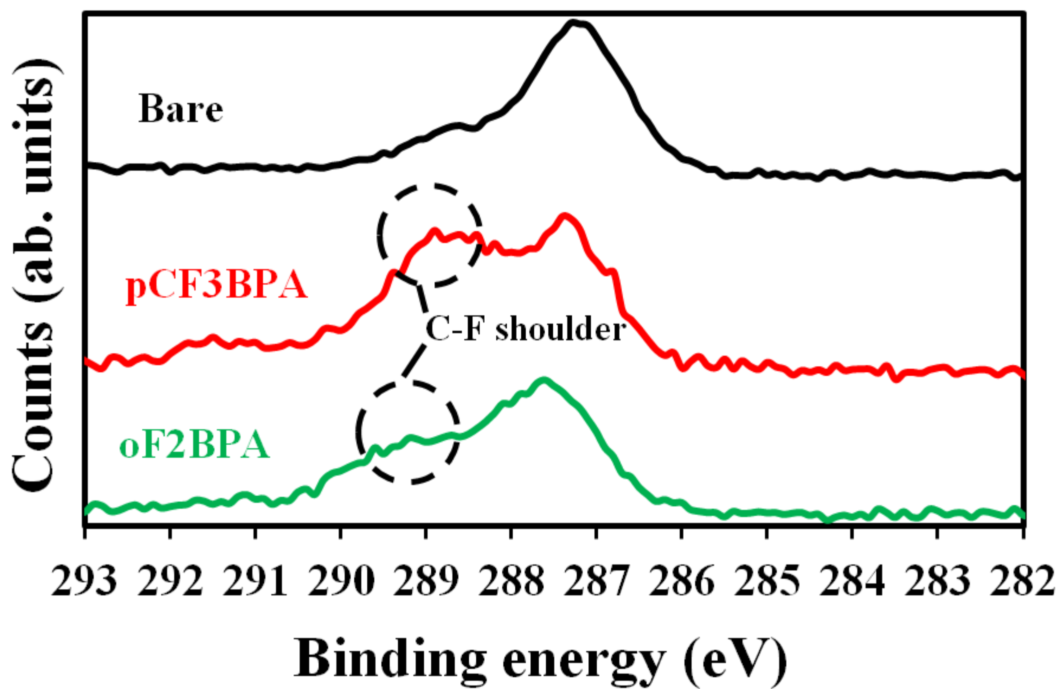

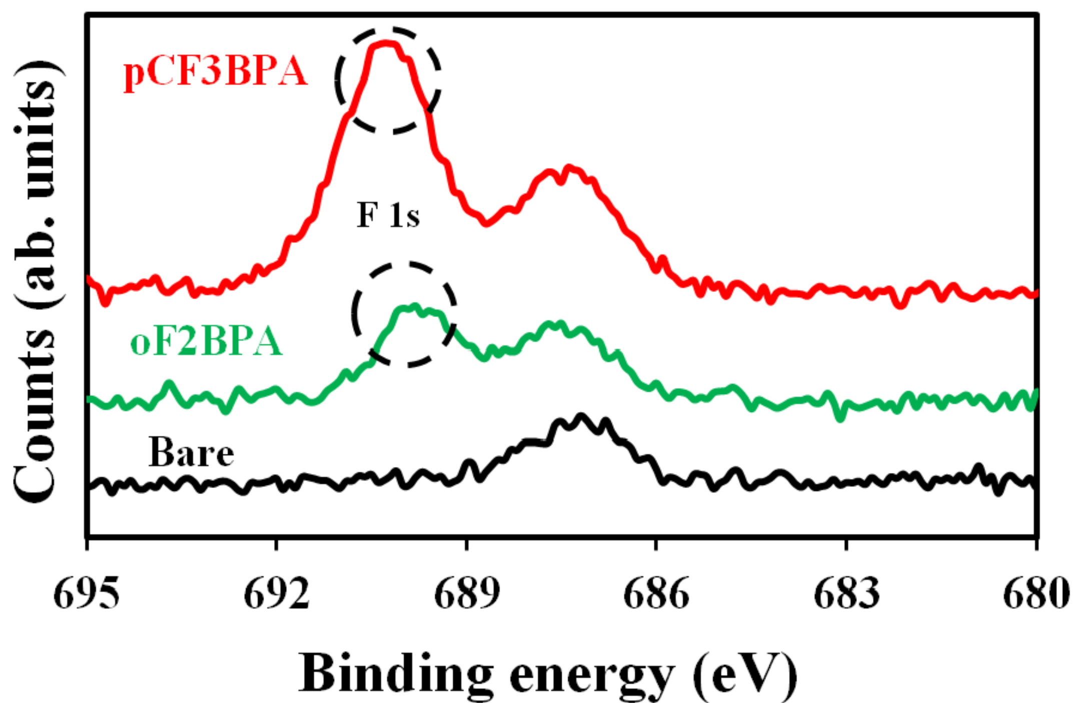

Figure 5.19. Core level (Top) C 1s spectra and (Bottom) F 1s spectra acquired on bare Al_2O_3, and oF_2BPA and pCF_3BPA treated Al_2O_3.

5.2.2.4. Electrical data measurements on back-gated FET functionalized with PAs

To understand the effect of surface treatment with phosphonic acids on the electronic properties of graphene, back-gated field effect transistors devices were fabricated as explained in section 5.2.2.2. Figure 5.17 shows a schematic of these devices. Electrical measurements were performed similar to back-gated devices with SiO_2 as gate dielectric. Figure 5.20 shows source-drain current vs. gate voltage graphene, graphene/oF_2BPA, and graphene/pCF_3BPA FET. All devices are significantly p-doped before annealing, due to the presence of atmospheric dopants as explained in Chapter 4. After annealing at 200°C for 12 hours, the Dirac point for the graphene device had gone to almost zero. This is indicative of p-dopant removals by annealing as explained in Chapter 4. However, unlike devices with SiO_2 as gate dielectric, Al_2O_3 devices require an excess amount of annealing for atmospheric dopant removal. It is believed that the bonding mechanism/adsorption nature of atmospheric dopants on SiO_2 might be different than Al_2O_3.

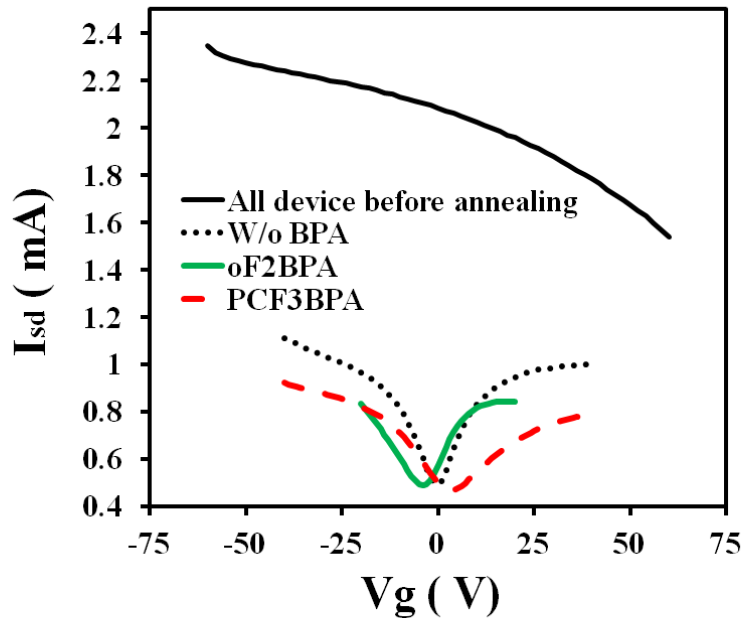

Figure 5.20. Source-drain current versus gate voltage heated at 200°C for 12 hours as a function of gate voltage for graphene, graphene/oF_2BPA, and graphene/pCF_3BPA FET.

As expected, the Dirac point for the graphene/oF_2BPA sample was around -5 V and that for a sample of graphene/pCF_3BPA was around 5 V. This is indicative of n- and p- doping induced by oF_2BPA and pCF_3BPA on graphene film. The enhanced shift in APTES and PFES treated devices is partially due to low dielectric capacitance in SiO_2 compared to Al_2O_3. In addition, oF_2BPA and pCF_3BPA are monolayers, in contrast to APTES and PFES, which contain multi layers of those chemicals.

5.3. Graphene p-n junction using SAMs

5.3.1. Introduction

Most graphene junctions to date have been fabricated using multiple electrostatic gates, [122] electrical stress-induced doping, [125, 177] chemical treatment by gas exposure, [126] chemical modifications on top of the graphene, [127, 171, 178] and modification of the substrate by changing the local electrostatic potential in the vicinity of one of the contacts [34]. However, current methods for electrostatic gating require a number of fabrication steps that may not be easily scalable to industrial levels, and that are usually expensive. In addition, chemical doping on top of graphene can degrade the carrier mobility in the device by introducing defects and impurities in the graphene. In addition, physisorbed dopant molecules are not stable and may desorb, resulting in changes in the electronic properties of the graphene.

In this section, we utilize the approach explained in section 5.3.1 to pattern a graphene FET channel containing a thin layer of SAMs in selected regions for formation of p-n junctions. Section 5.3.2 will utilize APTES as n-dopant and PFES as p-dopant, while section 5.3.3 will utilize APTES as n-dopant with intrinsically p-doped CVD graphene.

5.3.2. P-N junction through intentionally n- and p-doped graphene

As explained earlier in this chapter, interface modification with APTES and PFES can result in formation of n- and p- type graphene FET devices. A graphene p-n junction will be obtained by patterning both modifiers on the same dielectric and will be verified through the creation of a field effect transistor (FET). Characteristic I-V curves will be utilized to indicate the superposition of two separate Dirac points, which confirms an energy separation of neutrality points within the complementary regions. This method will minimize doping-induced defects and will result in thermally stable graphene p-n junctions for temperatures up to 200°C.

5.3.2.1 Fabrication method

The fabrication of the graphene p-n junction is schematically illustrated in Figure 5.21. First, the source and drain contacts (gold 50 nm thick) were defined using conventional electron-beam lithography and lift-off processes on a highly p-doped Si substrate with a 300 nm thick SiO_2 layer to create back gated field effect transistor structures, using a method similar to that explained in section 5.2. The resulting channel size is 50 μm by 1 mm. APTES was deposited on half of the channel using the solution processing sequence described in section 5.2. Next, half of the channel in the FET device was patterned with photoresist. After development, the other half of the channel was treated with UV-Ozone for 15 minutes to remove the exposed APTES and produce a hydroxyl-terminated surface. PFES treatment of the other half of the channel was performed using the solution processing sequence described in section 5.2. Finally, the resist was removed to expose the APTES coated region prior to transfer of graphene on top of the SAMs coated SiO_2.

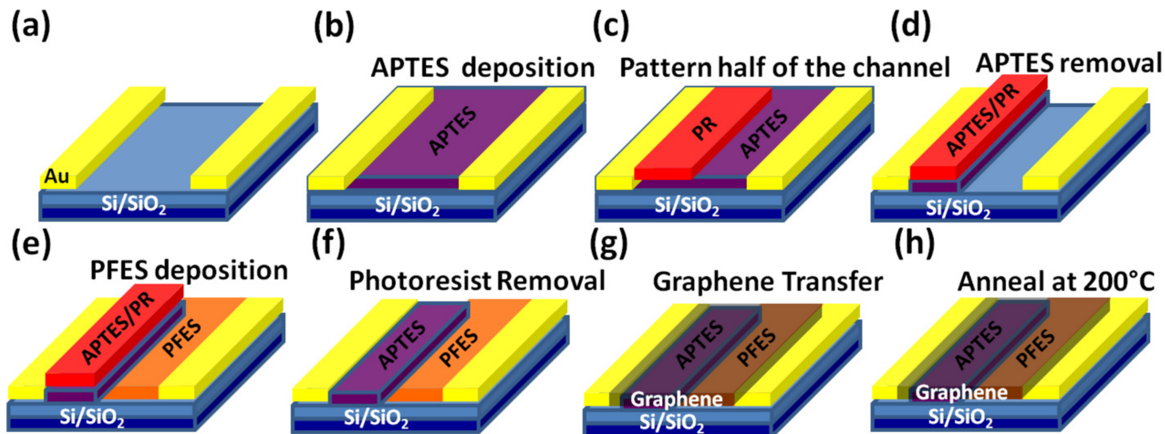

Figure 5.21. Schematic of the graphene p-n junction fabrication steps using APTES and PFES.

5.3.2.2 Characterization

Contact angle measurements and X-ray photoelectron spectroscopy were performed on both the APTES and the PFES-treated sides of the channel, and results similar to those explained in section 5.2 were obtained. To ensure the presence and formation of the patterned SAMs on the channel, XPS mapping was utilized [see Figure 5.22]. XPS mapping was performed using a 30 micron spot size with a step size of 28 microns, and a Gaussian smoothing algorithm (Thermo scientific) was applied to the raw data.

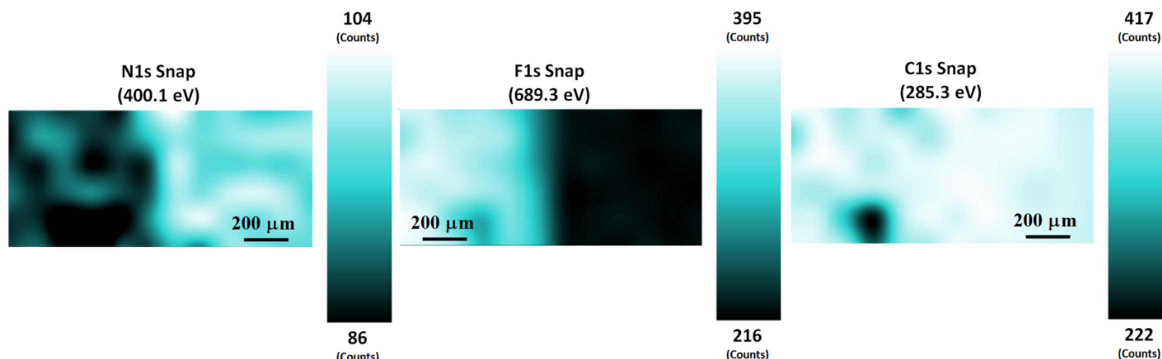

Figure 5.22. (Left) N1s binding energy centered at 400.1 eV and (Middle) F1s binding energy centered at 689.3 eV. (Right) C1s binding energy centered at 285.3 eV.

Figure 5.22 (Right) shows the intensity of the N1s map with a well-defined boundary that indicates the presence of amine only on half of the channel. Similarly, the F1s map indicates the presence of fluorine in the other half of the channel. For the core level C1s mapping, a binding energy centered at 285 eV was selected.

5.3.2.3 Electrical data measurements

Electrical data measurements were performed on fabricated p-n junctions in a nitrogen atmosphere using a method similar to that explained earlier. As-fabricated devices indicated p-type characteristics due to excess amount of atmospheric dopants.

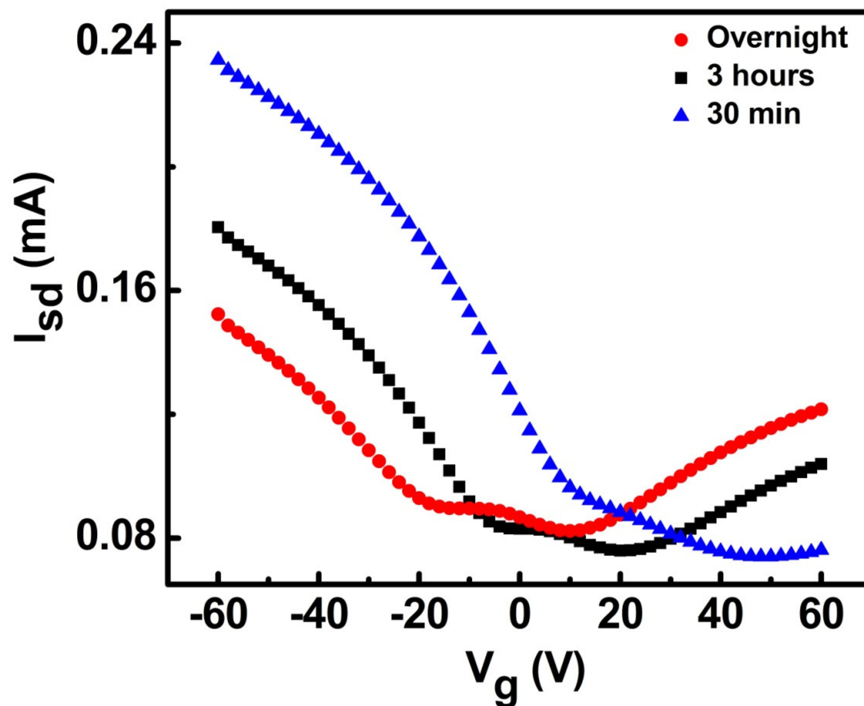

Figure 5.23. Drain-source current versus gate voltage for a graphene p-n junction measured after different annealing time. Both APES and PFES were used for surface modification.

After annealing at 200°C for 5 minutes a shift in the charge neutrality point to lower values was observed that indicated removal of atmospheric dopants. Further annealing provided control of the position of the junction until the neutrality point for the p- side of the channel was reached. When the annealing time increased to 3 hours, two Dirac points (peaks) were seen in the I-V curve: one located at V_{NP} = 20 V and the other at V_{NP} = −5 V. Figure 5.23 shows an I-V characteristic curve of the device, showing the superposition of these two separate Dirac points, which indicates an energy separation of neutrality points within the complementary regions. Annealing overnight resulted in a sharp p-n junction behavior with two neutrality points located at VNP = 10 V and VNP = -18 V. The amount of free amine and fluorine available on the substrate can be tuned by varying the APTES and PFES deposition time to fully control the transport behavior of the fabricated p-n junction.

5.3.3. p-n junction with intentionally n-doped and intrinsically p-doped graphene

In the process presented in this section, intrinsically p-doped CVD graphene that is obtained as a result of the particular transfer process, as explained in Chapter 4, [179] and that is utilized to deposit graphene onto the FET devices provides the basis for the opposite doping required to form a p-n junction in combination with the use of the APTES layers. Upon heating the fabricated device under an inert atmosphere, the intrinsically p-doped graphene is de-doped in a controllable manner, resulting in a dopant concentration profile that leads to formation of a p-n junction.

5.3.3.1 Fabrication method

Back-gated graphene-based p-n junctions with patterned p-n regions in the FET channel were fabricated and measured following the same basic process described in section 5.3.2. The difference here is that only one half of the channel was modified with APTES.

Figure 5.24 illustrates the fabrication steps involved in making the patterned p-n junctions in the FET channel devices using this method. Considering the similarity between this fabrication process and the one described in the previous section, we mention the important fabrication steps for the clarity purpose. The lithography and deposition processes (i.e. typical lift-off procedures) were used to form the gold electrodes on the 300 nm thick SiO_2 gate dielectric films on highly p-doped silicon wafers. Then, half of each of the channels in the FET devices were patterned with photoresist and hard baked. The device samples were then treated with APTES using the same solution processing sequence described earlier to deposit APTES in the half of each device channel that was not protected by hard-baked photoresist. The photoresist was removed by placing the devices in N-methylpyrrolidone (NMP) for 1 hour, followed by further sonication in acetone and inspection by optical microscopy to ensure removal of all photoresist.

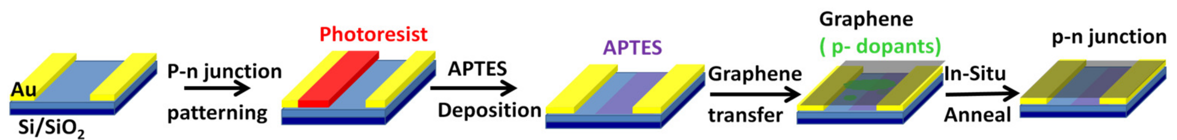

Figure 5.24. Schematic showing the process used to fabricate the graphene p-n junction using only APTES without PFES modification.

5.3.3.2 Characterization

As was done in section 5.3.2, contact angle measurements and XPS were utilized to ensure the presence of APTES in one half of the channel and of intrinsically p-doped graphene on the other half. The resulting patterned APTES layers were verified by XPS mapping, as illustrated in Figure 5.25. XPS mapping was performed using a 30 μm spot size with a step size of 28 μm, and a Gaussian smoothing algorithm was applied to the raw data similar to the one explained in section 5.3.2.2. The signal associated with 399.5

eV binding energy was used for mapping the N1s spectra. Figure 5.25 shows a well defined boundary between areas of the substrate coated with the APTES layer and those without.

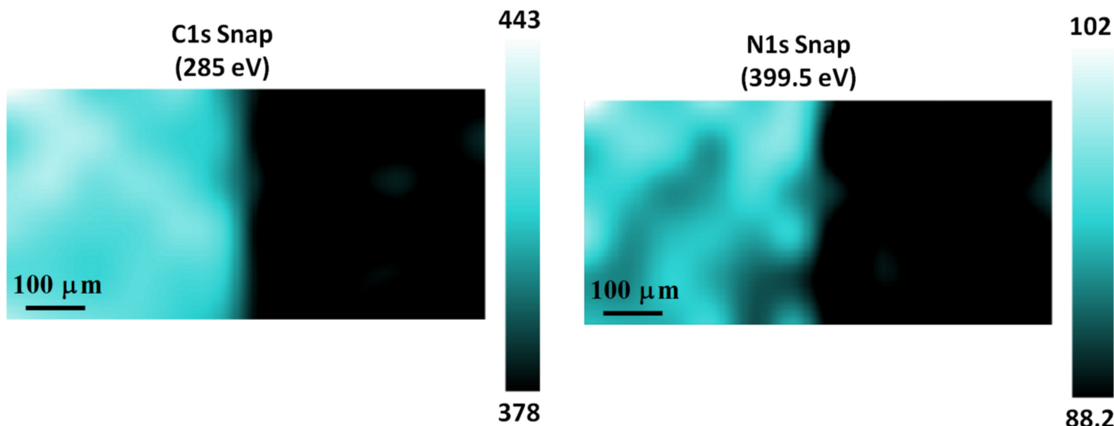

Figure 5.25. XPS mapping of the graphene p-n junction using APTES and intrinsically p-doped graphene for the (Left) C1s intensity at a binding energy of ~ 285 eV (Right) N 1s intensity at a binding energy of 399.9 eV.

Further analysis of the position of these boundaries with respect to the location and intensity of those peaks in the XPS that originated from the gold source and drain contacts confirms that the lithographic alignment was sufficient to locate these p-n junctions in the FET channels. C1s mapping using a binding energy centered at 285 eV was also performed. Again, a well defined boundary was observed in the patterned APTES samples, with the strongest C1s signal corresponding to regions containing the strongest N1s signal as well, consistent with the formation of a well defined patterned APTES layer.

5.3.3.3 Electrical data measurements

Electrical measurements were performed on the fabricated CVD graphene devices that contained the patterned APTES layers in the device channels; the devices were probed under inert atmosphere using a method similar to that explained earlier. As expected, as-made devices exhibited a heavily doped p-type characteristic, due

presumably to doping from adsorbed species. The two expected current minima region for the devices in the as-made state are located at sufficiently large positive gate potentials that they are difficult to measure without experiencing breakdown of the device dielectric.

After annealing the devices at 200°C for only 5 min, two minima in the I-V curve were clearly observed, corresponding to two Dirac points, as a result of desorption of p-dopants.

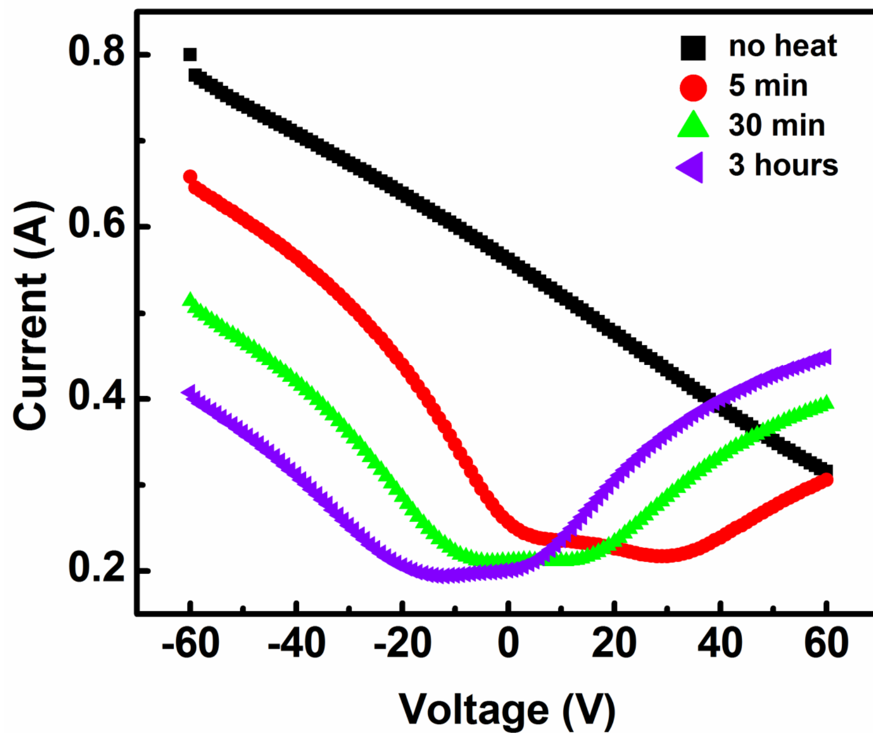

Figure 5.26. Source-drain current versus gate voltage as a function of heating times at 200°C for a graphene p-n junction using APTES and intrinsically p-doped film.

For V_g larger than approximately +35 V in this device, the device channel is effectively in an N/N+ doping configuration where both regions of the channel are p-doped, but the region of the channel that does not contain the APTES layer is more heavily p-doped. For V_g in the range of approximately 0 V to +35 V, the formation of a p-n junction in the

device channel occurs. For V_g less than 0 V, the device channel exists in a p+/p doping configuration where the regions of the channel containing the APTES layer are more heavily n-doped. After 30 min of annealing at 200°C, the device channel is N/N+ doped for Vg larger than +15 V, p-n doped for Vg between -10 V and +15V, and p/p+ doped for Vg less than -10V. The nice feature of the devices annealed for 30 min is that they behave roughly symmetrically in terms of the electrical response around Vg=0 V. Further annealing leads to additional shifts of the Vg range over which a p-n junction doping profile exists in the device channel to more negative Vg. It is also possible during these measurements to demonstrate the unique ambipolar character of the devices. Switching of the source-drain bias voltage from positive to negative values shows no rectifying behavior, as would be characteristic of an ambipolar device [128, 161].

5.4 Conclusion

This ability to control the n-doping characteristics of the device surface, i.e. through modulation of the density of APTES deposited (e.g. by controlling deposition time or solution concentration) on the gate dielectric, can be easily combined with the patterned p-n junction fabrication techniques to allow for full control of the position of the charge neutrality points in the I-V characteristics of the resulting FET devices. This unique p-n junction behavior of graphene, in contrast with the traditional rectifying behavior of conventional semiconductors, allows the development of graphene-based bipolar devices. Our simple method for producing patterned doping profiles in graphene films and devices facilitates the study of such phenomena, since it allows very fine and independent control over the characteristics of the FET I-V curves as compared to the more limited control possible with electrostatic substrate engineering, [161] and other fabrication techniques [126, 171, 178, 180-181].

In summary, this chapter has shown that it is possible to utilize APTES layers to n-dope graphene, to control the resulting doping level in graphene FET devices through control of the amount of APTES deposited onto the FET gate dielectric surface, to produce FET devices with patterned p- and n-doped regions through lithographic patterning of such APTES layers, and to use the combination of control of APTES deposition and patterning to tune the I-V characteristics of graphene FET devices. It has also been shown that use of such APTES doping schemes does not degrade the resulting graphene electronic properties as has been problematic in previously reported doping procedures, due to introduction of defects into the graphene layer. Overall, the methods described here allow for facile, controllable, and low temperature fabrication of graphene p-n junctions.

Furthermore, APTES and PFES were utilized simultaneously in a single FET device to induce n- and p-type characteristics in graphene without altering its structure. These SAMs bond to the substrate and are thermally stable. Formation of two separate Dirac points in the I-V characteristic curve is indicative of a graphene p-n junction. Variation in the duration of fictionalizing graphene with these SAMs and heat treatment period results in p-n junctions with controlled position and height.

CHAPTER 6

TRANSFER-FREE SYNTHESIS OF GRAPHENE ON DIELECTRIC SUBSTRATES

6.1. Introduction

As described in detail in Chapter 2, the deposition or synthesis of large-area, high quality graphene [2, 53] is important for developing electronic, optoelectronic, and sensor technologies. To this end, several techniques have been developed, including epitaxial growth from expensive single crystal SiC to yield high quality graphene films, [23, 55, 58] chemical reduction of solution deposited graphite oxide (GO), [25, 60-63] liquid phase exfoliation and solution deposition of graphite, [24, 26, 56] and chemical vapor deposition (CVD) on transition metals followed by transfer [28-30, 39, 71]. Among these, CVD is the most viable for fabricating large area graphene sheets with high quality, [29, 71] with the key feature of this method being the solubility of carbon in transition metals such as nickel at the typical synthesis temperature for graphene (900-1000°C) [28, 30]. CVD graphene has been explored extensively where the source of carbon atoms can be a hydrocarbon gas, [28-30, 39, 71] or it can be supplied by the decomposition of a carbon containing solid [74, 182] such as a polymer, [78-79, 183] diamond, [75] C_{60} [76] or HOPG [77] in contact with the transitional metal catalyst film. These methods have been explained in detail in Chapter 2.

However, using these methods, a graphene film must be transferred onto a second substrate after synthesis, because the metal layer used for growth is not compatible with device fabrication or operation [80]. In practice, it is difficult to transfer a pristine sheet

of large area graphene without leaving significant wrinkles, cracks, and voids. Such defect sites reduce charge transport and negatively impact the graphene electrical conductivity. Figure 6.1 shows AFM, SEM, and optical images of transferred CVD graphene where damage has been introduced to the film in the transfer process.

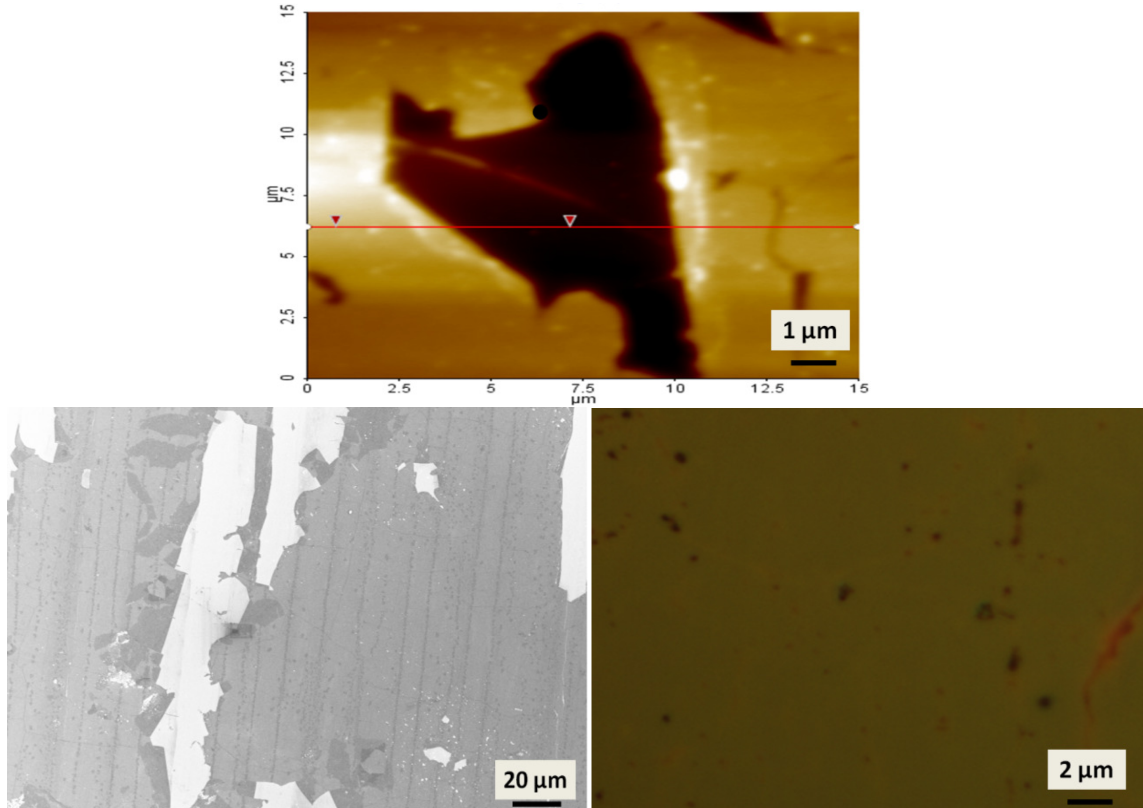

Figure 6.1. Different images showing the presence of cracks, voids, and contamination in transferred CVD graphene when care was not taken during the transfer. (Top left) AFM image (Top right) SEM image of transferred graphene with cracks. (Bottom) Optical image with contamination.

The goal of this chapter is to develop a process for transfer-free, large scale synthesis of graphene on dielectric substrates. Transfer-free synthesis is important as

most of transistor technology uses complementary metal-oxide semiconductor (CMOS) in which an oxide layer insulates the transistor gate from the channel. In addition, the possibility to pattern solid carbon source or thin film metals enables direct synthesis of patterned graphene on dielectric substrates. materials. Furthermore, well-organized and thin aromatic layers can be utilized as solid carbon source for low temperature synthesis since there is no need for high temperature to break chemical bonds in order to provide the carbon required for graphene synthesis. To this end, solid carbon source will be utilized to develop large area films. Then, trace carbon dissolved in metals will be used through a segregation process to form graphene layers [184].

6.2. Synthesis of graphene using solid carbon source

6.2.1. Introduction

Direct synthesis of graphene on dielectric substrates through surface catalytic decomposition of hydrocarbon precursors on thin copper films has been previously demonstrated and does not require a transfer step [81]. However, this method resulted in the partial coverage of the surface with graphene. The extension of this approach to include solid carbon sources can lead to a scalable method for full coverage or patterned graphene on dielectric substrates. In this section, an approach will be given to fabricate large area graphene directly on dielectric substrates by using solid carbon sources and without a need for transfer process. The carbon source, Poly(methyl methacrylate) (PMMA), was deposited on Cu-coated dielectric substrates to facilitate the graphene synthesis. During graphene growth, the sacrificial copper partially evaporated away similar to the method explained in [81] leaving graphene on the substrate. A wet etch step removed the residual Cu leaving a continuous coverage of graphene on the dielectric

surfaces. In the next sections, we will analyze how growth parameters affect graphene quality.

6.2.2. Methods

Copper films 300 nm thick were evaporated on a dielectric substrate using E-beam evaporation. The dielectric substrates (35 mm by 23 mm) were either silicon wafers coated with 300 nm thick thermal oxide films (SiO_2/Si), quartz, AlN, or sapphire. The solid carbon source used was PMMA (Sigma Aldrich M_w=950000). The PMMA was dissolved in anisole (Sigma Aldrich) at 4 wt%, after which it was spin-coated on the copper at 3000 rpm for 1 minute yielding 100 nm thick polymer films. The PMMA was cured at 180°C for 1 min on a hotplate and then annealed in a vacuum oven at 70°C for 2 hours to remove solvents [78]. The sample was placed inside a quartz tube and pushed into the hot zone of a growth furnace once the temperature reached 900-1000°C. It is important to note that earlier exposure of the samples to hot zone before the temperature reaches to growth temperature will not results in formation of graphene. The growth furnace is the same one that used for synthesis of CVD graphene films described in section 3.2 in Chapter 3.

The growth was performed under vacuum pressure in an H_2/Ar environment. The synthesis time varied from one minute to more than an hour. First, the sample was outside of the hot area in the furnace. Once the growth temperature was reached, the quartz tube was inserted into the hot area, and it remained there during the growth time. After growth, the sample was rapidly cooled to room temperature under hydrogen and argon gas flow prior to sample removal. Figure 6.2 shows schematic of graphene growth on a dielectric substrate using solid carbon sources. As illustrated, upon heating PMMA

was dissolved and provided a carbon source to the growth catalyst, Cu. Further heat treatment, resulted in moving carbon atoms inside the Cu. Depending on the growth temperature, Cu evaporated partially, leaving graphene both on top and underneath. After synthesis, the graphene was characterized using micro-Raman spectroscopy, scanning electron microscopy (SEM), XPS, and UV Vis spectroscopy.

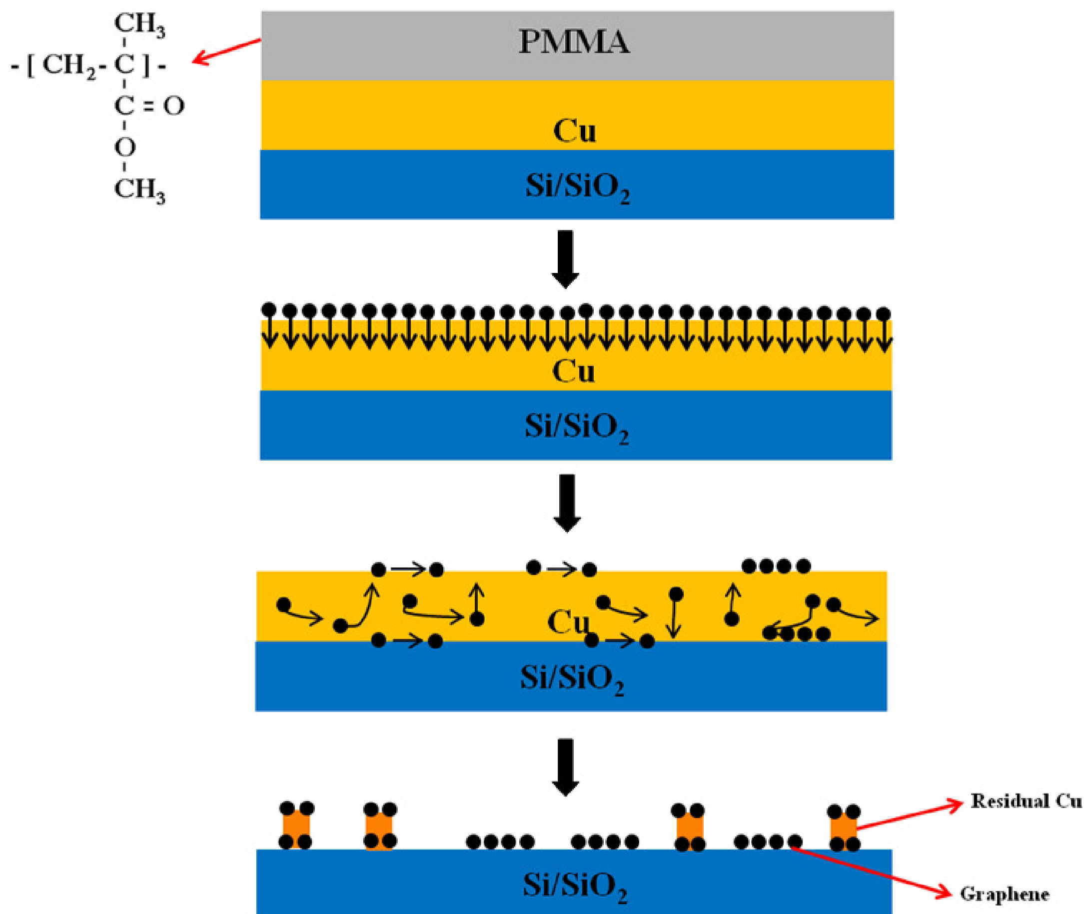

Figure 6.2. Schematic of graphene synthesis using solid carbon source on dielectric substrate.

6.2.3. Graphene synthesis on quartz

Figure 6.3 shows optical and scanning electron microscopy images of graphene grown on quartz after 40 minutes of synthesis. Large regions of graphene were found in

direct contact with the quartz substrate, while residual copper covered ~60% of the surface. Raman spectroscopy characterization of the graphene was performed by analyzing the intensities of the D, G, and 2D Raman peaks [130]. The G-peak (~ 1585 cm^{-1}) is due to first-order Raman scattering by the doubly degenerate zone center optical phonon mode, and the 2D-peak (2680-2700 cm^{-1}) is associated with second-order scattering by zone-boundary phonons [38, 44-46]. In defective graphite, the D-peak (1345-1350 cm^{-1}) is due to first-order scattering by zone-boundary phonons. Graphene peaks have been explained in further details in Chapters 2 and 3. The Raman fingerprint for CVD graphene was confirmed by using the 2D- and G-peaks' intensity ratio (I_{2D}/I_G) [29, 38, 44-46] and the width of the 2D-peak [38, 44-46, 130]. The graphene was identified in all spectra measured on samples both in the regions with and without Cu; this contrasts with reports from other projects that used hydrocarbon sources, in which graphene was found only in metal-free areas [38, 44-46]. The Raman spectra (Figure 6.3(b)) suggest that the sample consists of 1-3 graphene layers [29]. Monolayer and bilayer graphene was detected in metal-free areas and few-layer graphene was primarily found in regions with residual copper. The D-peak intensity was higher near the edge of the sample, suggesting the presence of intrinsic defects in the grains or of high density graphene domains [45].

To obtain further insight into the nature of our films, Raman mapping was performed. Figure 6.3(c) and (d) show a typical color map of the I_{2D}/I_G intensity ratio over a 15 μm by 5 μm region and over the full sample with a half maximum (FWHM) of the 2D peak which ranges from 35 cm^{-1} (dark color) to 55 cm^{-1}(light color), respectively. Overall, Raman mapping confirmed graphene coverage everywhere on the sample.

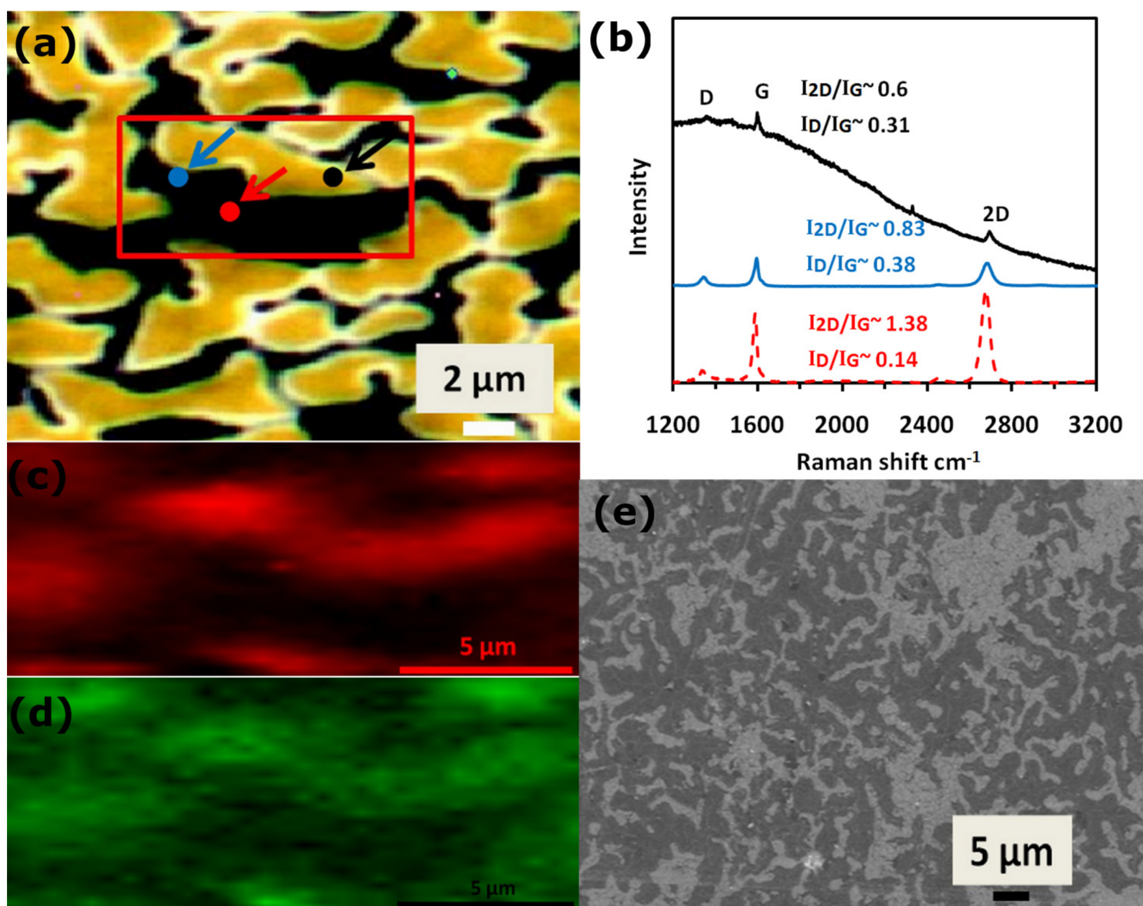

Figure 6.3. (a) Optical microscope image and (e) SEM image of a graphene sample grown on quartz after 40 min. The images reveal the incomplete removal of Cu through evaporation during the growth process. (b) Raman spectra from metal-free areas (red and blue lines) and Cu regions (black line) showing full coverage of graphene on the sample. Mapping of I_{2D}/I_G and FWHM(2D) of the same area in (a), respectively.

6.2.4. Graphene synthesis on SiO_2

Figure 6.4 shows an optical image of graphene on SiO_2/Si and the representative Raman spectra after 20 minutes of growth. Less than 15% of surface area was still Cu. Raman spectra again showed the presence of graphene in all regions.

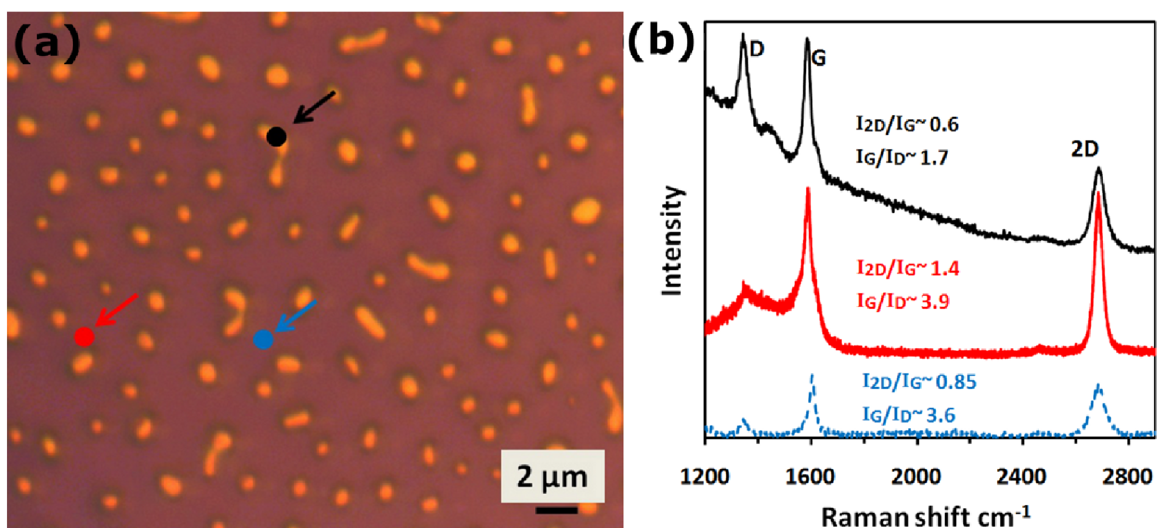

Figure 6.4. (a) Optical microscope image of a graphene sample grown on SiO_2/Si after 20 min of growth. The image shows graphene directly on the SiO_2 surface as well as residual copper with less than 15% surface coverage. (b) Raman spectra from metal-free regions (red and blue lines) and Cu regions (black line) show the presence of graphene everywhere on the sample.

6.2.5. Substrate effect

Figure 6.5 shows the optical microscope images of the graphene directly grown on SiO_2, quartz, AlN, and sapphire. Representative Raman spectra measured in metal-free areas show prominent graphitic peaks for all substrates [Figure 6.5(e)]. For the AlN and sapphire substrates, a high intensity defect peak and a low I_{2D}/I_G ratio indicate oxidized or highly defective multi-layer graphene. The highest quality graphene was synthesized on quartz and SiO_2 substrates, which may be a result of the potential for some oxides to graphitize carbon [16, 63].

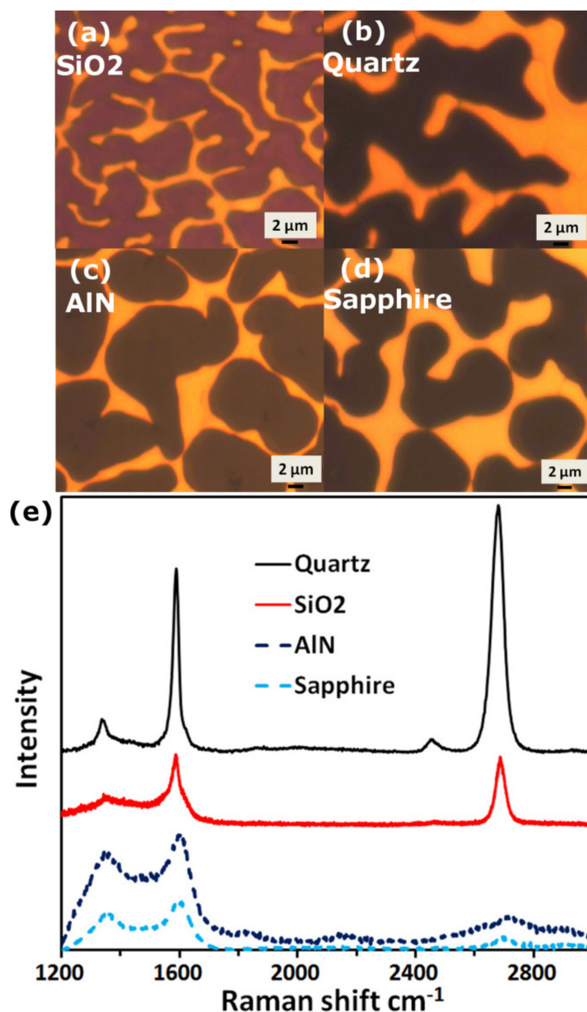

Figure 6.5. (a-d) Optical microscope images of graphene samples grown on quartz, SiO_2, AlN, and sapphire, respectively. (e) Representative Raman spectra from the metal-free regions on each substrate showing the presence of graphitic peaks.

6.2.6. Growth condition/evolution effect

6.2.6.1. Growth evolution on SiO2

We studied how process parameters affect graphene growth on quartz and SiO_2 by varying growth time, growth pressure, and H_2/Ar gas flow rate. Figure 6.6 shows the evolution of growth on SiO_2/Si substrates.

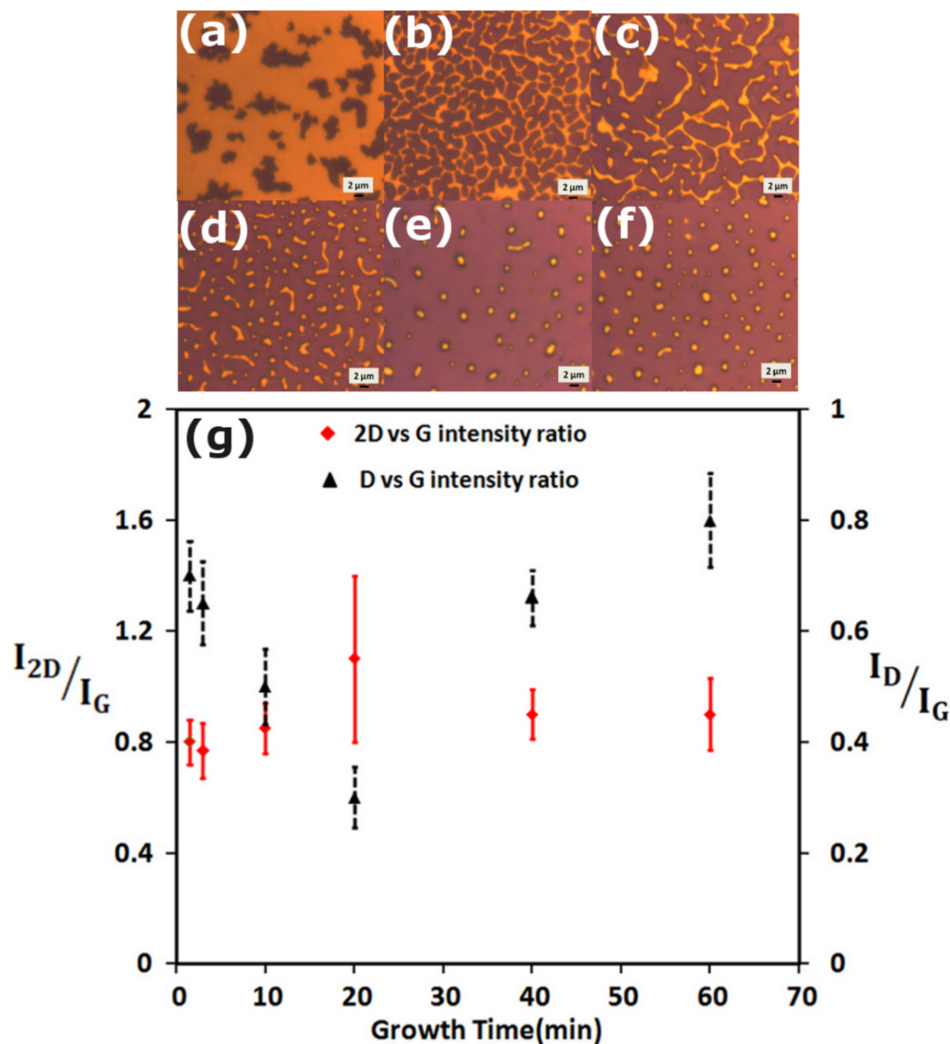

Figure 6.6. (a-f) Optical microscope images showing the residual copper coverage on SiO_2/Si substrates as a function of synthesis time for 1.5, 3, 10, 20, 40, and 60 minutes, respectively. (g) The dependence of the Raman spectra (I_{2D}/I_G and I_D/I_G) collected from samples shown in (a-f). The data suggests a maximum in the layer thickness (highest I_{2D}/I_G ratio) and a minimum in the defects in the graphene (lowest I_D/I_G ratio) after 20 minutes of growth.

Growth times as short as 90 seconds resulted in little removal of copper [Figure 6.6 (a)] while Raman spectroscopy showed the presence of graphitic peaks indicating graphene formation. Increasing the growth time to 180 seconds caused an increase in Cu

removal with a residual coverage area of 60% [Figure 6.6 (b)]. Further increase in the synthesis time resulted in more Cu removal, leaving residual particles of 1 µm in diameter with 5% surface coverage after 1 hour of processing. Figure 6.6 (g) shows Raman spectra from each sample in metal-free areas. The increasing I_{2D}/I_G ratio represents a decreasing number of graphene layers; a low ratio of the D- and G-peaks (I_D/I_G) can be interpreted as a larger grain size or a higher degree of graphitization [45]. An optimum growth time of 20 minutes was determined based upon minimizing the number of growth layers (I_{2D}/I_G =1.4), the level of defects (I_D/I_G = 0.25), and the residual copper coverage, which is held to less than 15%.

6.2.6.2. Growth evolution on quartz

In contrast to SiO_2, copper evaporation was less pronounced on the quartz substrate [Figure 6.7]. The amount of Cu evaporation increased after 20 minutes of growth time on quartz with approximately 50% residual Cu coverage [Figure 6.7(c)]. Increasing the growth time to around 90 minutes resulted in almost 70% removal of copper as shown in Figure 6.7 (f). Extended synthesis time up to (2 hours) was not effective in further removal of the residual Cu from the quartz substrate. However, the quality of synthesized graphene decreased drastically with an increase in growth time, as seen previously. It is believed that this changes can be due to etching of the graphene by H_2/Ar and was identified by an increase in the I_D/I_G from 0.14 to 0.7 between 40 and 90 minutes of growth time [Figure 6.7 (g)]. The best I_D/I_G ratio in the metal-free areas was ~ 0.25 and ~ 0.6 in Cu regions for samples grown on SiO_2/Si. A reduction in these values was seen for samples grown on quartz with I_D/I_G being ~0.14 in metal free areas and ~0.3 in Cu regions [compare Figure 6.7 (g) and Figure 6.7 (g)]..

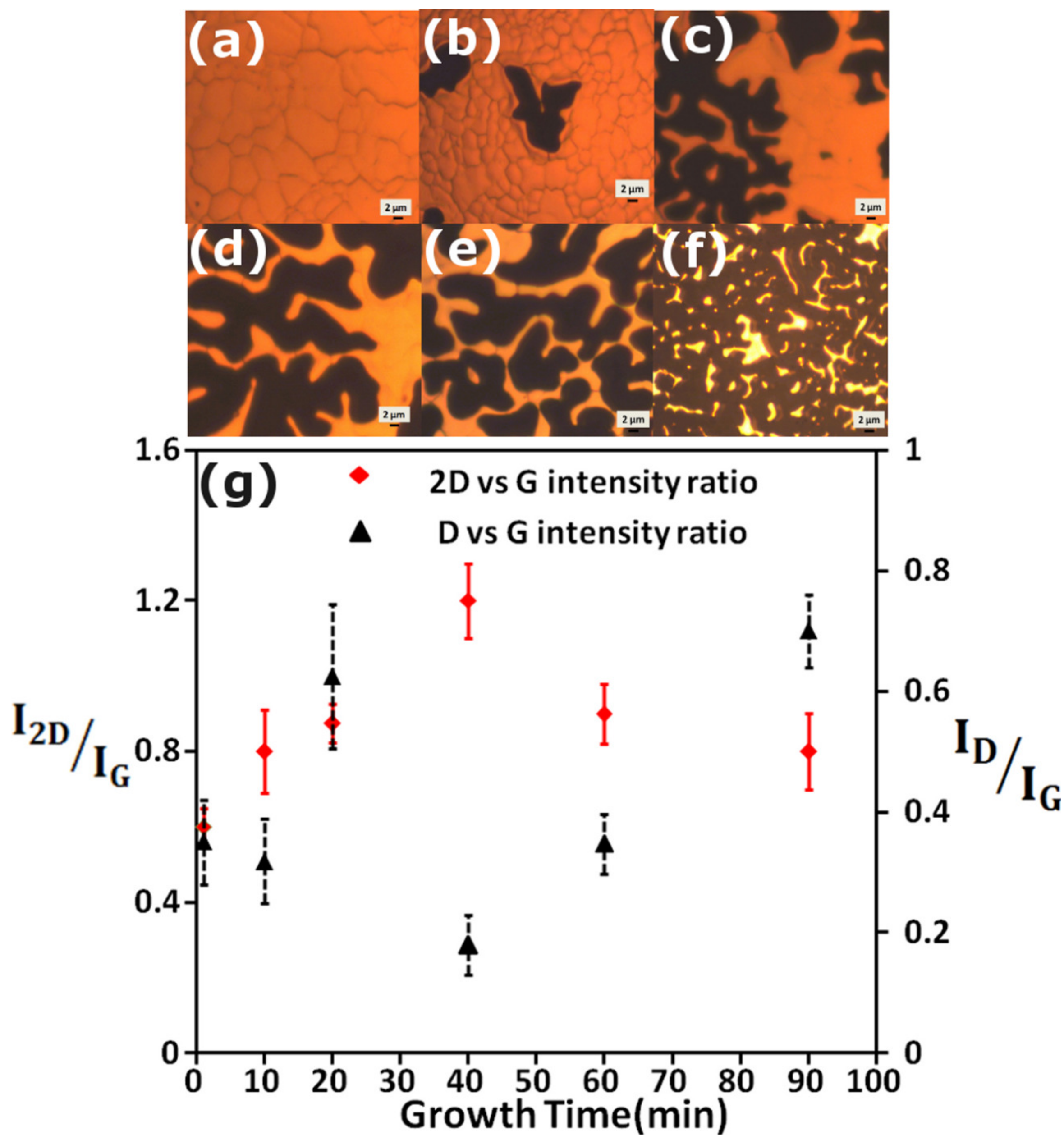

Figure 6.7. (a-f) Optical microscope images of the residual copper coverage on quartz substrates after 1, 10, 20, 40, 60, and 90 minutes growth, respectively. (g) Raman spectra collected from the samples in (a-f). The data suggests a maximum in the layer thickness (highest I_{2D}/I_G ratio) and a minimum in the defects in the graphene (lowest I_D/I_G ratio) after 40 minutes of growth.

This indicates improved quality in graphene synthesized on quartz. At present it is not clear if this is a result of the crystalline nature of the quartz or if it is due to the lower evaporation rate of the Cu films during synthesis

6.2.6.3. Effect of growth parameters

The extent of copper evaporation and the number of graphene layers synthesized also depended on the flow rate of hydrogen/argon and the vacuum pressure inside the quartz tube. Figure 6.8 shows the optical microscope image of the synthesized graphene on SiO_2/Si for different H_2/Ar flow rates and growth pressures. I_{2D}/I_G and I_D/I_G ratios from metal-free regions are plotted as a function of H_2/Ar flow rate and growth pressure [Figure 6.8 (g,h)]. As the H_2 flow rate increased from 3 sccm to 50 sccm, the I_{2D}/I_G ratio increased to more than 1.3 while I_D/I_G decreased to less than 0.25. This indicates a decrease in the number of layers and an improvement in the quality of the synthesized graphene. Hydrogen helps to remove excess carbon in the furnace, leading to a lower number of graphene layers. Further increase in the H_2 flow rate up to 100 sccm resulted in a slight decrease in the I_{2D}/I_G ratio and an increase in the I_D/I_G ratio up to 0.8, as too much hydrogen can result in defect formation in the graphene. The best quality graphene films were synthesized with a H_2/Ar flow rate of 50/500 sccm, while the measured growth pressure was ~ 1000 mTorr. The amount of Cu removal also depended on the growth pressure. Variation in the H_2 flow rate had a direct effect on the measured pressure inside the reaction chamber based on the pumping speed and conductance of the vacuum system. Lower pressures were useful for increasing Cu removal, as shown in Figure 6.8 . In contrast, higher gas flow rates resulting in higher pressures were useful for increased carbon removal [Figure 6.8 (e) and (f) vs. (b)]. Cu coverage was decreased to less than 10% with H_2/Ar flow rate of 50/50 sccm and a measured growth pressure of 450 mTorr [Figure 6.8 (e)].

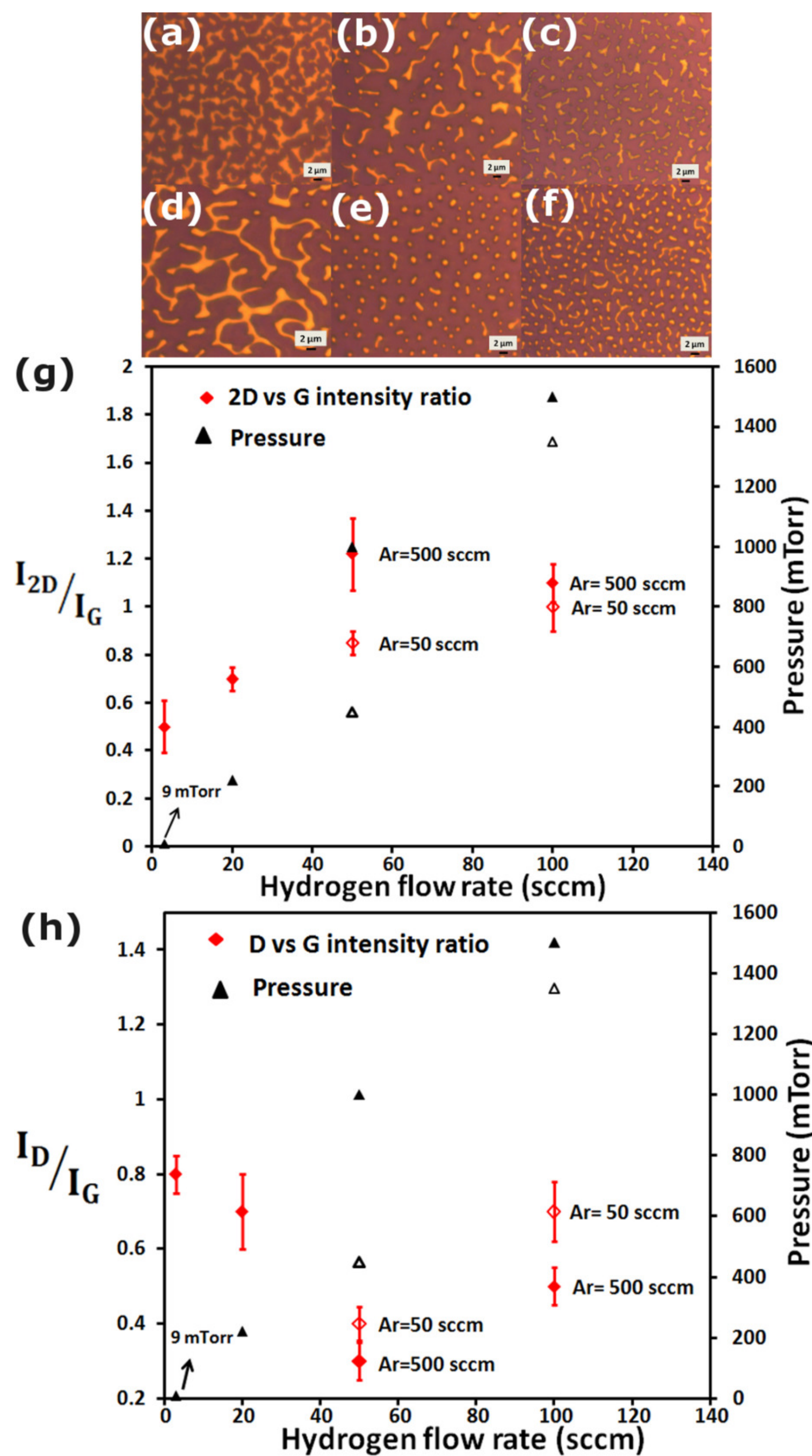

Figure 6.8. Optical microscope images showing the residual copper coverage after 20 minutes of growth on SiO_2/Si with H_2 flow rate (sccm)/Ar flow rate (sccm)/pressure (mTorr) as (a) 100/500/1500, (b) 3/50/9, (c)50/500/1000, (d)100/50/1350, (e)50/50/450, and (f) 20/50/220. (g,h) Average I_{2D}/I_G and I_D/I_G collected from the samples in (a-f).

These data indicate a maximum in the layer thickness (highest I_{2D}/I_G ratio) and a minimum in the defects in the graphene (lowest I_D/I_G ratio) for the flow rate conditions of H_2 = 50 sccm, Ar = 500 sccm, and P = 1000 mTorr. Residual Cu coverage decreased to less than 10% under these conditions.

6.2.7. Removing residual Cu

To remove residual Cu, samples were placed in a 30% $Fe(NO_3)_3$ aqueous solution for two hours. Afterwards, the graphene was treated with 10% HCl solution for 10 min followed by washing in deionized (DI) water similar to the method explained in section 3.3. in Chapter 3 for transfer of CVD graphene films. Figure 6.9 shows optical images of the sample before and after acid treatment. Raman spectroscopy was performed and confirmed the presence of graphene in regions where the Cu once existed [Figure 6.9 (d)]. Figure 6.9 also shows some wrinkles in the SEM image of the graphene grown on quartz after acid treatment. However, no cracks were observed and the level of wrinkles was far less than that observed by post growth and transfer methods.

XPS was employed to identify the elements present on the sample surface after acid treatment. XPS data were acquired using a spectrophotometer (VG Scientific ESCALAB 210) with an Al $K\alpha$ X-ray source ($h\upsilon = 1486.68\,\text{eV}$). XPS was utilized on several samples synthesized on SiO_2/Si after acid treatment. The survey scan spectra were collected at the binding energy (B.E.) of 0-1300 eV with a step size of 1 eV and a spot size of 400 μm, which prominently showed the C1s and O1s peaks and the lack of any peak associated with copper beyond the detection limit of Cu in XPS (0.004%) [Figure 6.9 (e)]. These data suggest that the acid treatment effectively removes all metal contaminants from the graphene film.

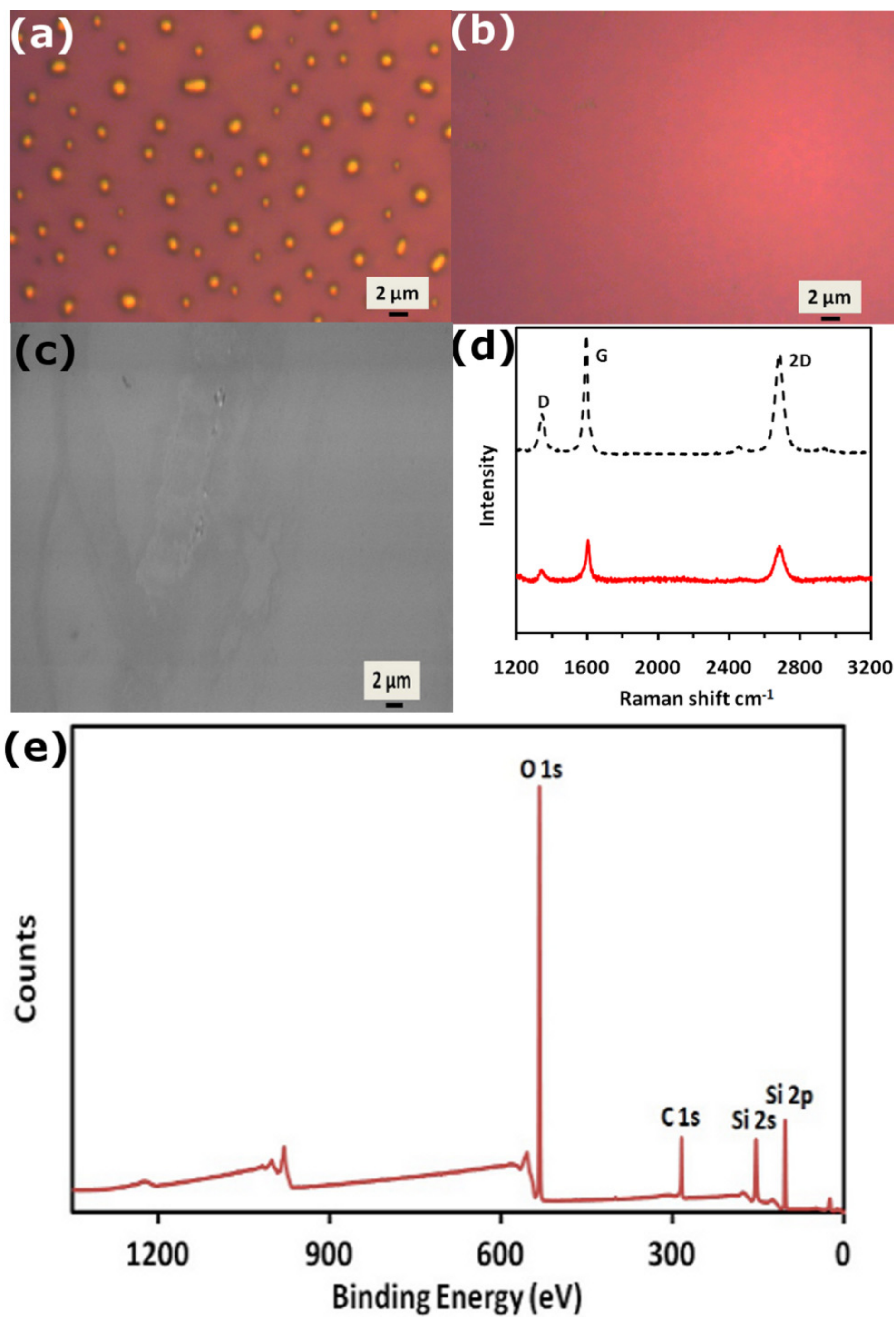

Figure 6.9. (a,b) Optical microscope images of graphene before and after acid treatment. (c) SEM image of the sample grown on quartz after acid treatment. (d) Raman spectra from two different points on the sample in (b) after acid treatment. (e) X-ray photo electron spectroscopy of the sample after acid treatment indicates the presence of C1s binding energy without any peaks for copper or Fe.

Finally, the optical transparency of an acid-treated graphene film synthesized on quartz was obtained using UV-Vis spectroscopy. To this end, a Cary 5E UV-Vis-NIR dual-beam spectrophotometer was used to measure the optical transmittance, from 400-2500 nm, of the samples directly grown on the quartz substrate. An average transmittance above 95% was observed at 550 nm wavelength, suggesting that the sample synthesized through our technique consists of primarily bilayer graphene, as each layer absorbs between 2-2.5% at room temperature [132].

6.3. Synthesis of graphene using trace carbon dissolved in metals

6.3.1. Introduction

A segregation phenomenon has been utilized to turn the trace amounts of carbon dissolved in bulk metals into graphene [39, 72]. Recently, research has shown that graphene films can be produced using this segregation method by allowing trace C found in Ni to diffuse through an outer Cu layer to form graphene. However, the graphene films found on the Cu film required a subsequent transfer to a second substrate after synthesis in order to remove the metal layers. In this section, we will describe an extension of the segregation approach to form graphene both on top and underneath a Ni/Cu bilayer film without the need for a transfer step. This is a fast, easy, transfer-free, and scalable method for full coverage and can lead to patterned graphene on dielectric substrates.

6.3.2. Methods

A copper film 150 nm thick and nickel film 10 nm thick were evaporated on a Si wafer coated with 300 nm of thermal oxide. The key to this process is that the evaporation utilized graphite crucibles for holding the metal sources and it diffuses into

the metal to leave trace amounts of carbon contamination. This trace carbon was utilized as the source for the graphene growth.

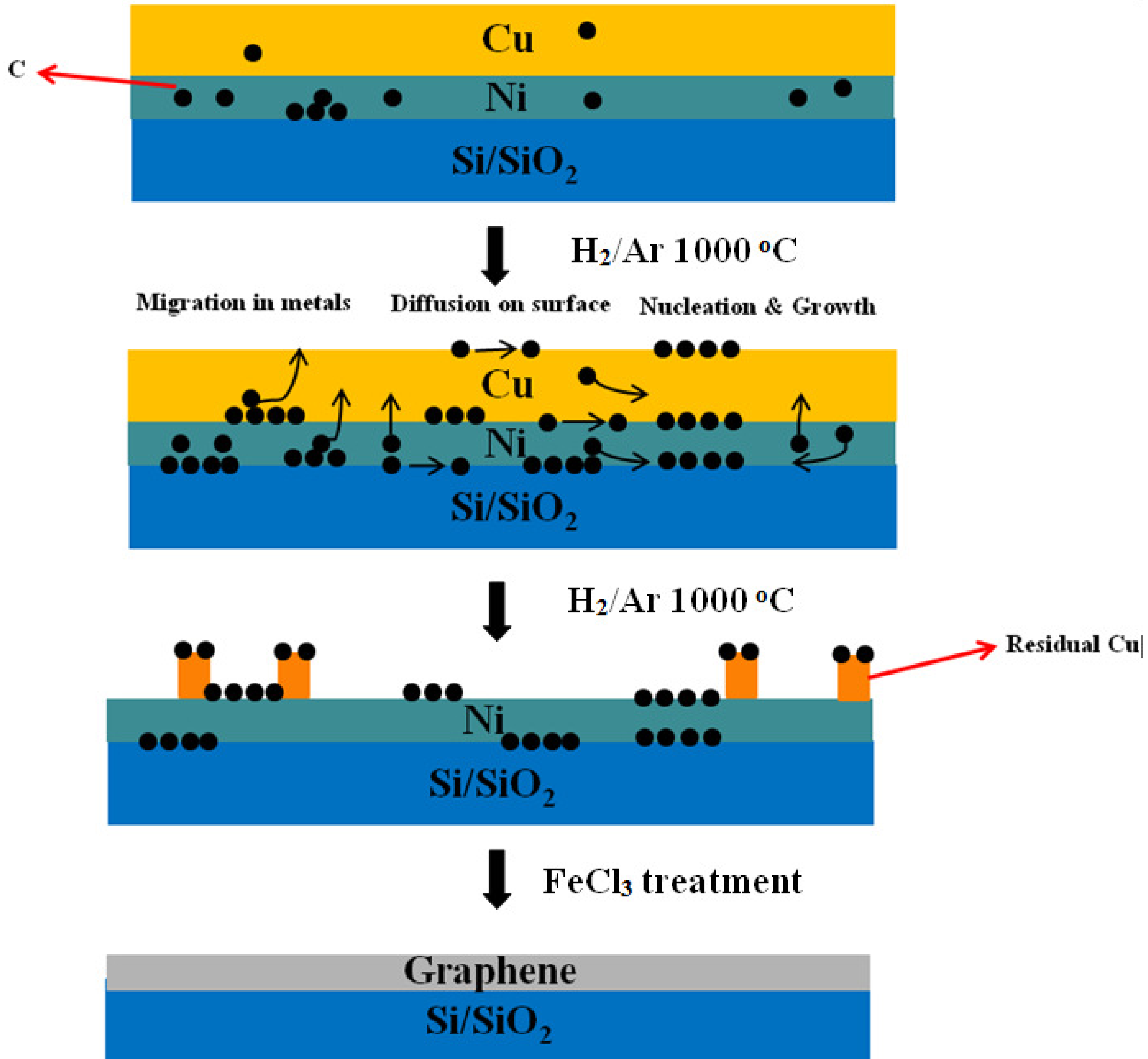

Figure 6.10. Schematic of graphene synthesis using trace carbon dissolved in metals.

To grow graphene, the sample was placed inside a quartz tube and pushed into the hot zone of a growth furnace operating at 1000°C. The same furnace that was used for

CVD growth and growth with solid carbon source was used for this task. The growth was performed for 30 minutes under flow rates of 50 sccm H_2 and 500 sccm Ar atmosphere at a pressure around 870 mTorr. Next, the sample was rapidly cooled to room temperature under the same gas flow rate. Similar to growth with a solid carbon source, the sacrificial copper evaporated away during the growth due to the high homologous temperature (>0.9) and the low pressure inside the chamber, [81] leaving graphene both on top and underneath the nickel film. A schematic of synthesis is shown in Figure 6.10.

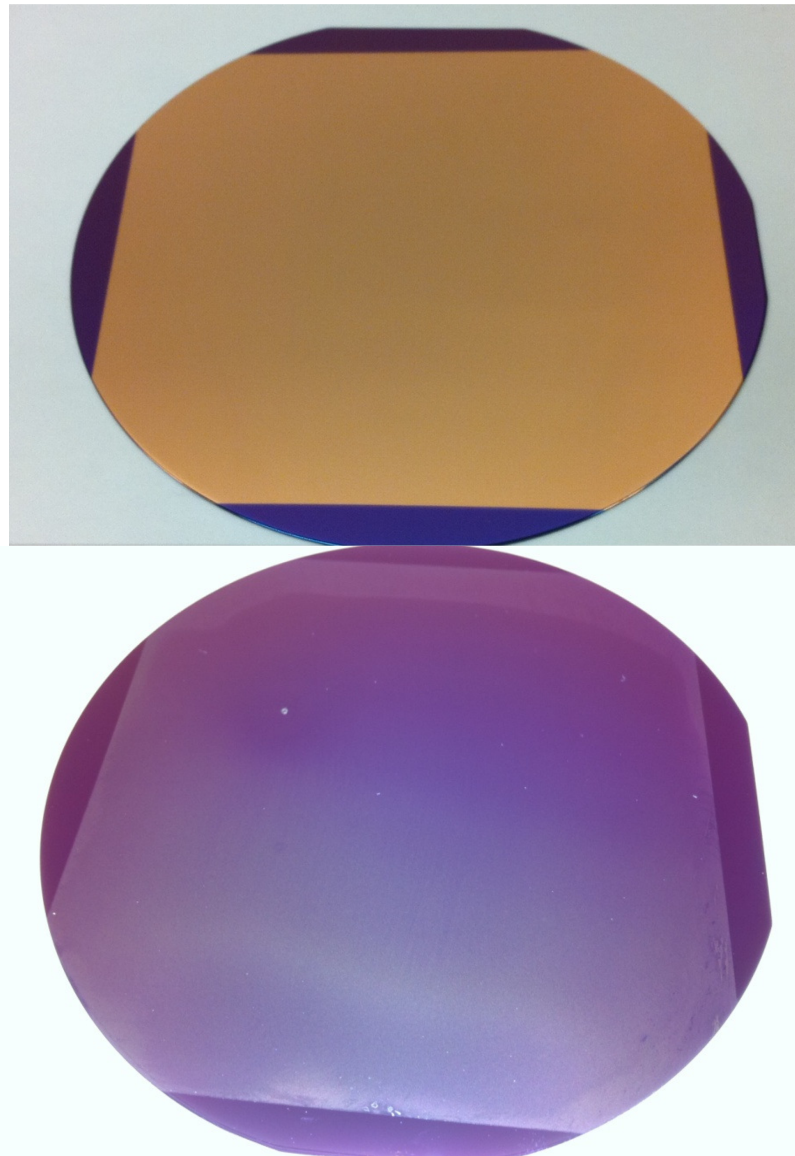

Figure 6.11. Graphene on SiO_2/Si (100 mm wafer) after 30 minutes of growth.

During synthesis, much of the Cu film evaporated away, leaving behind a discontinuous residual layer of Cu on the Ni. To remove the metals, the samples were treated post-growth with a 30% $FeCl_3$ acid solution for an hour, followed by a 10% HCl aqueous solution for 10 min prior to washing in deionized (DI) water similar to the methods explained in section 6.2. This process left the graphene directly on the SiO_2 substrate. Figure 6.11 shows a typical 100 mm diameter SiO_2/Si wafer coated with a Ni/Cu bilayer before and after synthesis. Layers of graphene can be observed by the color contrast on the wafer due to light interference effects. The lightest regions in the middle of the wafer correspond to monolayer or bilayer graphene, where the darker regions near the edges of the wafer are mostly few-layer graphene.

6.3.3. Characterization of metal sources

Secondary ion mass spectroscopy (SIMS) was utilized to chemically image the substrate. Sputtering by oxygen ions allows depth profiling where atomic masses from 1 up to >5000 amu (i.e. hydrogen up to large molecules) can be detected with a high mass resolution. SIMS is the most sensitive surface analysis technique, being able to detect elements present in the parts per billion range with a vertical resolution of ~ 2nm and lateral resolution as small as ~300 nm [see Figure 6.12 (top)]. Figure 6.12 (bottom) shows the intensity of detected ions versus sputtering time. A high intensity of Cu- ions was first detected which formed the outer layer of the Cu/Ni bilayer film. During the depth profile analysis, the carbon to copper ion intensity ratio (I_{C-}/I_{Cu-}) in this region was ~ 3.5 $x10^{-4}$. Further sputtering results in diminished Cu intensity and the appearance of Ni. This is indicative of reaching Cu/Ni interface. Simultaneously, an increase in the intensity of C was observed. The carbon to nickel ion intensity ratio (I_{C-}/I_{Ni-}) was ~ 7 $x10^{-}$

[2]. Comparing the ratio of I_{C-}/I_{Ni-} with the ratio of I_{C-}/I_{Cu-} indicates that the C solubility in bulk Ni is 2 orders of magnitude higher than in Cu. This is in accord with reported maximum solubility of C in Ni and Cu (2.7 % vs 0.04 %) [72].

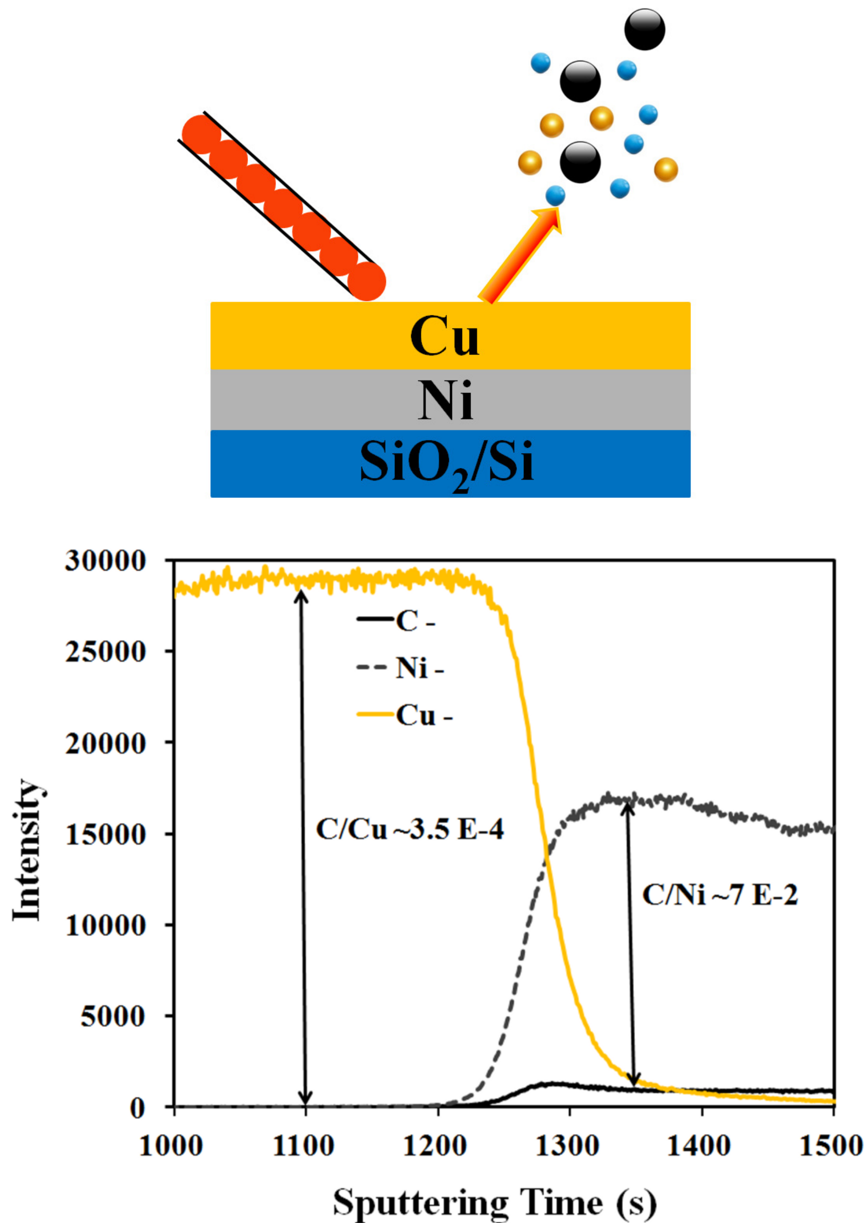

Figure 6.12. (Top) Schematic shows SIMS operation. (Bottom) SIMS results show the intensity of detected ions versus sputtering time, indicative of 2 orders of magnitude higher C solubility in Ni compared to Cu.

The distinct difference in the carbon solubilities of Ni and Cu suggests that the carbon in the Ni can act as a source for the formation of graphene. In general when these films are heated, Cu can diffuse into the Ni, and due to its lower solubility, it displaces excess carbon that acts as the source for the formation of the graphene layer. No additional carbon source is necessary for this to occur.

Another set of samples prepared through sputtering of Ni and Cu with similar thicknesses on SiO_2 did not result in formation of graphene through the same growth process. It is believed that the C atoms diffuse into the metal in the e-beam evaporator from the graphite crucibles used to hold the metal sources. Thus, while the differences in the solubility of C in each of the metals is important, the trace carbon appears to be an artifact of the method used to deposit the metals and the combination of these features allows for the synthesis of graphene without any additional carbon sources.

6.3.4. Characterization of synthesized graphene

Figure 6.13 (a) and (b) show optical microscope images of graphene grown on a SiO_2 substrate with Ni and Cu films before and after etching. Large regions of graphene were found on top of the Ni layer, while the residual copper covered less than ~5% of the surface. Raman spectroscopy characterization of the top-layer graphene was performed by analyzing the intensities of the D, G, and 2D Raman peaks [130] using a Jobin-Yvon micro-Raman system similar to the method explained in Chapter 2 and 3. The Raman fingerprint for CVD graphene was confirmed by using the 2D- and G-peaks intensity ratio (I_{2D}/I_G) [29, 45] and the width of the 2D-peak [38, 45, 130]. The graphene was identified in all spectra measured on samples both in the regions with and without residual Cu. Graphene on Ni had a I_{2D}/I_G ratio of 1.56 ± 0.06 and a full width at half maximum (FWHM) of $\sim 40 \pm 2$, suggesting a monolayer or bilayer film.

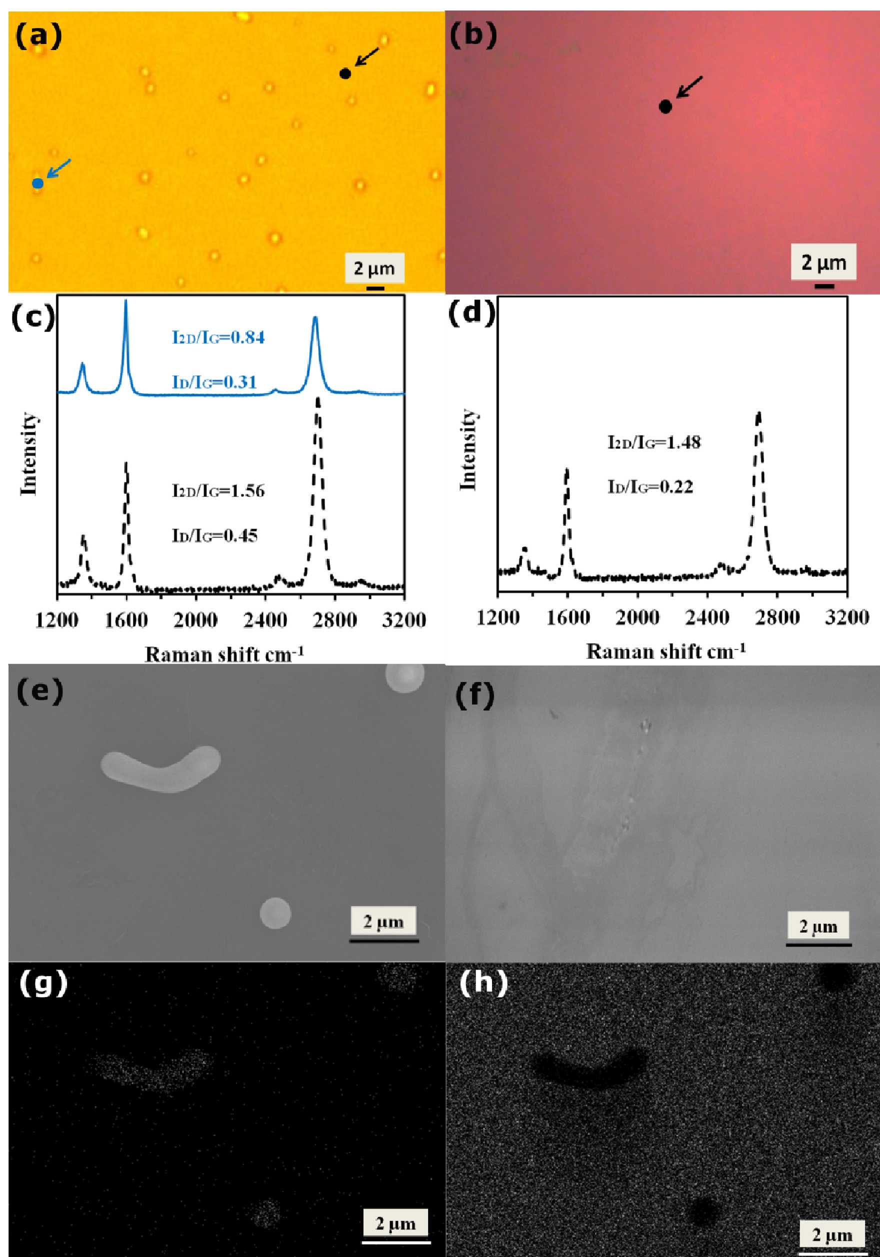

Figure 6.13. (a) and (b) Optical microscope image of graphene before and after acid treatment. (c) Raman spectra from Ni (black line) and Cu regions (blue line) showing full coverage of graphene on the sample. (d) Raman spectra from SiO_2 showing the presence of graphene after etching metals. (e) Secondary-electron SEM image of a graphene sample grown on Ni before etching. (f) In-lens SEM image of graphene on SiO_2 after etching Ni and residual Cu showing presence of wrinkles. (g) and (h) EDX pattern of the same area in (e).

In regions with residual copper, the ratio I_{2D}/I_G is ~ 0.84 ± 0.05 and the FWHM of 2D is ~ 50 ± 3.5, indicative of few-layer graphene [29]. The high D-peak intensity in copper-free areas is due to copper evaporation, suggesting the presence of intrinsic defects in the grains or a high density graphene domains [45].

After etching, both residual Cu and Ni films with graphene on top were removed, leaving the lower layer of graphene in direct contact with SiO_2. An I_{2D}/I_G ratio of 1.48 ± 0.05 and a full width at half maximum (FWHM) of ~ 41 ± 2 were measured, suggesting a monolayer or bilayer graphene on SiO_2 substrate. A typical sample was treated with oxygen plasma, prior to the etching step, to destroy the top layer graphene. After metal dissolution, Raman spectroscopy was performed and showed the presence of graphene. This excludes the possibility that graphene from the top of the nickel dropped to the bottom during the etching process. A Zeiss Ultra60 scanning electron microscope (SEM) was used to image the graphene before and after etching. Figure 6.13 (e) shows an SEM image of the graphene layer before etching. Visible regions of residual copper confirm the dewetting and evaporation of Cu. The SEM image, using an in-lens detector, in Figure 6.13 (f) clearly shows that there are wrinkle-like contrasts in the continuous graphene film after etching. However, no cracks were observed, and the level of wrinkles was less than that observed by post growth and transfer methods. It is believed that the difference between thermal expansion coefficients of graphene and Ni induces a thermal stress during growth that leads to formation of wrinkles [72].

By combining the distinct segregation performances of Ni and Cu, we were able to modulate the thickness and quality of synthesized graphene. A Cu layer was employed as a segregation controller, and a Ni layer with trace levels of C was used as the carbon

source. In comparison, a sample with a 10 nm Ni layer and no Cu was used in the same synthesis process. The Ni only layer resulted in a highly defective few-layer graphene film with I_D/I_G ratio of 1.8 ± 0.2 and I_{2D}/I_G ratio of 1.1 ± 0.15 [see Figure 6.14]. In addition, this method was tried using different thicknesses of Cu without any Ni film, and no evidence of graphene formation was observed. This is in accord with the previous report and is due to very low solubility of carbon in Cu [72].

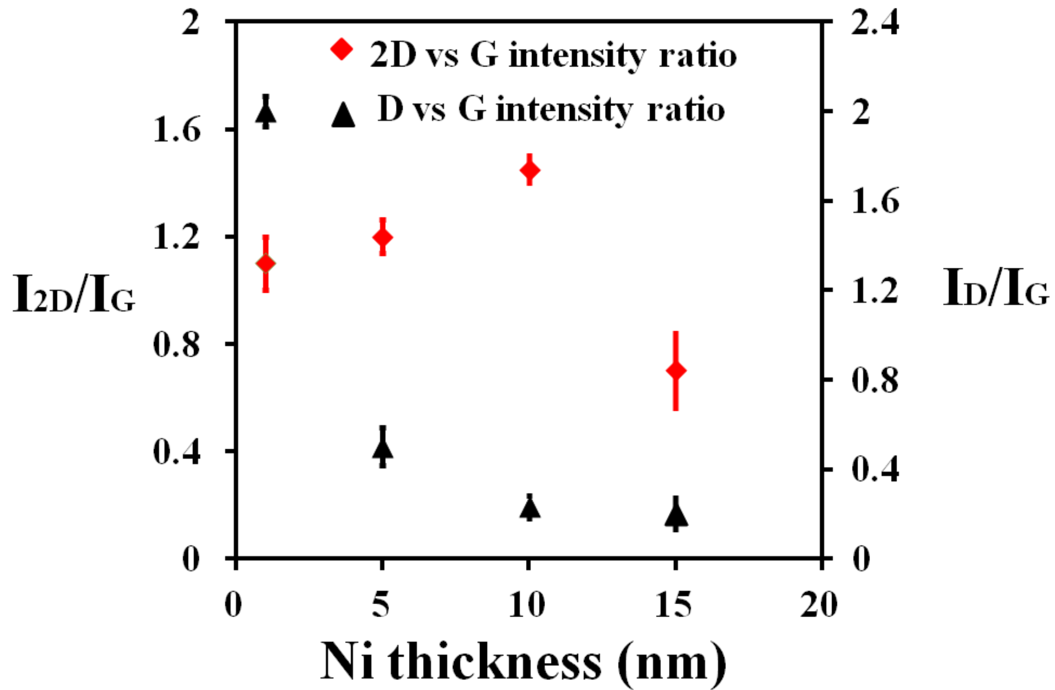

Figure 6.14. I_{2D}/I_G and I_D/I_G ratios as functions of Ni thickness.

6.3.5. Etching residual metal

X-ray Photoelectron Spectroscopy was employed to identify the elements present on the sample surface before and after acid treatment. XPS data were acquired using a spectrophotometer (VG Scientific ESCALAB 210) with an Al Kα X-ray source ($h\upsilon = 1486.68$ eV). The survey scan spectra were collected randomly at several points at

the binding energy (B.E.) of 0-1300 eV with a step size of 1 eV and a spot size of 400 μm.

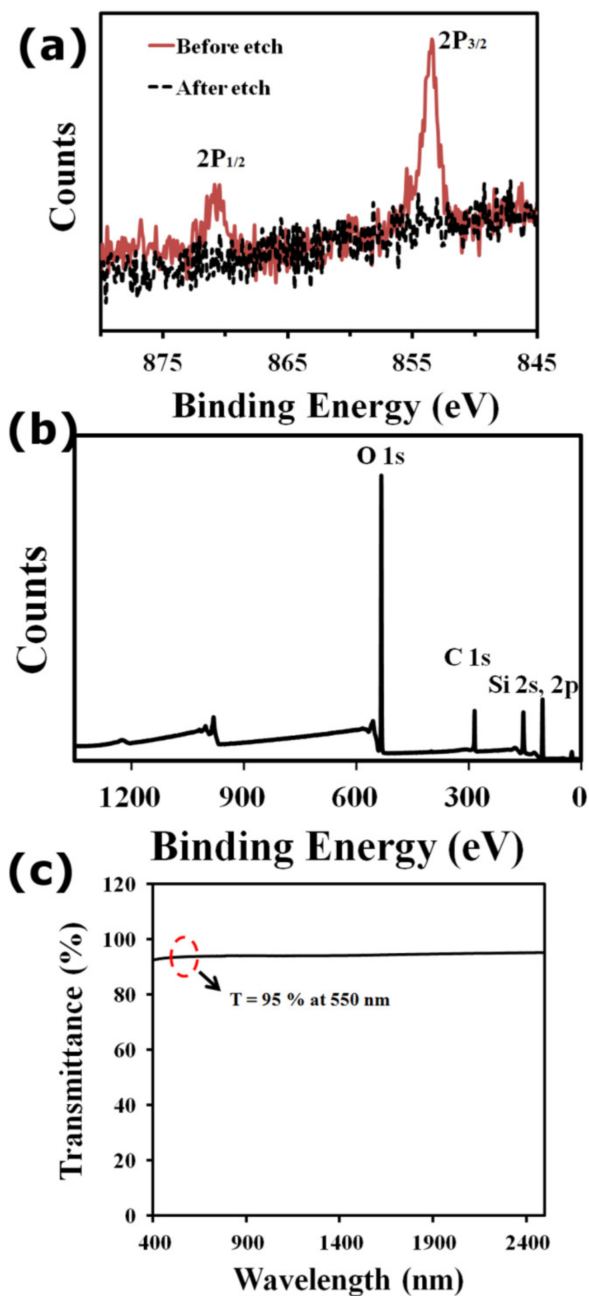

Figure 6.15. (a) Core level Ni XPS spectra shows removal of Ni after acid treatment. (b) Survey spectra collected randomly indicate the presence of C1s binding energy without any peaks for copper or Ni after acid treatment. (c) Average UV Vis spectra indicates the synthesized graphene in primarily bilayer showing ~95 % transmittance at 550 nm.

The same spot size with a step size of 0.5 eV was used for a core level scan. Comparison of Ni core level spectra before and after etching, shown in Figure 6.15 (a), suggests that the acid treatment effectively removed all metals from the graphene film as no Ni was observed beyond the detection limit of Ni in XPS (0.0055%). The survey spectra prominently showed the C1s and O1s peaks and the lack of any peak associated with copper or nickel [Figure 6.15 (b)]. Finally, graphene was grown on a quartz substrate with similar method.

A Cary 5E UV-Vis-NIR dual-beam spectrophotometer was used to measure the optical transmittance from 400-2500 nm of the samples directly grown on the quartz substrate after acid treatment. An average transmittance ~95% at 550 nm wavelength was observed in Figure 6.15 (c), suggesting that the sample synthesized through our technique consists of primarily bilayer graphene, as each layer absorbs between 2-2.5% at room temperature [132].

6.3.6. Patterned synthesis

To demonstrate the ability to perform patterned synthesis, a shadow mask was used to selectively evaporate Ni and Cu on the substrate with a channel size down to 30 µm wide [Figure 6.16 (a)]. Then, the samples underwent the synthesis process described previously. Figure 6.16 (b) and (d) show SEM images of the channel before and after metal etching. A zoomed image of the graphene is shown in Figure 6.16 (c). Raman spectroscopy was performed within the channel and on the areas believed to have graphene. No evidence of graphene formation was seen in the channels where the metals were not present. This indicates the ability to control and confine the synthesis of graphene layers to specific regions on the wafer surface without any post treatment patterning steps.

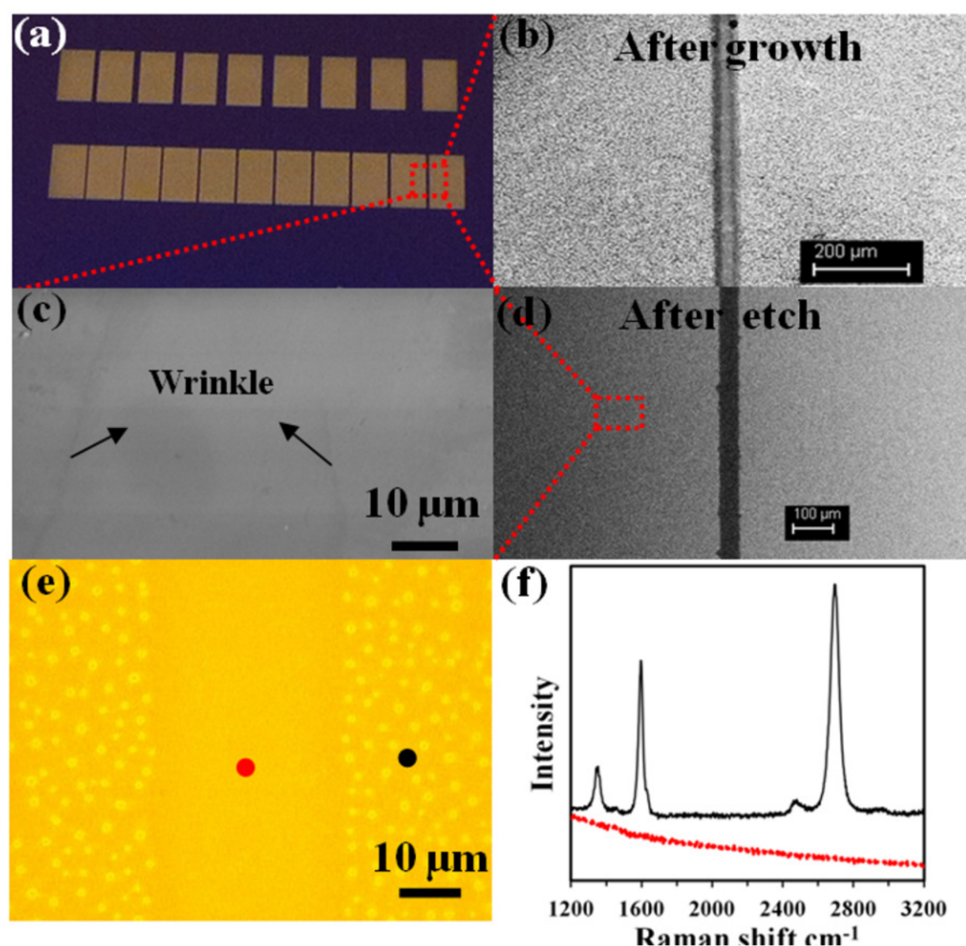

Figure 6.16. (a) Photograph of a typical patterned sample. (b) and (d) SEM images of a channel before and after acid treatment. (c) SEM image of a graphene sample showing wrinkles. (e) Optical image of a channel after growth, showing presence of Cu dots. (f) Representative Raman spectra show the presence of graphene on the areas where Ni and Cu were patterned. No graphitic peaks were observed at other areas (in the channel).

6.4. Conclusion

In this chapter, we report a new technique for producing large area, transfer-free graphene films on dielectric substrates. In the first section, our results demonstrate that the growth quality and Cu removal depend strongly on the type of growth substrate

utilized as well as the growth pressure and time. Quartz substrates were found to yield the highest quality films, although amorphous SiO_2 surfaces were better in terms of Cu removal during growth.

Synthesis using trace carbon dissolved in metals was tried in a totally different furnace for wafer-scale synthesis purposes, and the same quality graphene was synthesized. This indicates that this method is reproducible, unlike CVD graphene where the flow hydrodynamic of gaseous carbon is highly dependent on the furnace size and the gas flow rates. Our results demonstrate that the Ni provides the carbon source while the Cu film with significantly lower carbon solubility provides a medium extent of carbon in the bulk Ni/Cu after being heated at growth temperature. A controlled growth condition leads to formation of graphene both on top and underneath the Ni film.

Acid treatment post growth effectively removed the residual Cu after the synthesis step without liftoff of the graphene layer. Raman spectroscopy measurements after acid-treatment revealed the presence of continuous graphene layers across the substrate, while XPS confirmed the removal of all Cu and metal contaminants in the graphene film. This method, based on a solid carbon source, shows great potential for the direct synthesis of graphene on dielectric substrates including low cost SiO_2/Si substrates where the integration with other microelectronics may be possible.

CHAPTER 7

CONCLUSIONS AND FUTURE OUTLOOK

7.1. Conclusions

The research in this thesis has been conducted to advance the goal of developing graphene films for electronic device applications. To this end, graphene films were synthesized using CVD and transferred onto a variety of substrates for unintentional and intentional doping. In addition, issues with the transfer of CVD graphene were highlighted and overcome by developing new routes for transfer-free (direct) synthesis of graphene on dielectric substrates. The insight gained from investigating the impact of atmospheric dopants on graphene films was effectively leveraged to expand the present understanding of unintentional mechanisms for doping graphene films and to facilitate the development of stable and defect-free methods for intentional doping of these films. Transfer-free synthesis through trace carbon dissolved in metals opens a new pathway for patterned graphene where the carbon source is embedded in the growth substrate.

Important findings of this dissertation are as follows:

- Chapter 4 expanded the understanding of the impact that vacuum annealing, followed by exposure to oxygen and water vapor, has on the unintentional doping of CVD-grown graphene films. This chapter also presented the first known study to corroborate X-ray photoelectron spectroscopy analysis, work function measurements, in-situ Raman spectroscopy measurements, and mobility/carrier concentration measurements in order to clearly elucidate the effect of atmospheric dopants on the unintentional doping of graphene films. Observations of excess p-

dopant concentration on vacuum annealed graphene after re-exposure to air indicate that the removal of some intrinsic p-dopants creates room for water vapor and oxygen to be physically adsorbed on the graphene, which causes an increased concentration of p-type carrier. In-situ Raman measurements in a controlled environment (temperature/gas exposure) were performed for the first time on graphene samples; a hysteresis was observed in the position of graphitic peaks during heat up/cool down cycles. A hole doping concentration close to 1×10^{13} cm^{-2} on annealed and air-exposed graphene was obtained, and this correlates well with a 0.2 eV increase in the work function of graphene obtained from Kelvin Probe measurements. This chapter helps to utilize proper annealing of graphene FET devices for an optimum performance (increase in mobility and adjust carrier concentrations).

• Chapter 5 investigated the effect of self assembled monolayers (SAMs) on the electronic properties of graphene films. Monolithic and patterned SAMs were used to create n- and p-doped graphene, graphene p-n junctions, and FET devices containing p-n junctions in the device channels; these were created through transfer of CVD graphene onto SAMs coated substrates. X-ray photoelectron spectroscopy (XPS) mapping was also used to determine and present the first summarized report of the substrate treatment that was used to create n- and p-doping with a well defined boundary between areas of the substrate coated with the n- and p-type dopants. In-situ Raman spectroscopy was utilized in a controlled gas/temperature environment to investigate the doping of graphene film functionalized with SAMs. Simultaneous de-doping, through desorption of atmospheric dopants, and intentional p- and n- doping were observed by tracking the change in position of the graphitic peaks. Through examining defect peaks in Raman spectra before and after treatment, SAMs doping was shown not to result in introduction of defects in

graphene films. I-V measurements of FET devices containing patterned APTES layers show that it is possible to control the position of the two current minima (two separate Dirac points) in the ambipolar p-n junction.

• Chapter 6 provided the first report of the transfer-free synthesis of graphene films on dielectric substrates using solid carbon sources. Graphene films were synthesized through the thermal decomposition of poly(methyl methacrylate) on copper coated sapphire, quartz, Si/SiO_2, and AlN substrates in a low pressure H_2/Ar environment. This is the first report to indicate the formation of graphene both on top and underneath the transition metals, where a wet chemical etching process yielded graphene layers directly on the dielectric substrates. A similar approach was utilized to form graphene using trace carbon intrinsically dissolved in metals. The technique reported in this thesis could be scaled to large areas and is compatible with standard device fabrication technologies. Therefore, the research contribution of this dissertation can be leveraged with the present state-of-the-art in graphene films to advance the goal of manufacturing graphene-based field effect transistor (FET) devices. However, issues remain in the performance of these devices, and these must be addressed before graphene films can address commercial market needs. These primarily include further improving the carrier mobilities in these devices, improving the on/off ratio, and opening the bandgap through various chemical or electrostatic gating methods. These goals constitute future work and are discussed in the section to follow.

7.2. Future work

7.2.1. Improvement in the electrical properties of CVD graphene films

As explained earlier, CVD graphene films synthesized on Cu foil have undergone an annealing process under an H_2 environment in order to increase the grain size of the Cu. An increased grain size for Cu dictates an increased grain size for synthesized graphene. However, recent reports have shown that large grain size graphene can be obtained through two phase CVD growth, where the synthesis is stopped before super saturation of the catalyst Cu with C atoms dissolved from gas sources [73]. These graphene films have shown superior performance in FET devices where carrier mobilities have shown a significant increase.

In addition, the substrate has a significant impact on the performance of graphene based devices. Electron-substrate scattering and electron-impurity scattering have been shown as major issues with the performance of graphene FET devices. Recently, a group at Berkeley has shown that substituting SiO_2 with hexagonal boron nitride (hBN) can result in an order of magnitude increase in the carrier mobilities of CVD graphene films [109]. Therefore, another attempt towards higher carrier mobility is to utilize different substrates for graphene devices.

As explained in detail in Chapter 4, vacuum annealing has shown promise for removing contaminants and atmospheric dopants from graphene substrates. However, ultra high vacuum annealing at pressures as low as 10^{-8} Torr can result in complete removal of these groups. Furthermore, graphene films are washed with DI water many times during the transfer process, and this washing leaves significant dopants and impurities on transferred film. This process can be replaced by treating samples with solvents, such as methanol, that are less detergent in terms of induced impurities.

However, a comprehensive study that utilizes the impact of increased grain size graphene on modified substrate in conjunction with modified transfer process and proper

post transfer treatment is still lacking. An attempt to synthesize large grain size graphene followed by transfer onto hBN without using DI water, and utilizing instead ultra high vacuum annealing can result in a significant improvement in the carrier mobilities of CVD graphene films. This can open new pathways for CVD graphene applications on electronic devices.

7.2.2. Integration of CVD graphene films in OPV and OLED devices

The use of amine terminated SAMs were shown as an effective molecule to control the doping in graphene films in Chapter 5 of this work. More recently, an ultrathin layer of a polymer containing simple aliphatic amine groups, polyethylenimine ethoxylated (PEIE), was deposited on graphene and shown to lower its work function from 4.7±0.05 eV down to 3.8±0.1 eV indicating a large level of doping of the graphene with a simply polymer. Polyethylenimine, 80% ethoxylated (PEIE) (Mw = 70,000 g/mol), was dissolved in H_2O with a concentration of 35-40 wt.% when received from Aldrich. It was further diluted with 2-methoxyethanol (here after referred to as methoxyethanol) to a weight concentration of 0.4%. The solution was spin coated on top of the substrates at a speed of 5000 rpm for 1 min and with an acceleration of 1000 rpm/s. Spin-coated PEIE films were annealed at 100ºC for 10 min on a hotplate in ambient air. The thickness of these PEIE layers was determined to be around 10 nm by spectroscopic ellipsometry measurements (J. A. Woollam Co.) by considering a single-layer model (without surface roughness) and Cauchy refractive index dispersion characteristics.

Scanning Kelvin probe microscope (SKPM) techniques, similar to that explained in Chapter 4, were applied on the graphene before and after PEIE deposition and demonstrated that the work function can be lowered by over 1 eV. Figure 7.1 shows a schematic of the decrease in the work function of graphene after PEIE deposition. In contrast to the π-conjugated amine-containing small molecules and polymers considered earlier, for example APTES, PEIE is a band-gap insulator; it should not be regarded as a

charge-injection layer but rather as a surface modifier. The intrinsic molecular dipole moments associated with the neutral amine groups contained in such an insulating polymer layer, and the charge-transfer character of their interaction with the conductor surface, together reduce the WF of graphene.

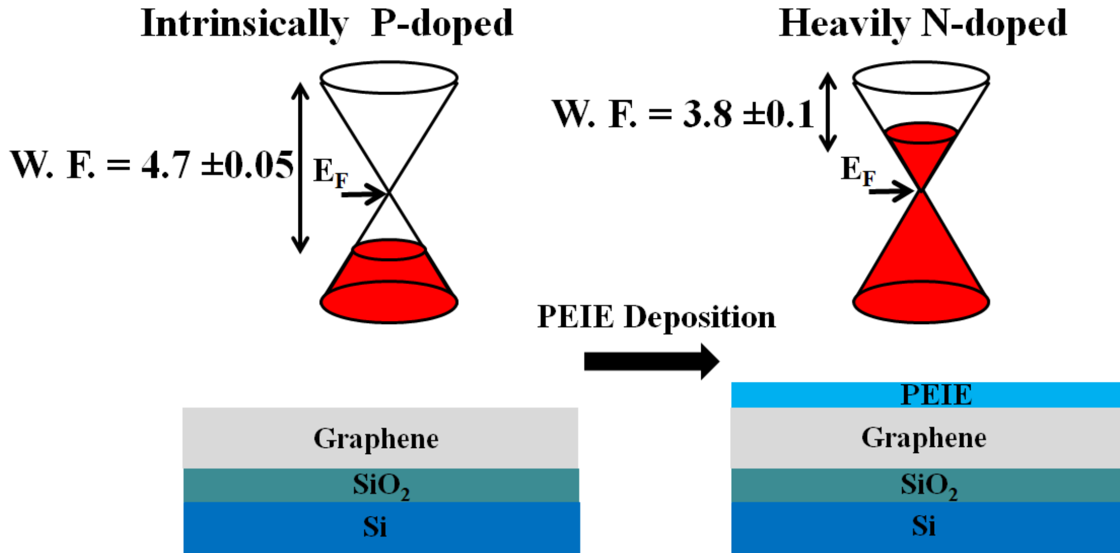

Figure 7.1. Schematic of decrease in work function of graphene after PEIE deposition.

Electrical measurements were performed on back-gated field effect graphene devices with a PEIE layer deposited on top, using a method similar to that explained in Chapter 3. Figure 7.2 shows $I_{D/S}$ vs. V_g for back-gated graphene with a layer of PEIE deposited on top using the method explained above. Unlike the graphene devices functionalized with APTES and PFES explained in Chapter 5, the Dirac point can be observed in these devices even without annealing. This indicates the significant impact of PEIE on the n-doping of graphene; it is dominant compared to the p-doping effect induced by atmospheric dopants. After annealing for only 30 minutes at 180°C, the Dirac point experienced a large shift to lower values, indicative of significant n-doping. The shifts in the Dirac point correlate well to the shift in the Kelvin Probe measurements,

verifying the changes in graphene doping. This method can be easily processed in air, from dilute solutions in environmentally friendly solvents such as water or methoxyethanol, and it does not suffer any change until a temperature of 190°C, making it compatible with the processing of printed electronic circuitry.

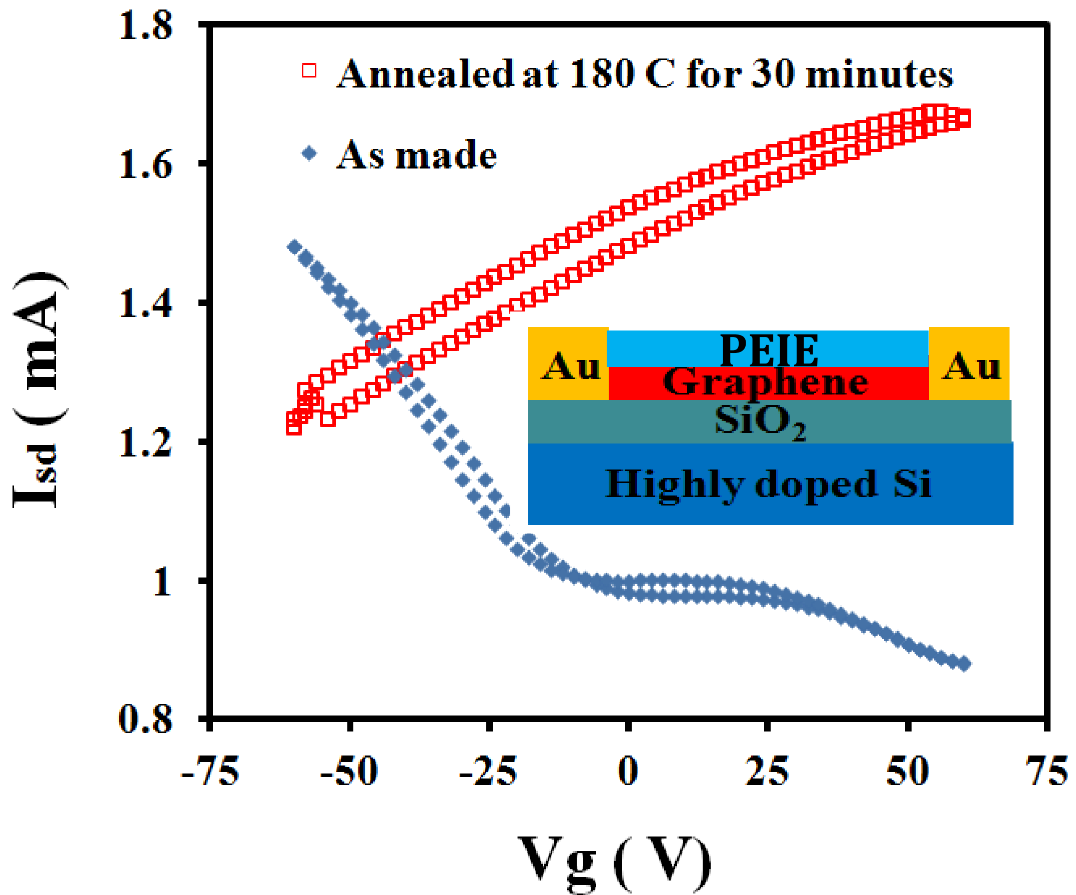

Figure 7.2. I-V characteristic curve for PEIE/graphene before and after heat treatment. Inset shows schematic of a back-gated graphene device with a thin layer of PEIE deposited on top.

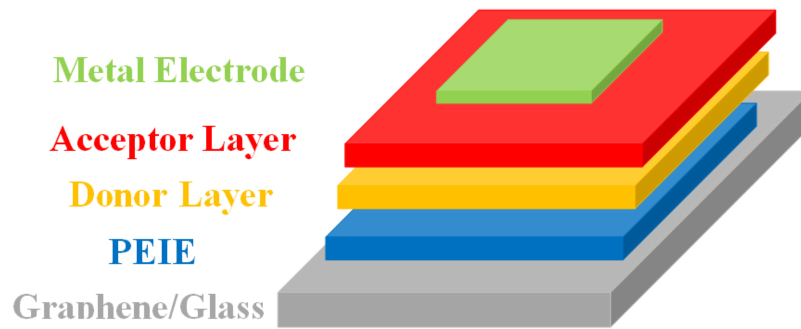

Figure 7.3. Schematic of an organic inverted-structure solar cell using graphene as electrode functionalized with PEIE for improved electron collection.

In the future, PEIE graphene films should be explored for application to organic electronics and photonics. In addition, the nature of the doping via PEIE should be studied in a more fundamental manner to understand the mechanism for substantial doping. Figure 7.3 shows a schematic of an inverted-solar cell in which graphene can be utilized as the cathode electrode. This chemical treatment, along with a layer-by-layer transfer of CVD graphene films for an increase in electrical conductivity, can be utilized to fabricate a solar cell or organic light emitting diode, where graphene can be utilized as a transparent conductive film. To collect electrons at the cathode effectively, the graphene work function can be lowered using a thin layer of PEIE deposited on top. This should increase the performance of this device due to increased electron collections by modified graphene film.

7.2.3. Low temperature and transfer-free synthesis of graphene on dielectric substrates

In Chapter 5 of this thesis we demonstrated the formation of graphene films directly on dielectric substrates where there is no need for a transfer process. This is attractive because most of today's transistor technology uses complementary metal-oxide

semiconductor (CMOS) technology in which an oxide layer insulates the transistor gate from the channel. However, in order for the technique to be easily adapted for use in Si based technology, low-temperature reactions (400-450°C) are required to maintain the mechanical integrity of low dielectric constant (K) intermetal dielectrics. Such graphene nano ribbons (GNR) were synthesized on dielectric substrates in low temperatures [80]. To this end, there is a need to develop a technique to self assemble an aromatic monolayer on the surface and to further perform the consolidation towards graphitic like materials. Therefore, the solid carbon sources utilized in Chapter 5 can be replaced by well-organized, thin aromatic layers, where there is no need for high temperature to break chemical bonds in order to provide the carbon sources required for graphene synthesis. Some of these compounds could be bianthracene or polyanthracene, as these are building blocks for graphitization and graphene synthesis. These compounds, along with a thin catalyst layer such as Cu, can be utilized towards low-temperature formation of graphene films.

REFERENCES

1. Geim, A.K. and K.S. Novoselov, *The Rise of Graphene.* Nat. Mater., 2007. **6**(3): p. 183-191.

2. Novoselov, K.S., et al., *Electric Field Effect in Atomically Thin Carbon Films.* Science, 2004. **306**(5696): p. 666-669.

3. Iijima, S., *HELICAL MICROTUBULES OF GRAPHITIC CARBON.* Nature, 1991. **354**(6348): p. 56-58.

4. Wallace, P.R., *THE BAND THEORY OF GRAPHITE.* Physical Review, 1947. **71**(9): p. 622-634.

5. Charlier, J.C., et al., *Electron and phonon properties of graphene: Their relationship with carbon nanotubes*, in *Carbon Nanotubes: Advanced Topics in the Synthesis, Structure, Properties and Applications*, A.D.G.D.M.S. Jorio, Editor. 2008. p. 673-709.

6. Falkovsky, L.A. and S.S. Pershoguba, *Optical far-infrared properties of a graphene monolayer and multilayer.* Physical Review B, 2007. **76**(15).

7. Wu, X.S., et al., *Half Integer Quantum Hall Effect in High Mobility Single Layer Epitaxial Graphene.* Applied Physics Letters, 2009. **95**(22).

8. Murali, R., et al., *Breakdown current density of graphene nanoribbons.* Applied Physics Letters, 2009. **94**(24).

9. Wu, Y., et al., *High-frequency, scaled graphene transistors on diamond-like carbon.* Nature, 2011. **472**(7341): p. 74-78.

10. Falkovsky, L.A., *Optical properties of graphene*, in *International Conference on Theoretical Physics 'Dubna-Nano2008'*, V.A.N.V.O.S.Y.M. Osipov, Editor. 2008.

11. Bae, S., et al., *Roll-to-roll production of 30-inch graphene films for transparent electrodes.* Nature Nanotechnology, 2010. **5**(8): p. 574-578.

12. Hecht, D.S., L.B. Hu, and G. Irvin, *Emerging Transparent Electrodes Based on Thin Films of Carbon Nanotubes, Graphene, and Metallic Nanostructures.* Advanced Materials, 2011. **23**(13): p. 1482-1513.

13. Choe, M., et al., *Efficient bulk-heterojunction photovoltaic cells with transparent multi-layer graphene electrodes.* Organic Electronics, 2010. **11**(11): p. 1864-1869.

14. Park, H., et al., *Doped graphene electrodes for organic solar cells.* Nanotechnology, 2010. **21**(50).

15. Wu, J.B., et al., *Organic Light-Emitting Diodes on Solution-Processed Graphene Transparent Electrodes.* Acs Nano, 2010. **4**(1): p. 43-48.

16. Kim, S.R., M.K. Parvez, and M. Chhowalla, *UV-reduction of graphene oxide and its application as an interfacial layer to reduce the back-transport reactions in dye-sensitized solar cells.* Chemical Physics Letters, 2009. **483**(1-3): p. 124-127.

17. Ma, H., et al., *Interface Engineering for Organic Electronics.* Advanced Functional Materials, 2010. **20**(9): p. 1371-1388.

18. Robinson, J.T., et al., *Reduced Graphene Oxide Molecular Sensors.* Nano Letters, 2008. **8**(10): p. 3137-3140.

19. Novoselov, K.S., et al., *Detection of individual gas molecules adsorbed on graphene.* Nature materials, 2007. **6**(9): p. 652-655.

20. Ghosh, A., et al., *NO2 and humidity sensing characteristics of few-layer graphenes.* Journal of Experimental Nanoscience, 2009. **4**(4): p. 313-322.

21. Fowler, J.D., et al., *Practical Chemical Sensors from Chemically Derived Graphene.* Acs Nano, 2009. **3**(2): p. 301-306.

22. Berger, C., et al., *Ultrathin Epitaxial Graphite:‚Äâ 2D Electron Gas Properties and a Route toward Graphene-based Nanoelectronics.* The Journal of Physical Chemistry B, 2004. **108**(52): p. 19912-19916.

23. Berger, C., et al., *Electronic Confinement and Coherence in Patterned Epitaxial Graphene.* Science, 2006. **312**(5777): p. 1191-1196.

24. Li, X.L., et al., *Chemically Derived, Ultrasmooth Graphene Nanoribbon Semiconductors.* Science, 2008. **319**(5867): p. 1229-1232.

25. Li, D., et al., *Processable Aqueous Dispersions of Graphene Nanosheets.* Nat. Nanotechnol., 2008. **3**(2): p. 101-105.

26. Hernandez, Y., et al., *High-Yield Production of Graphene by Liquid-phase Exfoliation of Graphite.* Nat. Nanotechnol., 2008. **3**(9): p. 563-568.

27. Li, X., et al., *Large-Area Synthesis of High-Quality and Uniform Graphene Films on Copper Foils.* Science, 2009. **324**(5932): p. 1312-1314.

28. Kim, K.S., et al., *Large-Scale Pattern Growth of Graphene Films for Stretchable Transparent Electrodes.* Nature, 2009. **457**(7230): p. 706-710.

29. Li, X.S., et al., *Large-Area Synthesis of High-Quality and Uniform Graphene Films on Copper Foils.* Science, 2009. **324**(5932): p. 1312-1314.

30. Reina, A., et al., *Large Area, Few-Layer Graphene Films on Arbitrary Substrates by Chemical Vapor Deposition.* Nano Lett., 2009. **9**(1): p. 30-35.

31. Coraux, J., et al., *Growth of graphene on Ir(111).* New Journal of Physics, 2009. **11**.

32. Traversi, F., V. Russo, and R. Sordan, *Integrated complementary graphene inverter.* Applied Physics Letters, 2009. **94**(22).

33. Han, T.H., et al., *Extremely efficient flexible organic light-emitting diodes with modified graphene anode.* Nature Photonics, 2012. **6**(2): p. 105-110.

34. Chiu, H.-Y., et al., *Controllable p-n Junction Formation in Mono layer Graphene Using Electrostatic Substrate Engineering.* Nano Letters, 2010. **10**(11): p. 4634-4639.

35. Liu, H., Y. Liu, and D. Zhu, *Chemical doping of graphene.* Journal of Materials Chemistry, 2011. **21**(10): p. 3335-3345.

36. Walter, A.L., et al., *Highly p-doped epitaxial graphene obtained by fluorine intercalation.* Applied Physics Letters, 2011. **98**(18).

37. Castro Neto, A.H., et al., *The electronic properties of graphene.* Reviews of Modern Physics, 2009. **81**(1): p. 109-162.

38. Malard, L.M., et al., *Raman Spectroscopy in Graphene.* Phys. Rep., 2009. **473**(5-6): p. 51-87.

39. Yu, Q.K., et al., *Graphene Segregated on Ni Surfaces and Transferred to Insulators.* Appl. Phys. Lett., 2008. **93**(11): p. 113103.

40. Wang, Z.H., et al., *RAMAN STUDIES OF ELECTRON-PHONON INTERACTION IN KXC70.* Physical Review B, 1993. **48**(22): p. 16881-16884.

41. Jiang, J., et al., *Electron-phonon matrix elements in single-wall carbon nanotubes.* Physical Review B, 2005. **72**(23).

42. Maultzsch, J., et al., *Phonon dispersion in graphite.* Physical Review Letters, 2004. **92**(7).

43. Xiao, W., M.I. Baskes, and K. Cho, *MEAM study of carbon atom interaction with Ni nano particle.* Surface Science, 2009. **603**(13): p. 1985-1998.

44. Ni, Z.H., et al., *Probing Charged Impurities in Suspended Graphene Using Raman Spectroscopy.* ACS Nano, 2009. **3**(3): p. 569-574.

45. Tuinstra, F. and J.L. Koenig, *Raman Spectrum of Graphite.* J. Chem. Phys., 1970. **53**(3): p. 1126-1130.

46. Lin, Y.C., et al., *Clean Transfer of Graphene for Isolation and Suspension.* ACS Nano, 2011. **5**(3): p. 2362-2368.

47. May, J.W., *Platinum Surface Leed Rings.* Surf. Sci., 1969. **17**(1): p. 267-279.

48. Eizenberg, M. and J.M. Blakely, *Carbon Monolayer Phase Condensation on Ni(111).* Surf. Sci., 1979. **82**(1): p. 228-236.

49. Eizenberg, M. and J.M. Blakely, *Carbon Interaction with Nickel Surfaces: Monolayer Formation and Structural Stability.* J. Chem. Phys., 1979. **71**(8): p. 3467-3477.

50. Rosei, R., et al., *Structure of Graphitic Carbon on Ni(111)- a Surface Extended-Energy-Loss Fine-Structure Study.* Phys. Rev. B, 1983. **28**(2): p. 1161-1164.

51. Land, T.A., et al., *STM Investigation of Single Layer Graphite Structures Produced on PT(111) by Hydrocarbon Decomposition.* Surf. Sci., 1992. **264**(3): p. 261-270.

52. Oshima, C. and A. Nagashima, *Ultra-thin Epitaxial Films of Graphite and Hexagonal Boron Nitride on Solid Surfaces.* J. Phys.: Condens. Matter, 1997. **9**(1): p. 1-20.

53. Novoselov, K.S., et al., *Two-dimensional Gas of Massless Dirac Fermions in Graphene.* Nature, 2005. **438**(7065): p. 197-200.

54. Zacharia, R., H. Ulbricht, and T. Hertel, *Interlayer cohesive energy of graphite from thermal desorption of polyaromatic hydrocarbons.* Physical Review B, 2004. **69**(15).

55. Sutter, P.W., J.I. Flege, and E.A. Sutter, *Epitaxial Graphene on Ruthenium.* Nat. Mater., 2008. **7**: p. 406-411.

56. Li, X.L., et al., *Highly Conducting Graphene Sheets and Langmuir–Blodgett Films.* Nat. Nanotechnol., 2008. **3**(9): p. 538-542.

57. de Heer, W.A., et al., *Large area and structured epitaxial graphene produced by confinement controlled sublimation of silicon carbide.* Proceedings of the National Academy of Sciences of the United States of America, 2011. **108**(41): p. 16900-16905.

58. Emtsev, K.V., et al., *Towards Wafer-Size Graphene Layers by Atmospheric Pressure Graphitization of SiC(0001).* Nat. Mater., 2009. **8**(3): p. 203-207.

59. Lin, Y.M., et al., *100-GHz Transistors from Wafer-Scale Epitaxial Graphene.* Science, 2010. **327**(5966): p. 662-662.

60. Eda, G., G. Fanchini, and M. Chhowalla, *Large-Area Ultrathin Films of Reduced Graphene Oxide as a Transparent and Flexible Electronic Material.* Nat. Nanotechnol., 2008. **3**(5): p. 270-274.

61. Tung, V.C., et al., *High-Throughput Solution Processing of Large-Scale Graphene.* Nat. Nanotechnol., 2009. **4**(1): p. 25-29.

62. Stankovich, S., et al., *Graphene-Based Composite Materials.* Nature, 2006. **442**: p. 282-286.

63. Dikin, D.A., et al., *Preparation and Characterization of Graphene Oxide Paper.* Nature, 2007. **448**(7152): p. 457-460.

64. Stankovich, S., et al., *Synthesis of graphene-based nanosheets via chemical reduction of exfoliated graphite oxide.* Carbon, 2007. **45**(7): p. 1558-1565.

65. Yang, W., et al., *Carbon Nanomaterials in Biosensors: Should You Use Nanotubes or Graphene?* Angewandte Chemie-International Edition, 2010. **49**(12): p. 2114-2138.

66. Choucair, M., P. Thordarson, and J.A. Stride, *Gram-scale production of graphene based on solvothermal synthesis and sonication.* Nature Nanotechnology, 2009. **4**(1): p. 30-33.

67. Ramon, M.E., et al., *CMOS-Compatible Synthesis of Large-Area, High-Mobility Graphene by Chemical Vapor Deposition of Acetylene on Cobalt Thin Films.* Acs Nano, 2011. **5**(9): p. 7198-7204.

68. Nandamuri, G., S. Roumimov, and R. Solanki, *Chemical vapor deposition of graphene films.* Nanotechnology, 2010. **21**(14): p. 145604.

69. Hayes, A. and J. Chipman, *Mechanism of solidification and segregation in a low-carbon rimming-steel ingot.* Transactions of the American Institute of Mining and Metallurgical Engineers, 1939. **135**: p. 85-125.

70. Cao, H., et al., *Electronic transport in chemical vapor deposited graphene synthesized on Cu: Quantum Hall effect and weak localization.* Applied Physics Letters, 2010. **96**(12).

71. Levendorf, M.P., et al., *Transfer-Free Batch Fabrication of Single Layer Graphene Transistors.* Nano Lett., 2009. **9**(12): p. 4479-4483.

72. Liu, N., et al., *Universal Segregation Growth Approach to Wafer-Size Graphene from Non-Noble Metals.* Nano Letters, 2011. **11**(1): p. 297-303.

73. Yu, Q.K., et al., *Control and characterization of individual grains and grain boundaries in graphene grown by chemical vapour deposition.* Nature Materials, 2011. **10**(6): p. 443-449.

74. Hofrichter, J., et al., *Synthesis of Graphene on Silicon Dioxide by a Solid Carbon Source.* Nano Lett., 2010. **10**(1): p. 36-42.

75. Garcia, J.M., et al., *Multi Layer Graphene Grown by Precipitation upon Cooling of Nickel on Diamond.* Carbon, 2011. **49**(3): p. 1006-1012.

76. Perdigao, L.M.A., et al., *Graphene Formation by Decomposition of C-60.* J. Phys. Chem. C 2011. **115**(15): p. 7472-7476.

77. Xu, M.S., et al., *Production of Extended Single-Layer Graphene.* ACS Nano, 2011. **5**(2): p. 1522-1528.

78. Sun, Z.Z., et al., *Growth of Graphene from Solid Carbon Sources.* Nature, 2010. **468**(7323): p. 549-552.

79. Li, Z.C., et al., *Low-Temperature Growth of Graphene by Chemical Vapor Deposition Using Solid and Liquid Carbon Sources.* ACS Nano, 2011. **5**(4): p. 3385-3390.

80. Rummeli, M.H., et al., *Direct Low-Temperature Nanographene CVD Synthesis over a Dielectric Insulator.* ACS Nano, 2010. **4**(7): p. 4206-4210.

81. Ismach, A., et al., *Direct Chemical Vapor Deposition of Graphene on Dielectric Surfaces.* Nano Lett., 2010. **10**(5): p. 1542-1548.

82. Schedin, F., et al., *Detection of individual gas molecules adsorbed on graphene.* Nature Materials, 2007. **6**(9): p. 652-655.

83. Lafkioti, M., et al., *Graphene on a Hydrophobic Substrate: Doping Reduction and Hysteresis Suppression under Ambient Conditions.* Nano Letters, 2010. **10**(4): p. 1149-1153.

84. Aubry, J.M., et al., *Reversible binding of oxygen to aromatic compounds.* Accounts of Chemical Research, 2003. **36**(9): p. 668-675.

85. Jurchescu, O.D., J. Baas, and T.T.M. Palstra, *Electronic transport properties of pentacene single crystals upon exposure to air.* Applied Physics Letters, 2005. **87**(5).

86. Collins, P.G., et al., *Extreme oxygen sensitivity of electronic properties of carbon nanotubes.* Science, 2000. **287**(5459): p. 1801-1804.

87. Abdou, M.S.A., et al., *REVERSIBLE CHARGE-TRANSFER COMPLEXES BETWEEN MOLECULAR-OXYGEN AND POLY(3-ALKYLTHIOPHENE)S.* Advanced Materials, 1994. **6**(11): p. 838-841.

88. Ryu, S., et al., *Atmospheric Oxygen Binding and Hole Doping in Deformed Graphene on a SiO(2) Substrate.* Nano Letters, 2010. **10**(12): p. 4944-4951.

89. Ni, Z.H., et al., *The effect of vacuum annealing on graphene.* Journal of Raman Spectroscopy, 2010. **41**(5): p. 479-483.

90. Nourbakhsh, A., et al., *Tuning the Fermi Level of SiO(2)-Supported Single-Layer Graphene by Thermal Annealing.* Journal of Physical Chemistry C, 2010. **114**(15): p. 6894-6900.

91. Cheng, Z.G., et al., *Toward Intrinsic Graphene Surfaces: A Systematic Study on Thermal Annealing and Wet-Chemical Treatment of SiO(2)-Supported Graphene Devices.* Nano Letters, 2011. **11**(2): p. 767-771.

92. Wei, D.C., et al., *Synthesis of N-Doped Graphene by Chemical Vapor Deposition and Its Electrical Properties.* Nano Letters, 2009. **9**(5): p. 1752-1758.

93. Panchokarla, L.S., et al., *Synthesis, Structure, and Properties of Boron- and Nitrogen-Doped Graphene.* Advanced Materials, 2009. **21**(46): p. 4726-+.

94. Guo, B., et al., *Controllable N-Doping of Graphene.* Nano Letters, 2010.

95. Wang, X.R., et al., *N-Doping of Graphene Through Electrothermal Reactions with Ammonia.* Science, 2009. **324**(5928): p. 768-771.

96. Shi, Y., et al., *Work Function Engineering of Graphene Electrode via Chemical Doping.* Acs Nano, 2010. **4**(5): p. 2689-2694.

97. Gunes, F., et al., *Layer-by-Layer Doping of Few-Layer Graphene Film.* Acs Nano, 2010. **4**(8): p. 4595-4600.

98. Kim, K.K., et al., *Enhancing the conductivity of transparent graphene films via doping.* Nanotechnology, 2010. **21**(28).

99. Yang, Y. and R. Murali, *Binding mechanisms of molecular oxygen and moisture to graphene.* Applied Physics Letters, 2011. **98**(9).

100. Wang, X., et al., *N-Doping of Graphene Through Electrothermal Reactions with Ammonia.* Science, 2009. **324**(5928): p. 768-771.

101. Jin, Z., et al., *Large-Scale Growth and Characterizations of Nitrogen-Doped Monolayer Graphene Sheets.* Acs Nano, 2011. **5**(5): p. 4112-4117.

102. Lin, Y.-C., C.-Y. Lin, and P.-W. Chiu, *Controllable graphene N-doping with ammonia plasma*. Vol. 96. 2010: AIP. 133110.

103. Zhang, C., et al., *Synthesis of Nitrogen-Doped Graphene Using Embedded Carbon and Nitrogen Sources.* Advanced Materials, 2011. **23**(8): p. 1020-1024.

104. Dong, X.C., et al., *Doping Single-Layer Graphene with Aromatic Molecules.* Small, 2009. **5**(12): p. 1422-1426.

105. Das, B., et al., *Changes in the electronic structure and properties of graphene induced by molecular charge-transfer.* Chemical Communications, 2008(41): p. 5155-5157.

106. Meyer, J.C., et al., *The structure of suspended graphene sheets.* Nature, 2007. **446**(7131): p. 60-63.

107. Bolotin, K.I., et al., *Ultrahigh electron mobility in suspended graphene.* Solid State Communications, 2008. **146**(9-10): p. 351-355.

108. Du, X., et al., *Approaching ballistic transport in suspended graphene.* Nature nanotechnology, 2008. **3**(8): p. 491-5.

109. Dean, C.R., et al., *Boron nitride substrates for high-quality graphene electronics.* Nature Nanotechnology, 2010. **5**(10): p. 722-726.

110. Kobayashi, S., et al., *Control of carrier density by self-assembled monolayers in organic field-effect transistors.* Nature Materials, 2004. **3**(5): p. 317-322.

111. Ito, Y., et al., *Crystalline Ultrasmooth Self-Assembled Monolayers of Alkylsilanes for Organic Field-Effect Transistors.* Journal of the American Chemical Society, 2009. **131**(26): p. 9396-9404.

112. Pernstich, K.P., et al., *Threshold voltage shift in organic field effect transistors by dipole monolayers on the gate insulator.* Journal of Applied Physics, 2004. **96**(11): p. 6431-6438.

113. Vosgueritchian, M., et al., *Effect of Surface Chemistry on Electronic Properties of Carbon Nanotube Network Thin Film Transistors.* Acs Nano, 2010. **4**(10): p. 6137-6145.

114. Park, J., et al., *Work-Function Engineering of Graphene Electrodes by Self-Assembled Monolayers for High-Performance Organic Field-Effect Transistors.* Journal of Physical Chemistry Letters, 2011. **2**(8): p. 841-845.

115. Liu, Z.H., A.A. Bol, and W. Haensch, *Large-Scale Graphene Transistors with Enhanced Performance and Reliability Based on Interface Engineering by Phenylsilane Self-Assembled Monolayers.* Nano Letters, 2011. **11**(2): p. 523-528.

116. Wang, R., et al., *Control of Carrier Type and Density in Exfoliated Graphene by Interface Engineering.* Acs Nano, 2011. **5**(1): p. 408-412.

117. Yan, Z., et al., *Controlled Modulation of Electronic Properties of Graphene by Self-Assembled Monolayers on SiO(2) Substrates.* Acs Nano, 2011. **5**(2): p. 1535-1540.

118. Shin, W.C., S. Seo, and B.J. Cho, *Highly air-stable electrical performance of graphene field effect transistors by interface engineering with amorphous fluoropolymer.* Applied Physics Letters, 2011. **98**(15).

119. Wang, X.M., et al., *High-Performance Graphene Devices on SiO(2)/Si Substrate Modified by Highly Ordered Self-Assembled Monolayers.* Advanced Materials, 2011. **23**(21): p. 2464-+.

120. Wang, R., et al., *Control of Carrier Type and Density in Exfoliated Graphene by Interface Engineering.* Acs Nano, 2011. **5**(1): p. 408-412.

121. Abanin, D.A. and L.S. Levitov, *Quantized transport in graphene p-n junctions in a magnetic field.* Science, 2007. **317**(5838): p. 641-643.

122. Williams, J.R., L. DiCarlo, and C.M. Marcus, *Quantum hall effect in a gate-controlled p-n junction of graphene.* Science, 2007. **317**(5838): p. 638-641.

123. Katsnelson, M.I., K.S. Novoselov, and A.K. Geim, *Chiral tunnelling and the Klein paradox in graphene.* Nature Physics, 2006. **2**(9): p. 620-625.

124. Cheianov, V.V., V. Fal'ko, and B.L. Altshuler, *The focusing of electron flow and a Veselago lens in graphene p-n junctions.* Science, 2007. **315**(5816): p. 1252-1255.

125. Yu, T.H., et al., *Local electrical stress-induced doping and formation of monolayer graphene P-N junction.* Applied Physics Letters, 2011. **98**(24).

126. Lohmann, T., K. von Klitzing, and J.H. Smet, *Four-Terminal Magneto-Transport in Graphene p-n Junctions Created by Spatially Selective Doping.* Nano Letters, 2009. **9**(5): p. 1973-1979.

127. Farmer, D.B., et al., *Behavior of a chemically doped graphene junction.* Applied Physics Letters, 2009. **94**(21).

128. Cheng, H.C., et al., *High-Quality Graphene p-n Junctions via Resist-free Fabrication and Solution-Based Noncovalent Functionalization.* Acs Nano, 2011. **5**(3): p. 2051-2059.

129. Chakraborty, B., A. Das, and A.K. Sood, *The formation of a p-n junction in a polymer electrolyte top-gated bilayer graphene transistor.* Nanotechnology, 2009. **20**(36).

130. Ferrari, A.C., et al., *Raman Spectrum of Graphene and Graphene Layers.* Phys. Rev. Lett., 2006. **97**(18): p. 187401.

131. Weber, J.W., V.E. Calado, and M.C.M. van de Sanden, *Optical constants of graphene measured by spectroscopic ellipsometry.* Applied Physics Letters, 2010. **97**(9).

132. Nair, R.R., et al., *Fine structure constant defines visual transparency of graphene.* Science, 2008. **320**(5881): p. 1308-1308.

133. Nelson, F.J., et al., *Optical properties of large-area polycrystalline chemical vapor deposited graphene by spectroscopic ellipsometry.* Applied Physics Letters, 2010. **97**(25).

134. Schaffler, F., *High-mobility Si and Ge structures.* Semiconductor Science and Technology, 1997. **12**(12): p. 1515-1549.

135. Yamashita, Y., *Organic semiconductors for organic field-effect transistors.* Science and Technology of Advanced Materials, 2009. **10**(2).

136. Geim, A.K., *Graphene: Status and Prospects.* Science, 2009. **324**(5934): p. 1530-1534.

137. Schwierz, F., *Graphene transistors.* Nat Nano, 2010. **5**(7): p. 487-496.

138. Schwierz, F., *Graphene transistors.* Nature Nanotechnology, 2010. **5**(7): p. 487-496.

139. Shen, Z.X., et al., *The effect of vacuum annealing on graphene.* Journal of Raman Spectroscopy, 2010. **41**(5): p. 479-483.

140. Thomson, S.W., *Reprint of Papers on Electrostatics and Magnetism.* 1884, London: MacMillan.

141. Hu, L., D.S. Hecht, and G. Gruner, *Percolation in transparent and conducting carbon nanotube networks.* Nano Letters, 2004. **4**(12): p. 2513-2517.

142. De, S. and J.N. Coleman, *Are There Fundamental Limitations on the Sheet Resistance and Transmittance of Thin Graphene Films?* Acs Nano, 2010. **4**(5): p. 2713-2720.

143. Liu, L., et al., *Graphene oxidation: thickness-dependent etching and strong chemical doping.* Nano Letters, 2008. **8**(7): p. 1965-70.

144. Dan, Y., et al., *Intrinsic Response of Graphene Vapor Sensors.* Nano Letters, 2009. **9**(4): p. 1472-1475.

145. Lu, G.H., et al., *Ultrafast room temperature NH(3) sensing with positively gated reduced graphene oxide field-effect transistors.* Chemical Communications, 2011. **47**(27): p. 7761-7763.

146. Lei, N., et al., *Simple graphene chemiresistors as pH sensors: fabrication and characterization.* Measurement Science & Technology, 2011. **22**(10).

147. Pantelic, R.S., et al., *Graphene: Substrate preparation and introduction.* Journal of Structural Biology, 2011. **174**(1): p. 234-238.

148. Calizo, I., et al., *Raman nanometrology of graphene: Temperature and substrate effects.* Solid State Communications, 2009. **149**(27-28): p. 1132-1135.

149. Calizo, I., et al., *Temperature dependence of the Raman spectra of graphene and graphene multilayers.* Nano Letters, 2007. **7**(9): p. 2645-2649.

150. Calizo, I., et al., *Variable temperature Raman microscopy as a nanometrology tool for graphene layers and graphene-based devices.* Applied Physics Letters, 2007. **91**(7).

151. DasA, et al., *Monitoring dopants by Raman scattering in an electrochemically top-gated graphene transistor.* Nat Nano, 2008. **3**(4): p. 210-215.

152. Pisana, S., et al., *Breakdown of the adiabatic Born-Oppenheimer approximation in graphene.* Nature Materials, 2007. **6**(3): p. 198-201.

153. Hollinger, G., et al., *X-RAY PHOTOELECTRON-SPECTROSCOPY OF THERMALLY GROWN SILICON DIOXIDE FILMS ON SILICON.* Chemical Physics Letters, 1975. **36**(4): p. 441-445.

154. Baikie, I.D., et al., *Work function study of rhenium oxidation using an ultra high vacuum scanning Kelvin probe.* Journal of Applied Physics, 2000. **88**(7): p. 4371-4375.

155. Zhou, Y.H., et al., *A Universal Method to Produce Low-Work Function Electrodes for Organic Electronics.* Science, 2012. **336**(6079): p. 327-332.

156. Ohta, T., et al., *Controlling the electronic structure of bilayer graphene.* Science, 2006. **313**(5789): p. 951-954.

157. Usachov, D., et al., *Nitrogen-Doped Graphene: Efficient Growth, Structure, and Electronic Properties.* Nano Letters, 2011. **11**(12): p. 5401-5407.

158. Zhao, L.Y., et al., *Visualizing Individual Nitrogen Dopants in Monolayer Graphene.* Science, 2011. **333**(6045): p. 999-1003.

159. Zhou, S.Y., et al., *Substrate-induced bandgap opening in epitaxial graphene.* Nature materials, 2007. **6**(10): p. 770-5.

160. Han, M.Y., et al., *Energy band-gap engineering of graphene nanoribbons.* Physical Review Letters, 2007. **98**(20).

161. Chiu, H.Y., et al., *Controllable p-n Junction Formation in Mono layer Graphene Using Electrostatic Substrate Engineering.* Nano Letters, 2010. **10**(11): p. 4634-4639.

162. Farmer, D.B., et al., *Behavior of a chemically doped graphene junction.* Applied Physics Letters, 2009. **94**(21).

163. Dai, H.J., et al., *N-Doping of Graphene Through Electrothermal Reactions with Ammonia.* Science, 2009. **324**(5928): p. 768-771.

164. Ast, C.R., et al., *Atomic Hole Doping of Graphene.* Nano letters, 2008. **8**(12): p. 4603-4607.

165. Heremans, P., et al., *Static solvent contact angle measurements, surface free energy and wettability determination of various self-assembled monolayers on silicon dioxide.* Thin Solid Films, 2006. **515**(4): p. 1433-1438.

166. Kowalczyk, D., et al., *Adsorption of aminopropyltriethoxy silane on quartz: An XPS and contact angle measurements study.* International Journal of Adhesion and Adhesives, 1996. **16**(4): p. 227-232.

167. Hooper, A.E., et al., *Evaluation of amine- and amide-terminated self-assembled monolayers as 'Molecular glues' for Au and SiO2 substrates.* Surface and Interface Analysis, 2001. **31**(9): p. 809-814.

168. Chirakul, P., et al., *Self-assembled monolayers of amine-terminated thiols.* Abstracts of Papers of the American Chemical Society, 1999. **217**: p. U668-U668.

169. Yokota, K., K. Takai, and T. Enoki, *Carrier Control of Graphene Driven by the Proximity Effect of Functionalized Self-assembled Monolayers.* Nano letters, 2011.

170. Wang, R., et al., *Control of Carrier Type and Density in Exfoliated Graphene by Interface Engineering.* ACS Nano, 2010. **5**(1): p. 408-412.

171. Brenner, K. and R. Murali, *Single step, complementary doping of graphene.* Applied Physics Letters, 2010. **96**(6).

172. Ashkenasy, G., et al., *Molecular engineering of semiconductor surfaces and devices.* Accounts of Chemical Research, 2002. **35**(2): p. 121-128.

173. Ishii, H., et al., *Energy level alignment and interfacial electronic structures at organic metal and organic organic interfaces.* Advanced Materials, 1999. **11**(8): p. 605-+.

174. Campbell, I.H., et al., *Controlling Schottky energy barriers in organic electronic devices using self-assembled monolayers.* Physical Review B, 1996. **54**(20): p. 14321-14324.

175. Campbell, I.H., et al., *Controlling charge injection in organic electronic devices using self-assembled monolayers.* Applied Physics Letters, 1997. **71**(24): p. 3528-3530.

176. Hotchkiss, P.J., et al., *Modification of the Surface Properties of Indium Tin Oxide with Benzylphosphonic Acids: A Joint Experimental and Theoretical Study.* Advanced Materials, 2009. **21**(44): p. 4496-+.

177. Rao, G., et al., *Raman and Photocurrent Imaging of Electrical Stress-Induced p-n Junctions in Graphene.* Acs Nano, 2011. **5**(7): p. 5848-5854.

178. Peters, E.C., et al., *Gate dependent photocurrents at a graphene p-n junction.* Applied Physics Letters, 2010. **97**(19).

179. Pirkle, A., et al., *The effect of chemical residues on the physical and electrical properties of chemical vapor deposited graphene transferred to SiO(2).* Applied Physics Letters, 2011. **99**(12).

180. Stander, N., B. Huard, and D. Goldhaber-Gordon, *Evidence for Klein Tunneling in Graphene p-n Junctions.* Physical Review Letters, 2009. **102**(2).

181. Young, A.F. and P. Kim, *Quantum interference and Klein tunnelling in graphene heterojunctions.* Nature Physics, 2009. **5**(3): p. 222-226.

182. Juang, Z.Y., et al., *Synthesis of Graphene on Silicon Carbide Substrates at Low Temperature.* Carbon, 2009. **47**(8): p. 2026-2031.

183. Byun, S.J., et al., *Graphenes Converted from Polymers.* J. Phys. Chem. Lett., 2011. **2**(5): p. 493-497.

184. Liu, X., et al., *Segregation Growth of Graphene on Cu-Ni Alloy for Precise Layer Control.* Journal of Physical Chemistry C, 2011. **115**(24): p. 11976-11982.